Modelling Columnar and Equiaxed Growth

David J. Browne, B.E., M.Sc.

St. Anne's College, Oxford

A thesis submitted for the degree of Doctor of Philosophy

in the University of Oxford

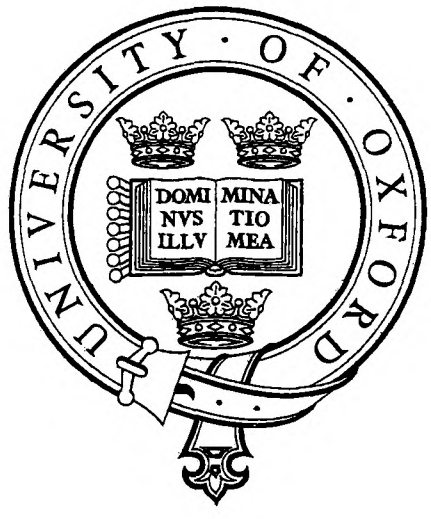

Department of Materials

University of Oxford

Trinity term, 2002

ABSTRACT

MODELLING COLUMNAR AND EQUIAXED GROWTH

David John Browne, B.E., M.Sc.,

St. Anne's College, Oxford

Submitted for the degree of D.Phil.

Trinity term, 2002

A novel computer model of the evolution of columnar and equiaxed microstructure during alloy solidification has been developed. A control volume finite difference model of conduction heat transfer is applied to a two-dimensional domain bounded by a relatively cold mould. The initial condition is that of superheated liquid, and nucleation occurs either at the mould wall, leading to columnar dendritic growth, or within the bulk liquid, leading to the growth of equiaxed dendrites. The columnar front or the equiaxed grain boundaries are represented by computationally sharp interfaces, which separate liquid from partially solid alloy. Interpolation between discrete computational markers is employed to describe these interfaces, and a front-tracking technique is used to predict the evolution of the grain structure, via movement of the markers, across the fixed grid. The front velocity is determined via considerations of the kinetics of dendrite growth. The heat equation is fully coupled to the front-tracking algorithm by means of source terms which represent the evolution of latent heat due to the dendritic growth (advancing tips and thickening mushy zone). The model, applied to binary Al-Cu alloys, is computationally efficient. It predicts the variation of the extent of liquid undercooling ahead of the growing columnar front, and new metrics have been established to determine the likelihood of the formation of an equiaxed zone here. The employment of these metrics to establish the influence of heat extraction rate and alloy composition agrees with reports from the literature. The model does not distinguish between individual grains of the columnar zone, but it is shown that this is not an important limitation for most metal casting applications. Direct simulation of the nucleation and growth of multiple equiaxed crystals has been carried out, in which the nucleation and growth of individual grains can be observed via animation, and the influence of melt superheat and heat extraction rate on equiaxed solidification has been determined.

To Ann Marie, Emily and Isabel

Preface

The work described in this thesis was carried out by the author under the supervision of Professor J.D. Hunt, FRS, primarily in the Department of Materials, University of Oxford, from January 1997 to September 2002. The author carried out some of the computer modelling work at the Department of Mechanical Engineering, University College Dublin. The research described here is original; no part of this thesis has already been accepted or is being concurrently submitted for any degree or other qualification in the University of Oxford or elsewhere. Where the work of others has been drawn upon it is acknowledged in the thesis.

Some of the work has already been published, as follows :

Browne, D.J. and Hunt, J.D., A model of columnar growth using a front-tracking technique, *Modelling of Casting, Welding and Advanced Solidification Processes IX,* (Eds. P.R. Sahm, P.N. Hansen, and J.G. Conley), Shaker Verlag, Aachen, 437-444, 2000.

Browne, D.J. and Hunt, J.D., Modelling of moving boundaries in multi-phase systems : a front-tracking approach, *Proceedings of the 3rd International Conference on Transport Phenomena in Multiphase Systems* (Eds. M.E. Poniewski, T. Wójcik and R. Pastuszko), Baranów Sandomierski, Poland, 227-232, 2002.

Browne, D.J., Banaszek, J. and Hunt. J.D., Front tracking on a fixed grid versus enthalpy approach in modelling of binary alloy solidification, *Proceedings of the International Mechanical Engineering Congress and Exhibition*, New Orleans, USA, paper IMECE2002-32871, 2002.

Acknowledgements

I would like to sincerely thank Prof. John D. Hunt, FRS, for the excellent supervision of this project since 1997. He has been a source of wisdom and encouragement throughout this work, and very good company. My thanks extend beyond assistance with the work laid out in this thesis, as 14 years ago Prof. Hunt took me on as a student for the degree of M.Sc., which I was awarded in 1990.

I would like to thank successive Heads of the Department of Materials at Oxford - Professors B. Cantor, FREng and G.D.W. Smith, FRS - for the provision of laboratory facilities. I am grateful also to the staff of the Department, who have been most helpful.

Thanks are due to the Principal, Secretary and Registrar, and other Fellows of St. Anne's College for their kind assistance over the years.

I dedicate this thesis to Emily and Isabel, who arrived in that order during the progress of the work, and to Ann Marie who has been with me from its inception. Thank you for your encouragement and for your patience, especially during my extended absences over five, three and six years, respectively.

I would like to thank Professor Paul Steen, School of Chemical Engineering, Cornell University, NY, USA, who facilitated my study there in the period immediately preceding my starting the D.Phil. project at Oxford. The following friends and colleagues were most helpful and supportive at Oxford : Dr. Q. Han, Dr. H. Dong, Mr. K. Seto, Dr. P. Emms, Dr. M. Yun, Dr. S. Lockyer, Dr. M. Sin, Dr. A. Chilton and Ms. Tracey Cockfield - thank you.

Thanks are due also to my colleagues at University College Dublin, in particular to Dr. Alun Carr, whose support, advice and friendship have been invaluable. Professor Jerzy ("Jurek") Banaszek, visiting Dublin from the Warsaw University of Technology, has been most helpful

with developing new insights into models of alloy solidification, and with the verification of the front-tracking model described in the thesis; thank you Jurek. I am also grateful to Professor Gerald Byrne for facilitating my Oxford D. Phil. studies. I would like to thank too Mr. Neal Murphy for taking a continual interest in my progress, and hereby wish him well in his own doctoral studies.

This work would not have been possible without the financial sponsorship of Materials Ireland, and I am particularly grateful to its Director, Mr. Jim Lawler, for enabling assistance in this regard.

My M.Sc. thesis was dedicated to my parents Tom and Pat. I am pleased to report that they, along with my mother-in-law, Joan, were of great help in looking after Emily and Isabel, particularly when Ann Marie and I took the very infrequent break from all of this. Thank you.

David J. Browne

St. Anne's College, Oxford,

Trinity term 2002

Contents

Chapter One

Introduction and Background Theory - Solidification

Chapter 1

Introduction and Background Theory - Solidification

1.1 Introduction

Practically all metal components have been through a solidification phase change at some stage. In some cases such solidification occurs early in the processing route e.g. at the alloy refinement stage. In others solidification is the net shape manufacturing stage e.g. in the investment casting of turbine rotors for automotive turbochargers. In cases where substantial processing occurs downstream of an early solidification stage, it may be that the as-cast microstructure is not that important as it subsequently may be altered significantly. But in shape casting processes there is often little or no subsequent processing before the resultant component goes into service. Here solidification microstructure is vitally important. Apart from defects, some of the dominant factors affecting the mechanical properties of a casting are its grain structure and grain size distribution. For this reason it is often desirable to control the grain structure of cast parts, and this can be facilitated by numerical models of the evolution of such structure during solidification. The development of such a model is the subject of this thesis. The two major zones of as-cast microstructure are the columnar zone and the equiaxed zone. In this chapter some of the underlying fundamentals of solidification are presented. In the next, issues relating to the numerical modelling of solidification are dealt with.

1.2 Nucleation of Solid

The driving force for any phase transformation is the difference in free energy (usually the Gibbs free energy G) of the initial and final states [1]. Transformation begins from identifiable centres in the original phase; a process called nucleation.

For a pure metal, solid and liquid are in equilibrium (G_S-G_L= ΔG=0) at the melting point T_m. For an alloy this can occur at the equilibrium liquidus temperature T_L, where the liquid is of the nominal composition C_o. Such equilibrium can also occur at lower temperatures, down to the solidus temperature T_S, with the liquid and solid compositions being as indicated by the equilibrium phase diagram. But this assumes that the solid and liquid already exist. In solidification processes, the metal is initially liquid and is cooled below the melting point or equilibrium liquidus temperature. Here solid is the thermodynamically favoured phase (i.e. $G_s<G_L$), but kinetic factors affect the initial appearance of solid embryos within the liquid. There are two components [2] in the Gibbs free energy of any solid : an interface or surface term G_i and a volumetric term G_v, such that

$$\Delta G = \Delta G_i + \Delta G_v \qquad (1.1)$$

ΔG_i is proportional to the area (A) of solid/liquid interface formed, and

$$\Delta G = \sigma A + \Delta g V \qquad (1.2)$$

where σ is the solid/liquid interface energy, and Δg is the change in free energy, per unit volume, between liquid and solid, which is negative provided the temperature $T < T_L$. For a spherical embryo of solid, radius r, to form from the melt :

$$\Delta G = 4\pi r^2 \sigma + 4\pi r^3 \frac{\Delta g}{3} \qquad (1.3)$$

ΔG is plotted against d=2r in Figure 1.1, which shows the free energy barrier to nucleation, which is seen to reach a maximum and then to start decreasing at d=d*. This defines the critical nucleus radius r*, below which an unstable embryo exists, and above which a grain starts to grow. The nucleation rate I (number of grains nucleated within a given melt volume and time) [2] can be expressed as

$$I \propto \exp\left(\frac{-\Delta G_n^*}{k_b T}\right) \tag{1.4}$$

provided the source of nuclei is not exhausted. ΔG_n^* is the maximum value of ΔG (occurs at r^*), and is inversely proportional to the square of the undercooling ΔT. As undercooling increases, nucleation rate should increase, i.e. undercooling reduces the activation energy barrier. At the liquidus temperature, $\Delta T = 0$, and so the nucleation rate becomes zero, since the energy barrier is infinite.

This all refers to homogeneous nucleation, in which solid forms within its own melt without the aid of foreign materials [4]. If the melt contains solid particles, or is in contact with a crucible, nucleation may be facilitated : heterogeneous nucleation. Here the solid/liquid interface is replaced by an area of low-energy between the crystal and a foreign solid : ΔG_n^* decreases and the nucleation rate rises. The efficiency of this inoculation is dependent upon the wettability of the added solid and the liquid metal, normally measured by the wetting angle, which is 0^o for complete wetting and is 180^o where no wetting occurs. Such inoculation is common practice in foundries by means of grain refiners i.e. via the addition of substances which are crystalline or form crystals at temperatures greater than the melting point. The result is that lower undercoolings are needed for nucleation.

Another source of heterogeneous nuclei is pre-existing solid dendritic fragments, formed either by (a) initial contact of liquid metal with the mould walls during filling; these are then

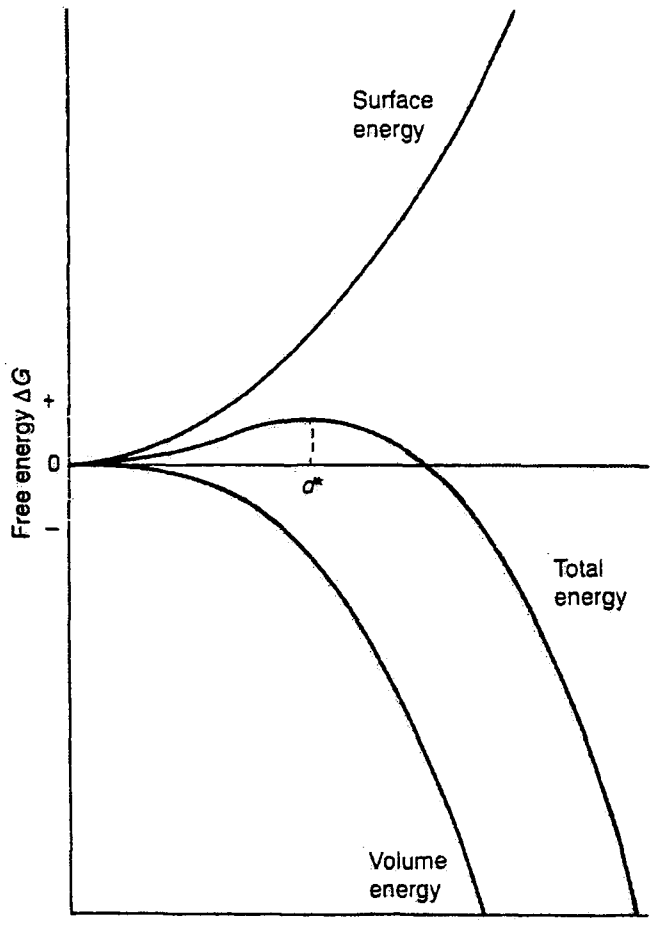

Figure 1.1 Variation in free energy on solidification (ΔG) with diameter of solidifying sphere [3].

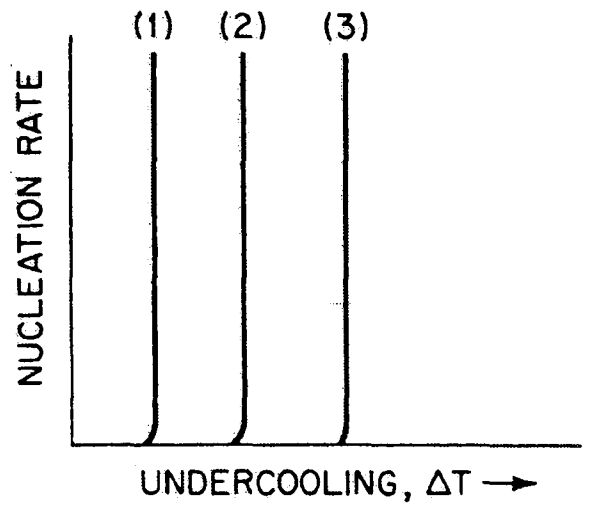

Figure 1.2 Nucleation-rate curves for metal : 1 and 2 for heterogeneous nucleation, 3 for homogeneous nucleation [4]

convected into the melt, or (b) dendrite arms from the columnar grains, which have become detached and float into the melt. As these nuclei are solid phase of the alloy, they are completely wetted.

Considering a transformation which occurs on cooling (such as solidification), as the temperature is lowered, ΔG_n^* decreases much more rapidly than does the available thermal energy. The probability of nucleation may then increase [1] rapidly with decreasing temperature. The assumption that the source of nucleation will not be exhausted, upon which the expression above for the nucleation rate I is based, is a crude one. The idea of a finite number of sites for nucleation is perhaps a better one for castings, as here homogeneous nucleation will never occur. This should mean that I will have its maximum at quite a low undercooling ΔT. Growth of solid is not included in this analysis, and such growth will of course remove potential sites for nucleation from the volume under consideration.

Flemings [4] shows the expected curves of nucleation rate versus undercooling for a metal containing inoculants of varying degrees of effectiveness (Figure 1.2). It can be seen that the assumption of nucleation at a fixed undercooling is not a bad one.

1.3 The Solid/Liquid Interface

In solidification, nucleation establishes a region in which the solid phase is stable, bounded by a solid/liquid interface, which progresses into the surrounding liquid as solidification proceeds. Such growth will be limited by [2] the kinetics of atom attachment to the interface, capillarity, and the diffusion of heat and mass. The relative importance of each of these factors depends upon the solidification conditions. The kinetics can play an important role in some substances. However, for the non-faceted growth morphology typical of a metal, it can be assumed that the kinetics of the transfer of atoms from the liquid to the crystal are so rapid that they can be neglected.

If one considers unidirectional solidification of a pure metal, in which the interface advances into a cooling liquid in a direction opposite to that of heat extraction, then the shape of the interface is planar. If a perturbation of the planar interface occurs such that a local protuberance of solid occurs, it will be remelted as it is hotter than the average interface temperature (Figure 1.3). So here the planar interface shape is stable. This is known as *constrained growth* and occurs, for example when solidification advances from a cool mould wall in a casting process. The situation is quite different for an alloy [2,3]. In this case the solid will reject solute into the liquid ahead of it (assuming a partition coefficient γ less than 1.0). This leads to a pile-up of solute, causing the interface temperature to be depressed from the equilibrium liquidus temperature, an effect known as constitutional undercooling. If there is a shallow temperature gradient G ahead of the interface, the region of constitutional undercooling can be relatively extensive (Figure 1.4). The formation of a cell begins with the breakdown of an unstable planar solid/liquid interface. As the tip of the perturbed interface can reject solute also in the lateral direction, it will tend to grow more rapidly than a depression, which tends to accumulate excess solute rejected by the tips. The cells can destabilise further to form sharp tips and secondary branches - they become dendrites. They are crystalline forms which adopt an orientation which is as close as possible to being parallel to the direction of heat flux, but follows one of the crystallographically preferred growth axes.

The above considers the advance of a "front" of solid into liquid. But solidification also occurs by nucleation within a bulk undercooled liquid. In such a case some of the surrounding liquid is cooler than the *unconstrained* growing solid equiaxed grain. Here the equivalent to the planar front in constrained growth is a spherical interface. But if a positive protuberance occurs in the interface of a pure metal, the solid grows locally into cooler liquid, and furthermore can reject heat laterally as first cells and then dendrites develop. These are known as thermal dendrites [2]. In alloys, rejection of solute is similarly facilitated by dendritic growth. And unlike with constrained growth, there is no positive gradient of

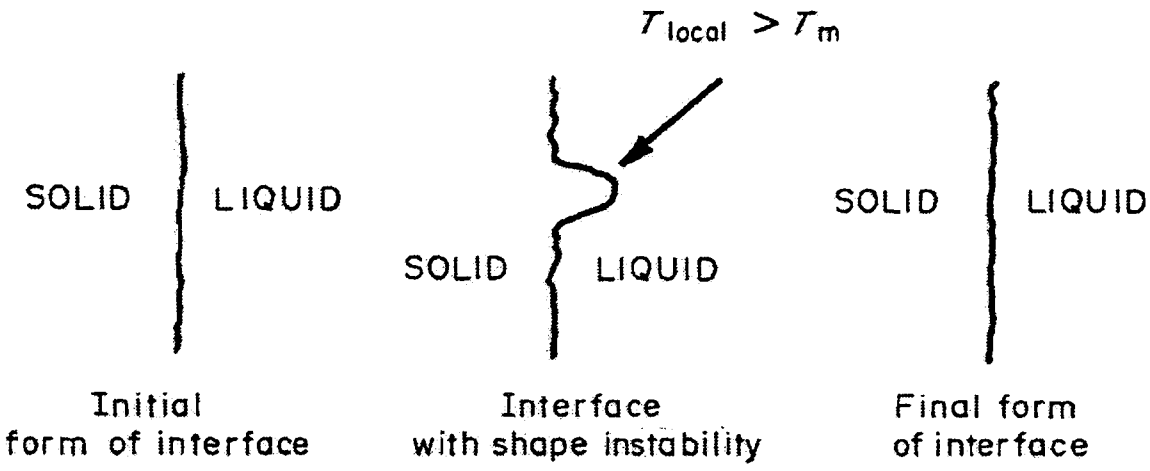

Figure 1.3 Formation of and re-melting of unstable protuberance in directional solidification of a pure metal [5].

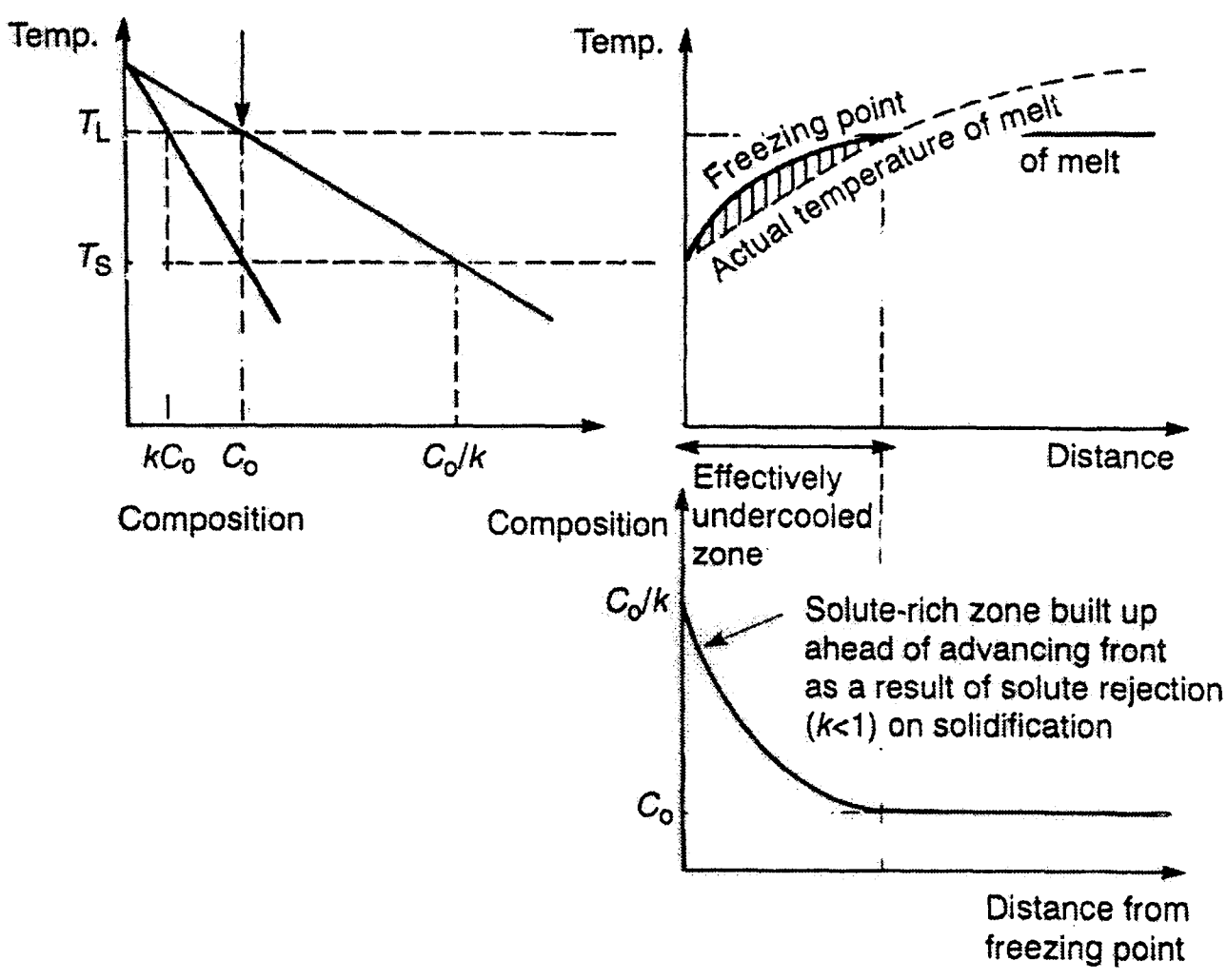

Figure 1.4 Illustration of the link between the phase diagram for a binary alloy and constitutional undercooling; steady-state growth with planar interface [3].

temperature which can prevent local constitutional undercooling at the tip. Equiaxed dendrites grow along all of the available preferred crystallographic directions when the heat extraction is isotropic. In cubic crystals, the six [001] axes form the trunks and therefore the crystal orientation can be easily determined.

From the foregoing it is obvious that, in most circumstances found in alloy casting processes, conditions are prevalent which are conducive to the breakdown of smooth solid/liquid interface morphologies, resulting in dendritic growth. It is this assumption that underpins much of the work reported in this thesis. The breakdown to cells and dendrites is favoured by low G and high V (interface velocity).

Segregation of solute over a large distance (e.g. that of an industrial casting) is known as macrosegregation [4]. It can occur in directional solidification via rejection of solute from the advancing interface. But in real casting situations it is a complex phenomenon, and is affected a great deal by fluid flow [6]. It is discussed in more detail later.

1.4 Dendritic Growth

The melt undercooling ΔT determines the driving force for the dendrite growth. The total undercooling is

$$\Delta T = T_L - T^* \tag{1.5}$$

where T_L is the equilibrium liquidus temperature of the alloy, and T* is the temperature of the dendrite tip. It consists of contributions from kinetic, constitutional and curvature effects [7,8], expressed respectively as

$$\Delta T = \Delta T_K + \Delta T_C + \Delta T_R \tag{1.6}$$

The kinetic effects are normally neglected. In some cases and additional thermal term ΔT_T is added for equiaxed growth [9,10], such that

$$\Delta T = \Delta T_T + \Delta T_C + \Delta T_R \tag{1.7}$$

and in this case

$$\Delta T = T_L - T_\infty \tag{1.7 a}$$

where T_∞ is the melt temperature far from the tip, as illustrated in Figure 1.5. Here

$$\Delta T_T = T^* - T_\infty \qquad \text{thermal undercooling} \tag{1.7 b}$$

$$\Delta T_C = T_L(R) - T^* \qquad \text{solutal undercooling} \tag{1.7 c}$$

$$\Delta T_R = T_L(C_0) - T_L(R) \qquad \text{curvature undercooling} \tag{1.7 d}$$

During columnar dendritic growth of alloys, the solute rejection rate, and therefore the growth rate, is influenced by the shape of the tip and, at the same time, the form of the tip is affected by the distribution of the rejected heat or solute [2]. The *isolated* dendrite shape can be described satisfactorily as a paraboloid of revolution. The mathematical solution of the diffusion problem for a paraboloid was developed by Ivantsov [11] in 1947, who deduced the relationship between the supersaturation Ω, the dendrite tip radius R, and the growth rate V :

$$\Omega = I(P_c) \tag{1.8}$$

where

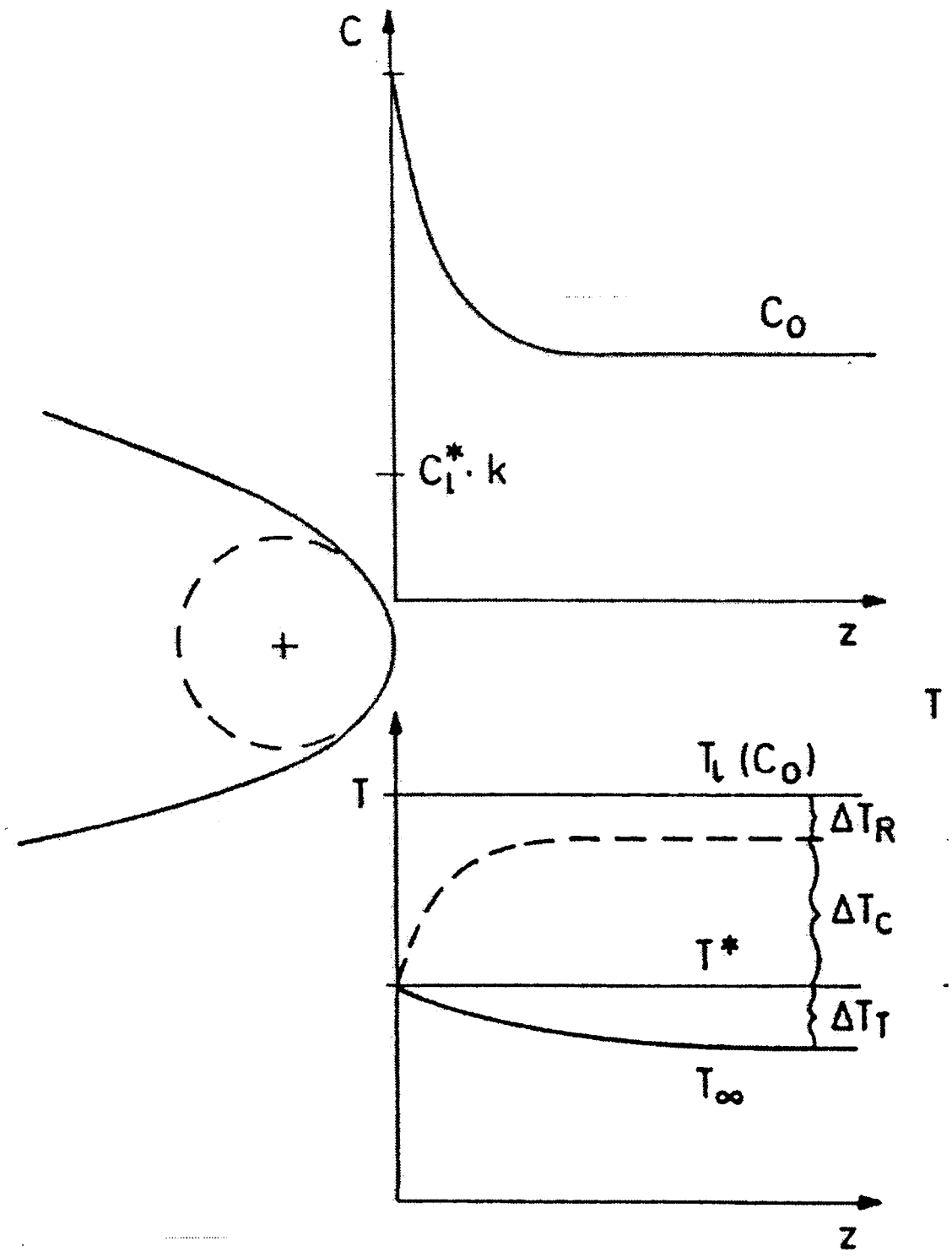

Figure 1.5 Diffusion fields and undercoolings at an equiaxed dendrite tip growing into an undercooled alloy melt [10].

$$I(P_c) = P_c \exp(P_c) E_1(P_c) \tag{1.8 a}$$

and the Peclet number for solute diffusion

$$P_c = \frac{VR}{2D} \tag{1.8 b}$$

where D is the diffusivity of solute in the alloy, I(P) is the Ivantsov function and $E_1(P)$ is the exponential integral function [12]. For a given value of Ω, there is not an unambiguous definition of R and V. Solution of the problem does not indicate whether the dendrite will grow quickly with small R or slowly with large R, but merely relates the sharpness of the tip to its rate of propagation. A sharper tip can grow more rapidly because it can reject solute (or heat in the case of a thermal dendrite) more efficiently. Another equation is required to solve the problem completely.

Langer and Müller-Krumbhaar [13-16] presented a case that a dendrite grows with a tip having a size at the limit of stability (marginal stability). They suggested that one can determine the expected tip radius by setting

$$R = \lambda_i \tag{1.9}$$

where λ_i is the shortest wavelength perturbation which can cause the dendrite to undergo morphological instability. Use of the theory fixes R (and therefore V) for a given supersaturation of solute Ω. This predicts a tip radius which is relatively large, so that the effect of curvature on the growth can be neglected [2] i.e. $\Delta T_R \sim 0$.

The Ivantsov solution is applicable also to thermal dendrites (pure metal solidification), in which case Ω is the dimensionless supercooling [9], and the Peclet number P is a thermal one (P_t) :

$$P_t = \frac{VR}{2\alpha} \qquad (1.8\ c)$$

where α is the thermal diffusivity of the liquid phase.

The marginal stability hypothesis involves the dynamical choice of one of the continuous Ivantsov family of zero surface tension solutions. However, in 1986 Kessler and co-workers [17] showed that, with the inclusion of surface tension in the analysis, the supposition that there is such a family of allowed steady state shapes is not correct. They found a unique steady state solution. Indeed one of the proposers of the marginal stability solution (Langer) conceded that surface tension and crystalline anisotropy destroys the Ivantsov family of solutions [18].

Burden and Hunt [19] measured dendrite tip temperatures during directional solidification of Al-Cu alloys as a function of velocity, temperature gradient and composition. The temperature gradient was varied between 0.5 and 60.0 °C/cm. The results of the experiments on interface temperature for Al-2 wt.%Cu showed that at high gradients and low velocities the tip temperature increases with increasing velocity. But for high enough velocities ($V>10^{-2}$ cm/s) the temperature decreases with increasing velocity, and becomes independent of gradient. The authors noted that for a zero gradient the interface temperature would be expected to decrease continually from the liquidus temperature for increasing growth rate. They also found that the total undercooling of the dendrite tips was mainly solutal, increasing with increasing solute content. The theoretical part of this work is discussed in the next chapter.

In general, dendrite morphology remains largely unchanged over wide ranges of cooling rate - it simply becomes finer as heat is extracted at a greater rate. A measure of the effects of solidification conditions is the dendrite arm spacing i.e. the spacing between primary, secondary, or higher-order branches. The driving force for secondary and tertiary arm growth is the supercooling in the region between primary dendrite arms. Relationships between secondary dendrite arm spacing (λ_2) and the solidification time t_f have the form [2,4] :

$$\lambda_2 = a t_f^n \tag{1.10}$$

where the exponent n is in the range 0.33 to 0.5.

1.4.1 Microsegregation and solidification path

Segregation of solute over the scale of the cell or dendrite spacing is microsegregation. This determines the non-equilibrium fraction solid in the alloy's freezing range [20]. It arises because solid is deposited over a range of temperatures.

Consider the binary eutectic phase diagram (Figure 1.6). At temperature T, solid of composition C_S is deposited near the dendrite tip, where the composition of the liquid is C_L. If it is assumed that equilibrium freezing occurs, whereby solidification rates are low enough to permit extensive solid state diffusion, resulting in the liquid and solid phases having homogeneous solute concentrations, the fraction liquid g_L can be expressed via the lever rule [2], as :

$$g_L = \frac{C_O - C_S}{C_L - C_S} = \frac{T_O^* - \gamma T^*}{T^*(1-\gamma)} \tag{1.11}$$

where

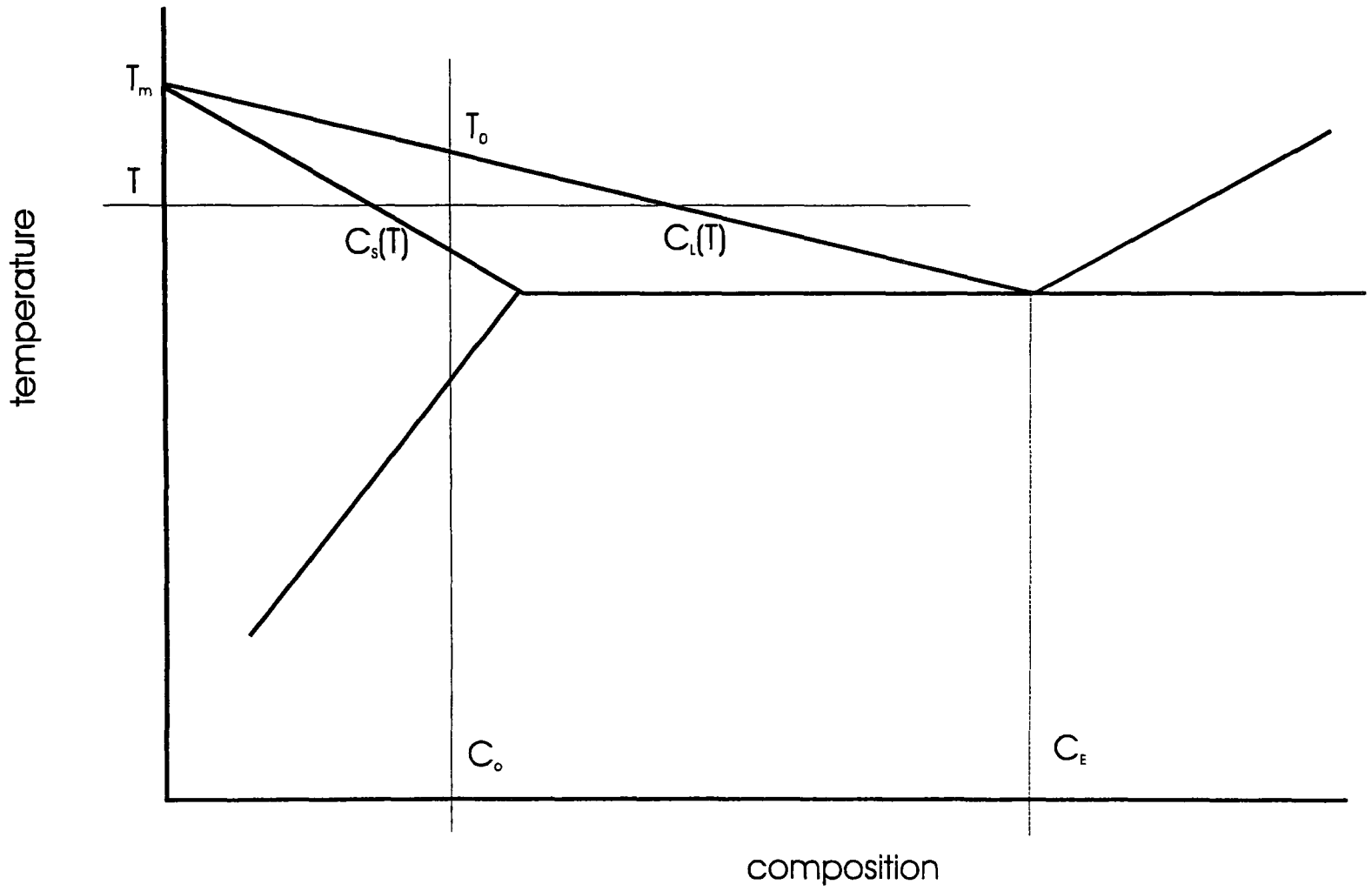

Figure 1.6 Schematic of binary eutectic phase diagram.

$$T^* = T - T_m \tag{1.11 a}$$

$$T_O^* = T_O - T_m \tag{1.11 b}$$

and the distribution coefficient is constant and given by

$$\gamma = \frac{C_S}{C_L} \tag{1.11 c}$$

In such a situation, it is obvious that the fraction liquid is zero at the solidus temperature. But in spite of the equilibrium nature of solidification, substantial solute redistribution occurs during solidification; the material is homogeneous only before and after solidification [4]. The evidence of solute partitioning disappears due its complete diffusion into the solid phase.

Under real solidification conditions, for example in casting processes, such equilibrium freezing does not occur. Diffusion of solute in the solid is *extremely* slow, to such an extent that it has been ignored in some analyses. If this is the case, then it is assumed that local solid composition does not change once it has been deposited. Microsegregation has been described [20] as the phenomenon in growing cells or dendrites where the concentration of solute is different at the centre than towards the edge of the single phase cell/dendrite. So maximum possible microsegregation occurs for the case in which there is zero diffusion of solute within the growing solid. If it is assumed that all of the rejected solute is pushed sideways into the interdendritic or intercellular liquid, thus increasing its composition (for $\gamma<1$), and that this liquid is completely mixed, the fraction liquid can be expressed [2] by the so-called Scheil equation :

$$g_L = \left(\frac{C_O}{C_L}\right)^{\frac{1}{1-\gamma}} = \left(\frac{T_O^*}{T^*}\right)^{\frac{1}{1-\gamma}} \tag{1.12}$$

In this case, $g_L > 0.0$ at the solidus temperature (T_S). Microsegregation increases C_L and so, for $\gamma<1$, reduces the equilibrium temperature at which liquid and solid co-exist i.e. there will be more liquid present. Comparison now is to equilibrium (lever rule) solidification where there is no microsegregation and $g_L = 0.0$ at the solidus temperature. We can thus conclude microsegregation occurs if $g_L > 0.0$ at T_S. Excess liquid (above that calculated by the lever rule) is an indicator of the amount of segregation [20].

The Scheil analysis overpredicts microsegregation [20] because (a) the cell/dendrite tip does not grow at the equilibrium liquidus temperature, (b) some diffusion does occur within the solid state, and (c) melting and re-freezing of previously solidified material takes place. The three effects are summarised below. A more complete analysis is to be found in [20].

Near a directionally grown cell or dendrite tip, the liquid between the cell/dendrites cannot be homogeneous, as was assumed in the derivation of the Scheil equation. Instead, solute is rapidly rejected by the tip. The build up of solute decreases the tip growth temperature and increases the solute deposited in the solid and thus decreases the amount of microsegregation.

In practice, even though the diffusion coefficients in solid are typically three to four orders of magnitude smaller than those in liquid, appreciable diffusion occurs in the solid because large times are involved. This diffusion will reduce the amount of microsegregation. The treatment of the solid state diffusion is usually the most important part of a theoretical treatment of microsegregation. Typically, fast diffusing elements approach the lever rule whereas slow diffusing elements show significant microsegregation. Also as γ approaches zero, lever rule behaviour is approached due to very strong partitioning.

During dendritic growth some of the solid deposited at high temperature is remelted. When this is replaced by additional material deposited at a lower temperature, the amount of microsegregation is reduced [4].

This discussion relates to the growth of a single phase solid solution during solidification. In practice, the formation of eutectic will often intervene [21]. Theoretical models of microsegregation are discussed in the next chapter.

1.5 Columnar Growth

In a casting process, the metal at the mould wall will be the coolest. Small equiaxed crystals form here, and from these emerge elongated crystals to form what is known as the columnar zone. In 1856, Robert Mallet reported [22] his observations of as-cast grain structure in cast iron cannon (Figure 1.7). He noted that "the principal axes of the crystals will always be found arranged in lines perpendicular to the bounding planes of the mass; that is to say, in the lines of direction in which the wave of heat has passed outwards from the mass in the act of consolidation...". These crystals formed either columnar or elongated equiaxed grains. Mallet also proposed plausible "laws" on the effects of mould material, pour temperature, and cooling rate on the grain size and type, and showed a high level of understanding of the formation of shrinkage porosity in castings. Mallet's interest in metal solidification was a result of his family foundry and engineering business in Dublin, which was quite profitable in the mid-19th century due to the expansion of the railway network in Ireland [23].

The columnar dendrites survive via a competitive growth process, in which those which are crystallographically aligned to the direction of heat flow are favoured. So in the case of directional constrained growth, most of the dendrites are arranged parallel to each other and a characteristic trunk spacing λ_1 can be defined [2]. This is also known as the primary spacing. In the growth of such an array of dendrites λ_1 can change without difficulty [4]. If spacing is too close, one primary arm falls behind and is eventually engulfed. If spacing is too large, a tertiary arm growing from a secondary arm catches up to the growing primary tips, and becomes one of them.

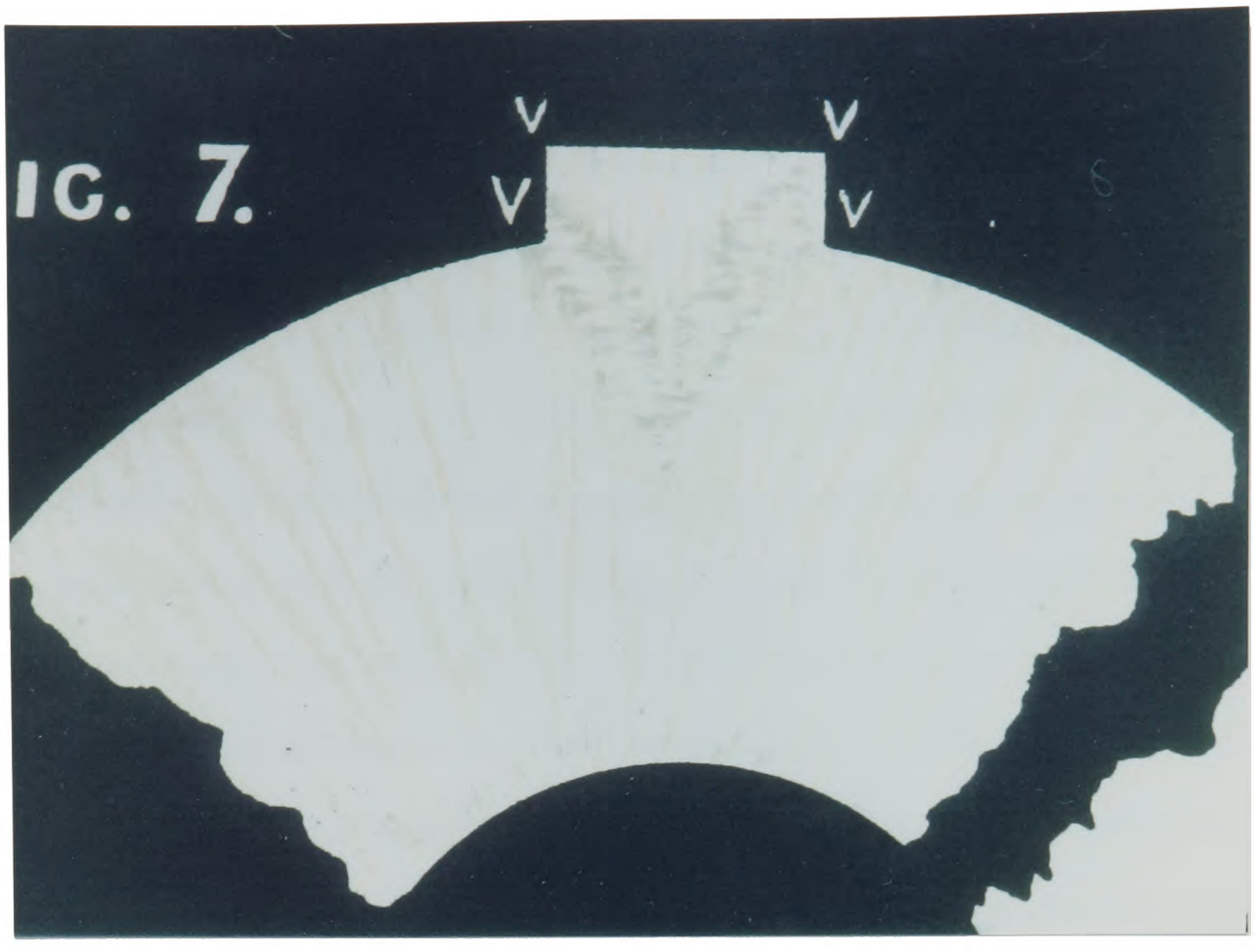

Figure 1.7 Grain structure in cast iron cannon - section through the vent-field [22].

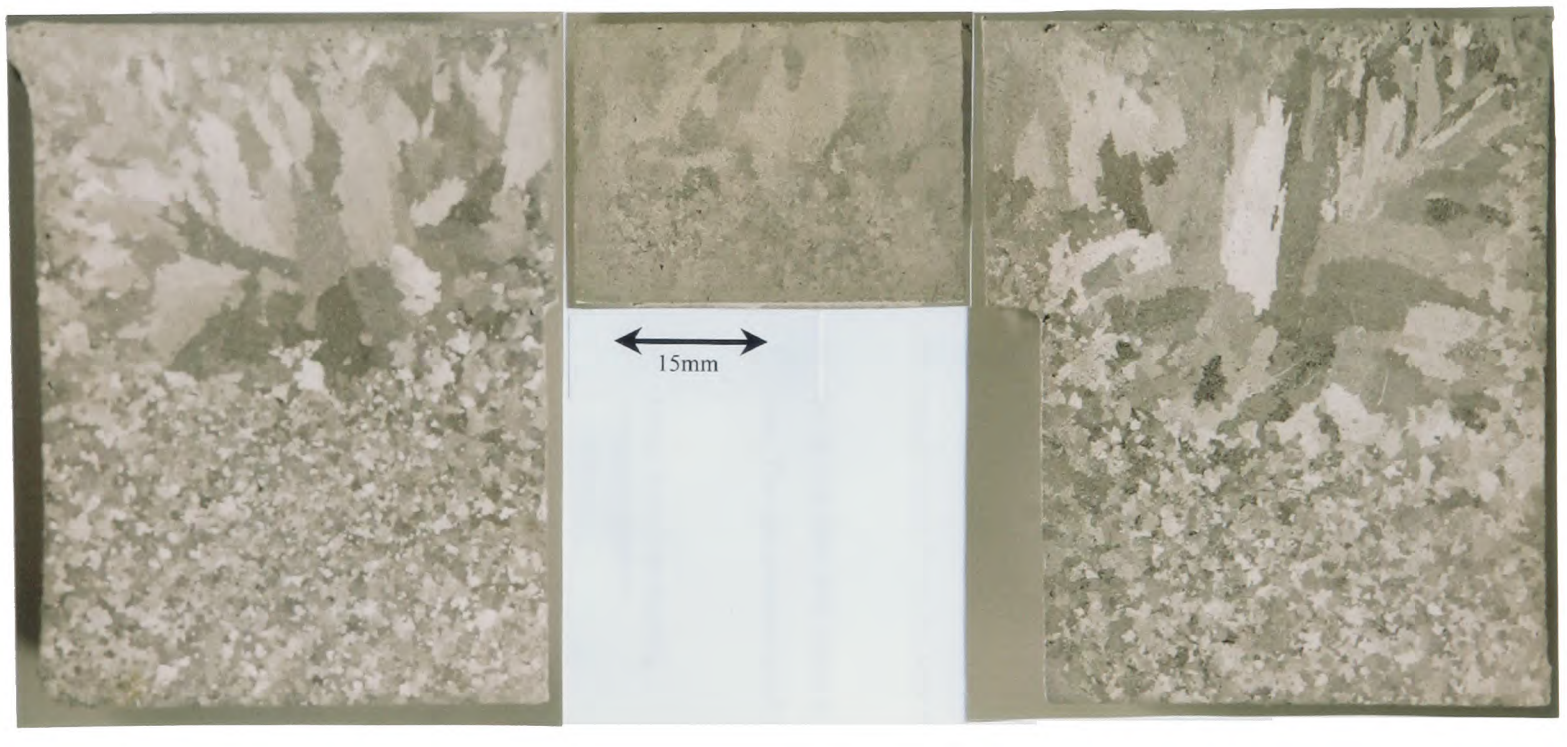

Figure 1.8 Grain structure in Al-4wt.%Si sand casting.

In opaque metallic systems, it is very difficult to observe such phenomena during solidification. In 1965 it was reported [24] that some transparent organic compounds have a low entropy of melting, and therefore freeze as metals do. This presented the opportunity of making direct observations of many of the phenomena which determine the structure of cast metals. Early candidate analogues to metals which were identified in this work included carbon tetrabromide, cyclohexanol, and succinonitrile. This most useful discovery has since resulted in great strides into the understanding of metal and alloy solidification, in both experimental and theoretical research. For example, succinonitrile has been used as an analogue to cubic metals for studies on dendritic growth [25-30] . In one study of directional growth [31], the variation in crystal shape and interface morphology of succinonitrile-acetone and succinonitrile-salol as a function of the misorientation θ with the direction of heat flow was investigated. The primary dendrite spacing λ_1 was found to increase with θ. Also, for non-zero θ, the side-branching was not symmetric. In the columnar zone of castings, crystals growing at high θ are likely to be impeded early on in the competitive growth process.

1.6 Equiaxed Growth

Equiaxed grains grow from nuclei within the bulk undercooled liquid. The heat produced by solidification must be transported through the melt. The growing crystals are thus hotter than much of their surroundings [2] and the heat flux is more or less radial and in the same direction as that of growth.

1.6.1 Origin and nucleation

The origin of nuclei which lead to equiaxed crystals has long been the subject of investigation. In an attempt to throw some light on the controlling phenomena, Jackson et al. set about to make use of their transparent analogue materials [32], over 35 years ago. Their

evidence showed that the equiaxed zone in castings is caused primarily by the remelting of dendrite arms where they are joined to the dendrite stem, in the columnar zone. It was suggested that the roots of secondary dendrite arms have a slightly higher solute content than outer portions of the arms. Thus, the melting point at such necks would be lower, curvature higher, and thermal fluctuations would tend to cause melting just at this location. Many detached crystals can be produced in this fashion. A solution of ammonium chloride in water was also used in this work. Here the fcc ammonium chloride phase grew dendritically during cooling of the solution. The dendrite directions were <100>. Gentle stirring of the melt caused new crystals to emerge from the region of columnar dendritic growth. The crystals, formed by the melting off of dendrite arms due to fluctuations caused by the stirring, were carried into the centre of the casting. In order for these crystals to grow, the centre of the melt must be constitutionally supercooled, a condition which usually prevails in the later stages of solidification of an alloy casting. In an unstirred system natural convection may lead to the same result.

Another suggested mechanism for the source of equiaxed nuclei was that they originate in the chill zone, then float, sink, or are carried away by convection to the centre of the casting, where they grow to produce equiaxed crystals [33]. In this case, as all the crystals nucleate immediately on casting, the mechanism was termed "big bang" nucleation.

In both the dendrite arm remelting and "big bang" theories, there is no energy barrier to heterogeneous nucleation in the undercooled liquid. In fact, nucleation need not strictly occur before growth - the only undercooling required is that for growth.

Another source of equiaxed nuclei is from the addition of grain refiners. Such inoculants are added to many molten alloys to produce a fine-grained equiaxed structure. Based on the heterogeneous nucleation theory already presented in summary form, the general characteristics of such inoculating agents are as follows [4]. They should produce a small contact angle with the growing solid. This should be the case for small lattice mismatch

between particle and solid and high chemical affinity between the two. The successful grain refiner should also be as stable as possible in the molten metal, possess a maximum of surface area, and have an optimum surface character - perhaps rough, or pitted.

It is likely that grain refining agents will remain crystalline at temperatures much higher than the liquidus temperature of the alloy. But in a situation in which equiaxed grains originate from small crystals either from the "big bang" or from dendrite arm detachment, then increasing the superheat will destroy these sources, and should dramatically change the final equiaxed grain size. If this does not happen, then it is likely that grain refiners are the cause of nucleation in the system under study.

A weakness of the "big bang" theory, however, is its inability to account for equiaxed grain formation which has been observed in experiments carried out in the absence of a chilled mould or a grain refiner [34]. In such a case the dendrite detachment mechanism, with the assistance of melt convection, is the likely source of equiaxed nuclei.

1.6.2 Growth

When heat flows from the equiaxed crystal into the melt, the dendrites can grow freely, as fast as the imposed undercooling permits [2]. The primary dendrite arms, for cubic metals, grow along the six <001> directions. This continues until impingement upon dendrites originating from other nuclei, and finally the grain boundaries form a continuous network throughout the solid. Final secondary dendrite arm spacings are readily measured. It has been demonstrated that this spacing is equal to that of columnar structures at equivalent cooling rates [4].

Despite the problems with study of the progress of solidification in opaque metals, a recent experimental study has been carried out into real-time equiaxed grain growth in solidifying aluminium alloys [35]. The technique uses a probe consisting of two electrodes, one of which is encased in a borosilicate tube which has an orifice into which the solidifying melt is drawn

via a negative applied pressure. A constant current is maintained between the two electrodes. For aluminium, the resistivity of the solid is 10^{-7} Ω.m, that of the liquid is 2.5 x 10^{-7} Ω.m, so that detection of solid grains entering the device causes a voltage change which is proportional to the volume of the particle. Primary silicon has a higher resistivity than the liquid aluminium. The device was used to determine the alteration in the number and mean diameter of equiaxed grains in solidifying hypo- and hyper-eutectic Al-Si alloys, in both quiescent and stirred melts. The authors propose to use the device to assess the efficiency of grain refining.

1.7 The Columnar-to-Equiaxed Transition

Study of the microstructure of many castings shows that both columnar and equiaxed grains co-exist (Figure 1.8). If a columnar solidification front is advancing into the undercooled liquid, heterogeneous nucleation and growth of equiaxed grains can occur, blocking off the constrained growth at the columnar-to-equiaxed transition (CET). The extent of the equiaxed zone is the result of competition between the columnar and the equiaxed grains [33]. It is found that enhanced convection promotes the equiaxed zone [34]. This provides evidence that dendrite detachment and transport, which is enhanced by convection [32], is an important influence.

Two modes of equiaxed growth have been observed [34] : grains in the bulk that sediment out form a pile at the base of a casting which then impedes the advancing columnar front, and equiaxed grains attach themselves to the columnar front and then start to develop some columnar characteristics (both evident in Figure 1.8). Sedimentation produces the fully equiaxed structure, whereas adhesion gives a branched columnar structure. Sedimentation is due to the change in density of the grain as a result of solidification shrinkage, not because of solute rejection, because most of the rejected solute is trapped interdendritically within the envelope of the grain.

As can be seen from Figures 1.4 and 1.9, an equiaxed zone is encouraged by a shallow temperature gradient in the bulk. This is another reason why convection can lead to a larger equiaxed zone. Indeed, very early work showed that motion of the liquid during solidification by rotating a casting, or stirring, decreased the length of the columnar zone, and produced equiaxed grains earlier in the process [36,37].

The greater the columnar growth undercooling, the more extensive will be the region of undercooled bulk liquid ahead of it. Indeed if there is no columnar dendrite tip undercooling, as is approximately the case for pure metals, it is difficult to generate equiaxed crystals. So higher levels of solute in an alloy favour the equiaxed zone.

The evolving grain structure has a significant effect on the formation of hot tears during casting solidification. An early study [38] showed that under certain conditions partially solidified castings can be deformed to quite large amounts without visible open or filled hot tearing defects. At a fraction solid of 0.45, it was found that the shear strength of coarse-grained aluminium alloys was much greater than that of grain-refined equivalent. Yet the latter could be deformed substantially without the introduction of serious defects. The authors reported that the better tear resistance of the fine-grained alloys is because they can more easily accommodate strain, not because they are stronger. It follows that the presence of an extensive highly immobile columnar zone will lead to poor hot tear resistance in castings.

Guven and Hunt [39] carried out experimental studies on the hot tearing in Al-Cu alloys, containing between 0.0 and 16.0 wt% Cu. They identified a range of compositions over which hot tearing occurred. Very pure and near-eutectic compositions did not hot tear. Within the hot tearing range, different phenomena were proposed at both low and high concentrations. For low concentration alloys, as each grain contracts the volume change is taken up by intergranular flow of solute-rich liquid. As solidification progresses such flow becomes increasingly difficult causing a pressure drop in the liquid, often leading to a hot

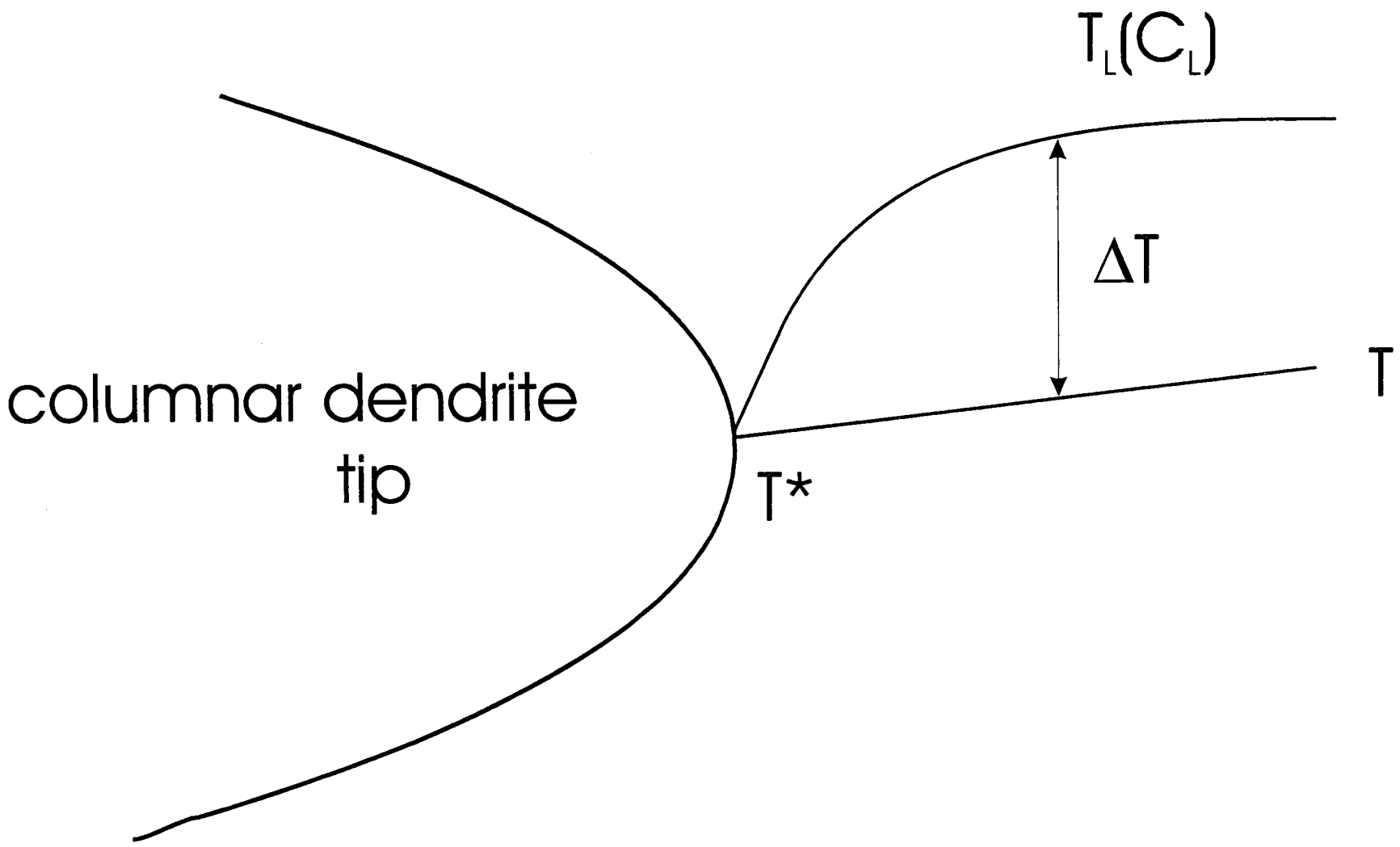

Figure 1.9 Undercooled liquid ahead of a columnar dendrite

tear. On the other hand, for higher alloy compositions the volume fraction of liquid may be large enough at the eutectic temperature for flow to occur easily. So the crack, if it forms, must occur in the solid. The authors report that the mechanism is probably one where a small amount of eutectic forms and is broken when the stress builds up.

As grain size affects hot tearing [40], any model of this type of tearing would need to predict grain size and type (e.g. columnar or equiaxed).

1.7.1 Summary

As discussed in Section 1.3, dendritic growth is favoured by low values of G/V. On the other hand, GV is an estimate of the magnitude of the cooling rate. So, as seen in Section 1.4, the scale of the microstructure is finer as GV increases, i.e. as t_f is decreased. So both G and V have a very significant effect on the morphology, scale and type of grains that are formed during the freezing of alloys, as illustrated in Figure 1.10.

1.8 The Effects of Fluid Flow

The flow of liquid in a solidifying system can have very significant effects upon the evolving microstructure. In many casting processes the bulk liquid undergoes thermally induced convection during solidification. Even small temperature differences can lead to convection in liquid metals. This has the effect of enhancing mass transfer at the solid-liquid interface by reducing the solute boundary layer [4]. It also leads to rapid dissipation of superheat such that it may be virtually gone before any solidification begins, with obvious implications for columnar and equiaxed growth. Bulk fluid flow causes dendrite arms and columnar grains to point preferentially upstream [4] because the flow washes rejected solute from the upstream side.

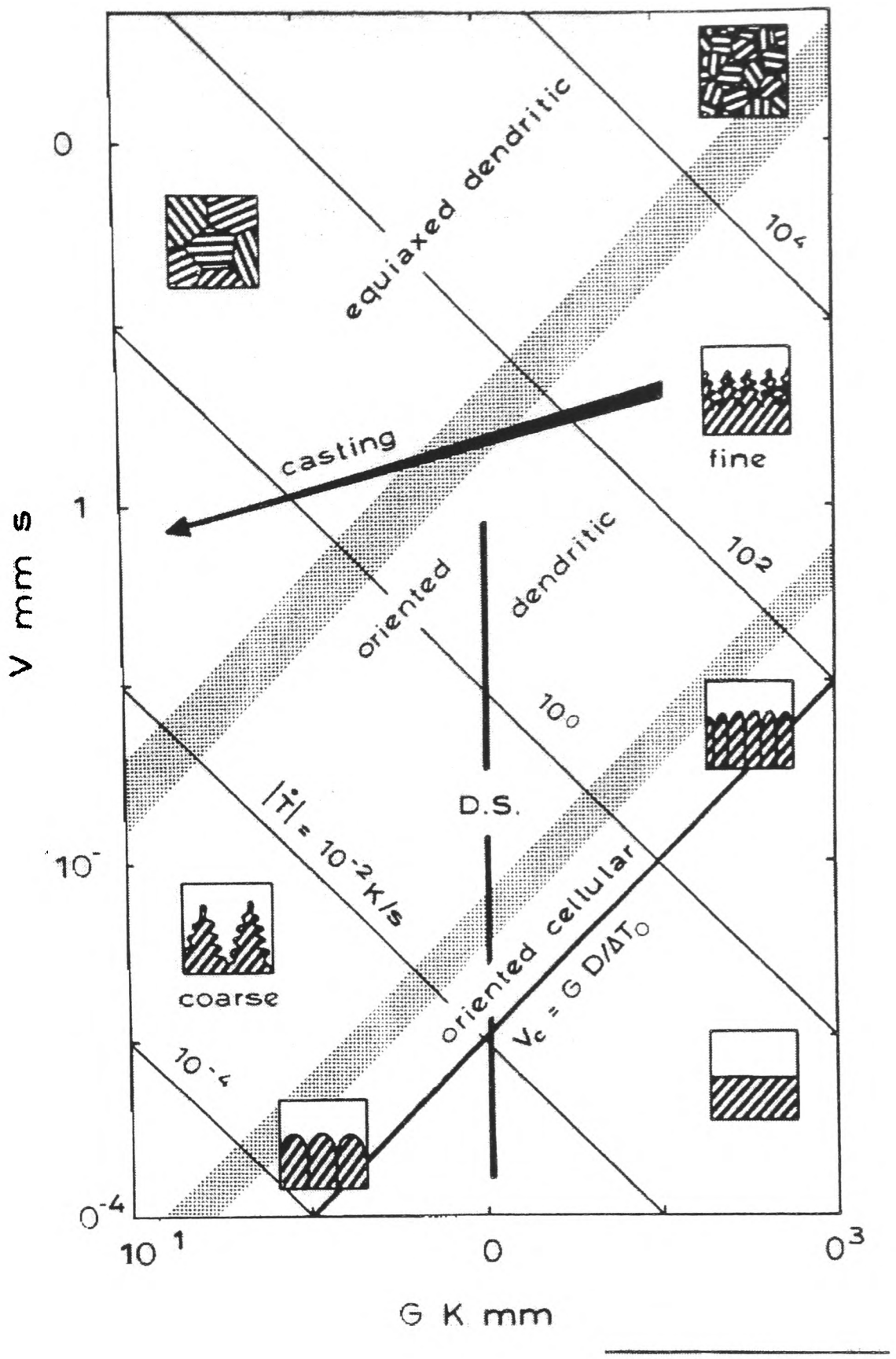

Figure 1.10 Schematic summary of single phase solidification morphologies in (G,V) space [2].

Density differences due to solute rejected during solidification also lead to convection. But convection in the bulk liquid is little affected by solutal effects since the solute does not diffuse significantly beyond the dendrite tips [4]. However, within the solid-liquid region behind the dendrite tips flow of interdendritic fluid is strongly affected by density differences arising from micro-segregation effects. When this solute flows within the mushy zone over large distances, macro-segregation occurs. Analytical equations were developed [6], the solution of which described the flow of solute-rich liquid to feed solidification and thermal contractions, for the case of solidification with planar isotherms. McDonald and Hunt [41] first outlined the physics behind the formation of "A segregates" in steel ingots and castings. They used the ammonium chloride/water analogue system to show that such segregation was caused by the formation of channels in the columnar mushy zone of a casting, through which preferential flow of solute-rich liquid occurred, provided such liquid increased in density with increasing temperature. When the columnar region is growing, the liquid still remaining between the dendrites has a much lower temperature near the ingot walls than at the dendrite tips. The composition of the liquid in contact with solid will vary with temperature. The density of the liquid thus varies because of changes in both temperature and composition. The authors proposed that resultant gradients in the liquid density gives rise to flow through the interdendritic regions. The NH_4Cl-H_2O system could be used because the density of liquid in contact with solid varies in the same manner as that in the Fe-C (or -S or -P) system. Crystals of potassium permanganate were used to trace the convection patterns. Pipe-like channels were observed forming in the model system, similar to the A segregates in cast steel. These pipes formed in the rising liquid region. It was noted that at the edge of the ingot, where the liquid was rising, it moved towards the hotter centre of the casting. Since the liquid was in equilibrium with solid at a lower temperature, it could dissolve off obstacles. (Because of the low melting point of the liquid [3], it dissolves dendrites as solute from the stream diffuses into the solid, reducing the melting point of the dendrites). Thus a series of streams developed, joining together to form a pipe, which continued to get larger. At the centre of the equiaxed zone, liquid was falling and moving towards cooler regions, thus depositing solid. Any channel that existed tended to block up, and the motion which occurred here was

through the equiaxed mass as a whole. It was observed that detached pieces of dendrites were often thrown out of the pipes, thus producing feedstock for the growth of the equiaxed zone. Thus, via the criteria of Jackson et al. [32], this so-called channelling has an effect on the formation of the CET. In later work McDonald and Hunt [42] showed how segregation defects caused by channelling could be reduced by adjustment of alloy composition to reduce density alteration with temperature and composition. They added zinc chloride to the NH_4Cl-H_2O system to form a ternary alloy which rejects both water and $ZnCl_2$ and for which changes in saturated liquid density with temperature were small. It was found that A segregates were eliminated. Experiments were later performed on metallic alloys. In studies of Sn-Zn [43] and Pb-Sn [44] solidification, radioactive tracer was injected into the partially solid region of a casting and the movement of the liquid studied by autoradiography. Macrosegregation in Pb-Sn alloys was also shown [45,46] to be caused by convective interdendritic flow at slow growth rates in unidirectional solidification experiments.

Other workers [47] developed mathematical expressions for predicting the onset of the flow instability leading to channel formation in the columnar mush. It was shown that this occurs when the component of fluid flow in the growth direction exceeds the isotherm velocity. The mathematical expression is presented in the next chapter. Temporal effects in interdendritic fluid flow leading to macrosegregation in Sn-Pb [48] and Al-Cu [49] were studied experimentally, and it was shown that due to the time taken for such flow to be established, only relatively large castings and ingots were affected. Further study of the unidirectional solidification in the NH_4Cl-H_2O system used dye tracers [50] to study the sequential development of salt-finger convection, chimney formation, plume convection and vertical channel formation. As explained by Hellawell et al. [51] in their comprehensive account of channel convection in partly solidified metal and analogous systems, the principal solutes segregating within these channels are those which are less dense than the solvent metal e.g. aluminium and titanium in nickel base superalloys. In the directional solidification of turbine blades, for example, such channelling leads to the "freckle" defect - essentially an equiaxed fragment taken along by liquid flow in the channel [52]. Such channelling may also occur in

the Earth's core, crustal magma reservoirs, hydrothermal systems at mid-ocean ridges and during the diagenesis of sedimentary rocks [53].

In any casting, the effect of flow upon equiaxed crystals will influence the CET. Griffiths et al. [54] carried out downward solidification experiments on Al-Cu and Al-Si alloys, and found that the equiaxed zone was much more extensive in alloys for which the solid was buoyant with respect to the bulk liquid i.e. Al-Cu alloys containing more than 10 wt.% Cu. Because of gravitational effects on the CET, in recent years there has been considerable interest in performance of controlled solidification experiments in microgravity conditions [55,56], in order to compare them to equivalent experiments on the ground, and in order to validate diffusion-only theories and models of solidification.

In summary, convective flow can markedly influence the transition from columnar to equiaxed dendritic growth, generally decreasing the length of the columnar dendritic zone and enhancing equiaxed grain formation. This is due to the melting off of parts of dendrites and to the decreased value of G. Dendrite fragments rejected ahead of the columnar front as a result of density driven interdendritic flow and subsequent channelling are a further source of equiaxed grains.

Chapter Two

Previous Work - Modelling

Chapter 2

Previous Work - Modelling

Having outlined some of the basic scientific knowledge underpinning this work in Chapter One, here the work of others in the numerical modelling of solidification and casting is reviewed.

2.1 Computational Heat Transfer (continuum models)

2.1.1 General

The processes of heat transfer and fluid flow are governed by fundamental principles of thermodynamics and mechanics. These principles are the conservation of mass, momentum and energy. The conservation principles, in turn, have local and global forms, respectively leading to differential and integral equations [57]. The work described in this thesis is generally limited to the modelling of solidification in the absence of convection, and for this diffusion-only heat transfer, the energy equation [58] must be solved :

$$\rho.C_p.\frac{\partial T}{\partial t} = k.\nabla^2 T + E \qquad (2.1)$$

where ρ is the density, C_p is the specific heat, T is the temperature, t is the time, k is the thermal conductivity, and E is a heat source which accounts for the release of latent heat during solidification. This integral version of the energy equation assumes C_p and k are constant [57]. It is possible to deduce the differential form by noting that this applies to arbitrarily small subvolumes of the region to which the conservation of energy applies. This process is known as discretisation, and the resultant algebraic equations can be solved by a

number of methods, often via the control volume (CV) or finite difference (FD) method [59,60], or via the finite element (FE) method [61,62]. There has been a growth in the application of FE methods to thermal diffusion, particularly where complex geometries, variable material properties, and complicated boundary conditions are encountered. But for simpler configurations and boundary conditions FD methods offer greater simplicity in formulation and programming [57]. The FD formulation generally requires less programming effort and usually much less computer storage. Many researchers base their FE models on commercial computation engines, but those employing CVFD methods normally develop their code from scratch, and thus have a much greater degree of control over (and responsibility for !) their models. The control volume approach is taken in the current work.

For diffusive initial value problems such as equation (2.1), the way in which time is discretised has a large effect on the type of numerical methods required for solution of the problem. In explicit methods, the dependent variable (temperature T in this case) is solved at each node via consideration of the temperatures of neighbouring nodes at the start of the time step. For linear problems, this means that values of T can be updated via a simple algebraic expression. Implicit methods, on the other hand, require that the value of T at a node is consistent with the temperatures of neighbours *at the same time*. This leads to the necessity to solve a system of simultaneous algebraic equations. An obvious advantage of the explicit approach is its simplicity, but there is a stability condition which limits the time step permissible [57]. Another advantage is that it is second order accurate in time, whereas the implicit method is only first order accurate in time, but unconditionally stable [63]. Both methods are second order accurate in space. One can combine the stability of an implicit method with the accuracy of a method that is second order in time via the semi-implicit Crank-Nicholson scheme or via the Alternating Direction Implicit scheme [57,58,63-65].

The systems of simultaneous equations which result from the implicit method can be solved in two ways - by direct or iterative methods [66]. If the equations are linear the direct method, applied once, can solve the problem. These methods are usually a variant of Gaussian

elimination. Using iterative methods, only an approximate solution is produced after a finite number of steps. Direct methods are usually faster if there is enough storage to carry them out. But the solution of non-linear equations is usually carried out iteratively, after being linearised in some way [59], for example via Newton's method [63]. On each iteration a direct method is used to solve for the approximate solution, and the error in the result is progressively decreased to convergence. In many cases, such as multi-dimensional steady-state diffusion, the system of equations is large and sparse [57]. This means that only a relatively small number of the matrix elements are non-zero. It is wasteful to use general methods of linear algebra on such problems, because most of the arithmetic operations devoted to solving the set of equations or inverting the matrix involve zero operands. It is also wasteful to reserve storage for unfruitful zero elements [63]. In such cases there are a number of specialised routines which exploit the sparsity of the problem [67-71].

2.1.2 With phase change - solidification

The analysis of heat flow is complicated when a phase change, such as solidification, occurs in the materials under investigation, and the source term E in equation (2.1) is non-zero. There are various methods of incorporating the latent heat into models of solidification. Some are based on micro-models of the treatment of the nucleation and growth of solid, and these are described in Section 2.3. Perhaps the easiest way to treat the heat source term is to incorporate it into the enthalpy H of the system, in which case the continuum approach may be used :

$$\rho \frac{\partial H}{\partial t} = k \nabla^2 T \qquad (2.2)$$

This is a formulation that holds in both the solid and liquid phases, and is known as the enthalpy method [72]. Its main advantage is that a solution does not require tracking of the phase interface. If g_L is the volume fraction liquid and L is the latent heat of fusion per unit

mass, then in the solidification range, provided the liquid and solid densities are assumed to be equal

$$H = C_p T + g_L L \tag{2.3}$$

$$\frac{\partial H}{\partial T} = C_p \frac{\partial T}{\partial t} + L \frac{\partial g_L}{\partial t} \tag{2.4}$$

and the phase change source term is that on the RHS in equation (2.4). How one can proceed from here is dependent upon whether there is a linear variation of g_L with T, because

$$\frac{\partial g_L}{\partial t} = \frac{\partial g_L}{\partial T} \frac{\partial T}{\partial t} \tag{2.5}$$

and

$$\frac{\partial H}{\partial T} = \left(C_p + L \frac{\partial g_L}{\partial T} \right) \frac{\partial T}{\partial t} = C^A \frac{\partial T}{\partial t} \tag{2.6}$$

C^A is known as the apparent (or equivalent) heat capacity, and the governing enthalpy equation becomes

$$\rho . C^A . \frac{\partial T}{\partial t} = k . \nabla^2 T \tag{2.7}$$

which has obvious similarities with the single phase heat conduction problem. Because the governing equation and the associated discretised equation have the general form of a heat conduction equation with non-linear term, the problem can be solved using a standard heat transfer code, with appropriate treatment of C^A [73]. In some cases the position of the

solidification front is inferred *a posteriori* from the results of an enthalpy method calculation [74]. The key to using this approach is to identify an appropriate approximation for C^A [72].

2.1.3 Treatment of enthalpy; models of microsegregation

As can be seen from equation (2.6), the implementation of the enthalpy method is dependent on the relationship between H and T, or g_L and T. In the previous chapter we saw that two such relationships are based on the lever rule, and the Scheil equation. Both are non-linear with T, requiring use of iterative techniques in the solutions [75], even for an explicit model [76]. These relationships are intimately connected with the way in which solute is redistributed during alloy solidification, as this alters the equilibrium melting temperature locally. In fact the Scheil and lever equations represent two extreme models of microsegregation in which solid state diffusion is either zero or infinite, respectively. Improvements on both assumptions are derived from models which account for a finite diffusion.

Brody and Flemings [77] postulated a one-dimensional model for microsegregation in which solid state diffusion was included, and put forward an analytical solution. They added an explicit finite difference treatment of diffusion, to compute solute distribution during the solidification process, but good agreement with experiment [78] was not achieved.

A large disadvantage of analytical solutions is that variations in the equilibrium partition coefficient γ_0, the dendrite spacing λ_2 and the diffusion coefficient in the solid D_S cannot be treated. Kirkwood presented a numerical model [79] of microsegregation which was later developed [7] to allow the change in dendrite spacing with time to be treated, according to equation (1.10). It was shown that such coarsening has a significant effect in reducing microsegregation, and that correctly accounting for the variation of D_S with temperature resulted in lower levels of homogenisation. In this model, the effects of coarsening (increasing λ_2) were treated by extending the size of the domain under study, introducing new liquid of average composition, thus conserving the overall composition. The physical

meaning of this [80] is that somewhere in the system a dendrite arm is melting and part of this solid together with its associated liquid is transferred at average composition to the element. This dilution effect is responsible for a reduction in microsegregation. The model predictions of microsegregation in Al-5wt.%Cu were in closest agreement with experiment when such dendrite coarsening and time-dependent diffusion coefficient were enabled. The authors also presented a proposed extension of their model to multi-component systems. Their model was extended by Howe [81] for modelling the process of microsegregation in multicomponent steels, including treatment of the peritectic solidification reaction from ferrite to austenite. Details of the numerical methods used for tracking the α/β and β/liquid boundaries are presented in [82].

Despite the disadvantages of analytical models, the speed at which they can be executed has continued to attract interest. One recent example is due to Voller [83], in which the simplifications that permit a semi-analytical solution include (a) the assumption that coarsening occurs at the same rate as that of overall solid growth and (b) the use of a simple integral equation to approximate the rate of back diffusion into the solid. Although highly simplified, the model is an advance on earlier analytical approaches [77] in that coarsening is considered, and with calibration by reference to the work of Kirkwood [7], reasonable agreement is reached with a more general numerical model of microsegregation and with experiment [84] for the case of solidification of an Al-Cu alloy. In particular, the correct increase in the final fraction of eutectic with solidification rate is predicted.

Recently, a comprehensive model of phase change in alloys (called *Alloy*) has been developed, which is based on numerical modelling of solute diffusion [85]. The diffusion solver can handle any number of phases and components. When columnar growth occurs in solidification a slice of the cell or dendrite taken perpendicular to the growth direction is considered. With the cooling conditions defined *a priori*, the primary spacing and tip undercooling are as predicted by earlier theoretical work by Hunt and Lu [86], which is discussed later, in Section 2.2. The diffusion equation for each component is solved within

each phase, with the Stefan formula used for the discontinuity at the moving phase boundaries, at which the calculated compositions must be consistent with the phase diagram. Concentration gradients lead to the growth and disappearance of phases, and the diffusion coefficients can vary with both temperature and composition. The diffusion problem has effectively been reduced, by axisymmetry, to a one-dimensional problem, and a control volume method is used to obtain a solution at each time step. The approach to tackling peritectic solidification is illustrated in Figure 2.1. The boundary between phases is always at a control volume centre, and these control volumes expand or contract as a phase grows or shrinks. The numerical formulation is implicit, and the Newton-Raphson technique is used to solve the non-linear simultaneous equations. The output from *Alloy* includes the cooling curve, a map of microsegregation, and a schematic representation of the microstructure. Currently phase diagrams and other thermodynamic data are obtained by *Alloy* directly from *MTDATA*, a thermodynamic database software package developed at the National Physical Laboratory, UK [88]. According to the authors [87], the flexible grid technique used is more efficient than the fixed grid techniques employed by other workers. They use the model to treat both peritectic and eutectic transformations in ternary Cu alloys, and by treatment of solid phase transformations after solidification, it is believed that predictions of final compositional variations across the microstructure will be more accurate. Predictions of the model are currently being compared with experimental results.

Unlike in both the Scheil and lever equations where H is simply a function of T, with a model such as *Alloy* which solves the diffusion problem in solidification rigorously, H is also a function of the cooling rate $\partial T/\partial t$ which may vary with time t, thus giving a more physically realistic treatment of the heat evolution than in equation (2.6). The amount of diffusion depends critically on the scale of the solid, which is set by the cellular or dendritic spacing. This in turn is determined by close study of dendritic growth, which is the subject of section 2.2. It has been suggested [20] that the estimation of diffusion distance is the weak step in all numerical models of this type.

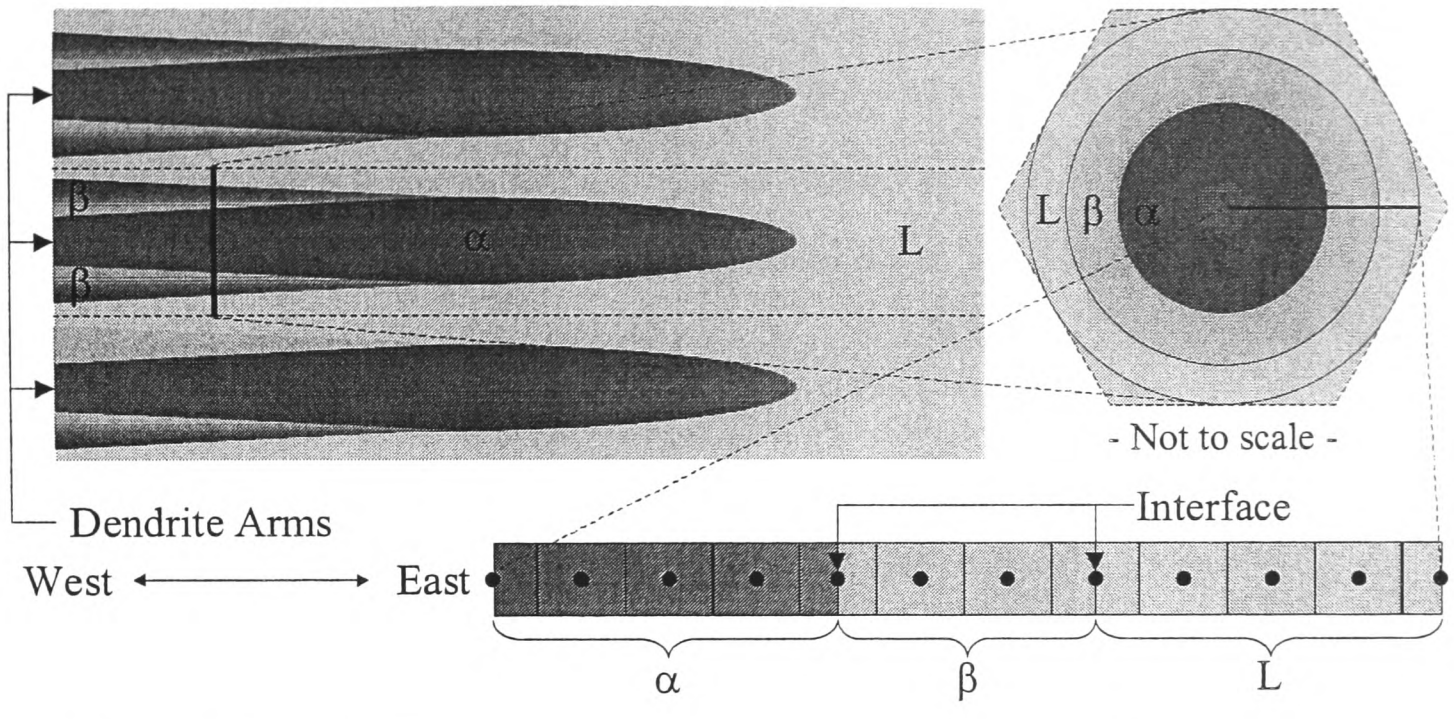

Figure 2.1 Schematic illustration of a volume element in *Alloy* [87].

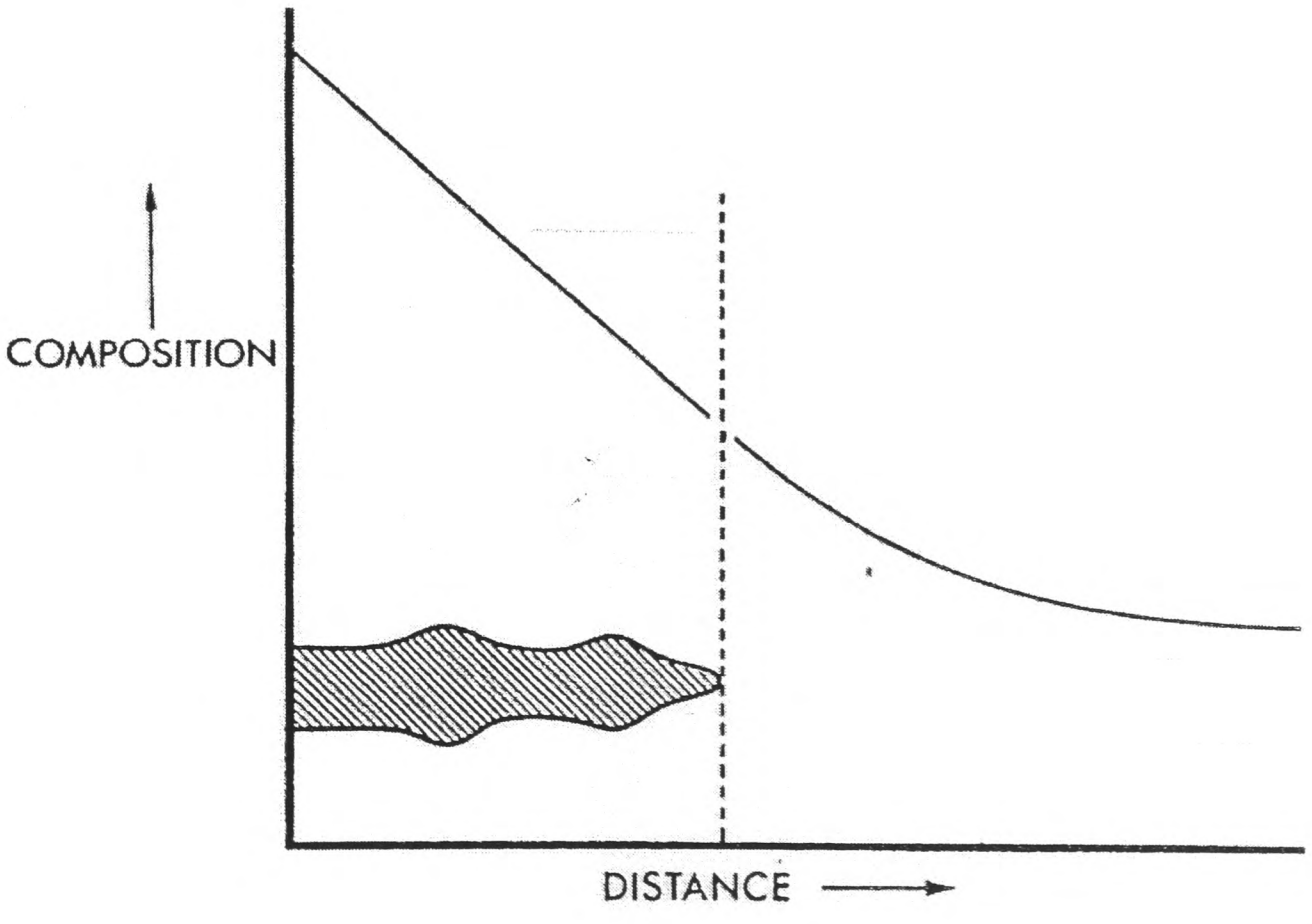

Figure 2.2 Schematic view of the average liquid composition between the dendrites and that ahead of the dendrite front [8].

2.1.4 With fluid flow

The physical effects of fluid flow during solidification were presented in Chapter 1. Here the modelling of such phenomena is reviewed. The rate of heat transfer by conduction is modified by the relative motion of the liquid in the system under study. This mode in which heat transfer is influenced by fluid motion is termed convection. In its presence, the energy equation (2.1) must be modified to take account of the velocity $\underline{V}$, and it becomes [57]:

$$\rho.C_p.\left[\frac{\partial T}{\partial t} + (\underline{V}.\nabla)T\right] = k.\nabla^2 T + E \qquad (2.8)$$

in which the second term within the square brackets represents the convective part of heat transfer.

Natural convection flows are generated because of density differences that arise due to temperature (or composition) variations in a body force field, such as gravity. So the flow is directly linked with the heat transfer process and the two have to be considered simultaneously. Since $\underline{V}$ depends on T, equation (2.8) is non-linear, even in single phase systems in which E is zero. An important approximation used in treatment of natural convection flows is the Boussinesq one [57], which assumes a linear dependence of density on temperature and neglects the density variation in the continuity equation.

In addition to treatment of natural thermal convection in the bulk liquid, flow through the dendritic mushy zone also needs to be considered in models of alloy solidification. This can be done by considering, for example, the columnar zone to consist of an array of solid cylinders, in which case inspiration could be drawn from treatments of flow about such obstacles [89-91]. Indeed analogy with flow through a bundle of capillary tubes was used by Mehrabian and Flemings [47] to develop an expression for the permeability of the mushy zone. This was then used to model such interdendritic flow, by use of the D'Arcy law for flow through porous media. This type of treatment finds uses beyond casting problems, such

as in the modelling of flow through sandstone [92] or reservoir rock [93]. In the mushy columnar zone in castings, the liquid flow is driven by gradients in liquid composition, and as stated in Chapter 1, the authors [47] developed an expression to predict the flow instabilities arising when there is a significant flow of interdendritic liquid from cooler to hotter regions. The mathematical statement for the requirement of remelting and hence channel segregate formation presented was

$$\frac{\underline{V}.\nabla T}{\varepsilon} < -1 \qquad (2.9)$$

where ε is the local rate of temperature change. It can be noted that for channel segregation to occur, the liquid should flow from cold to hot. A low cooling rate, and fast-flowing liquid in a large temperature gradient will facilitate such channelling, in agreement with experimental findings [3,48,49]. However, when broken down, equation (2.9) just states that channelling will occur when liquid flows from colder to hotter regions. A more complete mathematical treatment of channelling followed [94].

Streat and Weinberg [44] developed a model in which liquid flow through the dendritic array is estimated by considering the partially solidified alloy as a porous medium, the permeability of which, as in [47], was expressed by analogy with flow through a bundle of capillary tubes. They did not attempt to model channel formation. Nor did Schneider and Beckermann in their 2D model [95] of fluid flow in binary Pb-Sn solidification. They used an anisotropic permeability of the columnar mushy zone (different values parallel and perpendicular to the primary columnar dendrite arms), based on experimental evidence [96]. But for high volume fractions liquid (>0.7) they based the permeability value on flow through arrays of cylinders [90,91]. Both lever and Scheil microsegregation models were adopted, and the predicted levels of eutectic formation were higher using the latter assumption. In an analysis of the effect of gravity level on interdendritic flow in the mushy zone Dupouy and Camel pointed out [97] that in this zone the concentration gradients are the driving force for convection due

partially to the high ratio between thermal and solute diffusivities. They consider vertical upward solidification of an Al-Cu alloy. In this case solidification of hypo-eutectic is solutally stabilising (scalar product gradρ.**g** is positive), that of hypereutectic is destabilising as the rejected solute Al is lighter (scalar product gradρ.**g** is negative). Although they correctly predicted the onset of hydrodynamic stability, essentially via the relationship (2.9), as the model is 1D the real problem of channelling in castings was not addressed. Krane, Incropera and co-workers [98-100] developed a comprehensive 2D continuum mixture model of alloy solidification in which thermosolutal convection was considered in two types of mushy zone. The columnar zone was characterised as a porous medium, whereas two phase flow was considered in the equiaxed zone by characterising it as a slurry of free-floating dendrites. Despite the complexity of their models, they do not treat channel formation. In other work [101] predictions of macrosegregation from a 2D model, implemented in both finite volume and finite element formulations, are compared to earlier experimental work [45]. Reasonably good agreement was found "if the tendency to form remelting channels is averaged". The authors admit that there is no instability criterion (like (2.9)) built into the model, and so channelling effects cannot be predicted. Perhaps the best effort at modelling of channelling to date is that due to Poirier and co-workers [102]. Their 3D model of upward directional solidification is a continuum one, which uses a single set of equations governing conservation of mass, momentum, energy and solute, in the whole domain, with no tracking of interfacial conditions. The porous medium approach to the mushy zone is taken. The Boussinesq approximation is made for treating natural convection. The model was applied to a Pb-10wt.%Sn alloy, and favourable comparison with experiments [103,104] was reported. Recognising the need to deal with the onset of the channelling instability, the calculation was started by prescription of a small initial random perturbation to the solute concentration field. The system was allowed to evolve undisturbed thereafter. Because such channels are very narrow (~ 1mm) , a fine mesh resolution was needed to simulate their formation and associated segregation. Due to the resultant computational limitations, the domain dimensions had to be kept small (10 mm x 10mm x 20 mm high). Several channels penetrating into the mushy zone were predicted, although the

return of fluid into the mushy zone (which should cause local blockage by enhanced solidification) was not considered.

2.2 Models of Dendritic Growth

If models of columnar and equiaxed growth in castings are to be developed, they must be based upon sound theories of the kinetics of dendrite growth. The development of expressions which relate the tip velocity to its undercooling and to solutal diffusion are particularly needed. Such theories are the subject of this section.

As presented in Chapter 1, Ivantsov obtained analytical solutions for the growth of single isothermal and isoconcentrate dendrites [11]. This theory was developed further by Trivedi [105], who studied the growth of dendritic needles from a supercooled melt. Later Burden and Hunt [8] developed such a solution for non-isothermal dendrites, such as those growing under an imposed temperature gradient, the composition profile of which is shown in Figure 2.2. Neglecting the kinetic undercooling, and using a minimum undercooling criterion (the dendrite stability analysis [13] and its later dismissal had not yet been completed), the authors developed an expression for the tip undercooling of the form

$$\Delta T = \frac{GD}{V} + A\sqrt{V} \qquad (2.10)$$

in which A is a constant which is alloy-dependent and proportional to the composition C_o, and D is the diffusion coefficient for solute in the liquid. The first term was identified as being due to the matching of the composition variation between the dendrites to the average gradient ahead of the interface. The second term incorporates the undercooling due to rejection of solute at the tip [106]. At high gradient G and low velocity V the first term is dominant, so that undercooling initially decreases with increasing V. But as growth rates

increase the first term diminishes and undercooling starts to increase with V. This behaviour was found to be in close agreement with the careful experimental work [19] described in the previous Chapter. This work was later described by Flemings as a "unified view" [107], combining the theories of isolated dendrite tip growth with treatment of the interdendritic effects, and providing a "fresh basis on which to view the dendritic growth process". Hunt's analysis was later extended to predict the relationship between primary dendrite or cell spacings (λ_1) and G and V [108]. Via consideration of interdendritic diffusion of solute, and again assuming that the dendrites grow at the minimum undercooling, the following relationship was derived

$$\lambda^4 G^2 V C_o^{-1} = B \qquad (2.11)$$

where $\lambda=\lambda_1/2$ and B is a constant. The expression was consistent with available experimental data. It shows that spacing increases with decreasing temperature gradient and velocity and increasing composition. Spacing is more sensitive to changes in temperature gradient than to changes in composition and velocity.

In 1984 a special issue of *Materials Science and Engineering*, with a foreword by William Tiller [109] was published to mark the 30th anniversary of the elucidation of constitutional supercooling by Tiller, Bruce Chalmers and co-workers. However, in the same issue John Hunt warned against the general application of the concept to equiaxed growth. He argued [110] that there is no long-range solute layer built up ahead of a dendritic array, because most of the solute is pushed sideways between the dendrites. And constitutional undercooling was developed [109] to describe the morphological breakdown of a planar front. The difference with a growing dendritic front (columnar or equiaxed) is that here, for reasonably large spacings λ_1, a layer of solute does not have to be pushed into the bulk liquid for the front to advance. At low values of G we expect a large λ_1, from equation (2.11). This will also make

the first term on the right hand side of the relationship (2.10) small so that the dendrite tip kinetics can be calculated from

$$V = C_1 \Delta T^2 \qquad (2.12)$$

where C_1=1/A. This is consistent with an analysis [8,105] which stemmed partially from the Ivantsov theory of isolated dendrite growth. A separate treatment of a diffusion layer ahead of the growing front would over-specify the problem here. But in the case where λ_1 becomes very small, then a planar (constrained growth) or spherical (unconstrained growth) morphology is approached in the limit, and such diffusion must be treated. In that case, however, the link between solidification kinetics and the Ivantsov problem is broken, and equations (2.10) and (2.12) are no longer applicable. In the same special issue, Lipton, Glicksman and Kurz [9] developed an expression for the growth rate V of a free isothermal dendrite (the so-called LGK model) based upon the Ivantsov solutions for solute and heat rejection, and the marginal stability criterion [13]. As with the earlier work of the Hunt group, the analysis started via consideration of the contributions to the total tip undercooling. The authors concluded that in very dilute alloys thermal processes dominate, but otherwise it is the liquidus gradient around *the tip* that is the dominant factor. They explained [9] the reason for their observation that dilute alloys, at a fixed undercooling, exhibit an initial increase in growth rate with increasing C_0. According to the stability theory used, the dendrite tip grows with a radius R close to its limit of stability, and addition of small amounts of solute further destabilises the dendrite tip, driving it to smaller radii. Thus heat can be dissipated more rapidly, and so V rises despite the more slowly transported species. At higher levels of solute addition, however, V starts to decrease because of the slower diffusion of solute in comparison to heat. The LGK model predicts these effects. However, with the deconstruction of the marginal stability theory [17], the model cannot be regarded as physically sound, and furthermore no account is taken of potential dendrite interaction.

A numerical analysis of array growth developed by Hunt and McCartney [111] was used to model isolated dendritic growth [112] by setting the spacing very large. With G set to zero, the results could be compared to analytical solutions which used Ivantsov and the marginal stability theory (e.g. [9]). A fully implicit control volume method was used to solve for the concentration field and for the steady state axisymmetric interface shape. The authors showed that there was only one steady state solution for R when anisotropic surface energy was correctly incorporated into their model, and that this solution was very close to that predicted by the marginal stability criterion. The model was later used to study array growth in a finite temperature gradient [113]. The spacing in this problem provides an additional degree of freedom, which was solved by a study of the interaction of a central cell with six surrounding cells. The study found that the critical spacing is that for which the composition variation along the cell groove is nearest in composition to the equilibrium composition. This is the array stability limit, below which overgrowth would occur. Above this spacing a uniform array is established, and a factor of two is expected in the range of spacings possible. Large undercoolings are predicted at small spacings. The model spacing predictions compared well to experimental results, and $V(\Delta T)$ predictions matched very well to the experimental results from Burden and Hunt [19] for Al-2 wt.%Cu, but poorly to experiments [114] on Al-32wt.%Cu. It was thought that this was because of the greater level of convection in the latter case, which was not treated in the analysis. Because of the good correlation with experiments in which convection was very limited, the authors obtained analytical expressions [86] that fitted their numerical results. For a given alloy, the undercooling ΔT and the array stability limit spacing λ_1 could be calculated as a function of V and G. They expressed the undercooling as

$$\Delta T = \frac{GD}{V} + A_2 V^{\frac{1}{3}} \tag{2.13}$$

where A_2 is constant. The expression has obvious similarities to their earlier one (2.10). The first term is, again, related to the average gradient just sufficient to take away rejected solute

from a planar interface [108], the second is the undercooling necessary to get rid of solute from an isolated tip [115]. These analytical expressions for ΔT and λ_1 were used in the *Alloy* microsegregation program mentioned above. The minimum undercooling occurs when the two terms are equal. At this undercooling the transition from planar to cellular or dendritic front growth [115] occurs. Rounded dendrites are assumed until the second term exceeds ten times the first, and at higher velocities sharp dendrites are expected. For values of distribution coefficient approaching zero, however, the analytic expressions were a poor fit. A modified approach, again based on the Ivantsov solution for an isothermal isolated dendrite tip was used to yield an expression (see Appendix B of [115]) which could be used in such cases. Recently this expression was used to compute the growth undercooling of aluminide dendrites in Bridgman solidified aluminium alloys [116]. The predictions matched, within a factor of two, experimental measurements.

In 1987 Rappaz and Thévoz presented a different type of model for equiaxed dendritic growth [117]. They assumed a spherical grain envelope, within which complete solute mixing occurred, and from which solute was rejected and diffused into the extragranular liquid (Figure 2.3). Yet they proceeded to include the dendrite tip kinetics [119] derived from the Ivantsov theory for the isolated dendrite. This approach is not self-consistent because the only case in which solute must be rejected like this is in the limit where neighbouring primary dendrites interact to such an extent that the grain itself is spherical. Of course in this case the Ivantsov solution does not apply. It is not surprising that the authors found it difficult to match their model predictions with experimental cooling curves, in some cases altering the theoretical tip velocity by an order of magnitude in order to force such agreement. Indeed they concede in their paper that their assumptions are flawed and lead to errors which increase with grain size. The model used the explicit finite difference method to solve the problem. Later the authors developed an analytical version [118], in which they replaced a solution to the problem of diffusion outside the spherical grain envelope with an equivalent solute layer of thickness $\delta=2D/V$. This is the same as that expected for a planar front. The inconsistencies are apparent.

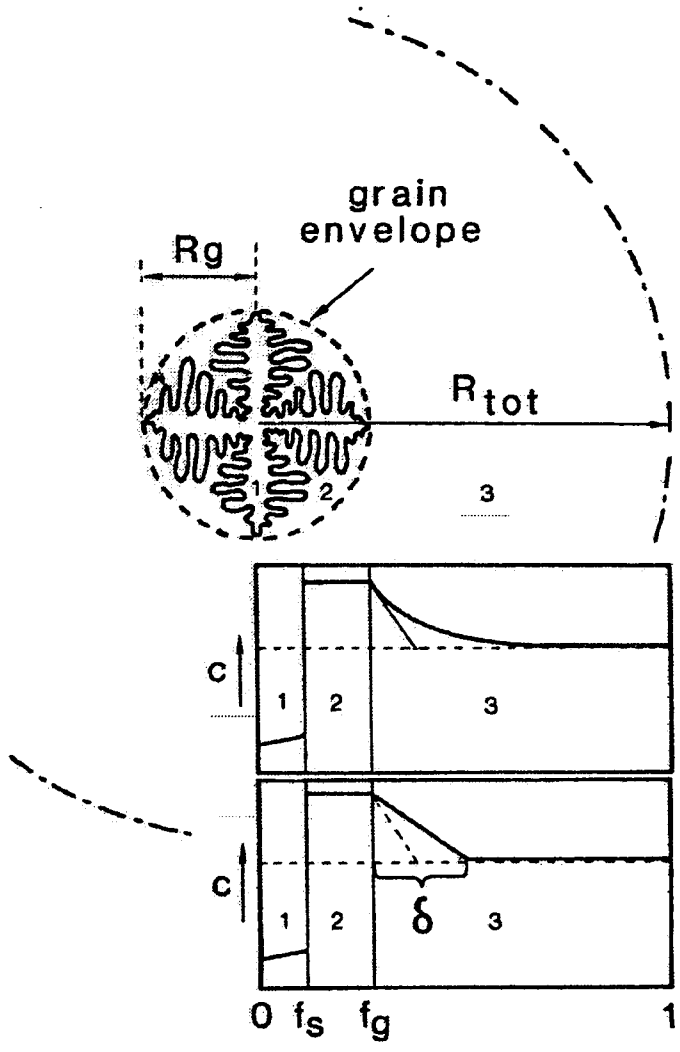

Figure 2.3 Model representation of equiaxed dendritic alloy solidification, indicating assumption of rejection of solute radially from the spherical grain envelope [118].

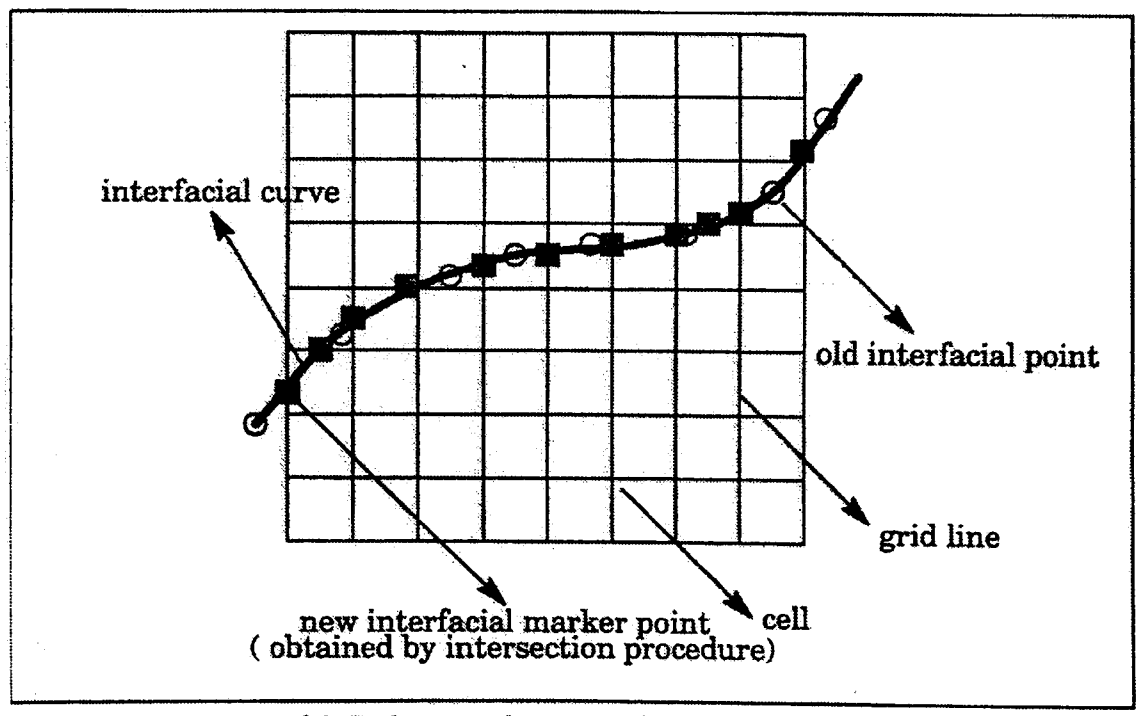

Figure 2.4 ELAFINT front-tracking procedure. Open circles are advanced markers; closed squares are new markers resulting from redistribution via intersection procedure [155].

2.3 Models of Microstructural Evolution

The development of a model of microstructural evolution in casting will generally require mapping of micro-models of Section 2.2 onto macro-models of Section 2.1.

2.3.1 Analytical models

In analytical models of microstructural evolution, no attempt is made to track individual phase interfaces. Rather consideration is given to the integral equation which describes a multitude of phase growth centres over the domain of interest. One such technique is known as the Avrami technique [120], which is described in [1]. Given some rate at which nuclei of new phase β form per unit volume of initial phase α (i.e. a nucleation law) and the growth rate of β, the rate of phase transformation can be calculated. Special consideration is given to the problem of impingement of different areas of β, either by zones of β growing into one another or by nucleation of β in an area which is already β. In this way some of the limits of not tracking individual phase transformation events are overcome. Such a treatment was used by Hunt [110] in an early 1-D model of the competition between steady state columnar and equiaxed growth. It was assumed that all equiaxed heterogeneous nucleation occurred at a single temperature, and that both columnar and equiaxed fronts advanced at a rate V given by equation (2.12). The volume fraction ϕ of equiaxed grains at the undercooling equal to that of the columnar front was taken as the clue to the final grain structure. For large ϕ a fully equiaxed structure was predicted (at high V, low G), whereas for small ϕ a fully columnar structure was expected (at low V, high G). The grain structure predicted in (G,V) space was affected by the number and efficiency of grain refiners, and by the alloy composition. Results from a more complete analysis, in which the heat evolved during growth is allowed to affect G, agreed quite closely with the simpler treatment. The model predicts that dendritic equiaxed growth will occur more easily for alloys with a large solidification range. The Avrami technique was later incorporated by the author into a numerical model of equiaxed

growth [121], in which the bulk undercooling is mapped ahead of an advancing columnar front. Details of the model of columnar growth are given in Section 2.3.3.2.

The first real effort to model microstructural evolution in 2-D came from Rappaz and co-workers [122]. They used an implicit macroscopic enthalpy-type method to solve the heat equation, with a large time step Δt. Onto this they superimposed a semi-coupled microscopic model, with a smaller time step δt, to combine nucleation, grain growth and grain interaction in order to yield a detailed description of equiaxed solidification. The microscopic treatment yielded an equation for the local change in fraction solid Δf_s, as follows

$$\Delta f_s = A.(T^{t+\delta t} - T^t) + B.V(\Delta T).\delta t \qquad (2.14)$$

where the first term represents the contribution made by the internal solid fraction of a solidifying grain, and the second the contribution made by the volume increase of the grain as its boundary advanced at a rate V in the melt undercooled by an amount ΔT. A and B are not constants and have to be calculated at each time-step and node. Each grain grows in a spherical manner, according to the model of [118], with a $V(\Delta T)$ expression from the LGK model [9,10], but is not tracked. Rather the average grain size and growth rate in a region is considered. Although this work was quite novel at the time, it unfortunately inherited the flaws of the Rappaz growth model outlined earlier. These shortcomings, when incorporated into a later model of equiaxed growth [123], resulted in an overprediction of the internal solid fraction of grains, as compared with experimental micrographs. The predicted structure was more globular than that found experimentally. This was probably due to the unrealistic mathematical retardation of the growth of the grain by considering it as a sphere from which solute must be rejected. Indeed the authors noted that this diffusion of solute away from the grain reduces the solutal undercooling, and therefore the grain velocity. The competition between the growth of the grain envelope ("dendritisation") and the growth of solid inside this envelope had earlier been treated by these authors [124], where the internal fraction of

solid tended respectively to decrease or increase. They concluded from the model predictions that low undercooling and convection favour grain globularisation.

In 1994 Steinbach [125] published details of a 1-D model of steady state equiaxed solidification similar to that of Hunt [110], but in which he incorporated the Rappaz ideas of solute diffusion outside of the grain envelope. The model predicted that, for low inoculation, the grain density varies monotonically with the density of inoculant, but reaches saturation above a certain percentage of inoculant. In the latter range, statistical distribution of nucleation sites plays a minor role, while deterministic laws control the nucleation. This was due to the suppression of nucleation within the thermal or solutal diffusion field around a growing grain.

An internal state variable approach, such as that used originally for studies of plasticity [126-128] and stress evolution during solidification [129], was used in an analytical model of equiaxed solidification by Grong at al. [130]. They studied the evolution of temperature, volume fraction of solid, and the number of nuclei using an Avrami-type approach. Heat flow was imposed in the model via study of experimental cooling curves.

2.3.2 Cellular Automata

In an article in *Scientific American* in 1970 [131], Martin Gardner explained the background to a mathematical game called "Life" developed by Cambridge mathematician John Conway. This simulation game resembles real life processes because of its analogies with the rise, fall and alteration of a society of living organisms. To play "Life" one needed a large checkerboard and a supply of flat counters. Starting with a simple configuration of counters ("organisms"), one to a cell, rules are applied via Conway's "genetic laws" for births, deaths and survivals. For example, if an empty "cell" is surrounded by exactly three neighbours (out of a total possible of eight), it is deemed to be a birth cell : a counter is placed on it in the next move. Depending on the initial pattern chosen, patterns evolve from one "generation" to

the next. The potential for use of computers here is obvious. Such techniques became known as "cellular automata" [132].

2.3.2.1 General

Wolfram [132] described a cellular automaton as consisting of a number of sites arranged in a one-, two-, or three-dimensional lattice. Each site has a distinct value at any time t. This is the "configuration" of the cellular automaton. At each time step, the value of each site is updated according to some deterministic rule. The rules for the evolution of a site depend only on a local neighbourhood of sites around it. The author claimed that cellular automata (CA) may be considered as idealisations of partial differential equations (PDEs) in which the dependent variables take on a finite set of possible values. Cellular automata process a large number of data in parallel, such parallel processing is found in many natural systems, and CA algorithms are particularly suited to parallel processing on a computer. In comparison to and unlike numerical solutions to PDEs, CA because of its discreteness involves exact numerical integration [133] - there are no truncation or round-off errors to worry about. Wolfram noted [132] that aggregation phenomena such as snowflake growth follow simple local rules but yield complex patterns, and could potentially be modelled by CA. Vichniac [134] suggested that CA could find natural applications to those areas of physics where the discretisation of space, rather than being an artefact of a numerical simulation, is a feature of the physical system itself (e.g. crystals). He suggested that CA (with probabilistic transition rules) could update very efficiently the lattice configurations of Monte Carlo samples, and that CA could treat nucleation and growth, phase co-existence and stability. CA could also be used [134] to treat entropy, from the statistical mechanics/thermodynamics perspective. The CA method was applied [135] to predict the mechanical behaviour of two-phase materials (e.g. metallic alloys). This model predicted that the overall viscosity of the material increases with strain, due to shape changes undergone by grains during straining - called "morphological" strain hardening. The authors noted that the viscosity of one of the phases could be zero i.e. a liquid, in which case their model could be used to study the behaviour of the mushy zone

during alloy solidification. The application of CA methods in solidification is the subject of the next sub-section.

2.3.2.2 Solidification

In 1984 Packard presented a CA model of solidification [136]. Sites on a lattice change from zero to one (solidification) according to a local deterministic rule. Depending on the exact rule, growth inhibition (physically related to the heat of solidification) can have varying levels of importance. The rule can also incorporate surface tension effects. A continuous variable can also be added at each lattice site to represent temperature. As parameters are varied in the growth law, the 2D model illustrates transition between different macroscopic growth forms. In one case the development of dendritic-style growth patterns is observed from the model predictions.

Rappaz and Gandin later developed a CA model [137] to predict microstructural evolution at a larger length scale - that of the grain. The initially liquid 2D domain is isothermal, and a constant cooling rate is applied. Potential nuclei are placed randomly among a large number of cells, and they start to grow when their allocated nucleation undercooling is reached. The crystallographic orientation of each grain is also chosen randomly. The overall shape of an equiaxed grain is approximated by a square in two dimensions, whose diagonals correspond to the <10> orientations. The growth along these directions is taken from another model based on the Ivantsov solution to the dendrite growth problem plus marginal stability - this is the KGT model [138], which is implemented here as a look-up table for a particular alloy in which V is ascertained as a function of ΔT. The assumption of a square shape, however, is only valid if four of the six dendrite trunks are in the plane under consideration. This may well occur for *one* grain, but for *many* grains this is highly unlikely. The use of probabilistic methods for nucleation and grain orientation is quite appropriate, but the authors proceed to treat growth (or "the entrapment of liquid by the growth of an existing solid neighbour") using a Monte Carlo procedure, despite the fact that the KGT law for dendrite tip kinetics is a deterministic one. This overly-complicates the model, yet the authors admit that using a

simpler deterministic approach to grain growth did not produce significantly different results, and a correction procedure has to be applied to the probabilistic growth model in order overcome dependence on the CA network, and to force agreement with the expected results (i.e. with those from the deterministic approach). Another shortcoming is the failure to treat latent heat evolution. Despite these shortcomings, the model does predict the outer equiaxed-columnar and the inner columnar-equiaxed transitions, with visualisation of the growing solid grains. The effect of alloy concentration on the CET is due to regulation of the growth kinetics, with a lower solute level providing faster columnar growth and thus a smaller equiaxed region. The effect of alloy concentration and cooling rate upon the resultant microstructure agree with experimental observations. The CA model was later coupled to an enthalpy method FE heat flow calculation [139]. A Scheil approximation was used to calculate the latent heat released by CA cells as they changed phase, and this was fed back into the macroscopic FE calculation. Nucleation undercoolings were randomly generated with a Gaussian distribution and attributed to randomly chosen cells of the Cellular Automaton. The coupled CA-FE model was applied to two solidification experiments : the Bridgman growth of an organic alloy and the 1-D solidification of an Al-7%Si alloy, and favourable agreement with experiment was reported. The model was used to analyse three columnar grains growing side-by-side in a linear temperature gradient [140], the central one of which was not aligned with the gradient. The central grain could not expand in the direction in which its primary arms were growing, because it was blocked by its better-aligned neighbour. As it was gradually overgrown by the grain on its other side, this central grain eventually disappeared as columnar growth continued. As columnar grains grew upwards, their density in a transverse section decreased. The model is useful in simulation of directionally solidified investment cast turbine blades with a constriction acting as a grain selector (in an effort to produce a single crystal blade). A 3D version of the CA model was later developed and used as a post-processor for a commercial FE solidification package, again for the investment casting of single crystal superalloy casting [141]. The microstructure model operates on the thermal field predicted by the FE model. The heat transfer coefficient (h.t.c.) was varied until the model predictions matched experimental thermal readings. Worse

still, the thermal conductivity of the alloy (CMSX-4) in the mushy zone was also altered to force agreement between model predictions and experimental observations. A more robust approach would be to separately determine thermophysical data and boundary conditions. For example, Browne and O'Mahoney conducted a comprehensive investigation into interface heat transfer in investment casting of aluminium alloys [142,143], using inverse methods [144]. Similar studies for twin-roll casting have also been carried out [76].

The problem of the dependence of grain shape on the CA grid orientation was tackled by Warnken at al. [145], who used a "rotated grid" concept. For each grain a separate basic CA subgrid was used to calculate the growth. An additional global grid contained general information such as the thermal field or the boundaries of the calculation domain. During a calculation each grain was continuously projected on the global grid by tracing the movement of the grain boundaries.

Recent CA-FE model predictions and experiments in Bridgman solidification of Al-Mg alloys reportedly [146] match well, in terms of mapping microstructure in (G,V) space, with the results of the earlier analytical work [110] alluded to in Section 2.3.1.

A similar approach to the modelling of the evolution of grain structure is due to Nastac and Stefanescu [147]. They fixed the cooling rate *a priori*, used the KGT model for growth kinetics, and also used the questionable approach of treating the extension of grains in a probabilistic manner. Their 2D calculation domain was quite small (5mm x 5mm). The CA approach was also used [148] in an attempt to simulate dendrite morphology as opposed to grain structure. But the function employed to predict secondary arm formation and coarsening was a two-parameter empirical one, making the model rather speculative.

2.3.3 Front-tracking

The Stefan problem involves the solidification or melting of a pure substance and is characterised by a distinct moving phase change boundary at which a heat balance condition has to be met [72]. In a heat conduction-controlled problem the governing equations are

$$\rho C_s \frac{\partial T_s}{\partial t} = \nabla.(k_s \nabla T_s) \qquad \text{in the solid} \qquad (2.15)$$

$$\rho C_l \frac{\partial T_l}{\partial t} = \nabla.(k_l \nabla T_l) \qquad \text{in the liquid} \qquad (2.16)$$

$$k_s \nabla T_s.\underline{n} - k_l \nabla T_l.\underline{n} = \rho L \underline{v}.\underline{n} \qquad \text{heat balance at moving solid/liquid interface} \qquad (2.17)$$

where $\underline{n}$ is unit normal on the phase interface, pointing into the liquid, $\underline{v}$ is the interface velocity and L is the latent heat per unit mass. Expression (2.17) is known as the Stefan condition. In these equations the specific heat and thermal conductivity are constant in each phase and density is set constant throughout the domain. Problems that involve a density difference across the phase change require an additional advection term to account for shrinkage-driven flows [149]. Temperature is the dependent variable in equations (2.15)-(2.17). But since the interface is, in general, an unknown curve whose position and shape vary with time, any discretisation poses a problem. If the enthalpy is used as a dependent variable along with temperature, then in this formulation, known as the enthalpy method, the interface is eliminated from consideration in the calculations. Shamsundar and Sparrow [150] demonstrated in 1975 that the enthalpy form of the conservation equation (2.2) is equivalent to the three differential equations (2.15)-(2.17). In general, phase change problems involve multi-component materials, and the phase change occurs over a mushy region in which a distinct solid/liquid interface cannot be identified. Here the enthalpy method is the most commonly used approach [72].

Serious efforts have been made, however, to track the interface and solve equations (2.15)-(2.17) separately in numerical models. These are generally classified as either Eulerian (fixed grid) or Lagrangian (deforming grid) models.

2.3.3.1 Eulerian

In fixed grid methods there is usually some device to track the trajectory of points distributed along the interface. The interface is then defined by interpolation, possibly using splines [151-153].

Charbon and LeSar presented a 2D model of equiaxed eutectic solidification [154] that coupled macroscopic heat diffusion with microscopic nucleation and growth of eutectic grains of lamellar grey cast iron. The heat equation was solved on a fixed grid via the enthalpy method and an implicit finite difference scheme. The resultant temperature field drove a stochastic nucleation model, followed by a deterministic growth model. It was assumed that the grains were small compared to the thermal gradient such that the temperature of each grain was considered uniform. So each grain was characterised by one radius i.e. it was assumed that the solid-liquid interface of the grain remained circular during growth. The solid-liquid interface of each grain was tracked, modelled by "the Jackson and Hunt relationship" to treat extension of the radius via an expression of the form of equation (2.12). The front-tracking treatment of equiaxed nucleation, growth and impingement could be considered as an alternative to the analytical approach [1] based on the work of Avrami.

The above work involves tracking of multiple circular shapes over a fixed domain. The tracking of more convoluted interfaces is far more difficult, and is the subject of research by Shyy et al. [155,156]. They developed the so-called ELAFINT (Eulerian-Lagrangian Algorithm For Interface Tracking) model, which involves front-tracking over a fixed grid via employment of "massless markers" which define the interface. As the front moves through the domain, at each time step new markers are generated from the intersection of the interface with the fixed grid i.e. with the control volume faces (Figure 2.4). This technique avoids the

problem of rarefaction or accumulation of markers as the interface expands or contracts. The model is used to track solidification of pure species by solving (2.15) in the solid, (2.16) in the liquid, and allowing the interface to be defined by the balancing (2.17).

The resolution of the ELAFINT model is determined by the grid spacing. However, the authors note [156] that this is not really a limitation as the interfacial marker motion is governed by gradients of the thermal field - equation (2.17) - and the maximum expected resolution of these gradients is governed by the grid spacing. So any improved resolution obtained by using several interfacial points per cell would be artificial. In the presence of the underlying grid, mergers or breakups can be accommodated by the algorithm (Figures 2.5 and 2.6). According to the authors, if body-fitted Lagrangian coordinates were used, treatment of such mergers in connection with marker-based methods would involve "intense logical manipulation".

The advantage in combining the Eulerian (field solver) and Lagrangian (interface tracking) methods here is that [156] the phases can be treated separately. Thus, unlike in completely Eulerian methods such as the enthalpy method, the interface separating the two phases can be explicitly defined and treated as a discontinuity. And, in contrast with purely Lagrangian methods, grid redistribution for conformity with the moving, distorting boundary is avoided. Thus, in each phase the operations involved in obtaining the flux estimates should involve points in the same phase and the interfacial values only. The authors used the ELAFINT model, for example, to follow morphological instabilities dominated by heat conduction and capillarity such as those pertaining to microstructural evolution in cellular or dendritic growth. This thesis, however, is more concerned with meso-scale modelling at the scale of CET prediction in a casting. But ELAFINT was also used on a macroscopic level to treat both conduction and convection (ignoring capillarity effects) to simulate the melting of gallium from a vertical wall [156]. Close agreement was found with the results of an enthalpy-based Eulerian model, but the ELAFINT model provided explicit information regarding interface shape.

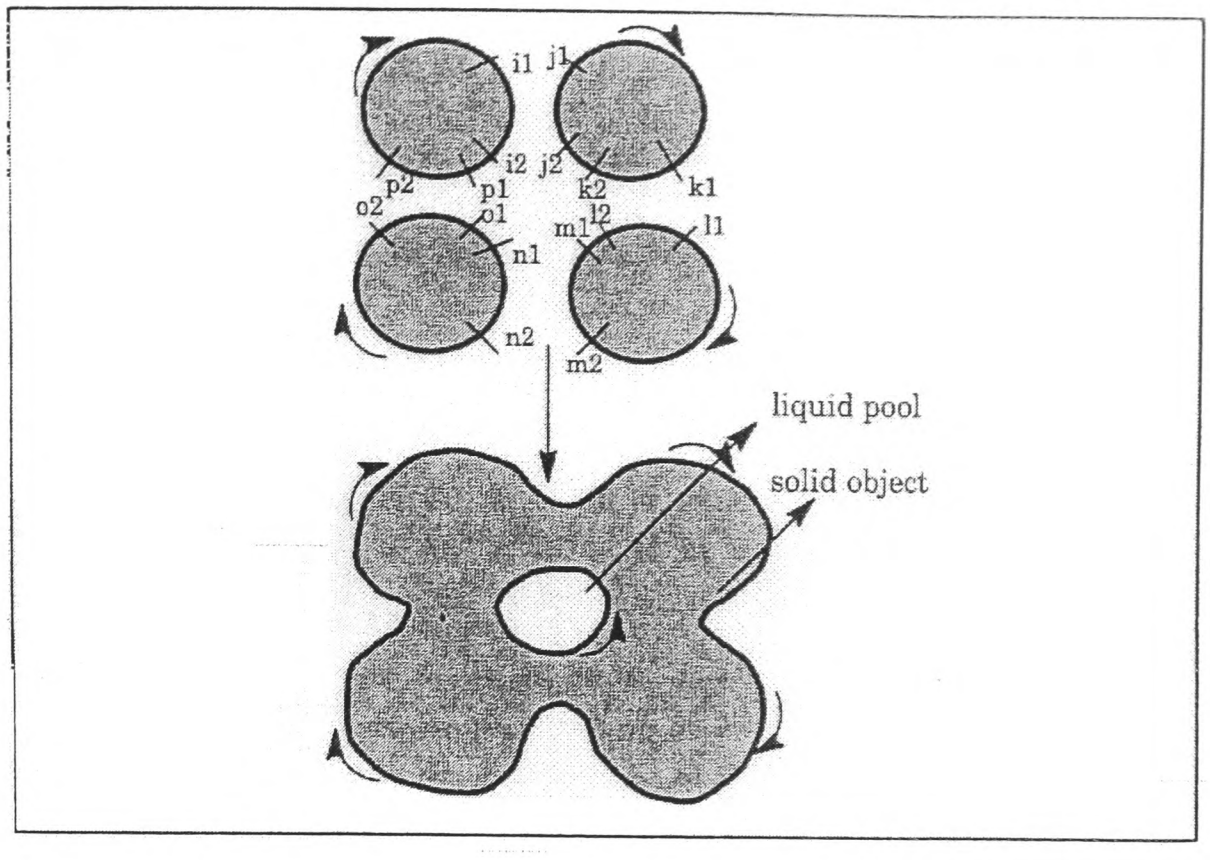

Figure 2.5 ELAFINT merger of multiple objects to create one single object [155].

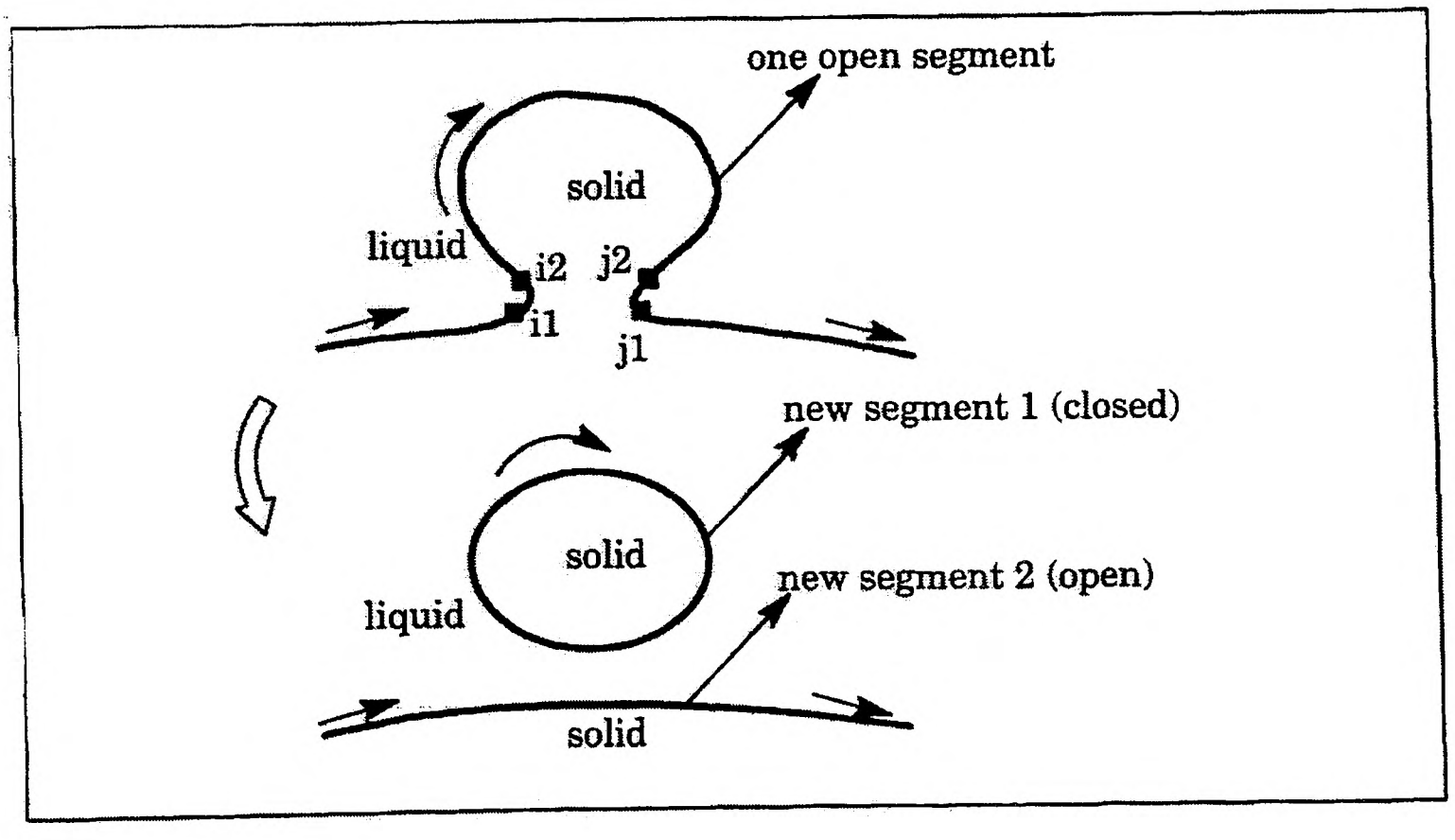

Figure 2.6 ELAFINT break-up procedure [155].

Other workers [157] also developed a front-tracking method to simulate 2D dendritic solidification of pure substances, based on a finite difference approximation of the heat equation and explicit tracking of the solid-liquid interface. Recently the use of a fixed grid front-tracking approach to describe multiphase flows, including the behaviour of gas bubbles in a liquid, based on the numerical simulation of interface dynamics and inter-phase heat and mass transfer, has been reported [158,159].

2.3.3.2 Lagrangian

An alternative to the employment of a fixed computational grid is to use one which conforms to the moving boundary or interface of interest [57,64,155]. Here co-ordinate transformations are used to generate the "body-fitted" curvilinear co-ordinate system to follow, for example, the phase interface in solidification. In 2D, the original co-ordinate system (x,y) is transformed into a new system (ξ,η) such that the curved boundaries in the (x,y) plane become (ξ,η) co-ordinate lines [149]. Note that $\xi=\xi(x,y,t)$ and $\eta=\eta(x,y,t)$. Corresponding to the regular straight-lined (ξ,η) mesh is a curvilinear (x,y) mesh, as illustrated in Figure 2.7.

In moving boundary problems the region changes with time t, but a fixed (ξ,η) mesh which corresponds to a moving (x,y) mesh can be used for all time. The movements of the boundary and of the mesh points in the original region appear only as changes in x and y at the corresponding fixed (ξ,η) points at each time step. The attraction of working in a simple, straight-lined fixed region such as a rectangle with no loss of accuracy in discretisation near curved boundaries are offset by the increased complexity of the transformed boundary conditions and PDEs, together with the additional work of generating the curvilinear mesh at each time step [149]. Also, in systems like equiaxed grain growth, the presence of many grains evolving probably makes such an approach impossible in multiple dimensions.

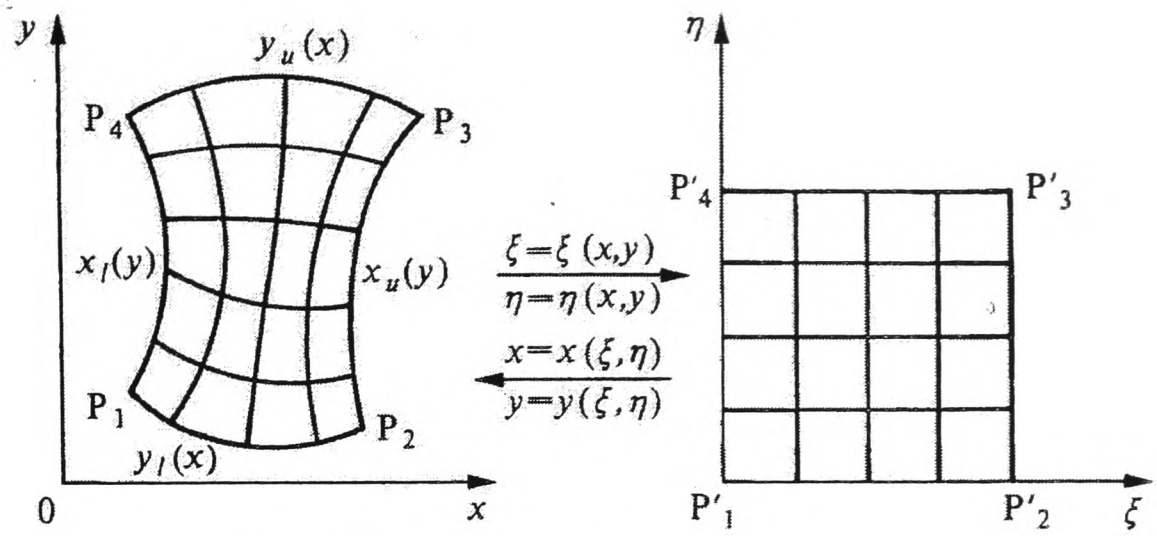

FIG. 5.1. Transformation to rectangular mesh

Figure 2.7 Coordinate transformation to a rectangular mesh [149].

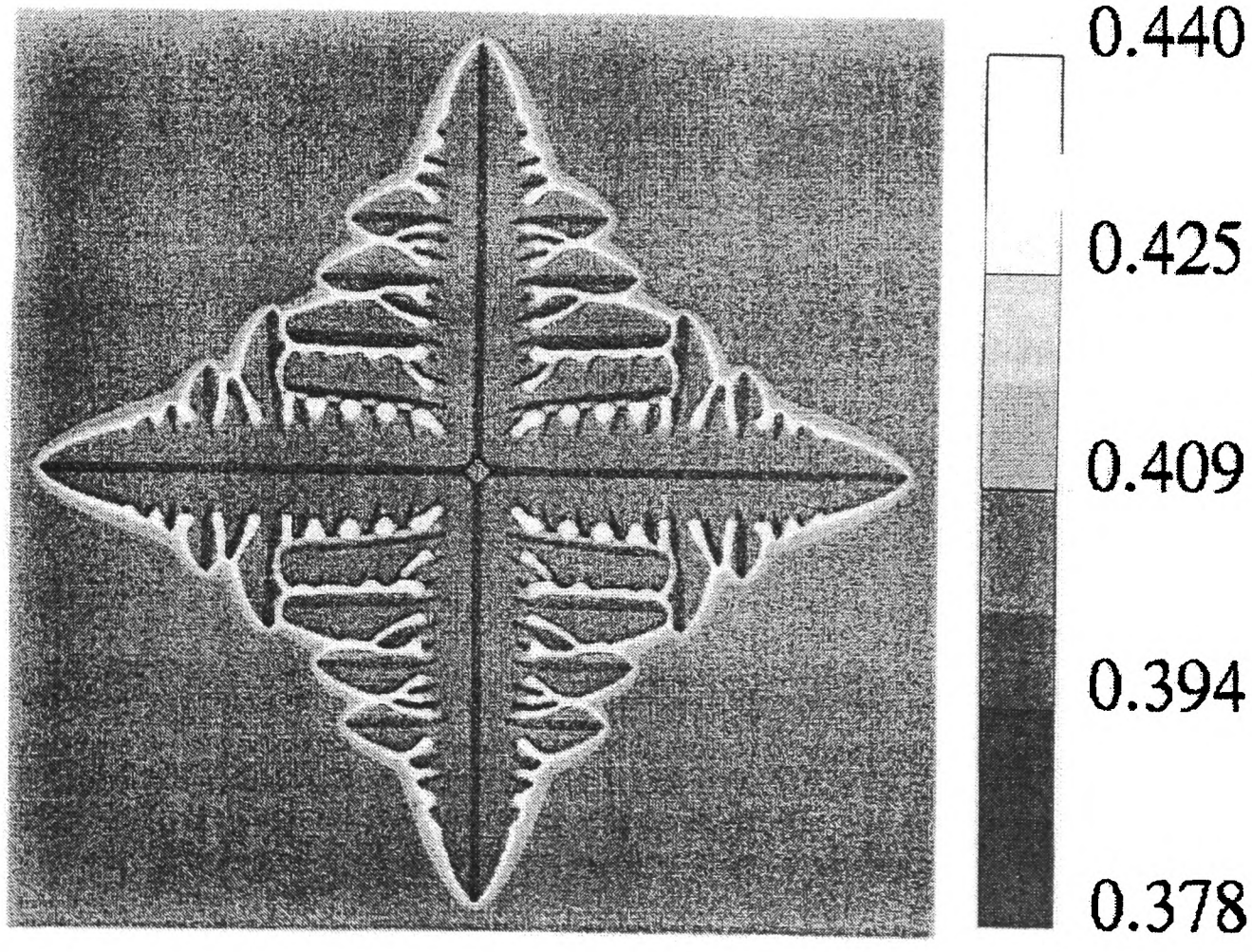

Figure 2.8 Phase field prediction of concentration profile for a crystal growing in a supersaturated melt. The shades of grey indicate the concentration of Cu in a Ni-Cu alloy [168].

Such an approach was used in the development of a 1D model [160] of the directional columnar growth of an alloy. During the calculation, both the velocity of the interface and its temperature was determined. The columnar front constituted the face dividing the last semi-solid control volume from the first liquid one, and as the front moved the dimension of these boxes changed. The predictions of this model were then coupled to a model of the evolution of an equiaxed zone [121] in the undercooled liquid ahead of the front.

A 2D axisymmetric Lagrangian implicit model of steady state cellular growth was developed by McCartney and Hunt [111,161]. The diffusion of heat and solute was modelled on either side of the phase boundary, but the shape was not known *a priori* and had to be obtained from the analysis. Transformation of the co-ordinate system to one moving at the array velocity V was carried out. The control volume (box) walls are arranged so that the interface goes through diagonal corners of an interface box, allowing the diffusion equation in both liquid and solid to be solved separately [112]. The positions of these box corners define the interface shape, and the resultant set of non-linear equations is solved using a Newton method. The model was later developed to study the transient growth of dendrites into a pure supercooled liquid [162], and for a detailed analysis of array growth [113]. The approach used to track the front is not, however, applicable to non-axisymmetric shapes or to convoluted 2D interfaces.

A 2D axisymmetric Lagrangian implicit model of the growth of oxide crystals by the Czochralski method has also been developed [163]. Here the field quantities of temperature, fluid velocity, and pressure were coupled to the system interfaces which comprise the solidification front, melt meniscus and crystal shape. The FE method of solution was used for solution of the field and interface equations, with the mesh defined so that interfacial boundaries lay along element edges, with solutions obtained by a quasi-Newton iterative scheme. A similar model, but treating 3D thermal-capillary problems and using the finite volume method, was later developed [164]. It was used to simulate the float zone growth of

silicon. Newton's method was used via employment of numerical differentiation to compute the Jacobian matrix.

2.3.4 Phase field

According to Wheeler [165] there are three approaches to modelling microstructure : (i) averaging (ii) free boundary and (iii) phase field methods. With averaging techniques, the microstructure is merely defined via fraction solid. Free boundary methods track the phase boundary as a sharp interface. Phase field methods are intermediate between the two extrema. They can more generally be termed "diffuse" interface models. Langer [166] and Caginalp [167] did much of the initial development of these models for the solidification of a pure material. Such models do not distinguish between solid and liquid phases *a priori*. Instead a phase field (ϕ) is postulated such that ϕ=1 in liquid, ϕ=0 in solid, and $\phi(x,y,z,t)$ varies continuously in a finite layer between solid and liquid. It can be considered to be akin to an order parameter. Thermodynamic principles are used to construct an expression for the free energy of the system, and phase boundaries migrate via consideration of interface kinetics. Both isothermal problems involving pure materials and problems for which the heat and species diffusion have to be solved simultaneously have been treated via the phase field method. In order to compute dendrites [168] as illustrated in Figure 2.8, surface energy anisotropy must be taken into account. The method has also been used to predict eutectic and monotectic structure formation [169] and dendritic growth with convection [170]. Because it can resolve the diffusion fields around dendrite arms and simulate the effects of interaction [171], the phase field method may be useful in illuminating the debate on whether or not a layer of solute is pushed ahead of a growing dendritic array or equiaxed grain, as discussed in Section 2.2. The method has also been identified [20] as having the potential to model the solidification path over the multi-component liquidus surface with considerable rigour.

In solidification processes the interface is in fact *very* thin - of the order of atomic distances. Yet the phase field models choose a *relatively* thick interface, the guiding principle being that it is still thin with respect to the microstructural features. In this respect, front-tracking

models such as those of Shyy [156] and Juric [157] are more appropriate, although undoubtedly more difficult to code and with the extension to 3D providing further real challenges. Computationally, however, the phase field method is more intensive and demanding [165]. Many control volumes are needed to cover the interface thickness, and as the grid is fixed one needs a very fine mesh to approach a less diffuse interface. Adaptive grids may work in certain circumstances, but due to the highly branched nature of the dendritic interface this is difficult, and will be even more so if multiple dendritic crystals are to be modelled. So the extension of the phase field method to simulate the evolution of microstructure in castings is a huge challenge from a hardware perspective. However, a phase field algorithm [172] has been used to model the growth of up to 14 equiaxed grains [173]. On the other hand, sharp interface models do not need to straddle the front with many control volumes, because the representation is discrete.

Recently a "pseudo-front tracking" technique, reportedly somewhat between the phase field and front-tracking methods, has been presented [174]. It was used to model, in 2D, primary phase formation during solidification in multi-component alloys. Although its predictions matched well with those of a phase field model, it was reported that the new model was up to four times more computationally intensive than the equivalent phase field formulation.

After review of the many types of model of microstructural evolution in castings, it was decided that the front-tracking work of Shyy and co-workers [156] provided the best basis on which to proceed in this work.

Chapter Three

Numerical Methods - Model Development

Chapter 3

Numerical Methods - Model Development

3.1 Introduction

To develop a new and novel multi-dimensional model of microstructural evolution in shape casting is the objective of this work. In particular, the meso-scale phenomena of both columnar and equiaxed solidification are to be simulated, and the model is to be an improvement on existing ones either in its treatment of physics, its computational overhead, or both. The new computational techniques developed here are to be tested and proven as far as is possible, with a view to extension of the model to predict the columnar-equiaxed transition in many casting processes. It is vitally important that the model compute, present, and distinguish between, zones of liquid, solid, and columnar and equiaxed mush, and simulate the temporal evolution of these zones within the domain as solidification proceeds. This is possible only by the treatment of solidification as a kinetic, and not simply a thermodynamic, process. The main goal is to develop new computing methodologies for the problem, test and validate them, and present them as the foundation for a new generation of research tools in the field.

The work done by others on this and related subjects has been summarised in Chapter 2. A model based on purely Lagrangian techniques will not be versatile enough to treat the problem of multiple sites of nucleation and zones of solidification; excessive complexity would be involved in having the grid follow multiple phase boundaries. Phase field methods have great potential in the study of micro-scale physics, but they are computationally very intensive, even allowing for the fact that they treat the solid-liquid interface as being more diffuse than they are in reality. The approach is not currently applicable to industrial scale casting processes.

Eulerian-Lagrangian sharp interface tracking has been identified as the most suitable approach to the modelling of casting microstructure in diffusive conditions, and with a view to a later treatment of convection. The technique can be used as an alternative to phase field modelling at the micro-scale, as established by other researchers, and instead of cellular automata models of grain growth, as established in this work. Although the boundaries being tracked here appear in simulations as sharp fronts, they represent, for the first time, the interface, not between solid and liquid, but between liquid and a zone of partial solid which is expanding across the fixed-grid domain. The expansion is driven by a computational device describing non-equilibrium solidification.

A full coupling of the emerging meso-scale solidifying structure with heat transfer is implemented. Unlike in previous front-tracking models (e.g. of the development of the liquid/fully solid interface morphology), the Stefan condition does not drive interface motion. Rather the front moves according to the computed rate of heat extraction from the system and a temperature-dependent analytical expression (equation 2.12) which is based on the consideration of isolated dendrite growth. The new model does not treat the contradictory physical phenomenon of solute diffusion ahead of an advancing dendritic array, as if it were planar. Further scientific research is needed if one is to be able to model correctly the growth of solid with a morphology between planar and dendritic with a very wide primary spacing, but the approach adopted here is self-consistent. Dendritic growth is modelled deterministically, and not in the spurious probabilistic manner characteristic of cellular automata models (these latter have been proven both inaccurate and wasteful of computer resources). Nucleation, on the other hand, is more difficult to predict - the new model enables a stochastic approach to this problem.

The reported model is to use essentially the same methodology to treat columnar and equiaxed solidification. Details are presented in Section 3.5. The application of the model to

columnar nucleation and growth is dealt with in Section 3.6. In Section 3.7, the modelling of equiaxed solidification is discussed.

In columnar solidification, one of the key predictions will be the extent of undercooling ahead of the advancing front; this is most important for the nucleation and growth of equiaxed crystals. Such simulations can only be done in non-equilibrium models of solidification.

In order to prove the model, a 2D computational domain is employed, as outlined in Section 3.2. This can later be extended to 3D, as discussed in the final Chapter. More detailed objectives of the model are presented in Section 3.3. The rest of the Chapter contains a summary of the salient technical details of how the model was put together. Its success and potential is evidenced in Chapter 4.

The formulation is an explicit one. The background to the choice of this numerical technique is discussed in Section 3.9, and in more detail in Appendix A.

The model should be capable of establishing the effect of foundry variables such as melt superheat, alloy composition, and heat extraction rate, on as-cast microstructure. Its use in supporting industrial casting activity and process development will be enhanced by its development in a Windows environment, with reasonable execution times on a personal computer.

3.2 The Model System

3.2.1 Geometry

In order to establish the feasibility of using the front-tracking approach, a relatively simple model casting system was chosen. The 2D casting is a simple square of side length w.

Because convection is not considered, only one quadrant - in this case the lower left one, is considered (Figure 3.1). The Cartesian co-ordinate system adopted has the origin (0,0) at the lower left corner, with (w/2,w/2) being at the centre of the casting.

3.2.2 Boundary conditions

The following boundary conditions are used :

at x=w/2 :

$$\frac{\partial T}{\partial x} = 0 \qquad (3.1\ a)$$

at y=w/2 :

$$\frac{\partial T}{\partial y} = 0 \qquad (3.1\ b)$$

at x=0 or y=0 :

$$q = h(T_s - T_m) \qquad (3.1\ c)$$

where q is the heat flux into the mould, h is the interface heat transfer coefficient, and T_s and T_m are the alloy and mould surface temperatures, respectively. In fact the mould temperature is fixed and constant.

3.2.3 Alloy and properties

It is assumed that the solidifying alloy is aluminium based. Ideally thermophysical properties should be entered as a function of temperature and phase [73,175], but constant values of density, specific heat and thermal conductivity are assumed in this model for simplicity.

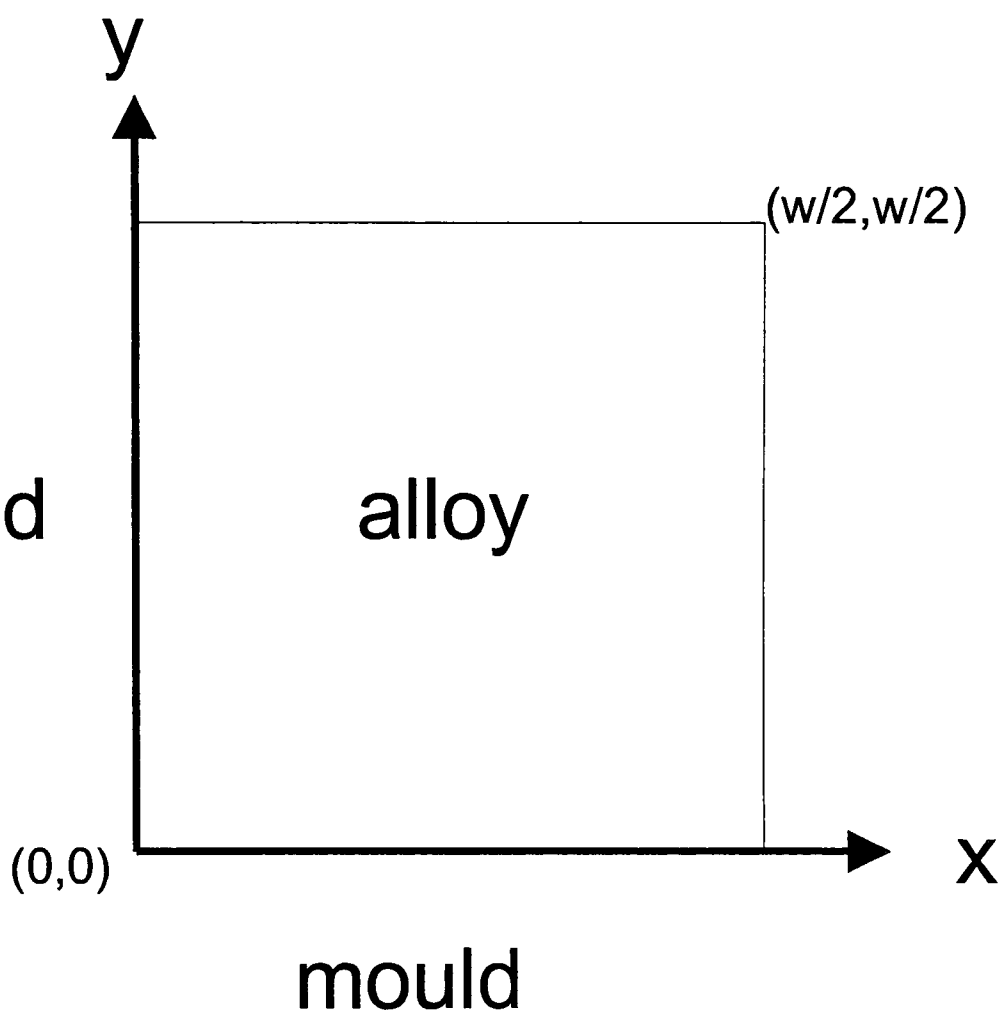

Figure 3.1 The model casting.

3.2.4 Initial conditions

It is assumed that the alloy is initially (t=0) isothermal and at a temperature T_a which is above the equilibrium liquidus temperature T_L.

3.3 Objectives of the Model

The main objective of the model is to predict non-equilibrium solidification of a binary alloy in a mould (Fig 3.1). This should enable simulation of the nucleation and growth of a front of columnar grains into the undercooled liquid. The presence of such a region of undercooled liquid ahead of the growing columnar dendrites will permit modelling of the nucleation and growth of equiaxed grains of solid, and the competition between columnar and equiaxed solidification will yield the CET.

3.3.1 Heat transfer

The control volume technique is to be used, on a fixed grid, to solve the energy equation in the domain. It was decided to develop an explicit model, due to the advantages of this approach as outlined in Section 2.1.1. Some issues related to the development of an implicit version of the model are discussed in Section 3.9 and Appendix A. Source terms are to result from latent heat evolution, as predicted by the phase change algorithm.

3.3.2 Phase change

The model must provide a picture of the evolving grain structure in the casting, and distinguish between columnar and equiaxed solidification. It was originally planned that a model of stress evolution during alloy solidification be developed, but it became clear that, without a verifiable picture of the evolving partition of liquid and solid phases, such a model would not be possible. Nucleation is to be treated in a simple fashion. It is to be assumed that dendritic growth occurs.

3.3.3 Columnar growth

On nucleation, solid growth from the mould wall is to be treated by tracking a front, which represents a curve joining the tips of the columnar dendrites, across the fixed grid. The temporal passage of the front is to be driven by dendrite tip kinetics. It was decided that the model need not distinguish between individual grains in the columnar zone, nor treat the emergence of columnar grains from the outer chill zone. The rationale for this is presented in Section 3.6.2.

3.3.4 Equiaxed growth

The use of non-equilibrium kinetics for columnar growth will enable the extent of the undercooled liquid ahead of the front to be predicted. A random placement of potential nuclei in the domain will allow nucleation and growth of equiaxed crystals to be simulated. The growth of these grains is to be treated in a manner exactly analogous to that of columnar crystals i.e. using the front-tracking approach.

3.4 Heat Model (without microstructure)

The heat equation (2.1) must be solved in the domain (Fig. 3.1). The source term E is calculated from the model of microstructural evolution. A 100 x 100 control volume grid is proposed. For heat conduction, the temperature T_0 of a typical control volume (Δx x Δy x 1), changes during the time step Δt due to the fluxes of heat f_n, f_s, f_e, f_w across its north, south, east and west faces, respectively, as shown in Figure 3.2.

These fluxes, in units of watts, are expressed as follows, assuming unit depth.

$$f_n = k.\Delta x.\left(\frac{T_N - T_0}{\Delta y}\right) \qquad (3.2\ a)$$

$$f_s = k.\Delta x.\left(\frac{T_S - T_0}{\Delta y}\right) \qquad (3.2\ b)$$

$$f_e = k.\Delta y.\left(\frac{T_E - T_0}{\Delta x}\right) \qquad (3.2\ c)$$

$$f_w = k.\Delta y.\left(\frac{T_W - T_0}{\Delta y}\right) \qquad (3.2\ d)$$

where T_N, T_S, T_E, and T_W are the temperatures of the nodes of control volumes to the north, south, east and west, respectively, of the central control volume. Along the mould wall, Newton's law of cooling (equation (3.1 c)) is used to find the flux f_w (if y=0) or f_s (if x=0). Consider the case along the left hand mould wall (Figure 3.3).

$$f_w = h.\Delta y.(T_m - T_s) \qquad (3.3\ a)$$

and

$$f_w = k.\Delta y.\left(\frac{T_s - T_0}{\frac{\Delta x}{2}}\right) \qquad (3.3\ b)$$

If the flux per unit area is expressed as

$$f_w^{'} = \frac{f_w}{\Delta y} \qquad (3.3\ c)$$

then from (3.3 c) and (3.3 a)

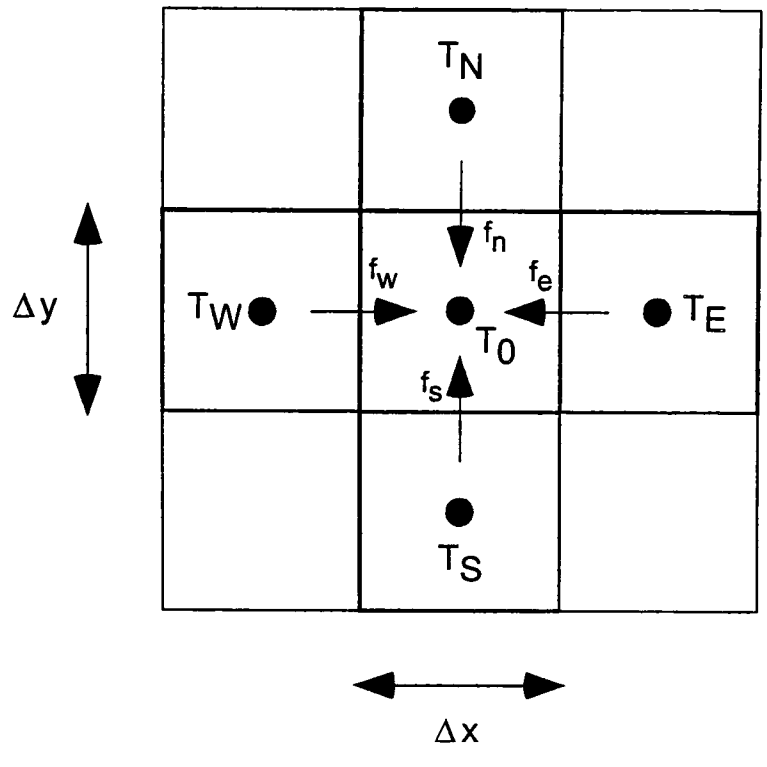

Figure 3.2 Heat fluxes into a typical control volume.

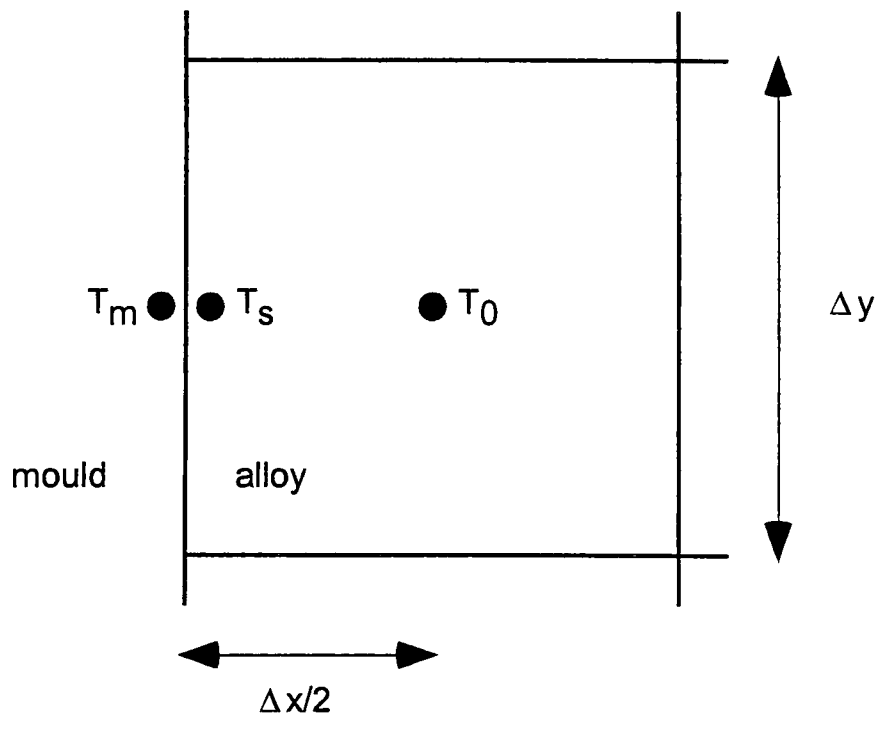

Figure 3.3 Typical surface control volume.

$$T_s = T_m - \frac{f_w^{'}}{h} \tag{3.3 d}$$

Inserting this expression for T_s into equation (3.3 b) yields

$$f_w^{'} = \frac{2k}{\Delta x}\left(T_m - \frac{f_w^{'}}{h}\right) - \frac{2k}{\Delta x}T_0 \tag{3.3 e}$$

Rearranging gives an expression for f_w', which when multiplied by Δy gives

$$f_w = \Delta y.\left(\frac{1}{\frac{\Delta x}{2k} + \frac{1}{h}}\right)(T_m - T_0) \tag{3.3 f}$$

A similar expression is developed for f_s for control volumes bordering the bottom mould wall. The total rate of heat conduction into a control volume is then calculated as

$$f_{tot} = f_n + f_s + f_e + f_w \tag{3.4}$$

Ignoring the latent heat effect (assuming E=0 in equation (2.1)), the change in the nodal temperature in a time step is calculated as

$$\Delta T_0 = \frac{f_{tot}.\Delta t}{\rho C_p \Delta x \Delta y} \tag{3.5}$$

The modification of this expression to account for latent heat is outlined in the next section of the thesis. As the conduction heat transfer model is explicit, the time step for stability is limited by the expression [57]:

$$\Delta t < \frac{\rho C_p}{2k\left(\frac{1}{\Delta x^2} + \frac{1}{\Delta y^2}\right)} \tag{3.6}$$

3.5 General Model of Microstructural Evolution

3.5.1 Introduction

The main contribution of this work is the development of a model of the non-equilibrium growth of solid in a freezing alloy. Subsequent to the review of possible methods of approaching this problem (see Chapter 2), it was decided to use a front-tracking method on a fixed grid. The grid is the control volume one alluded to in the previous section. Starting with a model for nucleation, the growth of the columnar front and equiaxed grain boundaries is to be tracked across the domain as they move. Previous versions of this approach had been used to model the growth of pure solid [156], using the Stefan condition (equation 2.17) to control the motion of the interface. The model was used to simulate dendrite growth. In this case, the problem is at a larger length scale : that of an alloy casting, and so it was decided to model the advance, not of the solid-liquid interface, but of an envelope of dendritic structure ahead of which all was liquid, and behind which a mushy zone exists. Along this new type of interface the fraction solid is zero, although it is expected that the interface is undercooled. It is this undercooling, rather than the Stefan condition used by previous workers, that drives solid growth in the new model.

The heat equation is first applied to the all-liquid domain, as described in Section 3.4. Although nucleation is a complex phenomena, as outlined in Section 1.2, for heterogeneous nucleation a good first order approximation is that nucleation occurs when a fixed undercooling (ΔT_n) is achieved (Fig. 1.2). Such an assumption is made in this model, for

both columnar and equiaxed solidification. Details are provided later. Here the situation is described in which some interface already exists and is growing through the cooling domain.

3.5.2 Interface tracking

The interface is defined at discrete points by massless marker particles (or *markers*). The two basic approaches to curve fitting can be described as "exact fit" and "best fit" [152]. If a large number of data points exist, perhaps from an experiment with some degree of error or scatter, then the best fit approach is appropriate - the fitted curve need not pass through every data point. In such an approach, the difference between the values given by the approximating curve and the supplied data is minimised, such that the error in obtaining values from the curve is small. On the other hand, an exact fit is appropriate if the given data are very accurate or are the results of numerical investigations [152]. The latter is true of this work, and so such an approach, which involves determining a curve that passes through every given data point or marker, is used to represent the interface in this model. It is interpolation. A polynomial of degree n can be devised to exactly fit (n+1) data points. An alternative is based on fitting a small set of data points with lower-order polynomials. Such interpolating polynomials that are employed to yield a piecewise exact fit to the data are known as spline functions [151,152]. In this model, for simplicity, a first order, or linear interpolation is used between markers. This would be a poor approximation if the curvature of the interface was required, for example to calculate capillarity at a dendrite surface, but in this case no such curvature term is required, and the approach adopted is sufficiently indicative of the solidification front, especially if a fine grid is employed. As will be seen later, markers always reside on the grid-lines of the computational mesh at the start of a time step. So at any time during the calculation, the interface and associated markers could appear as shown in Figure 3.4. Any general marker is denoted m, and the markers are numbered consecutively along the interface.

The direction of the progress of solidification is assumed to be normal to the front. These normals are found at the location of the markers by a simple geometric calculation involving

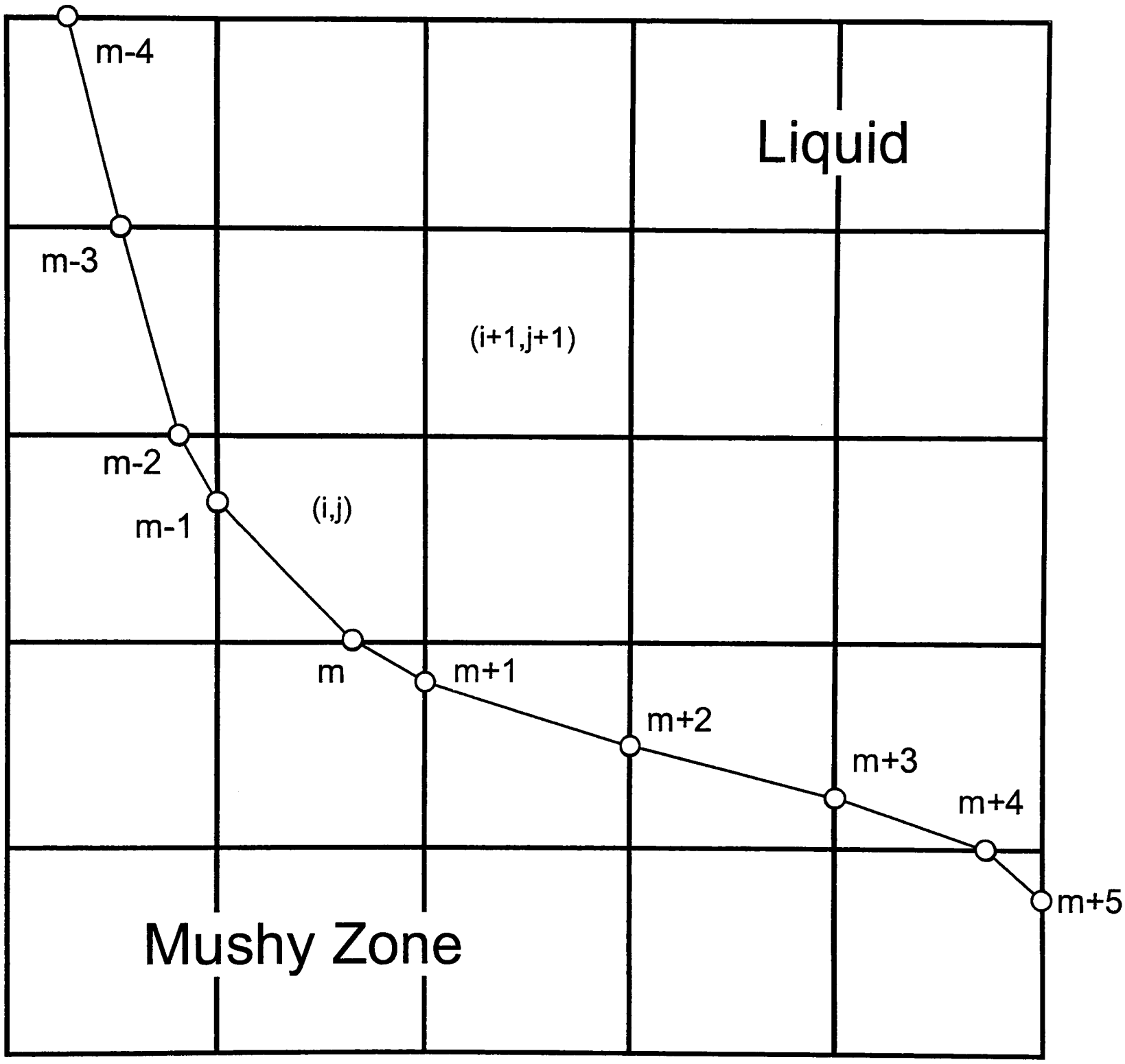

Figure 3.4 Schematic of interface, represented by markers *m*.

bisection of the angle between the two linear portions of the interface which meet at the marker in question. This is shown in Figure 3.5.

The marker *m* will progress along this normal, but the sense of its motion along this line has to be determined. In this work the convention has been adopted that as one "travels along" the interface, in the direction of increasing marker numbers, solid is always to the right (liquid to the left). The marker will advance into the liquid, provided it is undercooled. In Figure 3.5, therefore, it will travel upwards and to the right. Details of the method by which this convention is implemented numerically are presented later, as the approach is also relevant to calculation of the source term for the heat equation.

The magnitude of the advance of the marker into the liquid is determined by its undercooling ΔT_m. In order to calculate this, the temperature T_m of the marker is calculated from the four surrounding nodal temperatures by bilinear interpolation [63]. Such interpolation is second order accurate [176] and has been deemed "close enough for government work" [63]. To increase the accuracy of the interpolation scheme, at least nine nodal temperatures would have to be employed [177], which would cause excessive complication and create a problem near the domain boundaries. Marker undercooling is then calculated

$$\Delta T_m = T_L - T_m \tag{3.7}$$

The kinetics of dendrite tip advance is used to determine the velocity of the marker V_m, via equation (2.12), reproduced here

$$V_m = C_1 \Delta T_m^{\,2} \tag{3.8}$$

This expression is valid for isolated alloy dendrites and can be used [110] in cases where the primary spacing λ_1 is reasonably large. As outlined in Section 2.2, such a situation arises

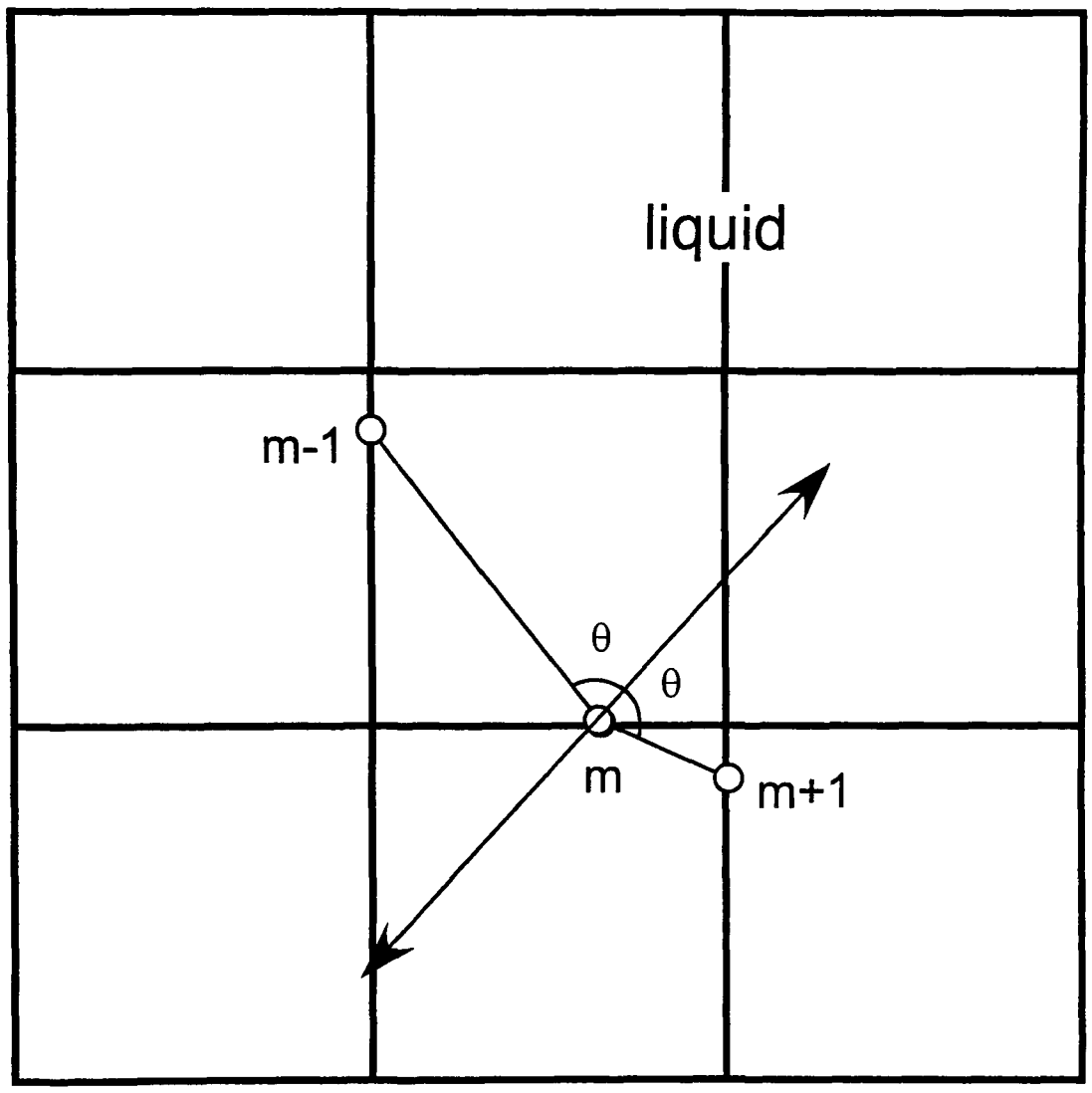

Figure 3.5 Calculation of normal to the interface at marker *m*.

when the thermal gradient G is low. In such cases a layer of solute does not have to be pushed into the bulk liquid in order for the front to advance. C_1 is an alloy-dependent constant which incorporates the effect of solute rejection at the dendrite tip [8,106].

This marker velocity, calculated at the start of the time step, is assumed to operate during Δt (explicit scheme). So the distance travelled by marker *m*, along the path identified, in the time step is expressed as

$$z_m = V_m.\Delta t \tag{3.9}$$

All markers are advanced simultaneously in this way, such that at the end of the relevant time step they will most likely have moved off the grid-lines, as illustrated in Fig. 3.6. The magnitude of the advance of these markers into the undercooled liquid is controlled by the length of the time step, but is generally very small because of the restriction on Δt in the explicit model (equation (3.6)). Although this adds to the computational effort, it ensures that none of the physics of microstructural evolution is lost, as could happen if a very large time step were used. The front can now be represented in its new position via piecewise linear interpolations between the latest position of these points. It can be seen that if such markers were allowed to continue to advance freely with time, they could rarefy or accumulate, depending on the nature of the advance of the front. In the case of rarefaction, the resolution at which the front is represented would be lowered. For this reason, the points at which the new front representation intersect the fixed grid are calculated. These points become the modified marker positions, and in this way the front is always represented at the resolution of the grid - marker rarefaction or accumulation cannot occur. Such a procedure also facilitates calculation of the heat source terms, as will be shown. The procedure is illustrated in Fig 3.7.

At the end of the time step we have a new representation of the solidification front : a series of line segments connecting points on the grid-lines of the computational mesh. The area of the domain covered by semi-solid material has increased, as this front has advanced. This

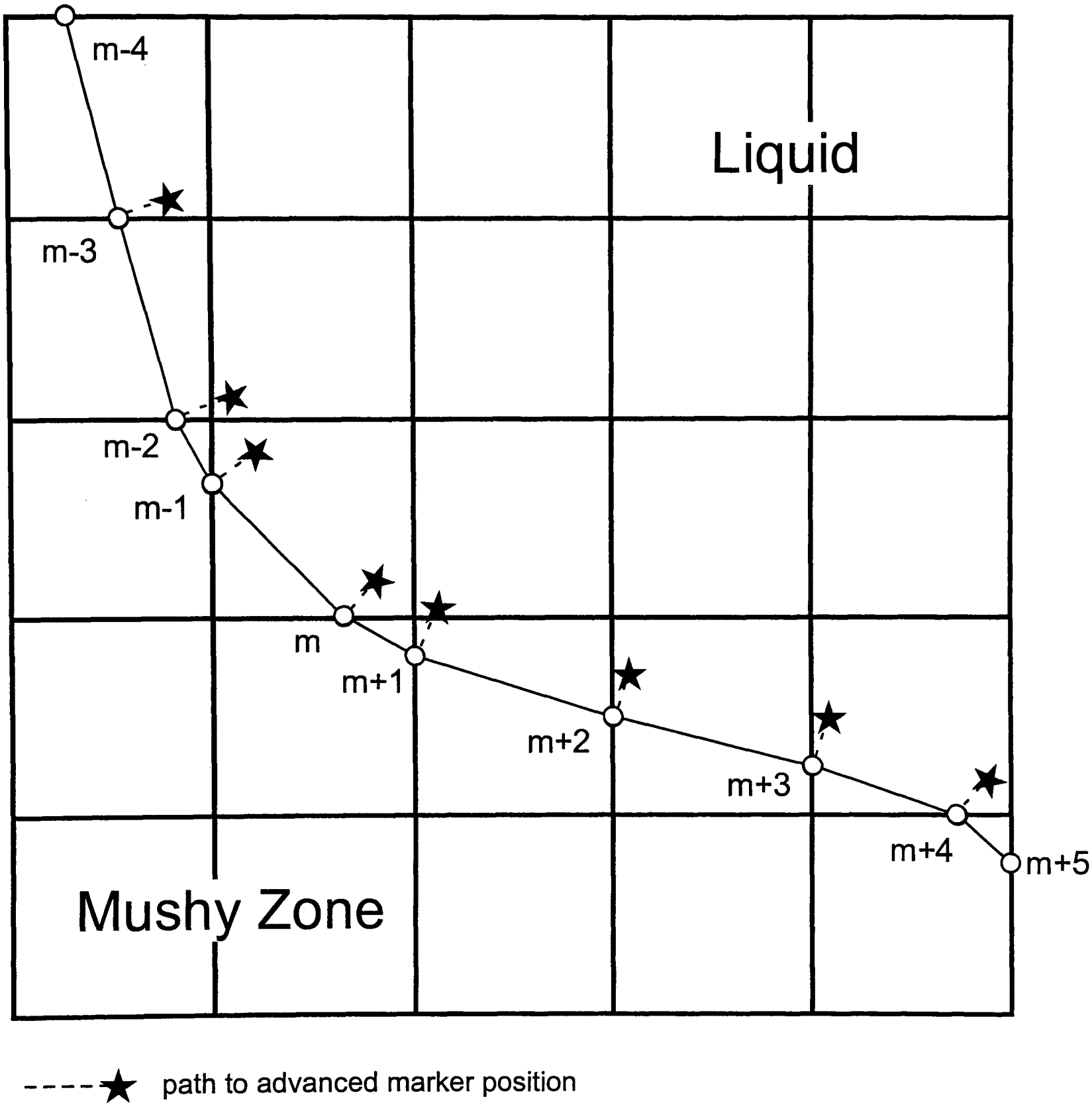

Figure 3.6 The advance of marker particles into the liquid.

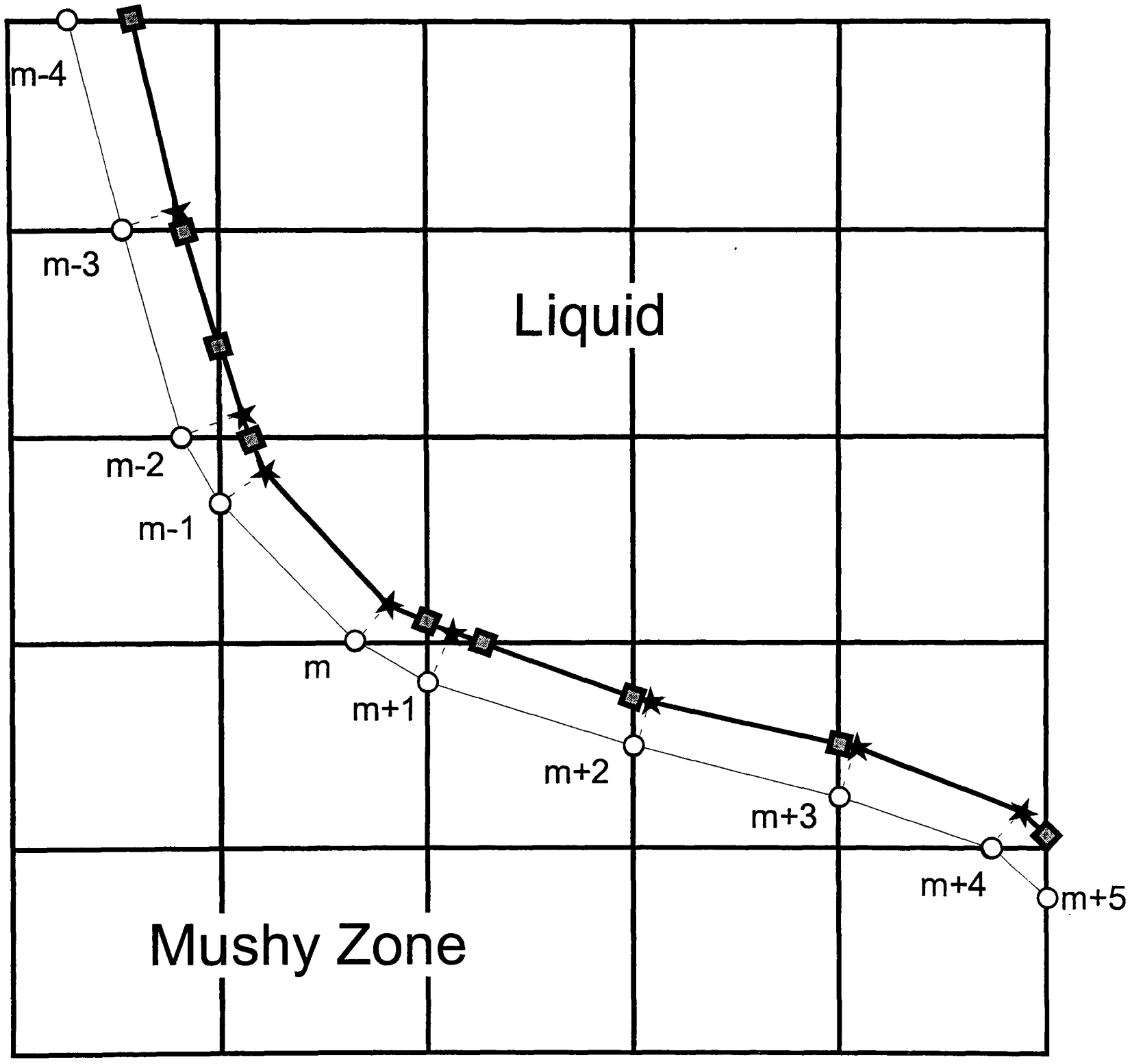

path to advanced marker position

intersection procedure creates new markers

the new representation of the front is not the heavy solid line shown - it is a new line created by linear interpolation between the new marker positions; in places this new line will diverge from the heavy solid line

Figure 3.7 Intersection procedure to find updated marker positions.

area needs to be calculated to account for latent heat release. The area of a c.v. which is partially covered by this mushy zone will either be triangular, trapezoidal, or a five-sided shape (see Figure 3.8).

In Fig 3.8(a) the solid (shaded area) is triangular in shape, in (b) it is trapezoidal and in (c) it is a five-sided shape. It can be seen that in all cases as one travels along the interface from marker *m-1* to marker *m*, solid is on the right hand side. It is obvious that in (c) the *liquid* area is triangular. So the area of the shaded section can be calculated via subtraction of the triangular area of liquid from that of the c.v.. In Fig. 3.8(b) the interface line defines two trapezoids - one liquid, one solid (or, rather, mush). The decision on the shape of the solid area depends on whether the markers at either end of the line segment are on vertical or horizontal grid-lines. The model determines this, and allocates a value to gridline (m) according to Table 3.1.

Position of marker m	***gridline(m)***
Vertical grid-line	2
Horizontal grid-line	3
Corner of c.v.	4

Table 3.1 procedure to account for marker location on computational grid.

The meaning of the value gridline(m) is summarised graphically in Fig 3.9. From Fig 3.8, it is obvious that a triangular area must be calculated if gridline(m-1)=2 and gridline(m)=3, or vice-versa. On the other hand if markers *m-1* and *m* both have values of gridline equal to 2 or 3, then a trapezoidal area must be calculated. If either gridline (m-1) or gridline (m) is equal to 4, then they reside on a corner of the c.v., and a triangular area needs to be calculated. Which triangle is liquid, or which side forms the base of the trapezoid of solid, is determined by the convention that solid is to the right as we travel along the interface.

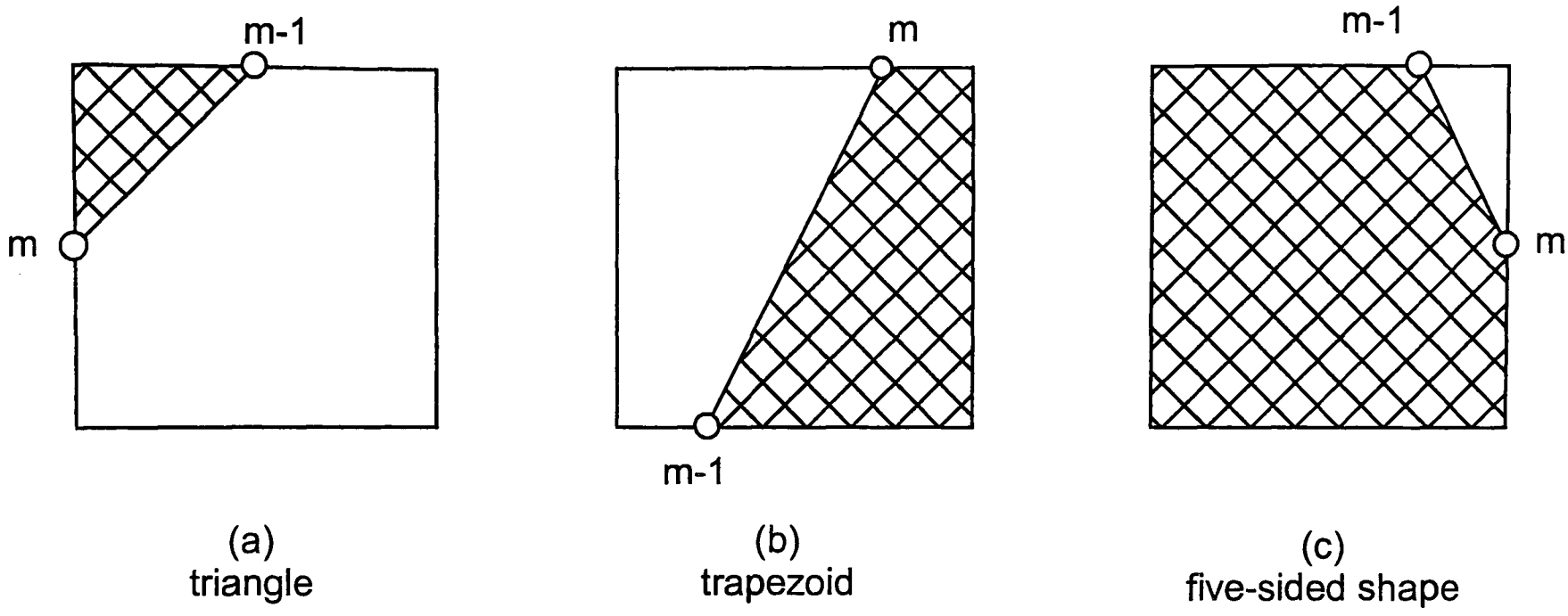

Figure 3.8 Possible shapes of semi-solid material (shaded) in a c.v. containing the interface.

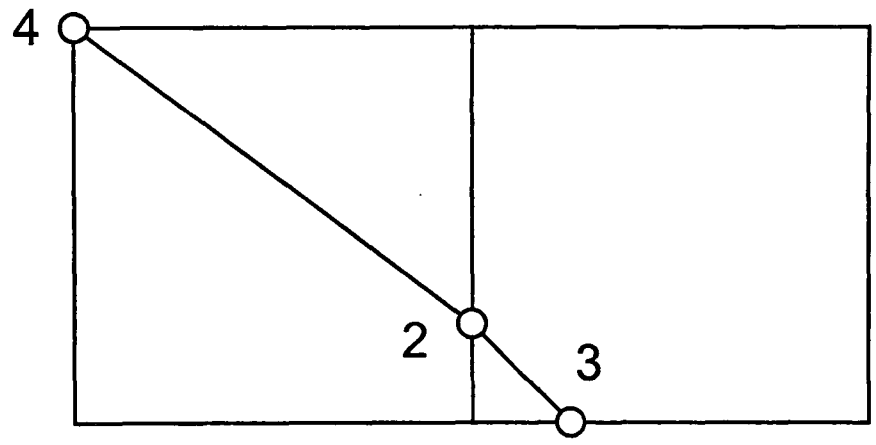

Figure 3.9 Values of gridline (m) for different intersections of marker *m* with the fixed grid.

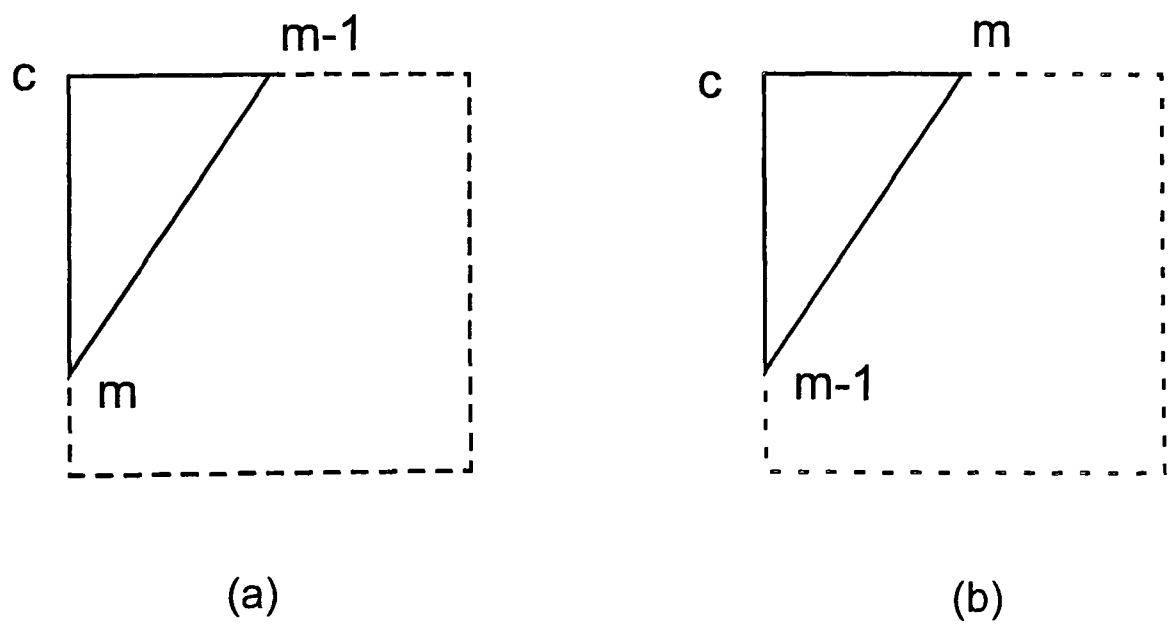

Figure 3.10 Two possible arrangements for a triangular area

For a triangle, consider the line from marker *m-1* to the corner, denoted *c* in Fig 3.10. The slope of this line is either zero (Fig. 3.10(a)) or infinity (Fig.3.10(b)), and this is easily computed by the model. In either case one can consider a circle, centred on point *m-1*, the radius of which is equal to the length of the linear segment of the interface joining markers *m- 1* and *m*. For the case of the slope referred to above as zero, such a circle is illustrated in Fig. 3.11(a). The first, second, third and fourth quadrants are conventionally [12] denoted I, II, III, IV, respectively. In the case illustrated it can be seen that marker *m* is in the second quadrant. The corner *c* is represented by the point at which a vertical line dropped from point *m* intersects the horizontal diametral line. In general, the quadrant in which *m* resides can easily be determined by comparison of its Cartesian position with respect to *m-1*. It is this quadrant which determines whether the triangle enclosed by points *m-1*, *c* and *m* is liquid or solid. The four cases are shown in Fig. 3.11(b). When the slope of the line from *m-1* to *c* is infinite, an analogous set of calculations is carried out - see Fig. 3.12.

For the case of gridline(m-1)=gridline(m)=3 (see Fig. 3.8(b)), the base for the calculation of the trapezoidal area of solid is the east side of the c.v. if y(m)>y(m-1). Otherwise it is the west side. Similarly, if gridline(m-1)=gridline(m)=2, the base of the trapezoid is either the south (if x(m)>x(m-1)) or the north face of the c.v.. Of course what is really being done here is numerical integration. The trapezoidal shape is a reminder that we are essentially using the trapezoidal rule for such integration.

This information on the state of each area of a c.v. is used to determine the direction in which the markers move along the normal to the interface (Fig. 3.5). If undercooled, a marker will move *away* from the solid. The slope m_n of this normal is known, and the magnitude of the travel of each marker is known, from equation (3.9). So the horizontal or vertical components (Δx^* and Δy^*, respectively) of z_m can be calculated :

$$\Delta x^* = \sqrt{\frac{z_m^{\,2}}{1+m_n^2}} \qquad (3.10\ a)$$

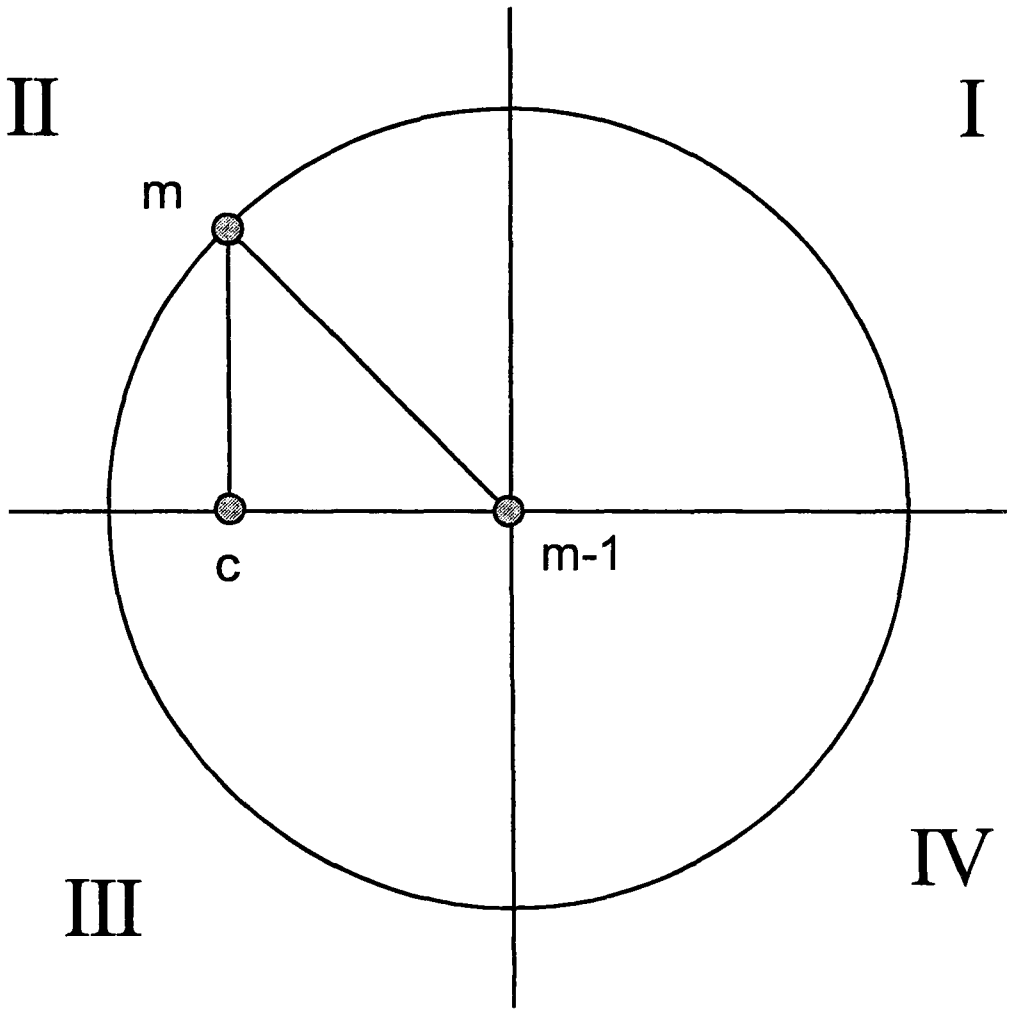

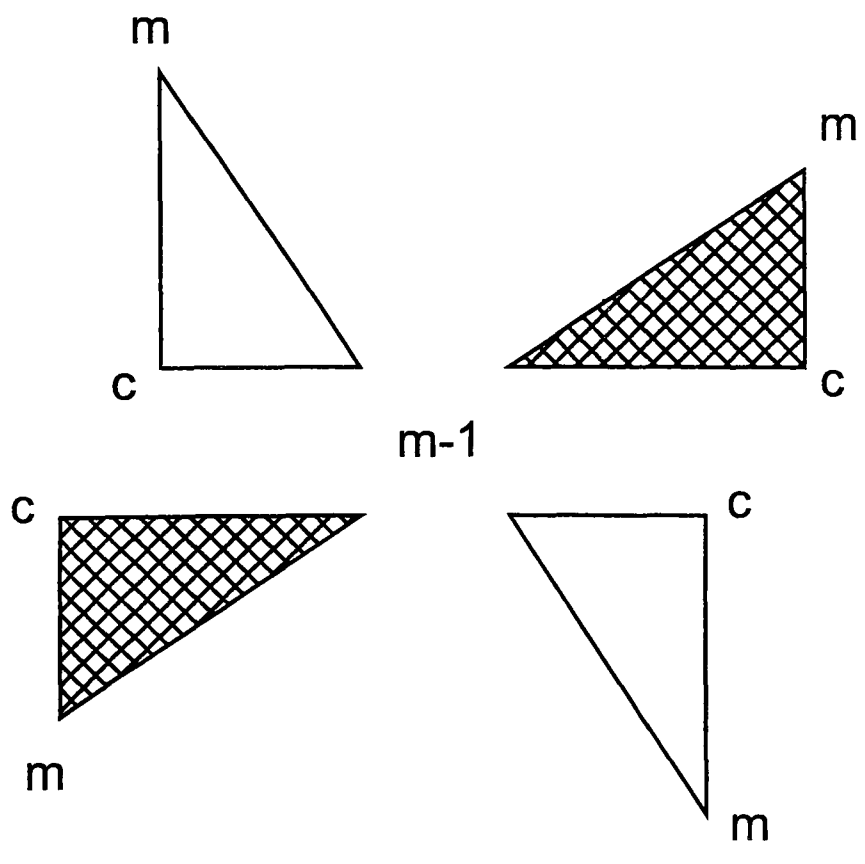

Figure 3.11 Method of determining the direction of advance of marker *m*; triangular area of semi-solid; marker *m* and c.v. corner *c* on the same vertical line.

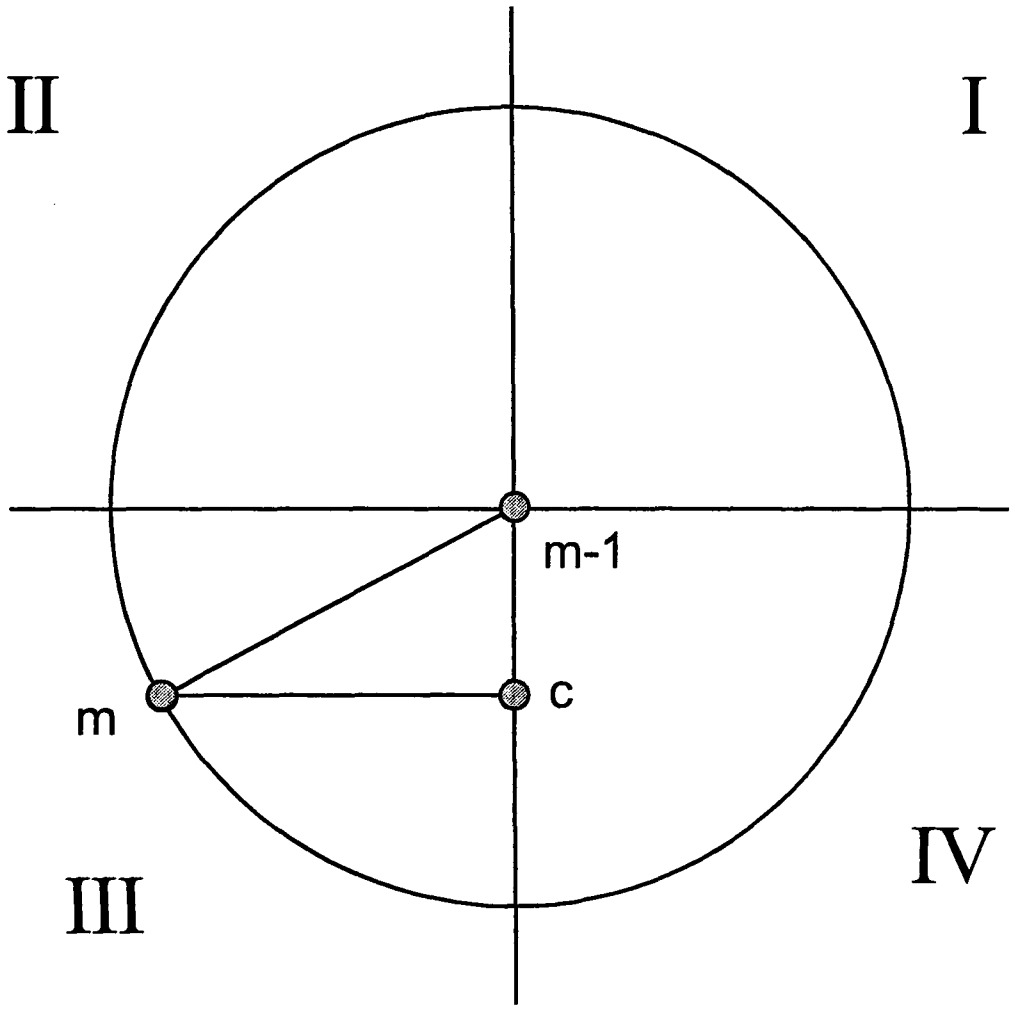

(a)

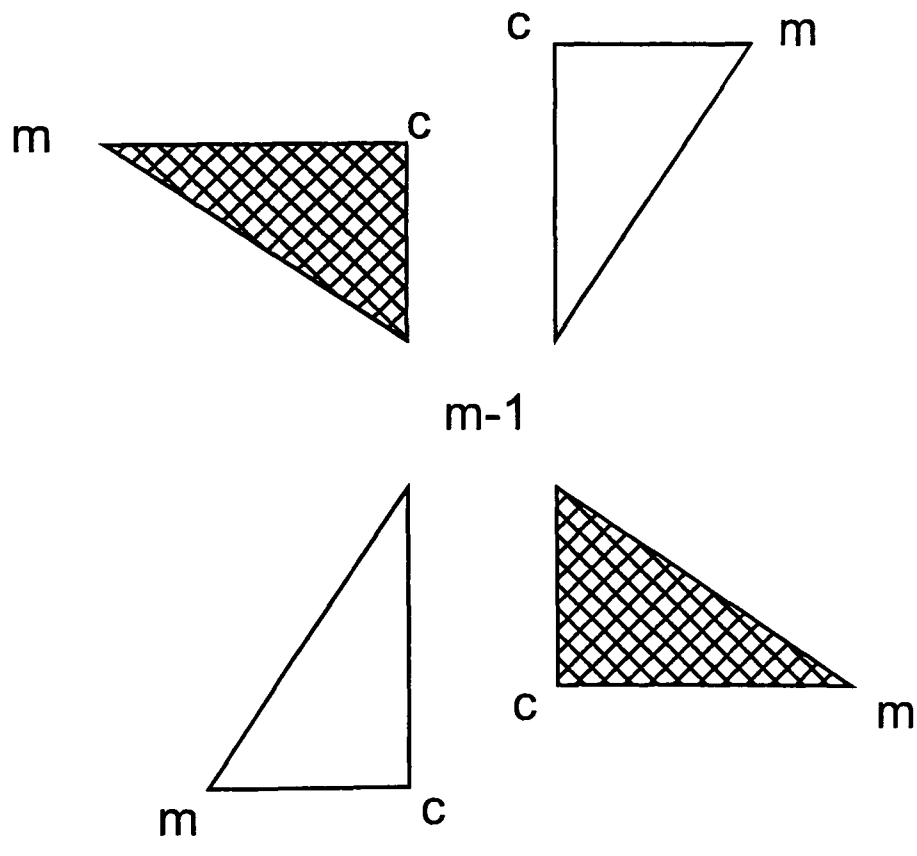

(b)

Figure 3.12 Method of determining the direction of advance of marker *m*; triangular area of semi-solid; marker *m* and c.v. corner *c* on the same horizontal line.

$$\Delta y^* = \sqrt{\frac{z_m^{\,2}}{\left(\frac{1}{m_n^2}\right)+1}} \qquad (3.10\ b)$$

If the sign of *either* Δx^* *or* Δy^* is known, the sign of the other can be calculated as

$$m_n = \frac{\Delta y^*}{\Delta x^*} \qquad (3.10\ c)$$

For the case of a triangular shape being outlined by the interface crossing a c.v., the situation is as illustrated in Fig. 3.11 or Fig. 3.12. The key information needed is whether a marker *m* will move towards or away from the corner *c*. If the geometry is as per Fig. 3.11(a), then one sets the sign of Δy^* (referring to the motion of marker *m*) according to the quadrant (Fig. 3.11(b)) as follows : I(+), II(-), III(-), IV(+). For example, if point *m* is in the fourth quadrant, then the corner *c*, which is above it, is liquid. The marker will move towards the liquid, i.e. in the positive y direction. Similarly, if the geometry is as per Fig. 3.12(a), the equivalent information, this time for Δx^*, is : I(-), II(-), III(+), IV(+).

For trapezoidal shapes, the sign of *either* Δx^* *or* Δy^* must also be calculated, and this depends on which face of the c.v. forms the base of the trapezoid (in Fig 3.8(b) the east face). For each possible base we have the following : west(Δx^*+), east(Δx^*-), north(Δy^*-), south(Δy^*+).

In this way, for control volumes through which the interface passes, the area covered by semi-solid as time proceeds can be calculated. In order to facilitate this, an algorithm is employed which assigns marker particles to particular control volumes - those which they border. For example, as illustrated in Fig 3.4, control volume (i,j) has two markers (*m-1* and *m*) bordering it, whereas control volume (i+1,j+1) has none. This is described in a subroutine,

called CVMarker, as cvmarkerid1(i,j)=m-1, cvmarkerid2(i,j)=m. That a c.v. has no markers assigned to it is reflected by the statement that cvmarkerid1(i+1,j+1)=cvmarkerid2(i+1,j+1)=-1, the default negative value meaning that there are no markers bordering that c.v.. Of course it is only for those c.v.s that have positive integer values of cvmarkerid1 and cvmarkerid2 that an area must be calculated. A FLAG value is attributed to each c.v. in the domain, in order to keep account of its status. Each c.v. (i,j) has a value of FLAG(i,j) which is updated as solidification proceeds, as per Table 3.2.

FLAG	status	control volume position		contains front
		along mould wall	internal	
0	L	✓		
1	L		✓	
2	F1	✓		✓
3	F1		✓	✓
4	F	✓	✓	✓
5	SS	✓	✓	
6	S	✓	✓	

Table 3.2 – control volume (c.v.) flags : liquid(L), front has just entered c.v.(F1), front passing through c.v.(F), semi-solid(SS), solid(S)

Figure 3.13 is a schematic of a c.v. for which FLAG(i,j)=4.

3.5.3 Latent heat evolution

E in equation (2.1) is the source term which accounts for the release of latent heat during solidification. It contains contributions due to the advance of the solidification front (E_a), and to subsequent thickening of the mushy zone (E_t) :

$$E = E_a + E_t \tag{3.11}$$

For the majority of control volumes (which are either fully solid or fully liquid), we use the single phase form of the heat equation (E=0). But if FLAG(i,j) is 3 or 4 then, during a time step, the contribution due to the advance of the front, in that time step, to the heat equation (via latent heat liberation) is included in the analysis, as follows

$$E_a = \frac{(d - d^0).g_s^0.L}{\Delta t.\Delta x.\Delta y} \tag{3.12}$$

Here d is the volume of a c.v. covered by semi-solid at the end of the time step, and d^o is that covered at the start of the time step. L is the latent heat of fusion per unit volume, and g_s^o is the solid fraction at the start of the time step. When the control volume (i,j) flag value is three (FLAG(i,j)=3), there is no mushy zone thickening term – see Table 3.2. If, after the *subsequent* time step, the interface still resides in a certain control volume (FLAG(i,j)=4), then there are now two terms to be included in the heat equation : one (E_a) to account for further growth, the other (E_t) to include the latent heat evolving due to cooling of the semi-solid already behind the front at the start of the time step.

$$E_t = \frac{d^0.(g_s - g_s^0).L}{\Delta t.\Delta x.\Delta y} \tag{3.13}$$

Here g_s is the fraction of solid at the end of the current time step. A linear variation of fraction solid with temperature, in the freezing range (between T_L and the solidus temperature, T_S) is assumed.

$$g_s = 0.0 \qquad \text{when} \quad T > T_L$$

$$g_s = \frac{T_L - T}{T_L - T_s} \qquad \text{when} \quad T_S < T < T_L \tag{3.14}$$

$$g_s = 1.0 \qquad \text{when} \quad T < T_S$$

It is mathematically convenient to use this, and computationally economic because the need for iteration is avoided. However, in future work a more physically realistic, non-linear relationship will be used, based for example on the lever or Scheil rules described in Section 1.4.

Equation (3.11) is incorporated into the heat equation by incorporation of an extra "flux" term - latent heat source term f_l - into equation (3.4), for appropriate c.v.s:

$$f_l = E.\Delta x.\Delta y \tag{3.15 a}$$

and

$$f_{tot} = f_n + f_s + f_e + f_w + f_l \tag{3.15 b}$$

and the thermal evolution is described as before by equation (3.5).

When the front passes out of a control volume, then the procedure will depend on the nodal temperature, T. If it is above T_S then a cooling latent heat term must still be calculated (no growth term now). If the temperature is below T_S, then the alloy is locally solid, and the single phase heat equation is again used (i.e. E=0).

3.6 Columnar Solidification

The general approach outlined in the previous section is used to track both columnar and equiaxed growth across the calculation domain. In the case of columnar growth, solidification starts at the mould wall. Crystallographic orientation is not treated in the model, so the emergence of the columnar front from the outer equiaxed zone is not predicted. However the latter is expected to be small, and it has been shown [31] that if the growth velocity is large, only steady state dendrites growing with preferential crystallographic directions can exist. This is discussed in more detail in Section 3.6.2.

3.6.1 Nucleation and initial growth

Sites for potential nucleation are placed, at the grid spacing, along the mould wall, as illustrated in Fig. 3.14. This spacing would seem to be the optimum for a technique relying on control volume methodology. In fact the surface of the alloy in contact with the mould could be regarded as a continuum for potential nucleation - the finite number of sites is simply a representative discretisation.

The temperature at these sites is found via the energy equation. First of all, the surface temperature $T_s(i,j)$ at mid-face (marked x in Fig. 3.14) of a surface control volume (i,j) is calculated, via equation (3.3 d), which when re-arranged for T_s yields, for control volumes along the left hand mould wall :

$$T_S(i,j) = \frac{\Delta x.h.T_m + 2k.T(i,j)}{\Delta x.h + 2k} \qquad (3.16\ a)$$

or for control volumes along the bottom mould wall :

$$T_S(i,j) = \frac{\Delta y.h.T_m + 2k.T(i,j)}{\Delta y.h + 2k} \qquad (3.16\ b)$$

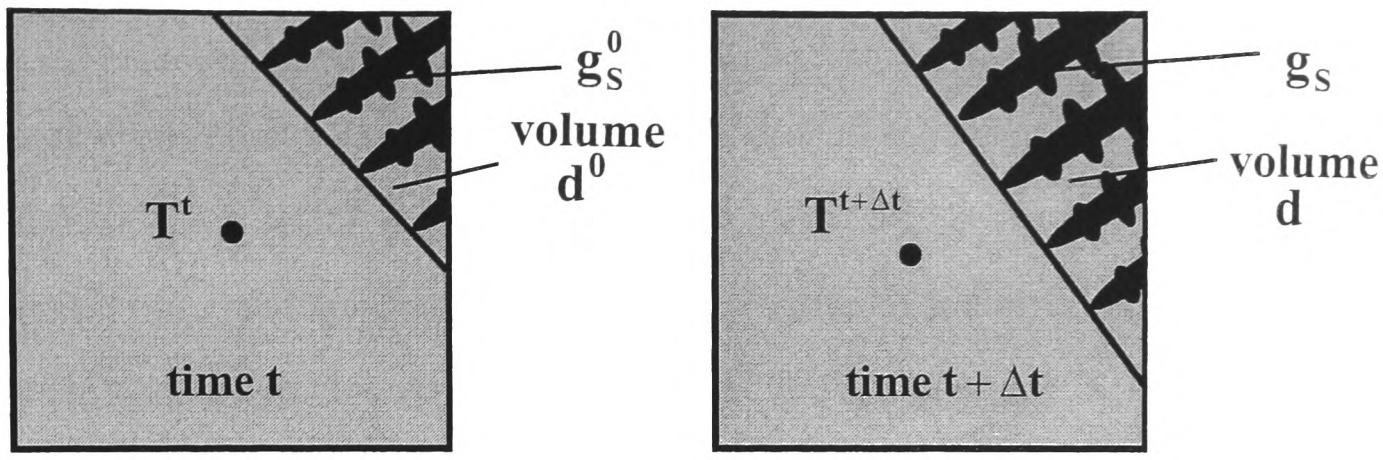

Figure 3.13 Schematic of the growth of dendritic solid into a c.v. (i,j) where FLAG(i,j)=4.

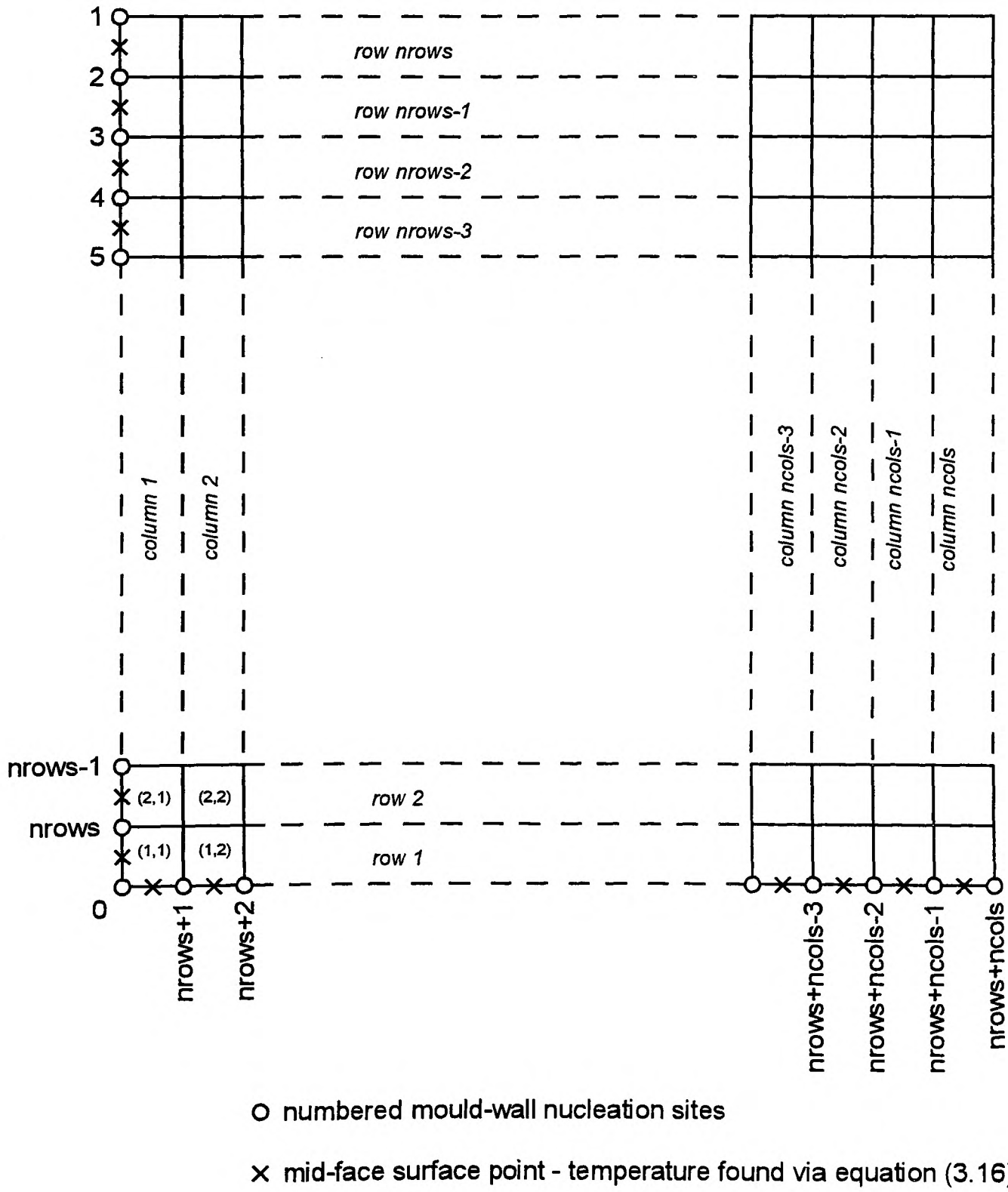

Figure 3.14 Computational domain showing position of sites for columnar nucleation.

The nucleation site temperatures $T_n(m)$ are then found via linear interpolation between the values of T_s on either side. These sites are numbered, as shown, 1 through (*nrows*+*ncols*), where *nrows* is the number of rows of control volumes and *ncols* is the number of columns of control volumes in the computational domain. So, for example

$$T_n(3) = 0.5\left[T_s(1, nrows - 1) + T_s(1, nrows - 2)\right]$$

The site in the corner is denoted marker number 0, has a temperature $T_n(0)$, and has to be treated slightly differently than the other sites. The corner control volume is illustrated in Fig. 3.15. Consider a diagonal heat flux entering the mould at the corner :

$$f_c = h.\left[T_n(0) - T_m\right] \qquad (3.17\ a)$$

This flux also passes through the alloy :

$$f_c = k.\frac{\left[T(1,1) - T_n(0)\right]}{L} \qquad (3.17\ b)$$

where

$$L = 0.5.\sqrt{\Delta x^2 + \Delta y^2}$$

Equating expressions (3.17 a) and (3.17 b), and rearranging gives an expression for the temperature at the corner nucleation site

$$T_n(0) = \frac{\sqrt{\Delta x^2 + \Delta y^2}.h.T_m + 2k.T(1,1)}{\sqrt{\Delta x^2 + \Delta y^2}.h + 2k} \qquad (3.17\ c)$$

and if $\Delta x = \Delta y$ then

$$T_n(0) = \frac{\Delta x.h.T_m + \sqrt{2}kT(1,1)}{\Delta x.h + \sqrt{2}k} \qquad (3.17\ d)$$

which is similar in form to equation (3.16 a).

When the undercooling at any site *m* has reached an arbitrary level, ΔT_{nuc}, it becomes activated. The validity of this assumption has already been discussed; further supporting evidence can be found in the basic theory of Turnbull and Fisher [178] who predicted a steep increase in nucleation rate if the temperature falls below the nucleation temperature. The marker will move normal to the front. Initially this means that it will move perpendicular to the mould wall, except for site 0 which will move in a diagonal direction towards node (1,1). The velocity of motion is given by equation (3.8). Once the marker has moved from the nucleation site, its temperature is calculated via bilinear interpolation. If it is within $\Delta x/2$ of the vertical mould wall, or $\Delta y/2$ of the horizontal mould wall, the four reference points for interpolation are the two nearest surface temperatures T_s and the two nearest nodal points of surface c.v.s. Once any marker has passed the first surface nodal point in the domain, bilinear interpolation using the four surrounding nodal temperatures is employed from there on.

In the model system under study (Section 3.2), it is expected that the first site to nucleate will be the corner one. This is shown in Fig. 3.16. The corner marker (0) moves along the direction shown. At some time it has reached point c_1, and the area of solid covered in c.v. (1,1) is the triangle $y_1 0 x_1$. At some later time marker 0 has reached point c_2. The interface now intersects the north and east faces of c.v. (1,1) at points a and b, respectively. Now the

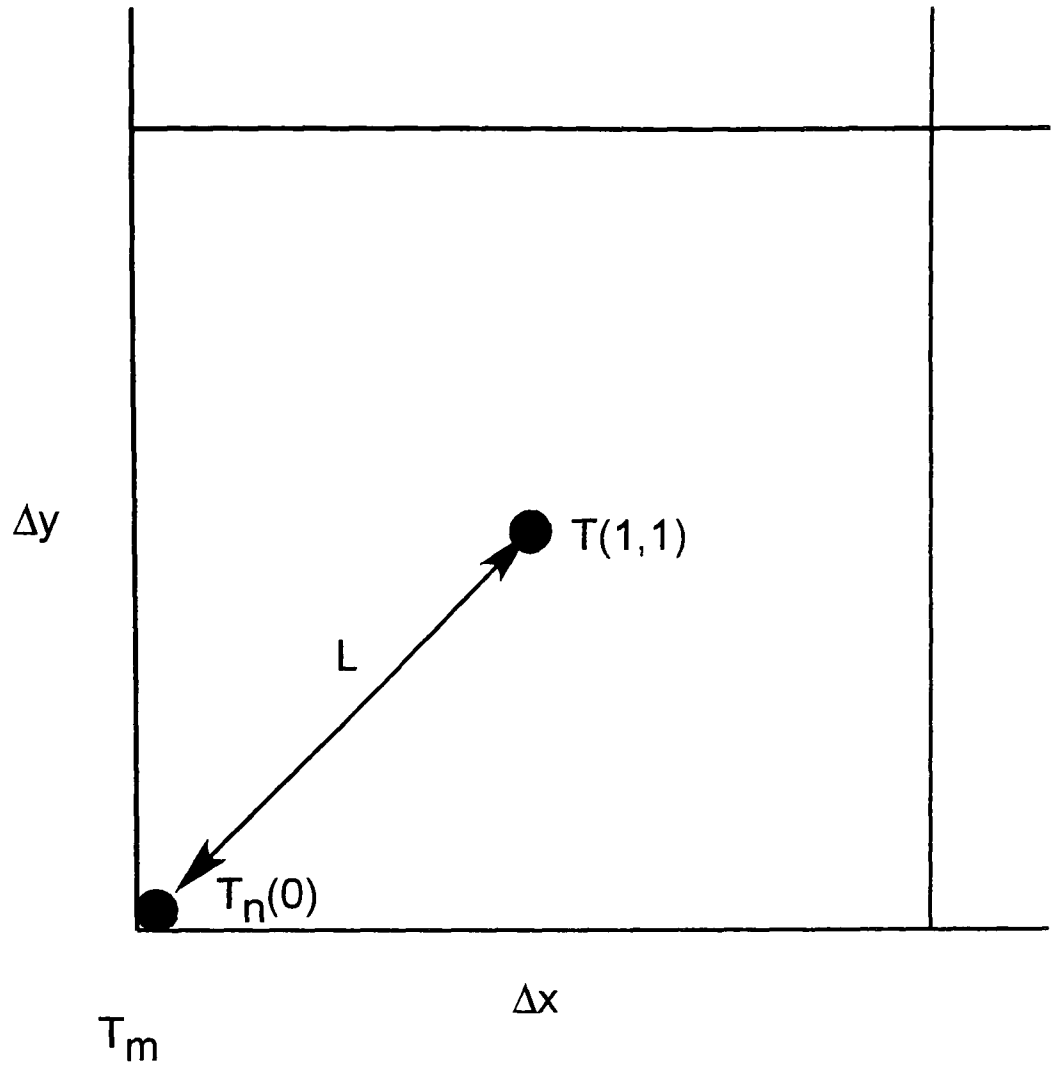

Figure 3.15 The corner control volume.

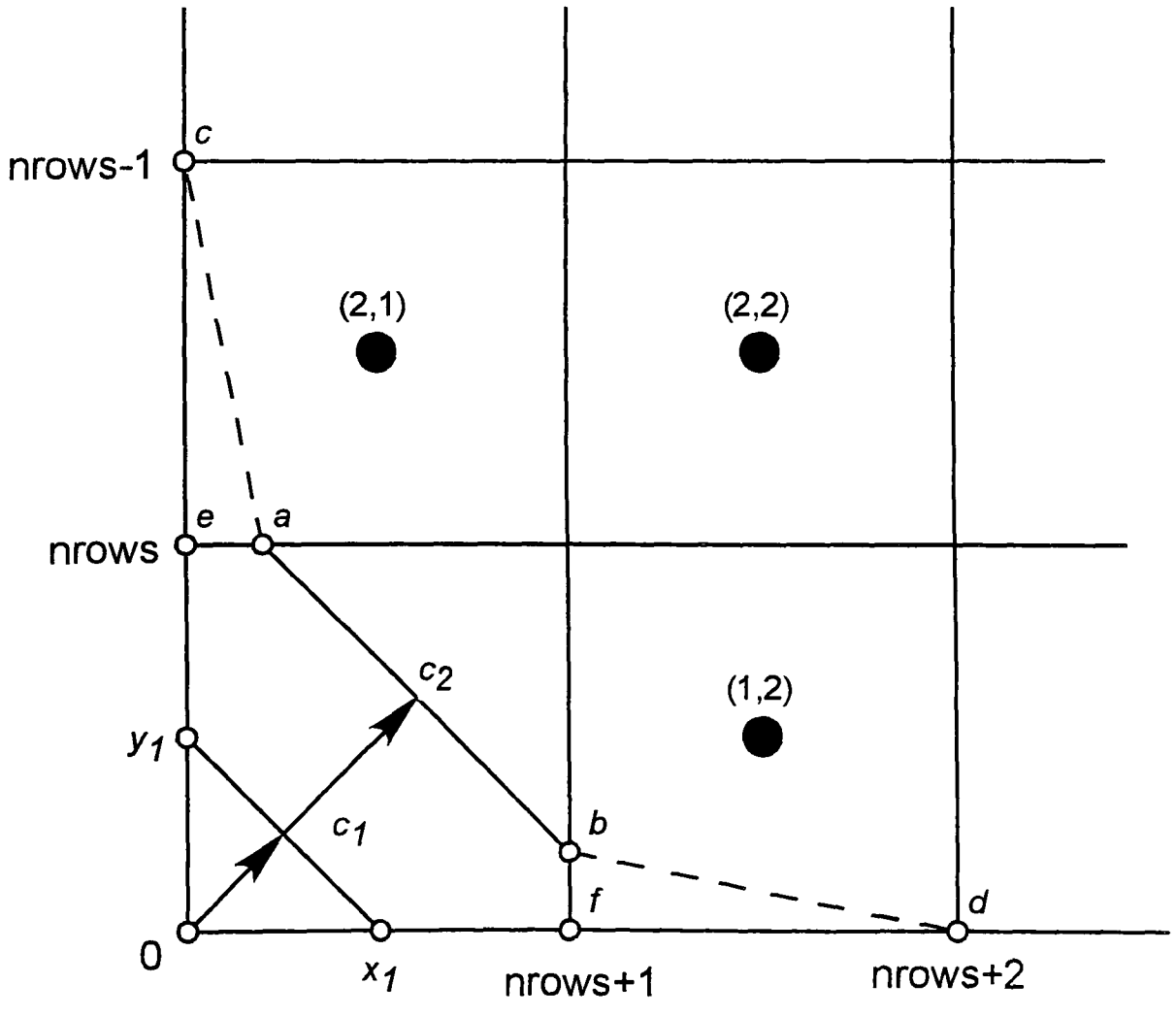

Figure 3.16 Initial growth of columnar marker *0* from the corner of the domain

area covered by solid is the five-sided shape ae0fb. In fact it is assumed that, if they had not already done so independently, markers *nrows* and *nrows+1* have nucleated and advanced a distance $|ea|$ and $|bf|$, respectively. As such, c.v.s (2,1) and (1,2) are covered by solid of triangular shape eac and bfd, respectively. At this stage marker 0 is surplus to requirements, and is discarded. The line segment $|ab|$ defines the interface in c.v. (1,1). In future, the marker at point a will move in a direction which bisects the angle between line segments ca and ab.

3.6.2 Continuing growth

Once the columnar solidification front has been established via nucleation and growth from the mould wall, it continues to advance into the undercooled liquid via the general algorithm outlined in Section 3.5. As illustrated in Fig. 3.14, there are originally *nrows+ncols+1* marker particles along the mould wall. As the front travels into the domain its length diminishes (provided it does not become very convoluted), and so it crosses the control volume grid in fewer places. This means that the number of marker particles decreases; this is dealt with by renumbering the markers at each time step as the intersections are re-calculated, starting with number 1 which is where the interface intersects the grid-line y=w/2. Although symmetry in the diagonal would be *expected* in a diffusion problem in a square domain, it is not *enforced* in the model.

The CA-FE model of Rappaz et al. [140] provides information on the crystallographic orientation of grains, and so the competitive growth of columnar grains from a chill, in which only those grains with the <100> direction closely aligned with the direction of heat flow survive, is simulated. This aspect of the CA-FE model is particularly important in the DS or single crystal dendritic alloy production for aerospace. But for more general castings, this detail may not be of high importance - rather it is grain size and the extent of the equiaxed zone that is of interest. If, in columnar growth, one grain has a substantial misorientation from the preferential growth direction, it will not survive due to being impeded and overgrown by the neighbouring crystals with better alignment. A columnar zone consisting of

three grains, the central one of which is misorientated at and angle θ to the direction of heat flow in directional solidification, is illustrated in Figure 3.17. The outlying grains, in contrast, are growing with the primary arms of their dendrites parallel to the direction of maximum thermal gradient. As such their growth velocity V_0 is the same as the velocity of the liquidus isotherm. The dendrites of the central grain extend at a higher normal velocity V_θ, where

$$V_\theta = \frac{V_0}{\cos\theta} \tag{3.18 a}$$

i.e. the vertical component of the growth rate is the same for both grains. Assuming that

$$V \propto \Delta T^n \tag{3.18 b}$$

and n>1, then the dendrite tips of the misorientated grain, which need to grow faster, do so at a higher undercooling. The tips of the central dendrites are a greater distance behind the liquidus isotherm than those of the perfectly aligned outer grains, i.e.

$$d_\theta > d_0 \tag{3.18 c}$$

Tip undercooling is a function of velocity, such that

$$\Delta T_0 = f(V_0) \tag{3.18 d}$$

and

$$\Delta T_\theta = f(V_\theta) \tag{3.18 e}$$

So, for a linear thermal gradient in the vertical direction

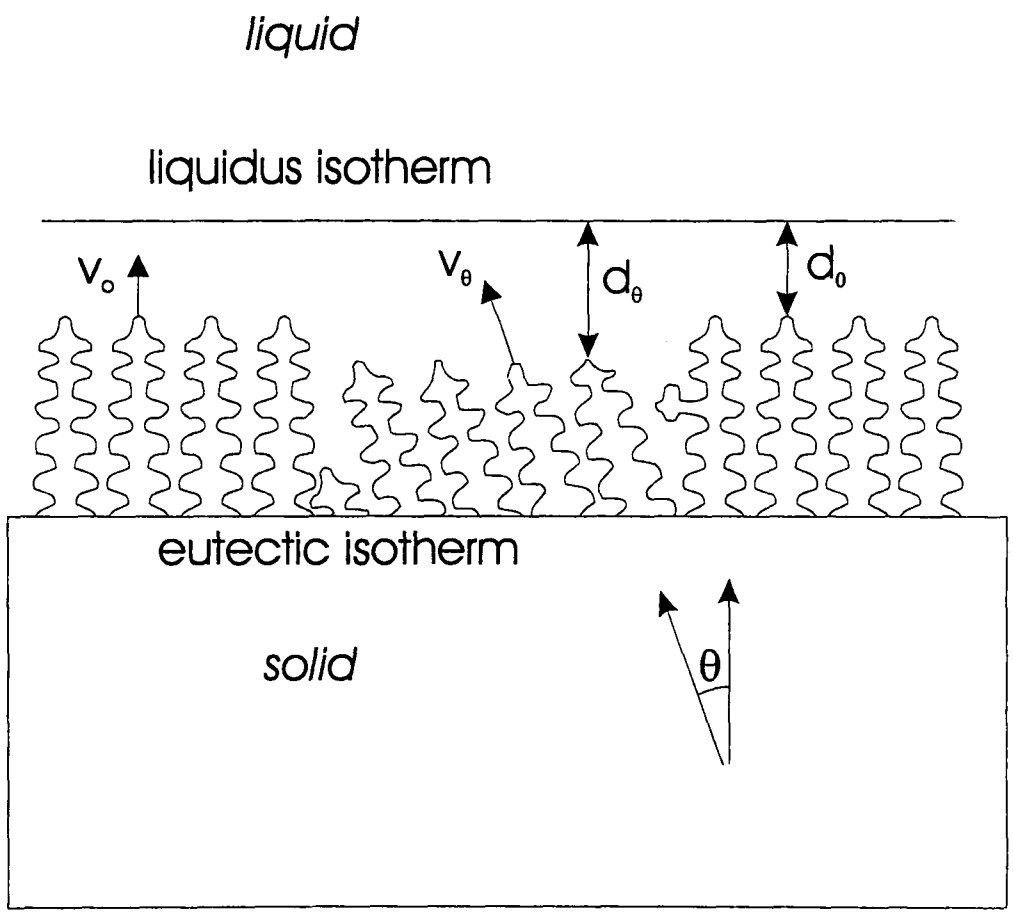

Figure 3.17 Schematic of the growth of three dendritic grains in the columnar zone; the central one is misaligned by an angle θ from the vertical temperature gradient.

$$\frac{d_\theta}{d_0} = \frac{\Delta T_\theta}{\Delta T_0} = \left(\frac{V_0}{V_\theta}\right)^{\frac{1}{n}} = (\cos\theta)^{\frac{1}{n}} = f_1(\theta) \qquad (3.18\ f)$$

If we calculate, for n=2, the variation of $f_1(\theta)$ with θ (Table 3.3), we get a picture of the ratio of the distance of the misorientated grain behind the liquidus isotherm to that of the grain with $\theta = 0$.

θ (degrees)	5	10	15	20	25	30
$f_1(\theta)$	1.002	1.008	1.017	1.032	1.050	1.074

Table 3.3 variation of relative grain distance behind liquidus isotherm with misorientation of crystal with reference to the direction of heat flow.

So, for crystallographic misalignment of up to 30° from the heat flow direction, the percentage difference in distance behind the liquidus isotherm from the perfectly aligned crystal is less than 7.5. And the distance d_0 itself is very small - the columnar growth undercooling predicted in this work being of the order of 0.5°C (see next Chapter) - at the scale of the casting. So, for the purposes of prediction and visualisation of generic columnar front growth, the effects of such misorientation can be safely ignored, as is done in our front-tracking model. As θ increases beyond 30° the discrepancy becomes more marked, but here the grain selection mechanism and competition will mean that such crystals will not emerge from the outer equiaxed zone.

The fact that this model does not treat such crystallographic orientation is not, in the light of the above analysis, a serious shortcoming for the prediction of as-cast structure in most shape castings. The model presented predicts the development of columnar grains and equiaxed

grains (see Section 3.7) and will in future predict the evolution of and competition between both forms of dendritic solidification.

3.7 Equiaxed Solidification

The treatment of equiaxed solidification is based on the general algorithm outlined in Section 3.5. This is analogous to the modelling of columnar solidification, as described. It was decided not to develop a separate model for equiaxed solidification, but rather to incorporate the columnar and equiaxed algorithms into one computer program. This is because much of the code used is common to both modes of solidification, and because the final goal is to couple the treatment of both forms of crystal growth to predict the CET. Of course there are parts of the program which are related only to one form of solidification, and there are subroutines which are dedicated to either the columnar or equiaxed problem. But as much of the code is universally applicable, the terminology used to describe the columnar front is very similar to that used for the equiaxed grain envelope. The columnar zone is treated as a grain with one boundary (and its origin) at the mould wall. In the code it becomes grain number k=0, with equiaxed grains being labelled k=1, 2, 3.....etc..

In the equiaxed model, sites for potential nuclei are placed arbitrarily in the domain. The energy equation is used to calculate the temperature at these sites, as in the columnar model. When the undercooling at a site exceeds the assigned nucleation undercooling for equiaxed grains (ΔT_{nuc}^{ex}), then that site becomes activated and growth starts according to the model of dendrite tip kinetics used to date (equation (3.8)). Latent heat is accounted for, as in the columnar model, via equation (3.11), and the FLAG values of Table 3.2 are used to determine the format of the energy equation in each control volume. Although the models of columnar and equiaxed growth are incorporated into one model, each form of growth can be considered in isolation by setting the nucleation undercooling for the other form artificially high.

The potential nucleus is placed at a point where a horizontal and a vertical grid line meet i.e. at the corner of a control volume. If a fine computational mesh is employed, there is an abundance of such sites, such that the ability to study the effects of random placement of nuclei is not seriously undermined. The grains grow out from their original nuclei, but they are not translated across the domain. In reality it would be expected that motion of equiaxed grains through the liquid could occur, at low fractions solid, due to gravitational effects. Some justification, however, for not including the solutal effects on grain sedimentation is the fact [110] that, for dendritic crystals, the rejected solute remains mainly within the grain, thus still contributing to its buoyancy. This assumption is consistent with the use of dendrite tip kinetics expressions (like equation (3.8)) which were developed from Ivantsov solutions of isolated dendrite growth.

Equation (3.8) was developed from an analysis of array dendritic growth, so its use for describing equiaxed dendritic growth implies that the latter can be also be considered akin to an array. In equiaxed growth the liquid gaps left by advancing primary arms are filled by side branching. For equiaxed solidification, G is small, and so the formation of the expression in equation (3.8) from that in equation (2.10) is valid. Also, as stated in Chapter 2, from equation (2.11) it is seen that spacing is very sensitive to changes in G, and will increase quadratically with decreasing G. So use of array growth theory for the equiaxed case is consistent with its origin in studies of isolated dendrite growth.

3.7.1 Single grain model

The model was first developed to predict the nucleation and growth of a single equiaxed grain. As illustrated in Fig. 3.18, the site chosen for nucleation is at an intersection of two grid-lines. The site becomes active when it is first undercooled below the nucleation temperature. Initial grain growth is isotropic because its initial representation is a point and so there is a single undercooling value driving growth equally in all directions. An initial circular growth would intersect the grid to the north, south, east and west of the nucleus.

After this first time step, the mushy-zone covers part of each of the four control volumes surrounding the nucleus, each of these containing an identical triangular area of semi-solid alloy. It is expected that there will be a gradient in temperature across the domain, and so each of the four markers will now be undercooled to a different extent. Growth will no longer be isotropic. However, the normals to the grain envelope will still be either vertical or horizontal. In the second time step, each marker travels a different distance, as illustrated. In the model system (Fig. 3.1), the liquid to the west and south of the nucleus should be more undercooled, resulting in grain anisotropy. The areas to be calculated for each c.v. latent heat term are still triangular, but no longer identical. The anisotropy means that the normals to the interface are no longer necessarily vertical or horizontal - it is expected that the markers will advance off the grid-lines during the third time step. Such off-grid-line markers are denoted * in Figure 3.18. As before, linear interpolation is used between these advanced markers to establish the position of the new markers at the intersection of the grid. Once the front passes out of the four c.v.s surrounding the nucleus, more than 4 marker particles are generated through the intersection routine. In Fig. 3.18 the grain envelope first breaches the limits of the c.v.s to the south and to the west of the nucleus, resulting in the increase in the number of marker particles to 8. This is different to the situation in columnar growth, where the number of marker particles should diminish in time as the length of the columnar front decreases. As before, as one travels along the interface in the direction of increasing marker particle number, solid is on the right hand side by convention. The calculation of the area covered by the mushy zone and determination of the growth direction is as described in Section 3.5. One exception to the convention is the "wrap-around" case from the last marker to the first (marker 8 to 1 in Fig. 3.18). Going from marker 1 to 8, liquid is on the right. Special code in the program takes this into consideration. It will be noted that the grain anisotropy increases with time. In Fig. 3.18 the expected evolution of the grain over 4 time steps is illustrated. This is simply a schematic; the amount of growth between time steps could be quite different. If the grid is made very fine to increase the possible randomness of nucleant locations, the time step must accordingly be lowered - equation (3.6).

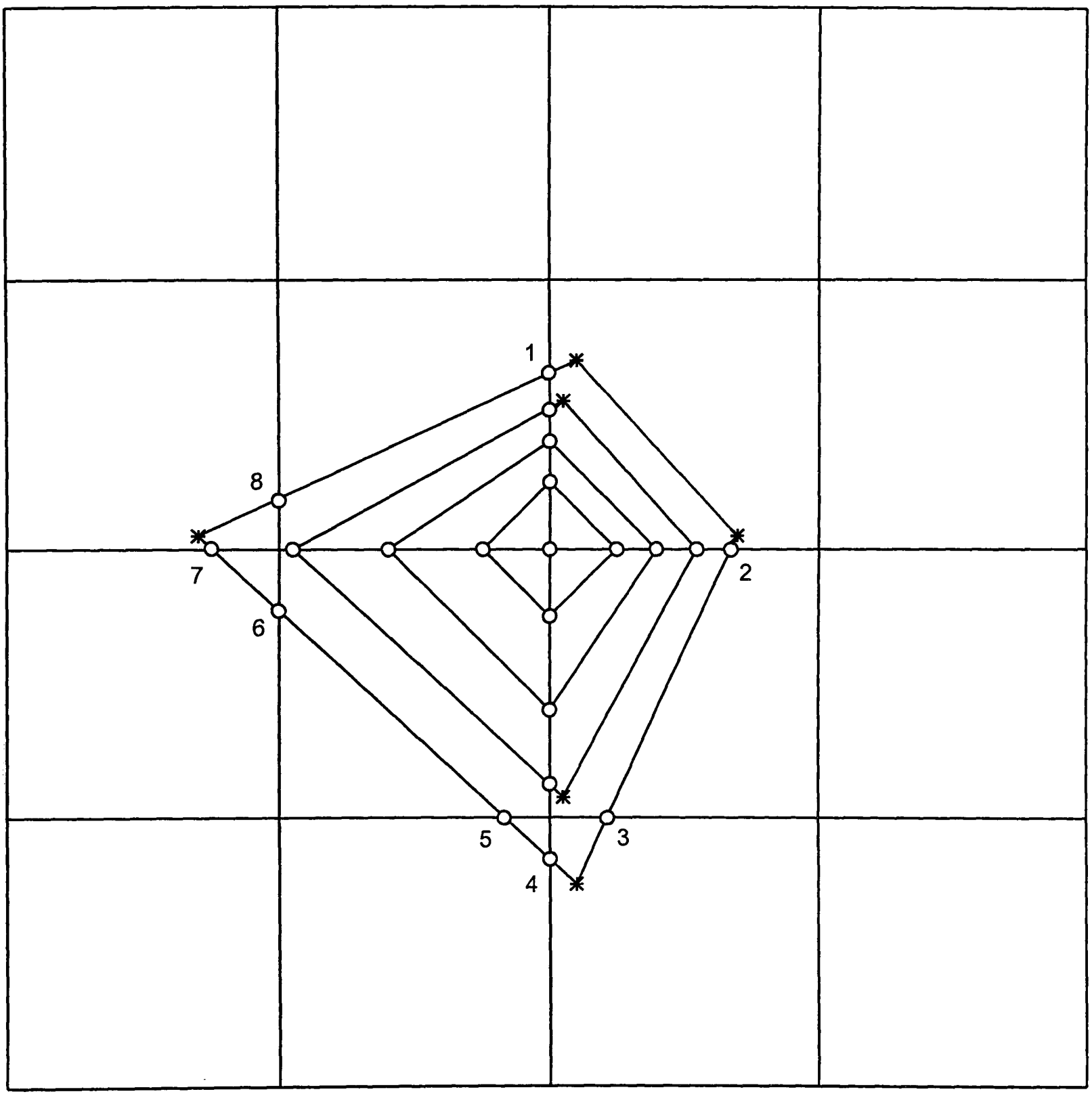

○ front marker

✱ advanced marker position

(where the advanced marker position and the subsequent intersection is very close, only the intersection front marker is shown)

Figure 3.18 Schematic of the growth of an equiaxed grain showing the possible shape of the grain boundary at 4 successive times after nucleation.

During development of the model of the single equiaxed grain, care was taken to structure the program code to facilitate treatment of the nucleation and growth of many such grains.

3.7.2 Multiple grain model

In Section 3.5, it was explained how the cvmarkerid1 and cvmarkerid2 fields were used to allocate pairs of markers to particular control volumes. This information is then used to identify those c.v.s in which a latent heat term has to be calculated. The technique is applicable to one area of equiaxed (or columnar) solidification in a c.v., but if there is at least one more distinct area of solidification (columnar and/or equiaxed) in a particular c.v. then the program will need to know to which distinct solidifying entity the markers belong. This is not *generally* (i.e. where only one area of solidification is passing through a control volume) required to calculate the latent heat terms, but is necessary for calculating how and in which directions the markers advance. For this reason the grain (k) to which each marker belongs is also established : cvgrainid1(i,j) and cvgrainid2(i,j). If two solidification entities have entered a control volume (i,j) then one also has to identify cvgrainid3(i,j), cvgrainid4(i,j), cvmarkerid3(i,j) and cvmarkerid4(i,j). Of course one would expect that cvgrainid1(i,j)=cvgrainid2(i,j) and cvgrainid3(i,j)=cvgrainid4(i,j). In this case impingement is about to occur, and now the identification of which markers m belong to which grains k is relevant to the calculation of the latent heat terms.

Of course, preceding growth of multiple grains during solidification, multiple nucleation sites must have been created as their origin. The independent attributes of such nuclei are their position and activation temperature. Both can be ascribed in either a deterministic (e.g. to check the algorithm and debug the program) or stochastic (in an attempt to model the probabilistic nature of nucleation) manner. The latter could be implemented by randomly selecting sites for nucleation, and then employing a statistical (e.g. Gaussian) distribution of nucleation undercoolings. If only one fixed value of nucleation undercooling is used, then nucleation will start where the bulk liquid undercooling is largest - probably near the corner (see Fig. 3.1). Once nucleation has occurred, equiaxed grains should be able to grow

relatively independently of one another if they are not significantly close. As they grow, their boundaries will get closer, until eventually impingement must be treated in the model, as mentioned above.

The impingement routine must be considered once two separate solidification fronts enter a c.v. (i,j). In order to alert the program to this situation FLAG (i,j)=7 is used. This is in addition to the other FLAG values outlined in Table 3.2. For an equiaxed grain, impingement may be with the columnar front, another equiaxed grain, or the mould wall (if a significant columnar zone does not exist).

Consider two grains entering a c.v.(i,j), as illustrated in Fig. 3.19(i). Grain *a* is represented by the line $|aa'|$, grain *b* by $|bb'|$. At this point FLAG(i,j)=7; two separate volumes of solid have to be calculated - both contribute to latent heat evolution. One approach to the treatment of impingement would be to continue such growth until the volume overgrown by solid equals the volume of the c.v.. After that no further growth would occur (E_a=0), essentially pinning points a, a', b and b'. From that point on latent heat will evolve only via thickening of the mushy zone ($E=E_t$), and FLAG(i,j)=5. Other parts of these grains continue to grow as normal. For the purposes of visualisation, such an impingement c.v. could be given a certain colour e.g. grey. After solidification, the grain boundaries would be represented by such grey c.v.s.. With such an approach, however, the grain boundaries are visible only at very low resolution, unless a very fine mesh is used (with associated computational penalty, especially for this explicit model). An exception would be perhaps if information only on the CET was required from the model. To utilise the resolution afforded by the front-tracking technique, an alternative approach is needed. In Fig. 3.19(iii) grains (a) and (b) overlap for the first time. The liquid area A is greater than the area of overlap B, and growth can continue until A=B (Fig.3.10(iv)). At this point the combined volume of both grains fills the c.v.. A line $|cc'|$ is drawn which bisects lines $|aa'|$ and $|bb'|$, and passes through A and B. As before the points a, a', b and b' are now pinned, but the line $|cc'|$ can be used to permanently represent the

grain boundary in such a control volume. Growth of other parts of these grains continues as normal, just with two markers on each pinned. The final total grain boundary will be the composite of similar lines $|cc'|$. An interpretation of the FLAG values for an impingement c.v.(i,j) is that it is being invaded when FLAG(i,j)=7, has been annexed when FLAG(i,j)=5, and consolidated when FLAG(i,j)=6.

The model system can be represented by the quadrant in Fig. 3.1 because it is expected that diffusion will occur symmetrically. This is true if x=w/2 and y=w/2 are axes of symmetry for the problem. However, for the stochastic process of equiaxed nucleation and growth, one cannot expect any grain to have a mirror "twin" in the facing quadrant. Thus, as illustrated in Fig. 3.20(b), the flux across these otherwise adiabatic boundaries can no longer be treated as zero, due to asymmetric latent heat affects and possibly recalescence. It can be argued that if the equiaxed grains are very numerous that the adiabatic assumptions still hold on average, but then one still has the problem of how to model the growth of an equiaxed grain *across* such a boundary. A full treatment of the problem would require that the computational domain be the entire mould and alloy - this would also enable convection to be treated. For the development and debugging of the multi-grain model, however, one quadrant can still be used if an artificial nucleus-free "buffer zone" is set up near the adiabatic boundaries. A similar zone near the mould wall means that impingement of grains with one another can be studied before development of code to deal with the grains reaching the mould surface.

3.7.3 Unresolved problems

The algorithm for equiaxed solidification has been presented. As outlined in the following Chapter, it has been used to predict nucleation and growth of multiple equiaxed grains. However, it has not as yet been possible to implement and check the proposed algorithm to deal with impingement. This is a priority for future work.

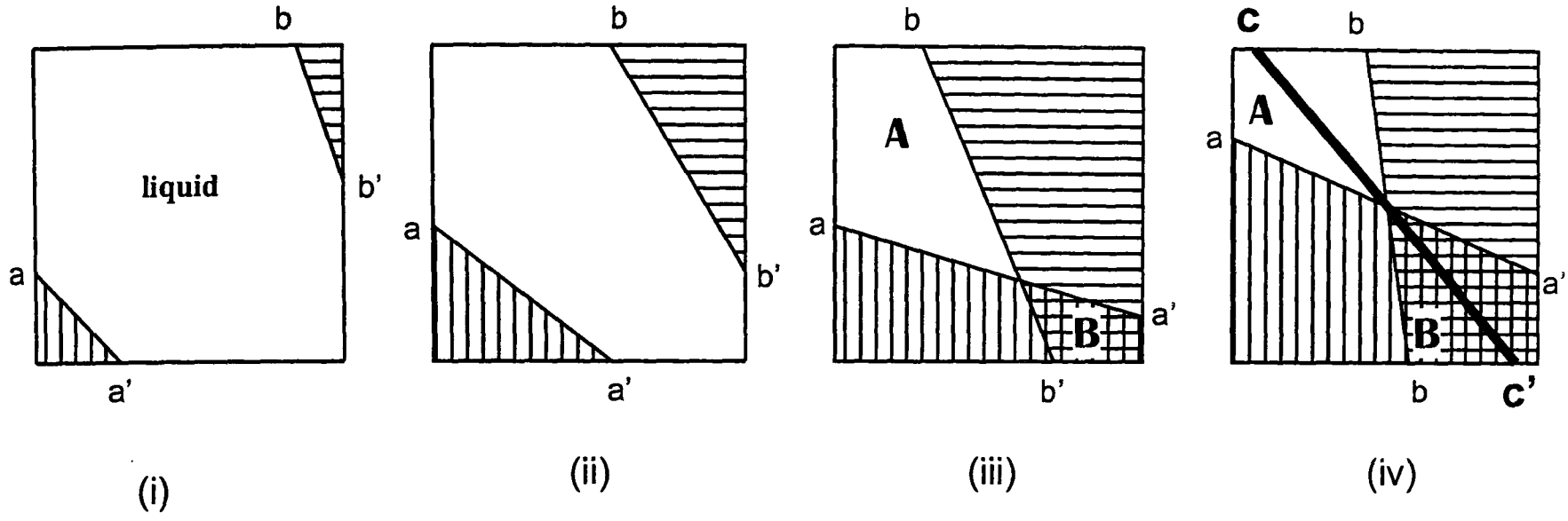

Figure 3.19 The impingement of grain *a* and grain *b* in a control volume.

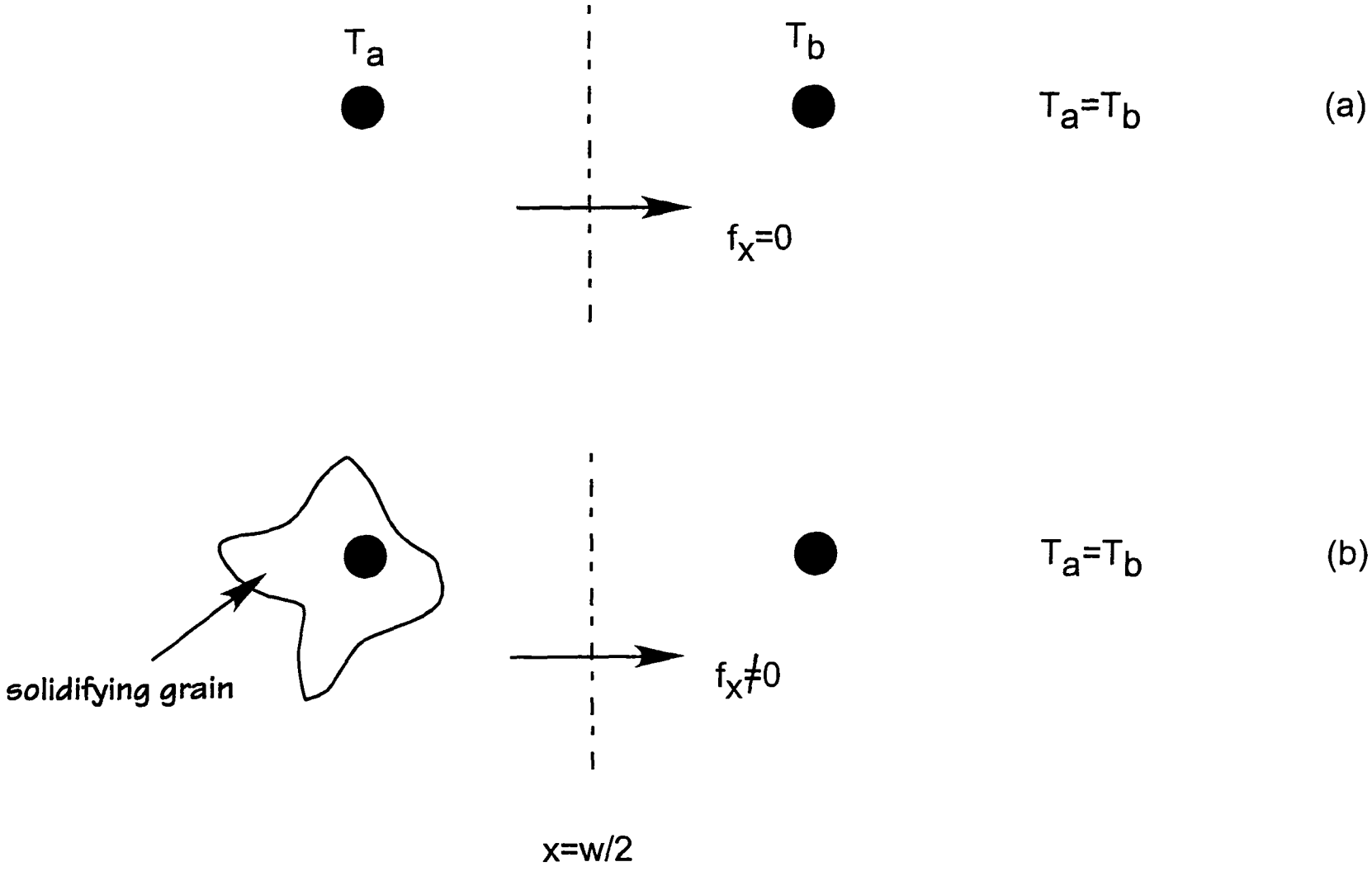

Figure 3.20 The breakdown of thermal symmetry due to equiaxed solidification.

3.8 Summary and the CET

The natural conclusion to these sub-models of columnar and equiaxed solidification, when impingement routines are successfully implemented, will be the ability to predict the Columnar-Equiaxed Transition, and the grain structure in the equiaxed zone. However, due to the scope of the work undertaken, such prediction has yet to be achieved. But, as evidenced by material presented in this Chapter and the next, the author is confident that this work can be continued, using the techniques suggested, to achieve such a goal. The approach outlined to modelling of impingement is sufficiently generic to enable predictions which are consistent with experimental observations e.g. small isolated equiaxed crystals could be engulfed in columnar growth, whereas a large volume fraction of equiaxed solid could halt columnar growth. Indeed, in a thermal gradient, it is not expected that so-called *equiaxed* crystals will necessarily grow equally in all directions. An extension along the direction of largest heat flux may be expected, in which case it is difficult to classify such grains as equiaxed. Certainly they could arise due to unconstrained growth, but it may be difficult to distinguish them from columnar grains in a sectioned and etched casting. In such a case it is difficult to define the CET (see Section 4.4). Furthermore, casting conditions may prevail which favour either a completely columnar or a completely equiaxed microstructure, and such an outcome should be predicted as the result of the competition between both forms of solidification.

3.9 Implicit Model

Explicit and implicit numerical methods are compared and contrasted in Section 2.1.1. The simplicity of coding with explicit methods should be balanced against their conditional stability. The modeller must make a judgement between the efforts and the possible rewards for each approach. In the case of finding a solution to transient heat transfer problems, the

implicit method is probably the best choice. This is true even if solidification is considered in a continuum manner (via the enthalpy method). However, the benefits of the implicit approach are not as clear for complicated models which attempt to make predictions at sub-continuum length scales, such as the front-tracking model of this thesis. If it is not clear *a priori* that a particular algorithm will work, it is perhaps best to attempt an explicit model. The resultant limitation on time step may increase the computational resources required, but if a new model cannot be implemented via an explicit formulation, then it is very unlikely that any attempt at a more complicated implicit one will succeed. This statement is supported by the experience of the author in carrying out this project. An implicit model was attempted first. A full report on these efforts is not possible in this thesis, but the basic problems encountered are outlined in Appendix A.

From a physical point of view, it is necessary to track grain boundaries as they move across the computational mesh. Although the implicit method would allow use of a large time step, this would have to be tempered by the necessity to capture the physics of the problem. For example, in a heavily grain-refined alloy, a large time step would favour growth in its competition with nucleation.

In both explicit and implicit models, the growth velocity is assumed to be constant during a time step Δt. The velocity is consistent with the temperature at the start of the time step for the explicit model, and with that at the end of a time step for the implicit case. But the larger Δt possible in the implicit formulation would not be consistent with an assumption of zero variation in velocity from one calculation to the next.

The contention of the author is that, for this particular problem, the explicit method is the optimal one.

3.10 Graphics

Any model of microstructural evolution would be incomplete without graphical animation of the appearance and growth of the microstructural features in question. When a model has been completed and is being used for predictive purposes, a post-processing graphics package is perhaps the best way to present the results. However, during code development and program debugging, run-time graphical output is more useful. This can be done via use of a separate Graphical User Interface (GUI), for which the program must be supplied in executable form.

In this project, the program was written using Compaq Visual Fortran. This comes with its own graphics facility called QuickWin - a Windows-based GUI. QuickWin instructions can be called from *within* the program, and these are compiled into the executable. The graphics operate within the same visual development environment as the mathematical model, and this facilitates debugging and code development. The programmer can see the graphics evolving in the relevant window, and if the program crashes it is easy to see where the problem occurred and to initiate debugging. For these reasons QuickWin was used in the development of the model. The coordinates of the marker particles of each grain are stored in arrays. These grains are then represented graphically by drawing lines between successive marker positions. Animation allows visualisation of grain growth. Multiple windows can be opened e.g. one can be used to show a cooling curve evolve from a "virtual thermocouple" reading. A disadvantage of QuickWin is that it is not portable to other compilers or operating systems. For this reason, most of the QuickWin graphics calls were placed in a separate subroutine (GRAFSUB), which can easily be disabled.

Chapter Four

Results and Discussion

Chapter 4

Results and Discussion

In this Chapter, the predictions of the front-tracking model, outlined in Chapter 3, are presented and discussed. The computer program was written in the FORTRAN 90 programming language, using double precision variables. Execution was on a Dell Pentium III 500MHz PC with 128 MB RAM. Run-time was typically less than five minutes for each simulation. At the end of the Chapter, the results of a few relevant solidification experiments are presented.

4.1 Alloy Thermophysical Properties

The model is tested on the Al-Cu system in this thesis. The thermophysical properties are considered invariant, see Table 4.1, their values being consistent with those from the literature [73,100,175,179].

Description	**Symbol**	**Value**	**Units**
latent heat of melting	L	1000	J/cm^3
thermal conductivity	k	1.0	W/cm K
specific heat	$\rho.C_p$	3.0	J/cm^3 K

Table 4.1 Alloy thermophysical data used in the model.

The analysis of Burden and Hunt [8] yields a dependence of undercooling ΔT upon dendrite tip velocity V (their equation 18) :

$$\Delta T = \frac{GD}{V} + (2)^{1.5}\sqrt{\frac{-m.V.(1-\gamma).C_o\theta}{D}} \qquad (4.1)$$

in which m is the liquidus slope, γ the partition coefficient, C_o the alloy composition, and θ a curvature undercooling constant. Neglecting the first term, as before, and using values for the other variables for the Al-Cu system [8], yields an expression of the form, in cm/s :

$$V = \frac{0.16}{C_o}.\Delta T^2 \qquad (4.2)$$

where C_o in this case is in wt.%Cu. So, for an alloy of Al-2wt.%Cu, C_1=0.08 cm/K^2s in equation (3.8). The liquidus and solidus temperatures are taken from the equilibrium phase diagram (Fig. 4.1), and for Al-2%Cu, T_L=655°C and T_S=614 °C.

In equilibrium solidification (Fig. 4.1), it is expected that some eutectic will form if over 5.7wt.%Cu is present. In the non-equilibrium case, the eutectic formation is expected in even purer alloys. A limitation of this work is that it does not treat the eutectic arrest. For this reason, only aluminium alloys containing up to 4% copper are considered.

4.2 Heat Model

Before nucleation occurs, the model is simply one of conduction heat transfer through a liquid (see Section 3.4). Once solidification is complete, the model again treats single phase heat transfer. However, as this work is primarily concerned with the evolution of grain

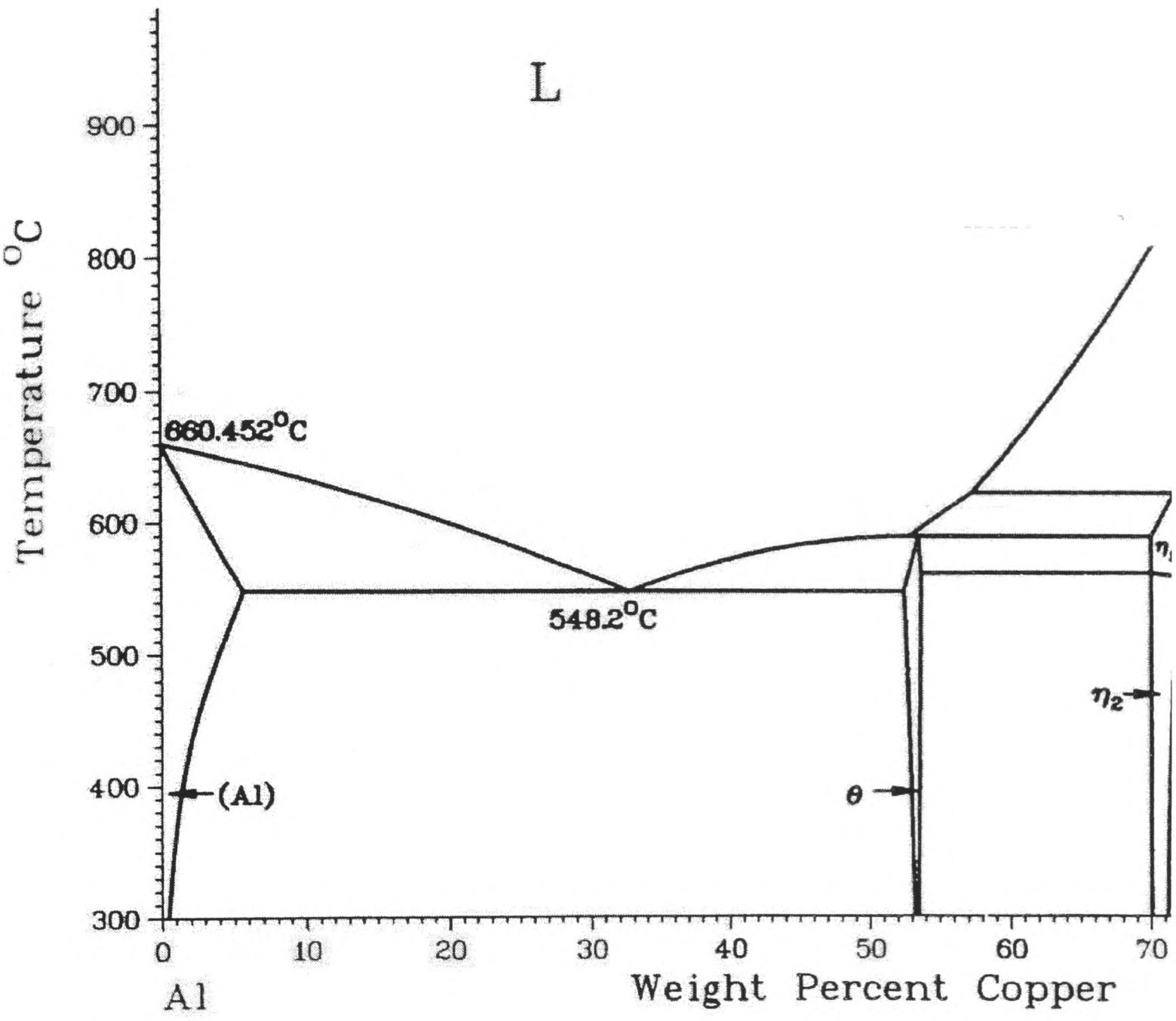

Figure 4.1 Al-Cu equilibrium phase diagram [180]

structure in a casting, the post-solidification cooling of the body is not of interest, and is not reported here.

The domain dimensions in all of this work are of an 18 x 18 cm square casting. The mould temperature T_m=400°C and the interface heat transfer coefficient h=0.3 W/cm^{2}K. The liquid alloy initial temperature T_a=700°C. The columnar nucleation undercooling ΔT_n=2°C.

Calculations were performed on a 100 x 100 c.v. grid, for an Al-2%Cu alloy. Equiaxed solidification was disabled by setting the equiaxed nucleation undercooling artificially high (ΔT_{nuc}^{ex}=400 °C). The time step was set at 0.00575s, which is less than the maximum permitted for stability in explicit schemes (equation (3.6)).

Under such conditions, the lowest predicted temperature was at the corner, as expected. The wall nucleation temperature (653 °C) was first reached at this location, after 0.2185 s (38 time steps). A colour-coded map (Fig. 4.2) of the thermal field in the corner (17 x 17 c.v.s), at this time, clearly shows this. Of course the temperature right at the mould wall surface will be lower (equation (3.17)) than that of the corner c.v. node.

Once nucleation occurs, the thermal field will be affected by latent heat release. In the case of equiaxed solidification (with columnar growth disabled), heat can diffuse from a large area of the domain before nucleation, particularly if the nuclei are far from the mould wall.

4.3 Columnar Solidification

4.3.1 Nucleation and initial growth

Once the corner marker has nucleated, columnar growth starts. Figure 4.3 shows the progress of nucleation at the mould wall with time. Due to the extra surface available for heat transfer

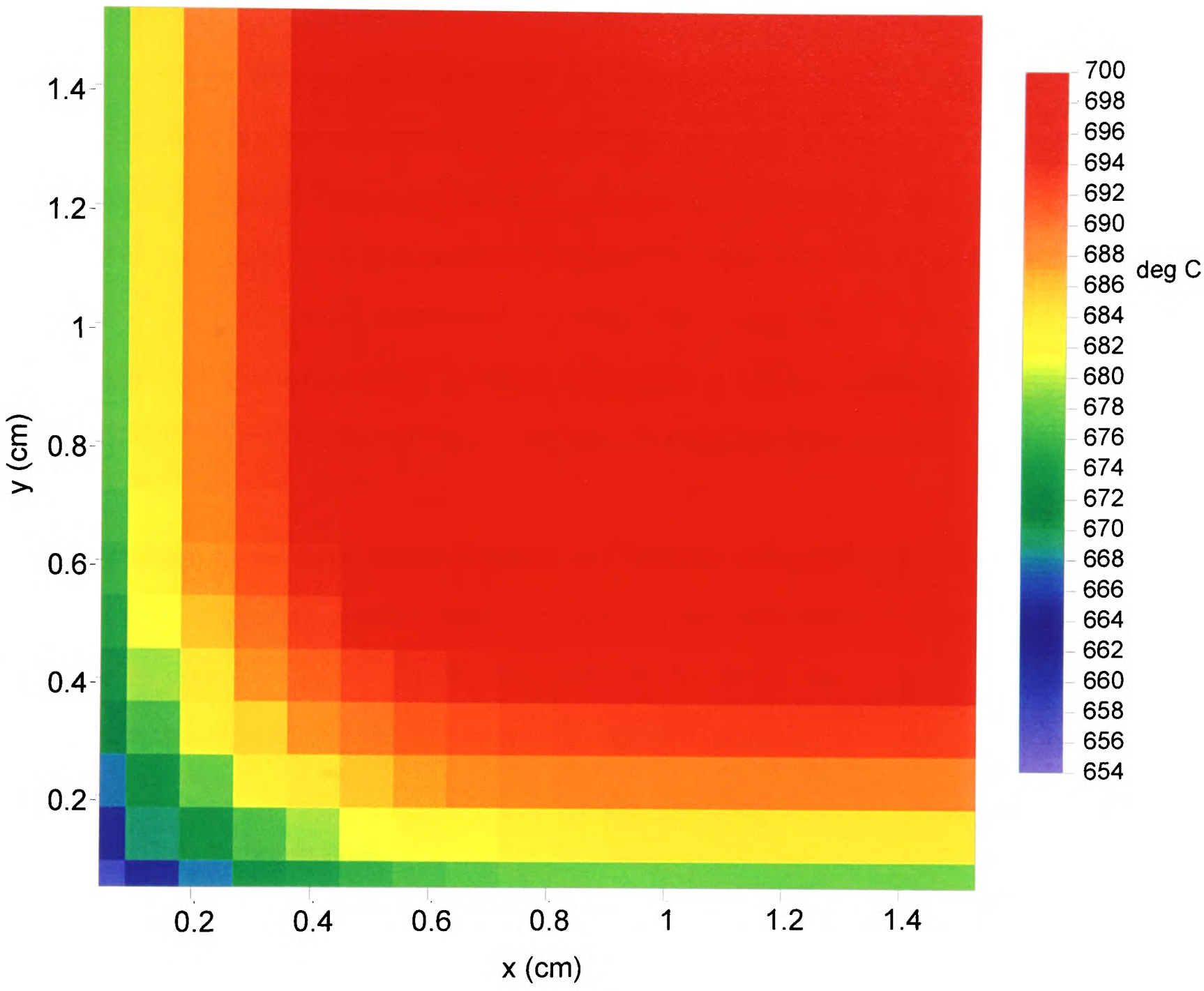

Figure 4.2 Thermal field in the domain corner; t= 0.2185 s

at the corner, this is where the temperature falls below that required for nucleation for the first time. Nucleation then progresses from the corners, in a symmetric fashion, along the x and y axes. The step-function nature of the curve shows that nucleation does not occur at each time step. The step height is 2, or a multiple of 2, indicating a symmetry along both mould walls i.e. for every nucleation event at (0,a) there is an equivalent event at (a,0). After 0.8395s, there is a sudden cascade of nucleation along the mould wall, as the remaining sites all nucleate together. This occurs because of the very small thermal gradient along the walls, far from the corner. This is illustrated in Figure 4.4, in which the thermal profile at the alloy surface, along the vertical mould wall, is plotted. The temperatures are those at sites *nrows* through *1* (in decreasing order), as shown in Figure 3.14. The low thermal gradient along the mould wall can also be seen in Fig.4.2. Now all 201 sites have been activated.

The position of the front at t~1s is shown in Figure 4.5, along with the original nucleation sites. Only a 23 x 23 subset (lower left corner) of the computational domain is shown, in order to improve visibility of the front markers. It can be seen how, for tightly-spaced markers, linear interpolation can successfully represent curvature

4.3.2 Continuing growth

Columnar solidification then proceeds towards the centre of the casting. The progress of the front is illustrated in Figure 4.6. It should be noted that symmetry across the diagonal, from the mould corner to the casting centre, is not *imposed* in the model. However, from the boundary conditions, it is expected. A non-robust scheme would result in early asymmetry due to numerical noise, resulting in unphysical breakdown in symmetry. This does not happen in this case, and the front converges exactly at the centre of the casting (after 153.364 s). This inspires confidence that the columnar model is setting the correct thermal conditions in the bulk liquid for the equiaxed model to face.

The variation of the undercooling of marker particle number one, throughout solidification, is shown in Fig. 4.7. This marker, originally positioned at (0,w/2) is chosen because it moves

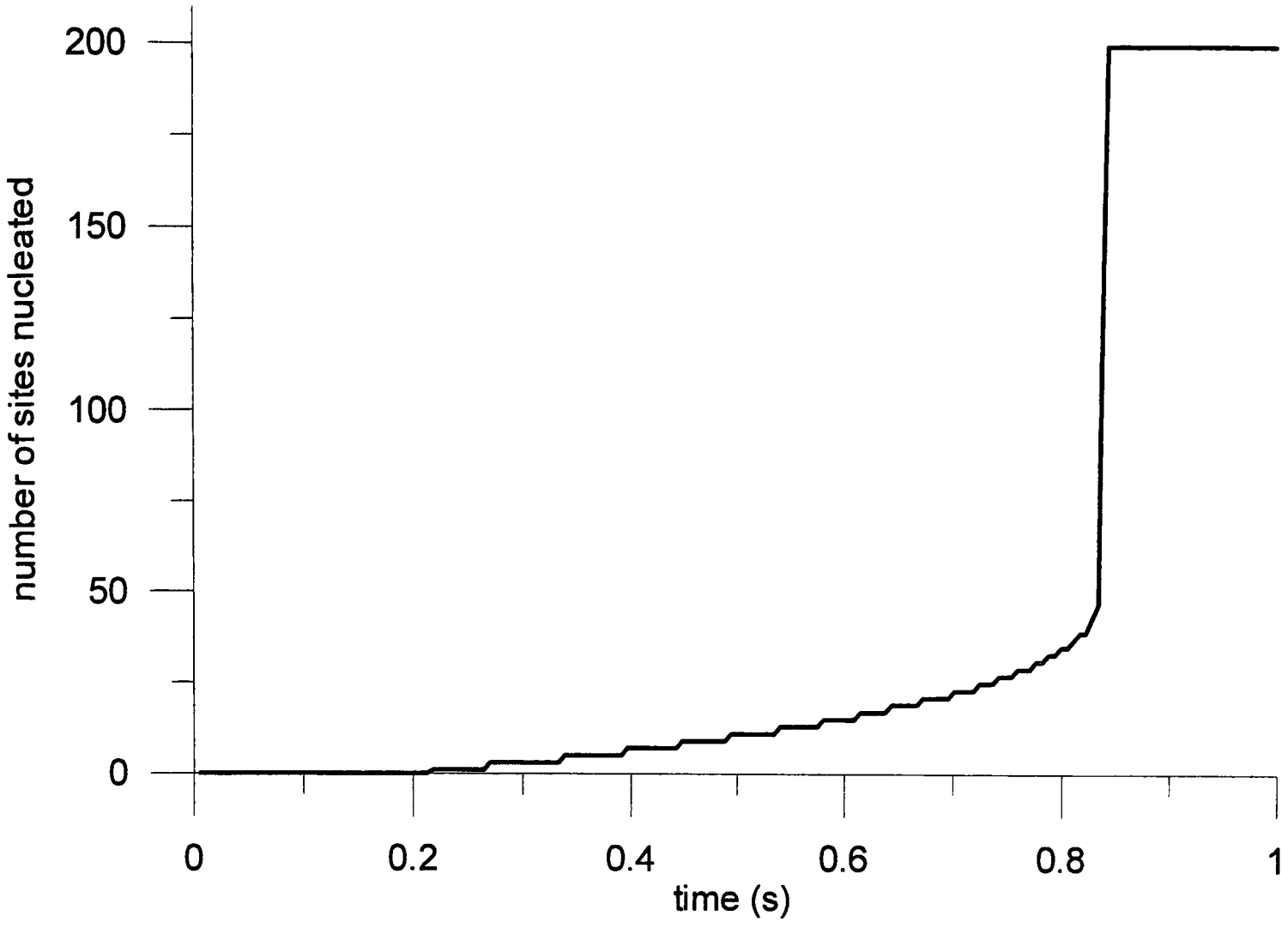

Figure 4.3 Cumulative number of surface sites nucleated as a function of time

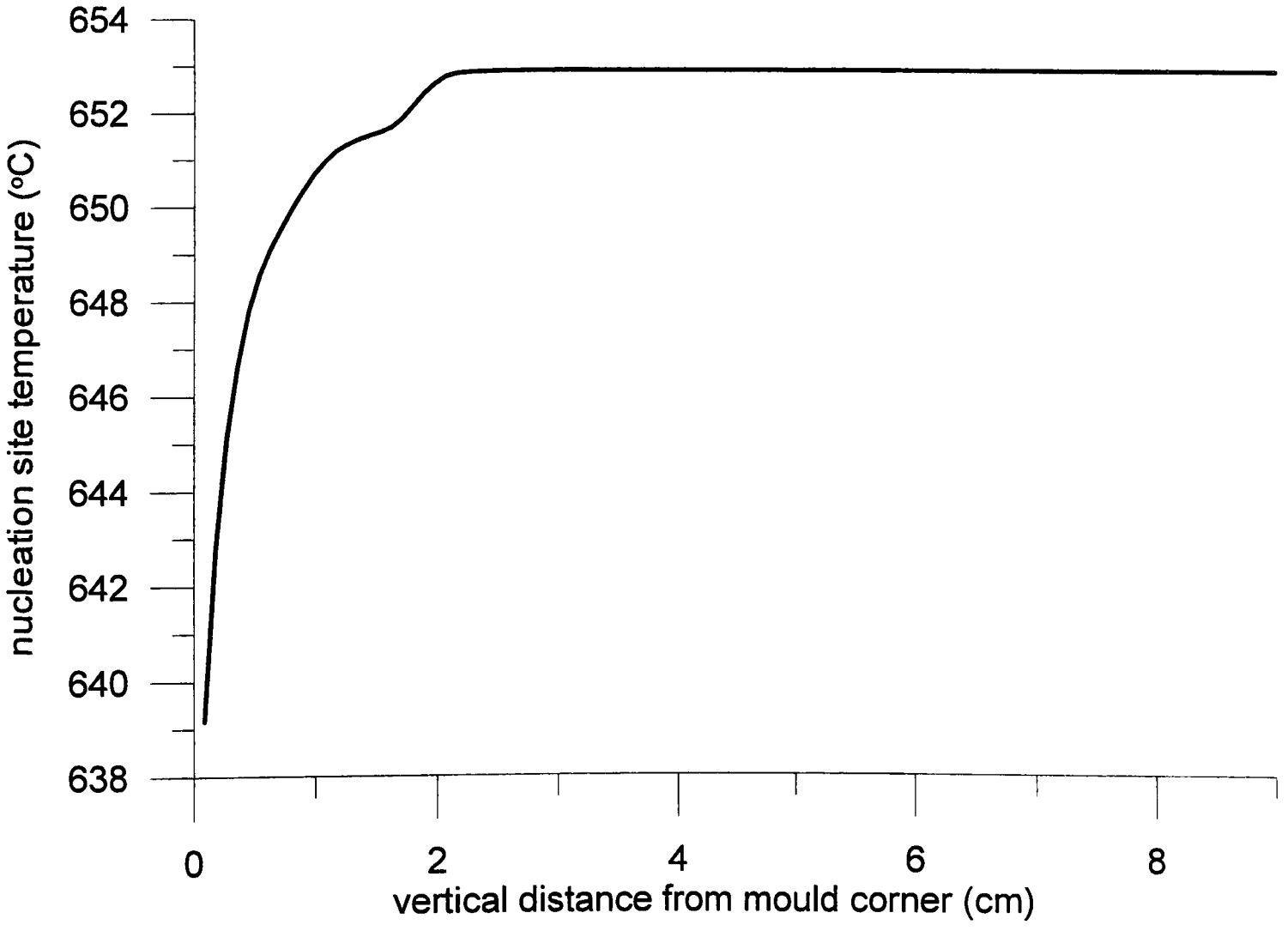

Figure 4.4 Variation of nucleation site temperature along vertical wall; t=0.8395s

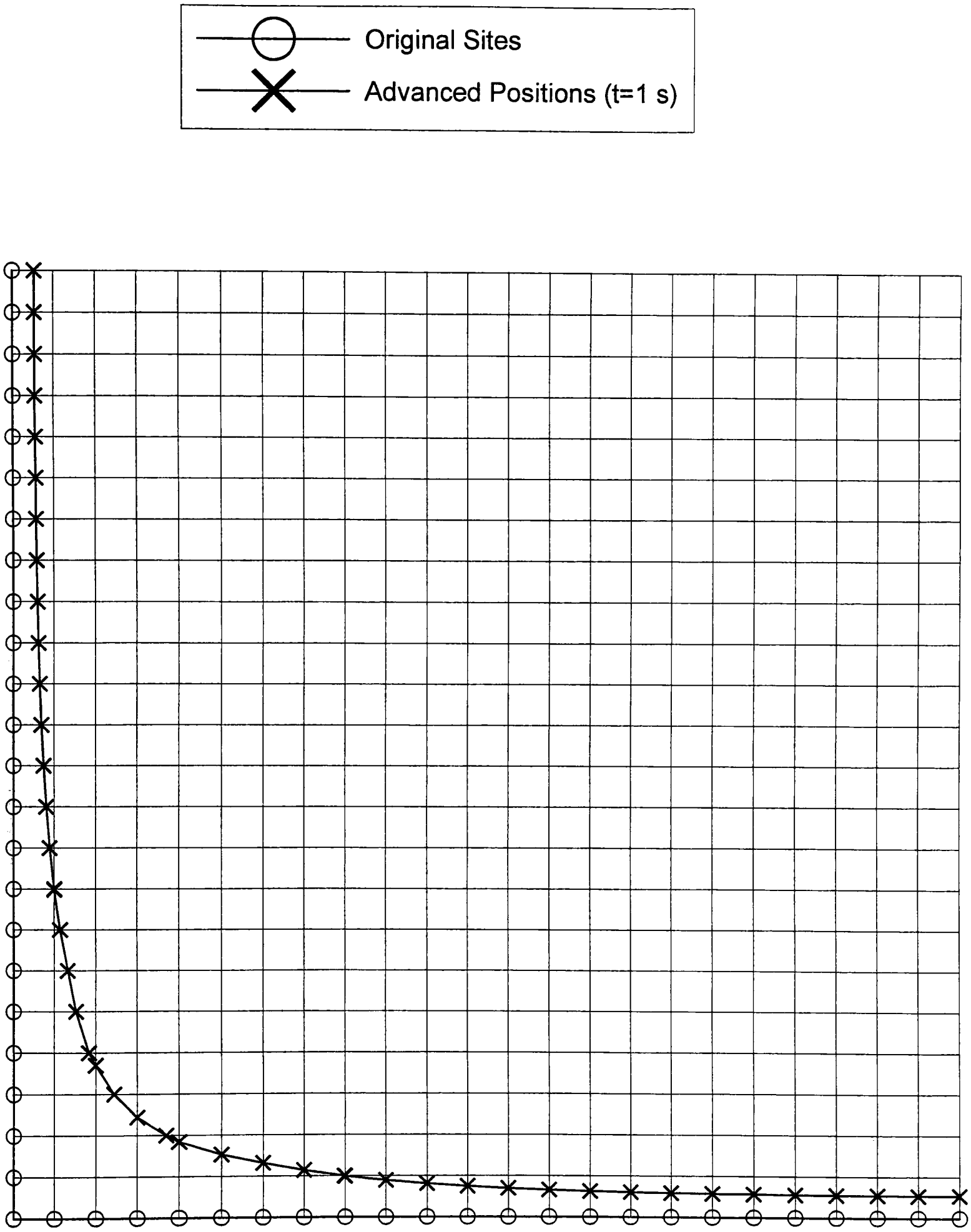

Figure 4.5 Position of columnar front, near mould corner, at t=1s

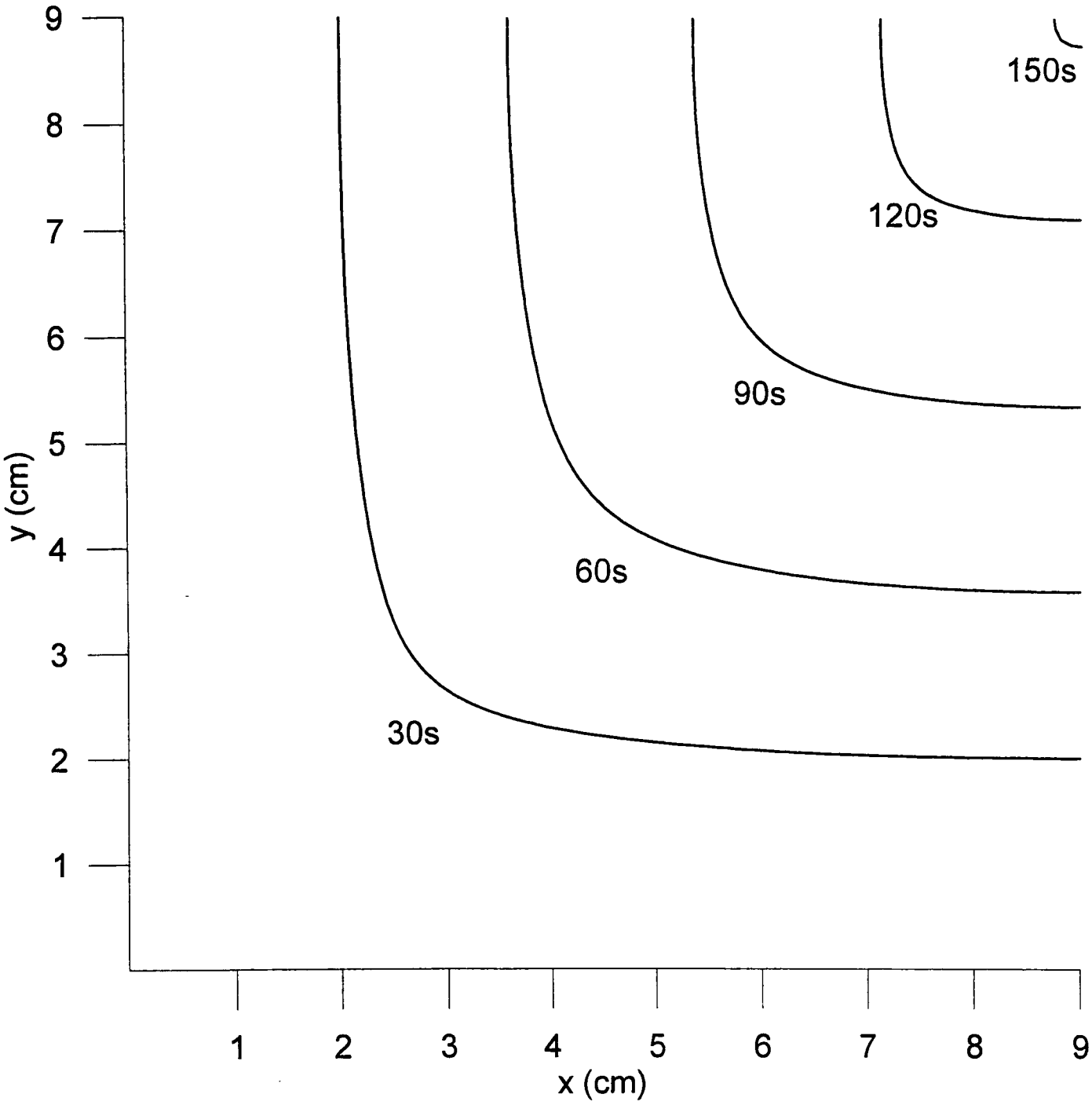

Figure 4.6 Progression of the columnar front across the domain

continuously along the straight line y=w/2 and, unlike other markers, does not become renumbered or relocated due to the intersection routine. The data is plotted every second. The velocity of this marker is plotted in Fig. 4.8, again every second. As expected (equations (3.8) and (4.2)), the shape of the velocity plot mirrors that of the undercooling. We note slight oscillations in marker velocity and undercooling, perhaps due to the employment of bilinear interpolation. This marker nucleates at 0.8395s, and reaches the centre of the casting at 153.364s, having travelled 9 cm. So its average velocity was 0.059 cm/s. And so, from equation (4.2), its average undercooling during solidification was 0.859°C. In fact this marker has less distance to travel to the centre of the casting than others, so one would expect other parts of the columnar front to grow at a lower temperature. Figure 4.9 shows that this is the case. The undercooling of both marker one and the front average are shown at the times at which the front position in Fig.4.6 is plotted. The average undercooling of the columnar front exceeds that of marker one by about 0.035°C for most of its growth.

Study of nodal temperatures ahead of the advancing front shows that the first bulk liquid undercooling occurs near the mould corner, after 0.90275 s, and the magnitude is 0.027°C. The maximum undercooling in the bulk (calculated from nodal temperatures T(i,j) where FLAG(i,j)=1) increased with time, reaching a value of 0.893°C at 96.14s. This occurs quite close to the centre of the front, but it should be noted that its magnitude is very similar to that of the columnar dendrite tips, indicating that serious competition can be expected from equiaxed grains under these conditions. The highest undercooling occurs in the bulk liquid as the columnar solidification is near completion. So this is at the centre of the casting, and the undercooling reaches 0.929°C. Again, we would expect that equiaxed growth would have initiated before this point. The predicted cooling curve at a position x=3.6 cm, y=4.5 cm is shown in figure 4.10. It shows a reduction in slope (absolute value) during solidification, as expected.

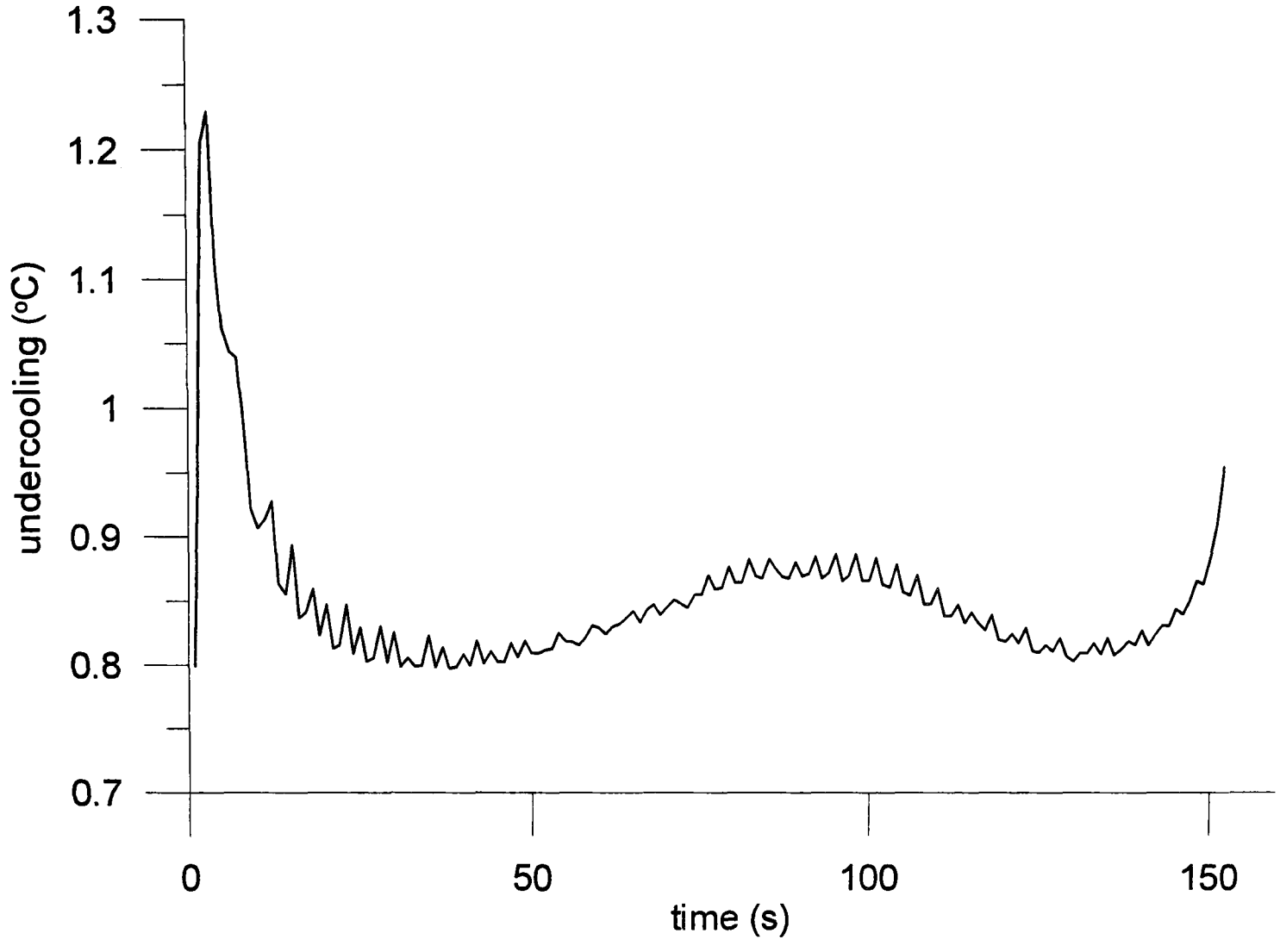

Figure 4.7 variation of undercooling of marker no.1 with time

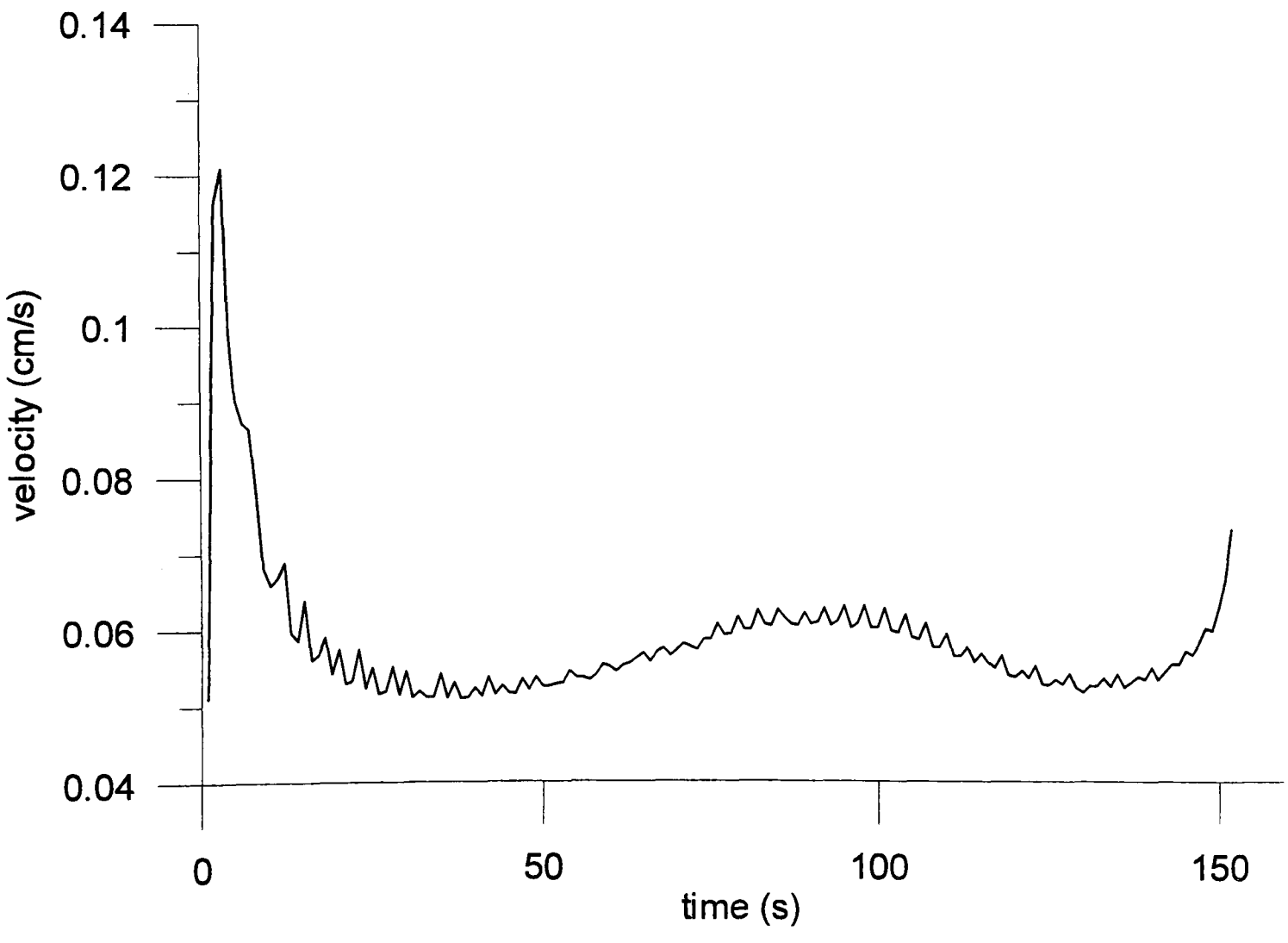

Figure 4.8 variation of velocity of marker no. 1 with time

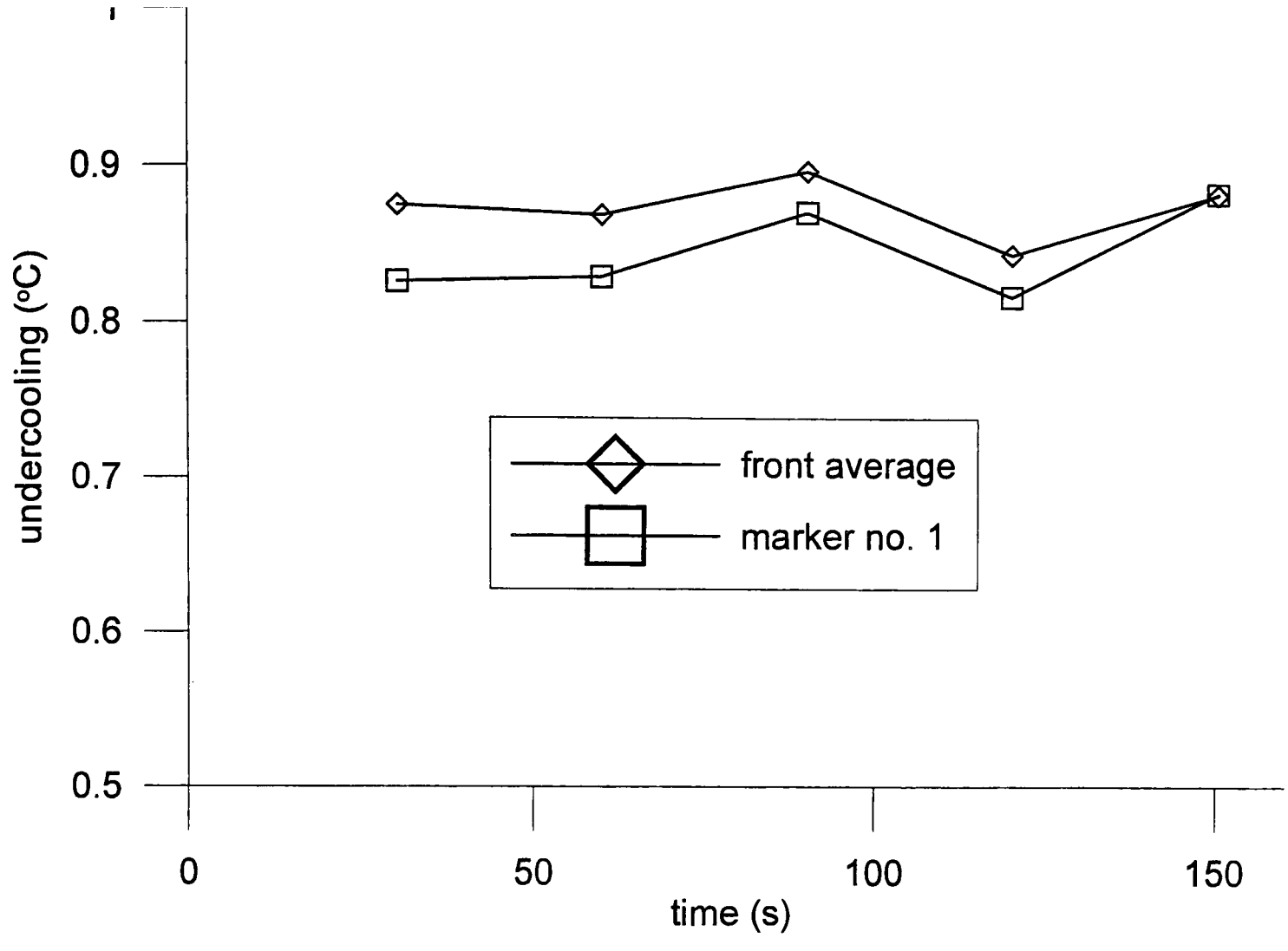

Figure 4.9 Average undercooling of columnar front, and undercooling of marker no.1, v. time

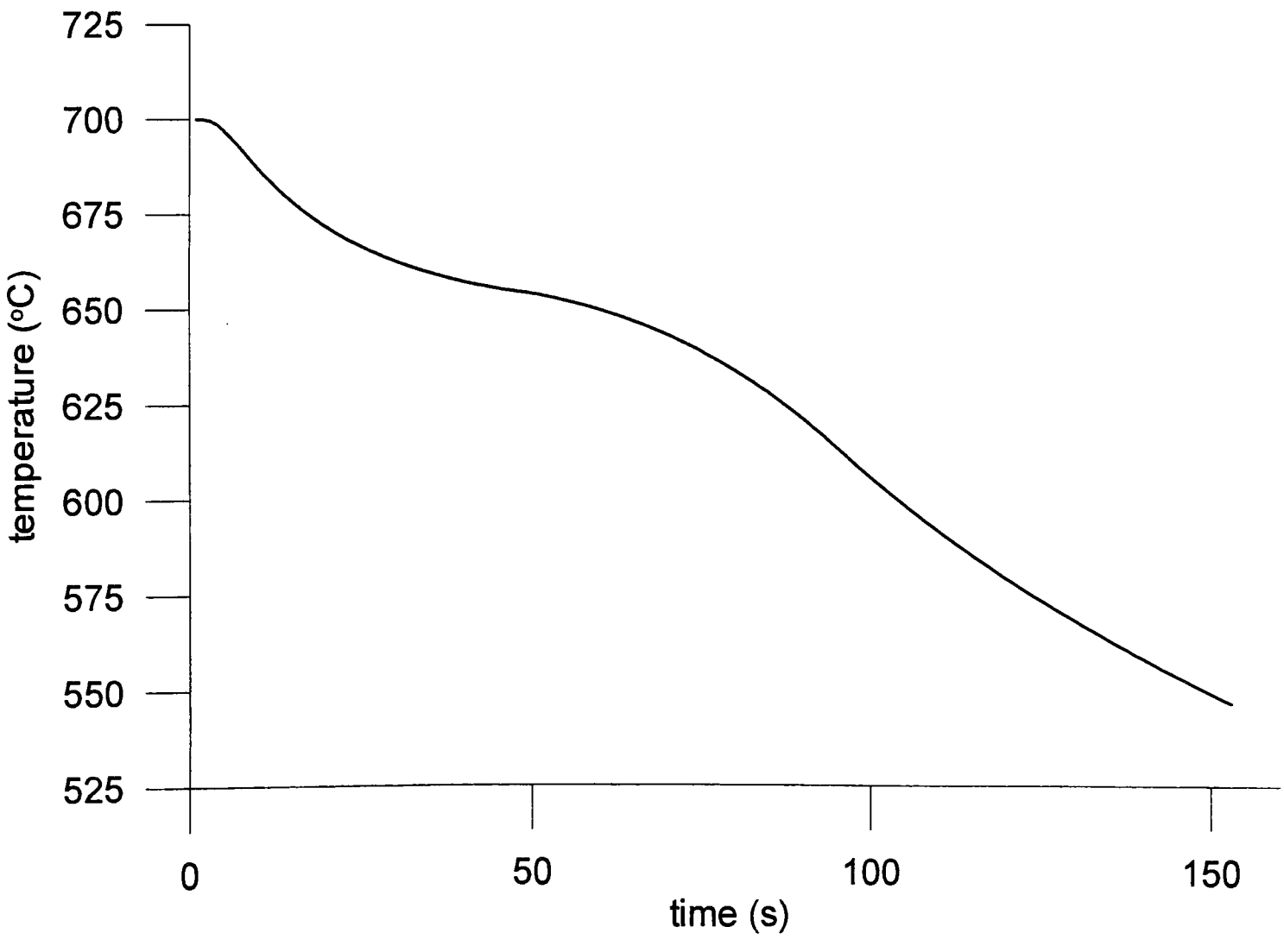

Figure 4.10 Cooling curve : T(40,50) as a function of time

Various types of information can be extracted from the model. Figure 4.11 is a colour-coded image map of the thermal field after 60 s. The temperature range shown is from 470 to 660°C. The same data is used to produce the contour plot of Figure 4.12.

Figure 4.13 shows the position of the columnar front (from the marker particle positions) superimposed (in thick line) on the thermal contour map. As stated already, this is not an isotherm, although the temperature along the front does not vary appreciably. For example, the difference between the average and the maximum front temperature at 60s is less than 0.04°C. With the average front undercooling (Fig. 4.9) of 0.83°C, this represents a deviation of 4.8%. When expressed as front temperature (°C) , the deviation is only 6×10^{-3} %. So, at the scale of the casting and for the purposes of visualisation one would expect the average front temperature isotherm and the tracked front to be practically coincident. A plot of both contours at the scale of Figure 4.13 would confirm this. Even at higher resolution (Fig. 4.14) the two curves are not easily distinguishable. Here the line closest to the lower left corner is the front. Although not used for computational purposes, it is therefore proposed that the average front temperature isotherm be used to represent the front visually. This is adopted for practical reasons - the isotherm contour plotting software can readily shade areas of superheated liquid, undercooled liquid, mushy zone and solid. For this picture, the bounding isotherms are those of the liquidus, "front" and solidus, respectively. In Fig. 4.15, the white area is solid, the dark grey is the mushy zone, medium grey is undercooled liquid, and light grey is supercooled liquid. Again, the time is 60 s.

The area of undercooled liquid is clearly visible in Fig. 4.15, but this does not show the extent of undercooling. This is shown in the 3D wireframe picture of undercooling in Fig. 4.16. The near corner is the centre of the casting. The computational grid is shown, and the vertical elevation is the magnitude of liquid undercooling. Near the casting centre is superheated liquid, behind the undercooled ridge (or ravine) is the columnar mushy zone, and solid. The ridge is travelling towards the corner, and its position is shown at 90s. A c.v.(i,j) is checked for undercooling U(i,j) if it has a FLAG value of 1 (see Table 3.2), or a value of 3 or

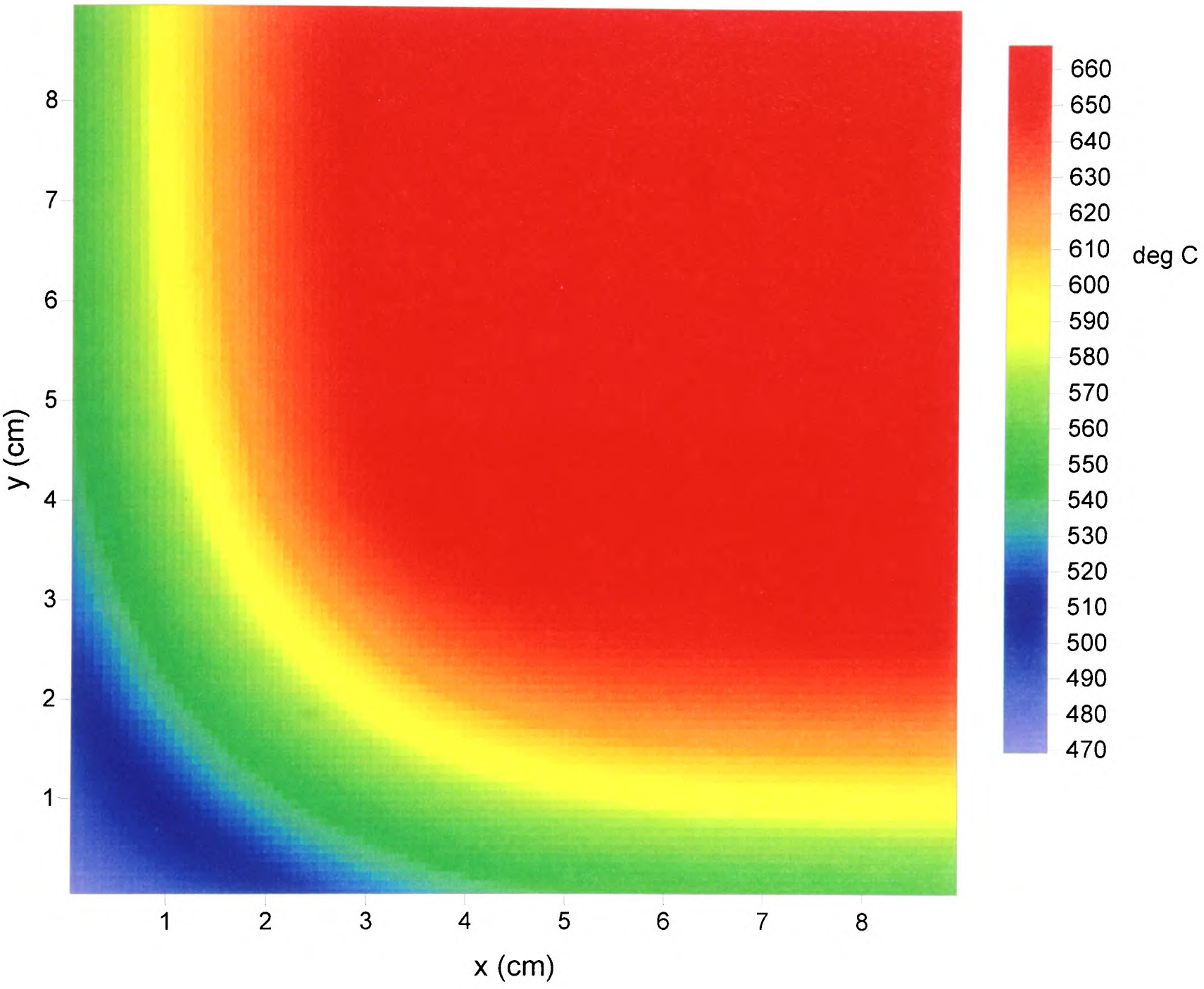

Figure 4.11 Thermal field; t=60s

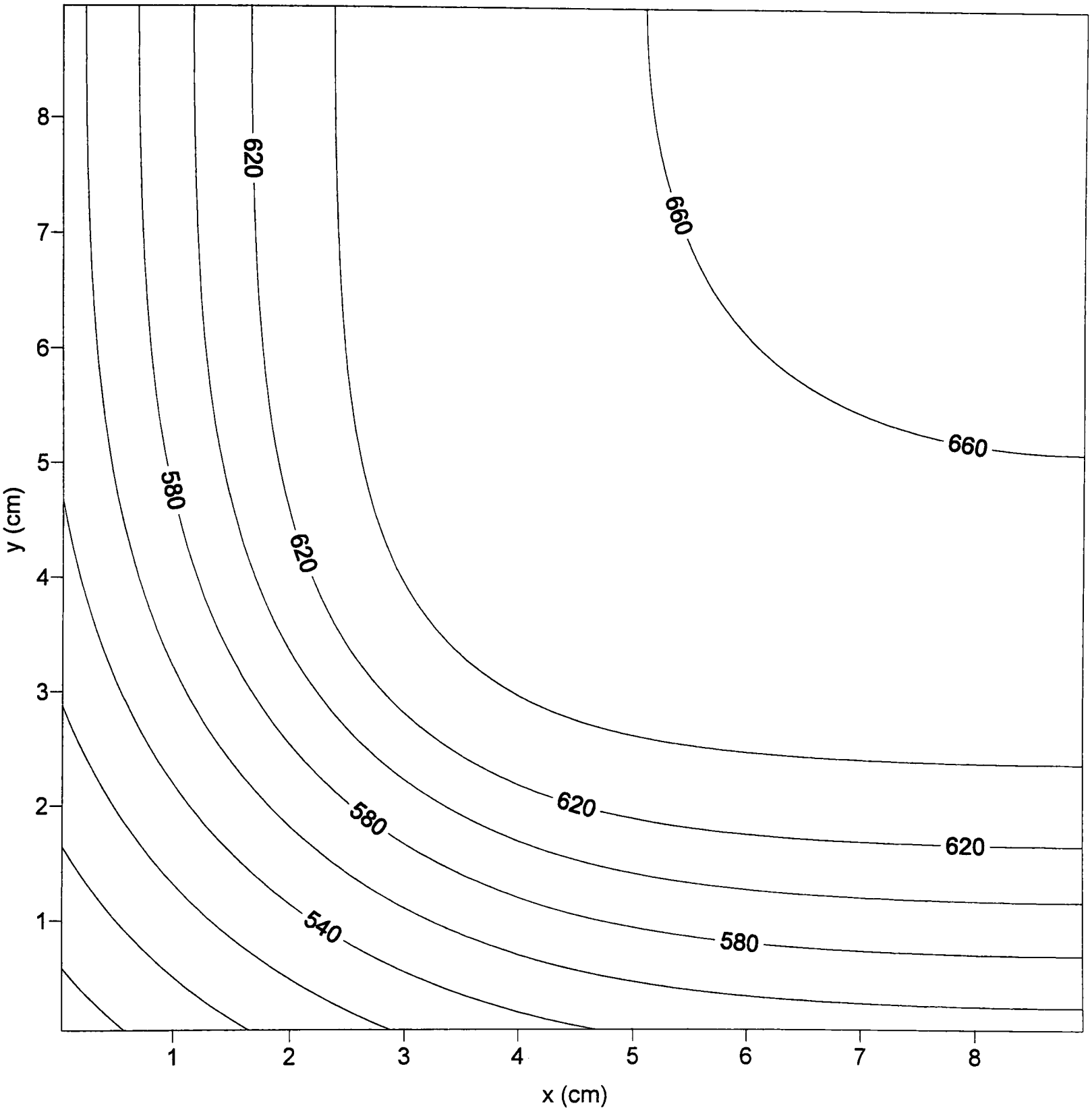

Figure 4.12 Thermal contour plot, Al-2%Cu, t=60 s

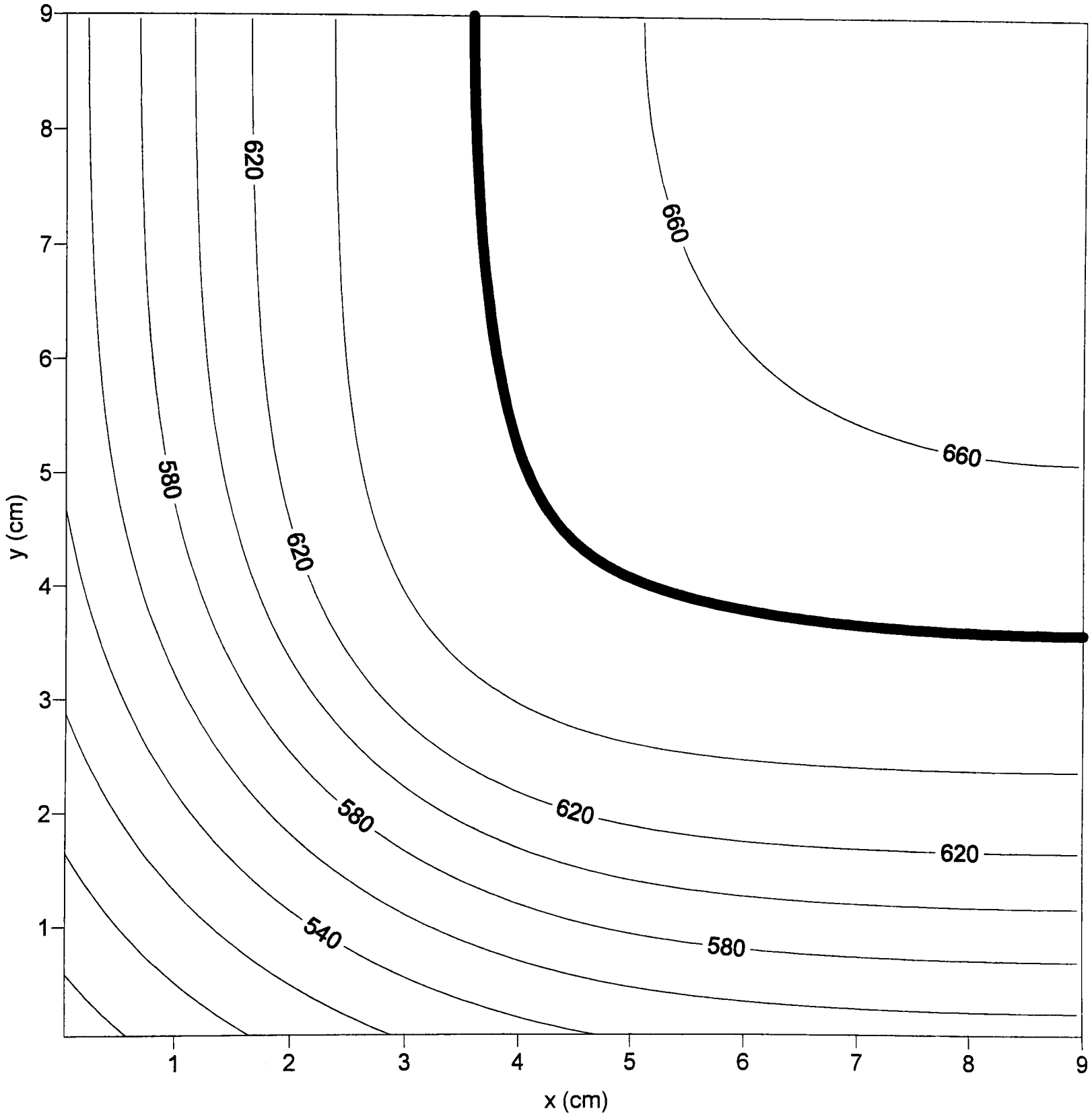

Figure 4.13 Thermal contour plot, Al-2%Cu, t=60s; thick line is columnar front

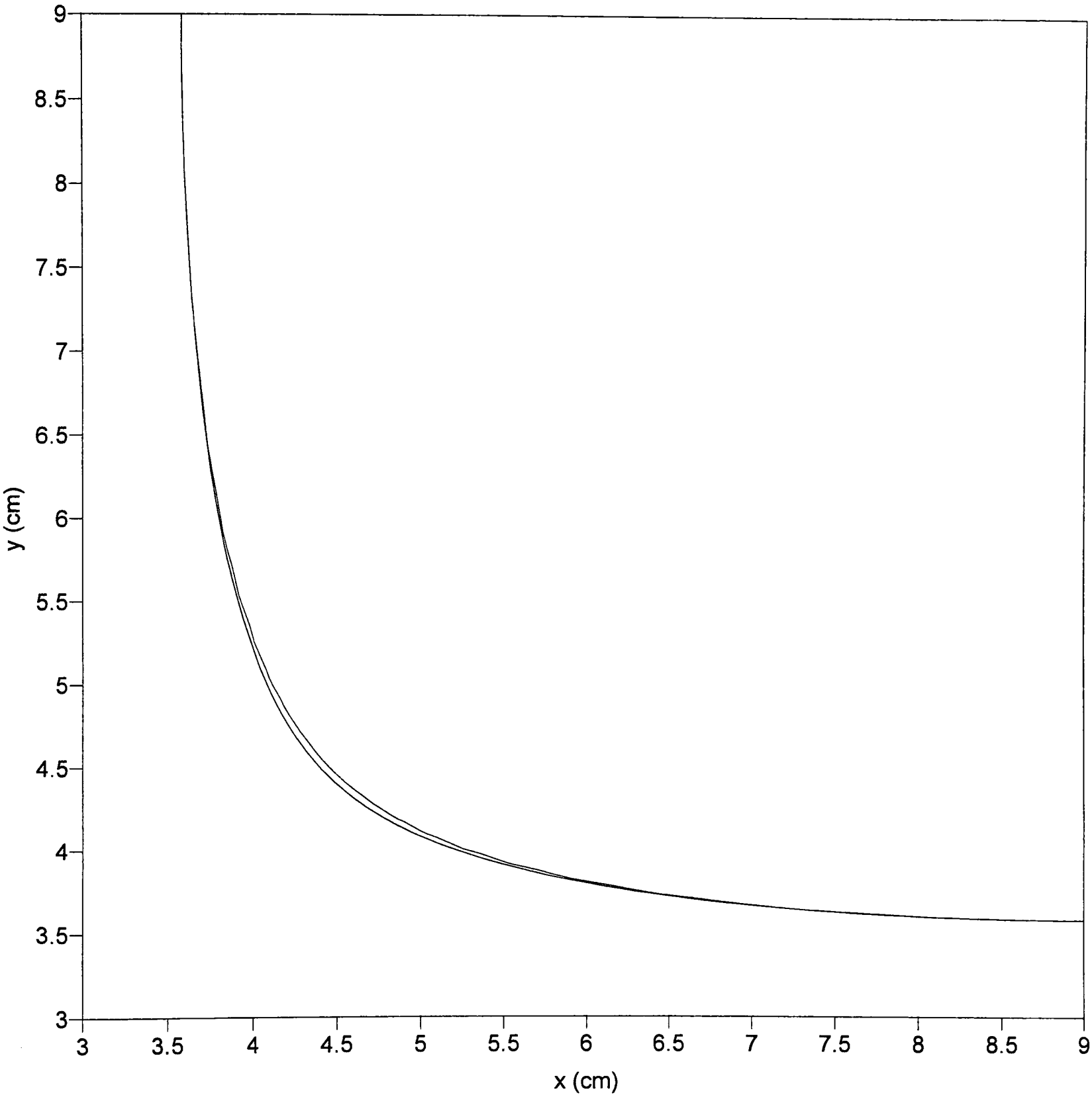

Figure 4.14 Average front isotherm (upper right); columnar front (lower left) Al-2%Cu, t=60 s

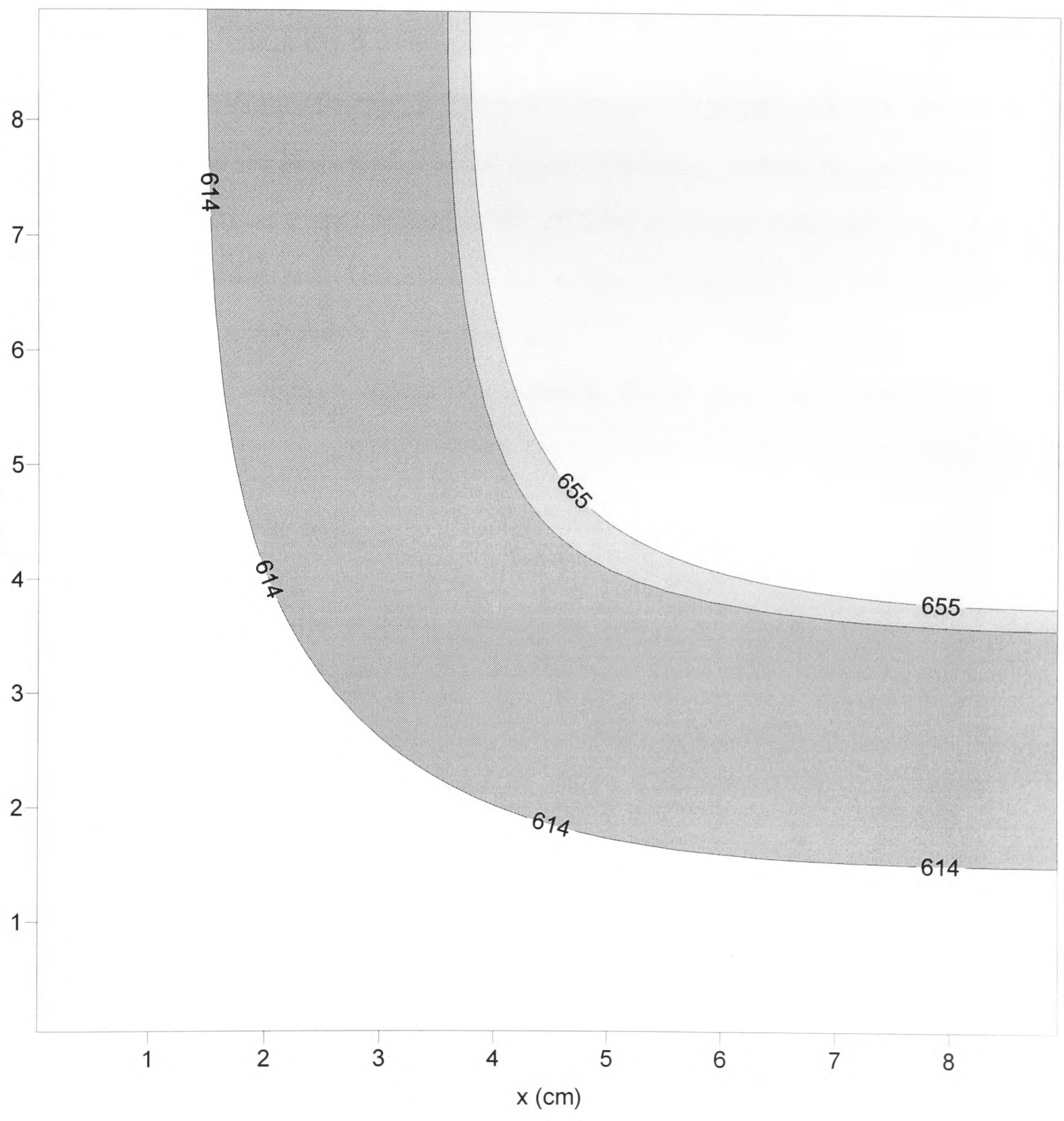

Figure 4.15 Regions of solid (white), mush (dark grey), undercooled liquid (medium grey) and superheated liquid (light grey); Al-2%Cu; t=60 s

4 provided less than half the c.v. is covered by the columnar mushy zone i.e. the nodal point should still be liquid. This information is also represented by a 3D surface plot of undercooling, in which its magnitude is colour-coded (Fig. 4.17).

The closer any nucleation site is to the front, whilst still being undercooled, the greater is the probability of nucleation. However, in this case the time for growth is limited. The reverse is true of sites close to the leading edge of the undercooled ridge. Indeed, figures 4.16 and 4.17 could be considered as a map related to the probability of equiaxed nucleation. And the *volume* under the ridge is an indication of the potential for equiaxed growth (preceded by nucleation). This is a snapshot at a particular time. If we need to follow the process with time, we can calculate this volume at regular time intervals. We can define an equiaxed index $I_{ex}(t)$:

$$I_{ex}(t) = \sum_{i=1}^{nrows} \sum_{j=1}^{ncols} U(i,j)\Delta x_j \Delta y_i \Big|_{t=const.} \qquad (4.3)$$

where

$$U(i,j) = T_{liq} - T(i,j) \qquad (4.4)$$

and is calculated, as described, only in undercooled liquid c.v.s - elsewhere U(i,j)=0. For the conditions under discussion, this index is plotted in Fig. 4.18. The peak is of relevance (5.9 cm^2K), as is the time of the peak (98.55 s). If there is to be a CET, it should occur at or before this time. The position of the CET would the be that of the columnar front at this time. Note that, at the start of solidification, the equiaxed index is very small, as the extent of the undercooled region ahead of the front is small. The index increases with time, but eventually starts to decrease as columnar solidification converges at the casting centre and the undercooled region again shrinks. This is illustrated in Fig. 4.19, in which the temporal advance (Fig. 4.19 (a) & (b), widening (Fig. 4.19(c)) and disappearance (Fig.4.19(d) & (e)) of the undercooled zone can be seen. The equiaxed index in equation (4.3) varies with time,

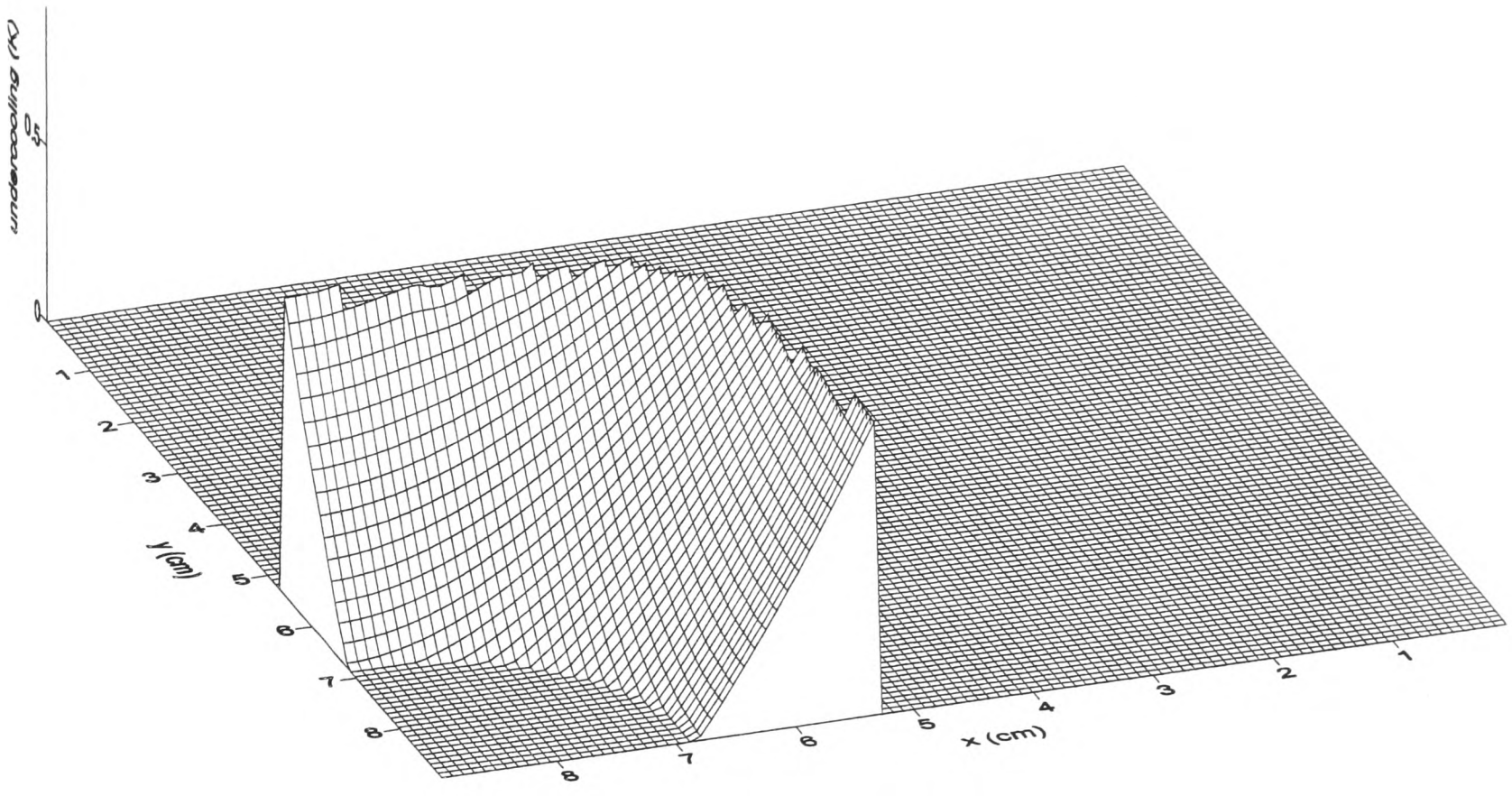

Figure 4.16 3D wireframe map of liquid undercooling; Al-2%Cu, t=90s

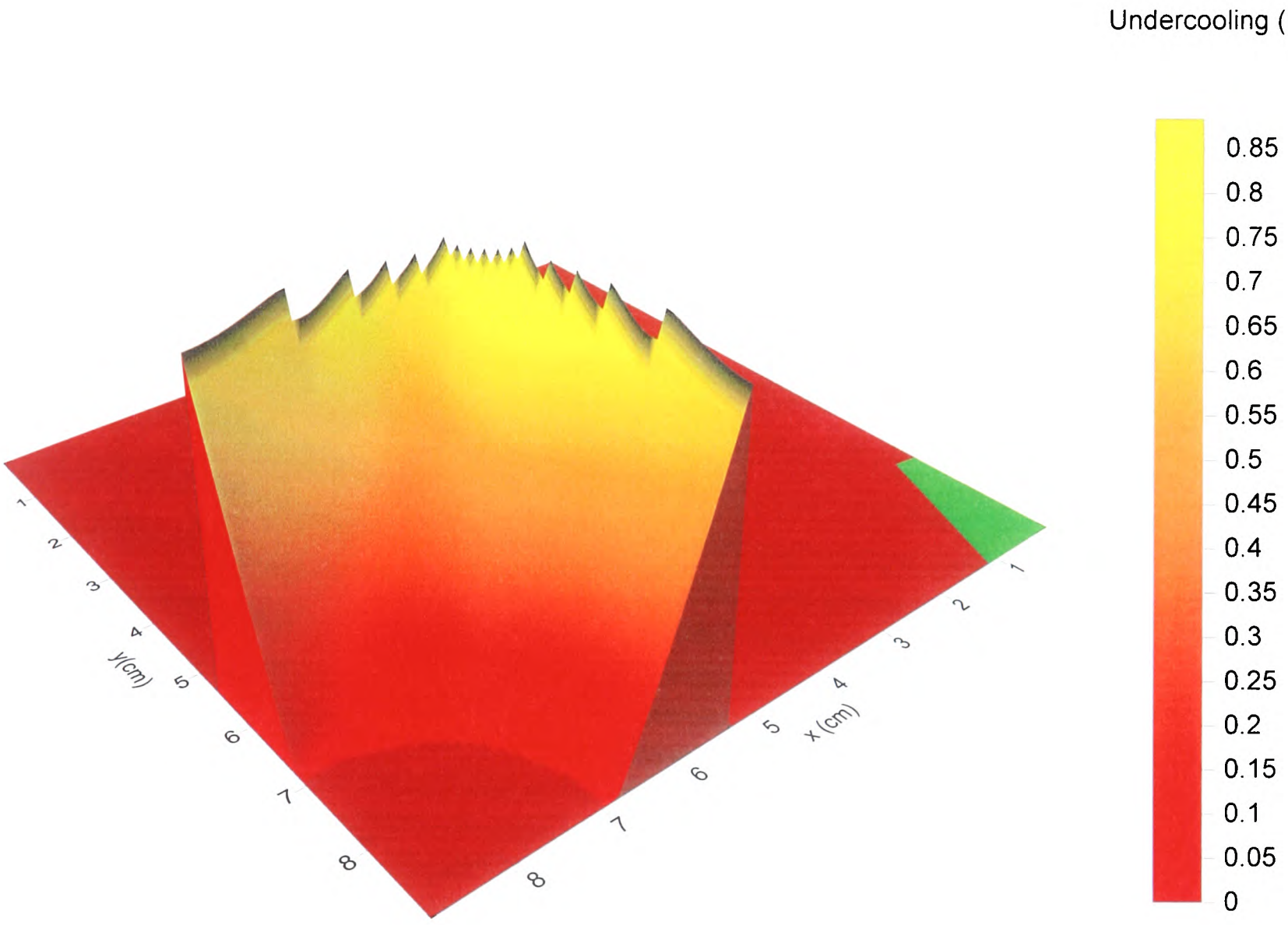

Figure 4.17 Undercooled liquid region; Al-2%Cu; t=90s

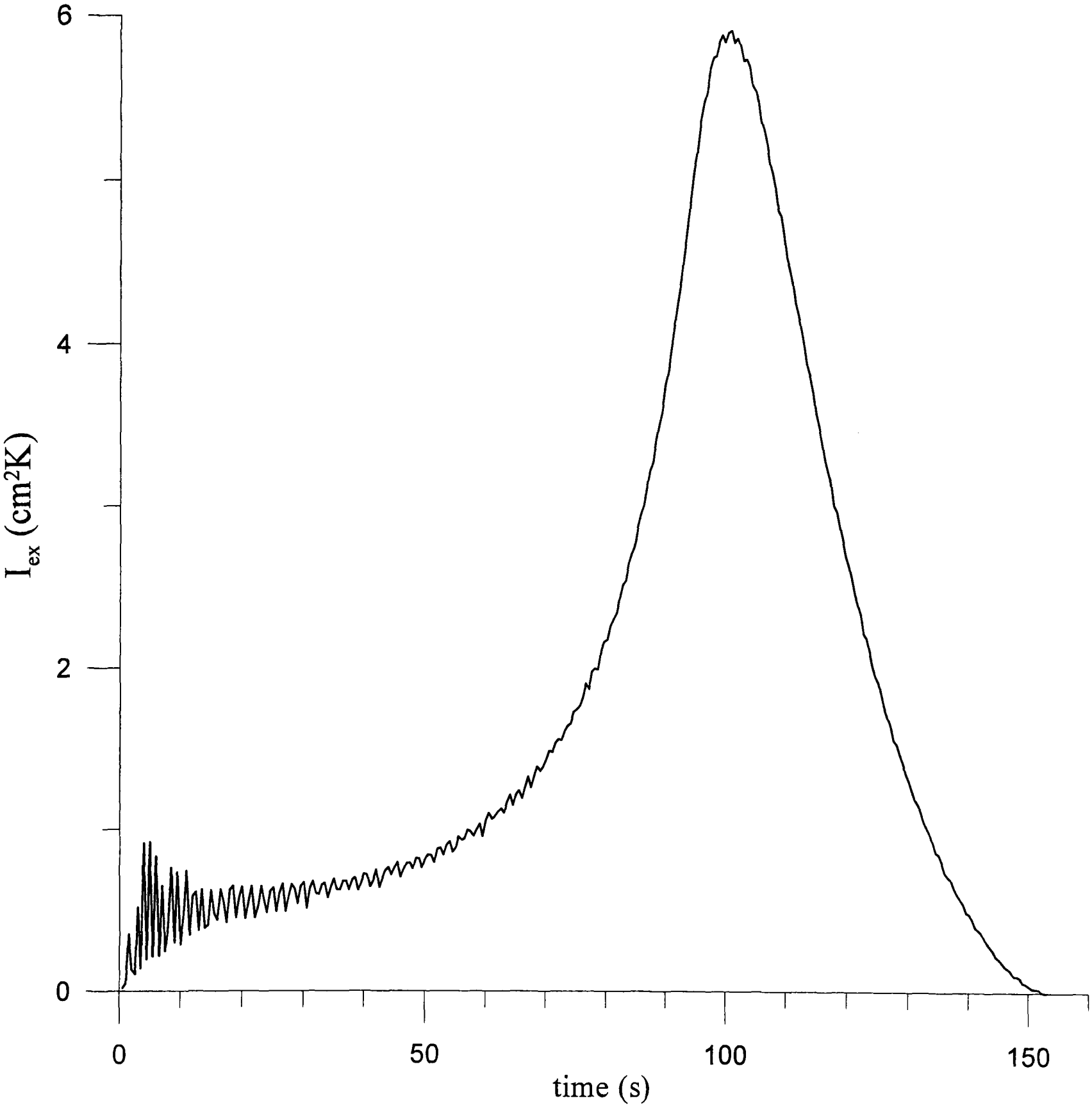

Figure 4.18 Equiaxed index as a function of time; Al-2%Cu, h=0.3 W/cm^2K

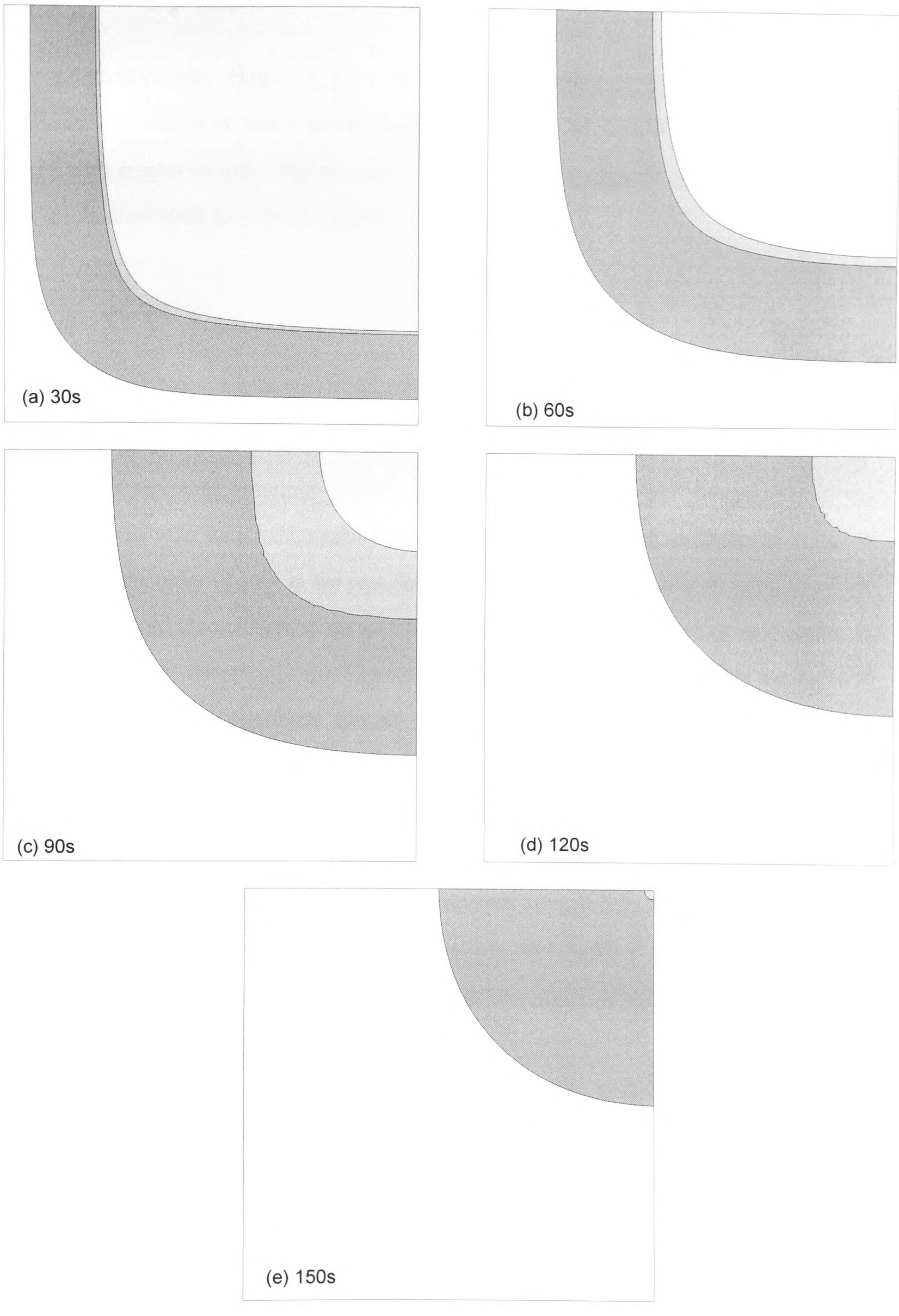

Figure 4.19 Solid (white), mush (dark grey), undercooled liquid (medium grey), and superheated liquid (light grey), at indicated times; Al-2%Cu

for a certain process. However, it would be useful to have a metric to establish *for each process*, the relative tendency to form an equiaxed zone. This could be done by integrating $I_{ex}(t)$ with respect to time. The resultant is the summed equiaxed index for any process p, $I_{ex}^{s}(p)$. In discretised form this becomes

$$I_{ex}^{s}(p) = \sum_{t=1}^{n} \sum_{i=1}^{nrows} \sum_{j=1}^{ncols} U(i,j)\Delta x_j \Delta y_i \Delta t \Big|_{\Delta t=1s} \qquad (4.5)$$

where the summation is taken every second until the end of the process at time $t=n$ seconds. In fact the temporal sampling interval can be varied, but should be consistent across processes p in order for it to be useful for comparative purposes. As the undercooled region is present for the order of 100s in the processes under study here, a 1 s interval is sufficient for such integration. If solidification is rapid, this will shorten the time for which any location is undercooled, thus lowering $I_{ex}^{s}(p)$. The equiaxed grains need time to *grow* after nucleation if they are to present a significant enough volume fraction to impede columnar growth and cause a CET. For the process (call it p_1) in question, $I_{ex}^{s}(p_1)$=269.4 cm^2Ks. This will be compared to the value from other processes in due course. Note that the best way to get information on the formation of the equiaxed zone is to actually model the nucleation and unconstrained growth of solid, and this is covered later in this Chapter. However, the presented technique is a method of ranking processes with regard to their equiaxed potential, without having to consider individual nucleation events, growth and impingement.

Equation (4.3) gives the volume under the undercooling ridge, such as that illustrated in Fig. 4.16. This graphic is produced using *Surfer® 8* software from Golden Software Inc., USA. In this package the area under this surface is calculated by numerical integration as 3.796 cm^2K. The cruder calculation of equation (4.3) used in the current model gives a value of 3.863 cm^2K. The difference is only 1.8%, and this is quite acceptable as the index is relative.

The input data used for the model so far is presented in Sections 4.1 and 4.2. The alloy is Al-2%Cu (wt.% is inferred from here on), and the heat transfer coefficient (h) is 0.3 W/cm^2K. The effects of varying h and alloy concentration C_0 are now investigated. A matrix of numerical experiments with three levels of h (0.15, 0.3 and 0.5 W/cm^2K) and three levels of C_0 (1, 2 and 4 % Cu) was used. From the phase diagram (Fig. 4.1), the liquidus and solidus temperatures of these alloys are presented in Table 4.2, along with the value of C_1, from equations (3.8) and (4.2). It should be noted that the alloys chosen exhibit significantly different freezing ranges.

C_0 (wt.%Cu)	T_L (°C)	T_S (°C)	T_L-T_S (°C)	C_1 (cm/K^2s)
1.0	658	641	17	0.16
2.0	655	614	41	0.08
4.0	650	575	75	0.04

Table 4.2 alloy-specific data

Figure 4.20 shows the plots of $I_{ex}(t)$ for each case. For any particular alloy it can be seen that the peak index, and time for which levels of $I_{ex}(t)$ exceed zero, are greatest for the lowest heat transfer coefficient. Also, the more concentrated alloys have higher peak values of $I_{ex}(t)$, for any given value of h. These peak values are given in Table 4.3.

Composition (wt.%Cu)	h (W/cm^2K)		
	0.15	**0.3**	**0.5**
1.0	5.655	4.571	4.066
2.0	7.047	5.938	5.284
4.0	8.815	7.446	6.752

Table 4.3 - peak values of $I_{ex}(t)$, in cm^2K, for each process

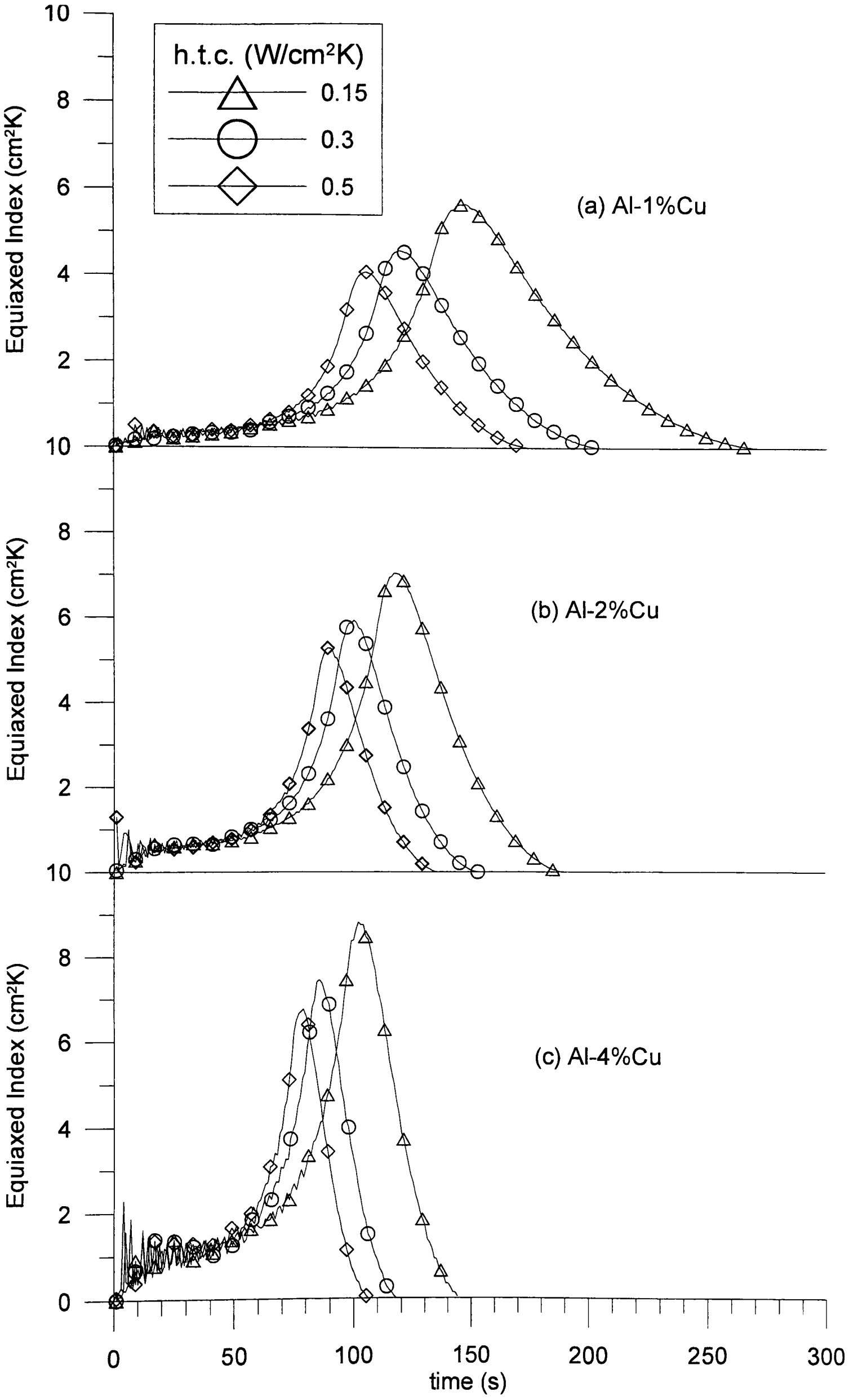

Figure 4.20 Equiaxed index as a function of time for three different alloys

The average front undercooling was calculated every 30 s for each process. The results for each alloy are sufficiently different (the h.t.c. has a smaller effect) to enable all nine plots to be shown, and clearly distinguishable, on one graph (Fig. 4.21). Increasing the solute content in the alloy has a very significant effect on increasing the front undercooling. For a given alloy, raising the rate of heat extraction increases the undercooling of the columnar front, but the effect here is less dramatic.

Composition (wt.%Cu)	**h** (W/cm^2K)		
	0.15	**0.3**	**0.5**
1.0	458.6 (270.1)	275.0 (204.1)	206.4 (174.1)
2.0	394.6 (188.1)	269.4 (152.1)	212.5 (134.1)
4.0	387.8 (144.1)	266.4 (116.9)	220.4 (105.1)

Table 4.4 Value of $I_{ex}^{s}(p)$ for each solidification process, and time (seconds, in brackets) for columnar front to reach the centre of the casting.

The values of $I_{ex}^{s}(p)$, in cm^2Ks for each process are shown in Table 4.4, along with the time taken, (s) in brackets, for the columnar front to reach the centre of the casting. It can be seen that it takes longer for the columnar front of the more pure alloy to reach the centre of the casting. Obviously, this time is reduced at higher h.t.c.s. The reason for the slower arrival of the pure columnar front at the centre is that there is a relatively high fraction solid just behind the front in this case. From the data used to plot Fig. 4.21, for $h=0.3W/cm^2K$, the average front undercooling (°C) is 0.530 (Al-1%Cu), 0.874 (Al-2%Cu) and 1.390 (Al-4%Cu). But the more dilute alloys have a lower freezing range (Table 4.2), and the average fraction solid

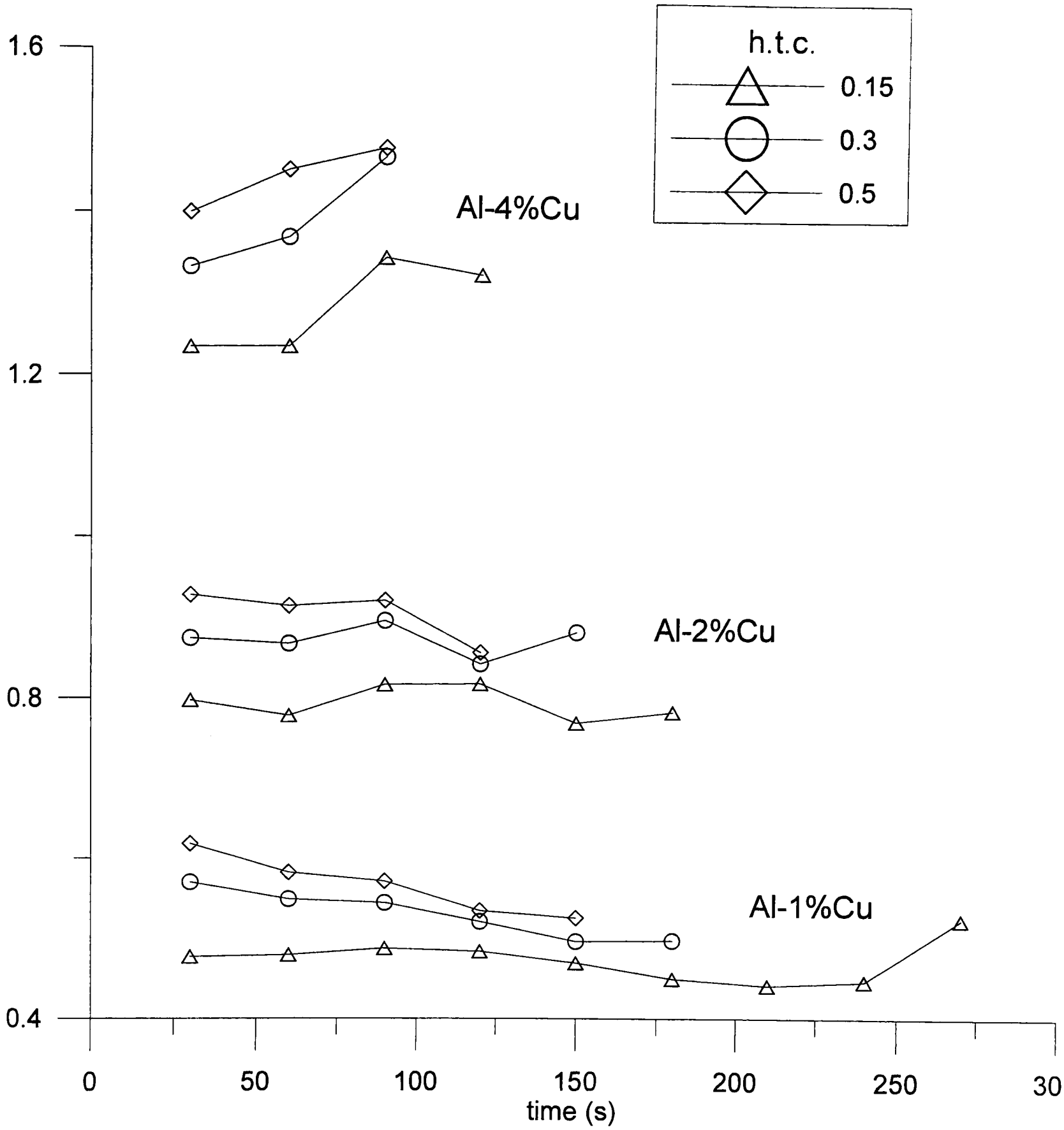

Fugure 4.21 Average front undercooling as a function of time for three different alloys

(equation (3.14)) at the columnar front of these alloys is 0.031, 0.021 and 0.018, respectively. These differences are quite small, but cause a significant positional shift in the columnar front due to the very small thermal gradients in these regions. Fig. 4.22 shows the temperature profile along the half-diagonal from the mould corner to its centre, at various times, for an Al-2%Cu alloy with h=0.3 W/cm^{2}K. The result of this is that the Al-4%Cu has the lowest values of $I_{ex}^{s}(p)$. If this were used as a metric for equiaxed solidification then the conclusions would be opposite to those of peak values of $I_{ex}(t)$. For both metrics, lower h.t.c.s favour equiaxed growth. However, as outlined in Section 1.7, one would expect that higher levels of solute would favour the formation of the equiaxed zone. As such, the peak values of $I_{ex}(t)$ would seem a better indicator for equiaxed solidification. The values of $I_{ex}^{s}(p)$ are too sensitive to the effect of the fraction solid at the front, described above, and the linear variation of this in the freezing range (equation (3.14)) is in any case an over-simplification.

Figure 4.23 shows, for Al-2%Cu and h=0.3 W/cm^{2}K, the variation with time of the front position along the half-diagonal line and its temperature. From pairs of (position, temperature) at fixed times, taken from Fig. 4.23, the front location can be superimposed on the curves of Fig. 4.22 - see Fig. 4.24. The latter is drawn at higher temperature resolution, and without the markers indicating the times, thus making the front position more visible. It is very clear that the thermal gradient reduces beyond the front, and becomes very flat towards the end of solidification.

4.3.3 Verification and testing of model

It is not possible to validate this model with an experiment, due to the effects of convection (discussed in Section 1.8). Details of a solidification experiment, which serves to illustrate this point, are presented in Section 4.5. However, as the model presented here is novel, some form of benchmark test is required. To this end, the results were compared to those predicted by an enthalpy method (see Section 2.1.2) model. This fully implicit model [181,182] was implemented on a 100 x 100 control volume finite difference grid. Using the same data as was used to generate Figures 4.22 and 4.23, the predictions of the enthalpy model are

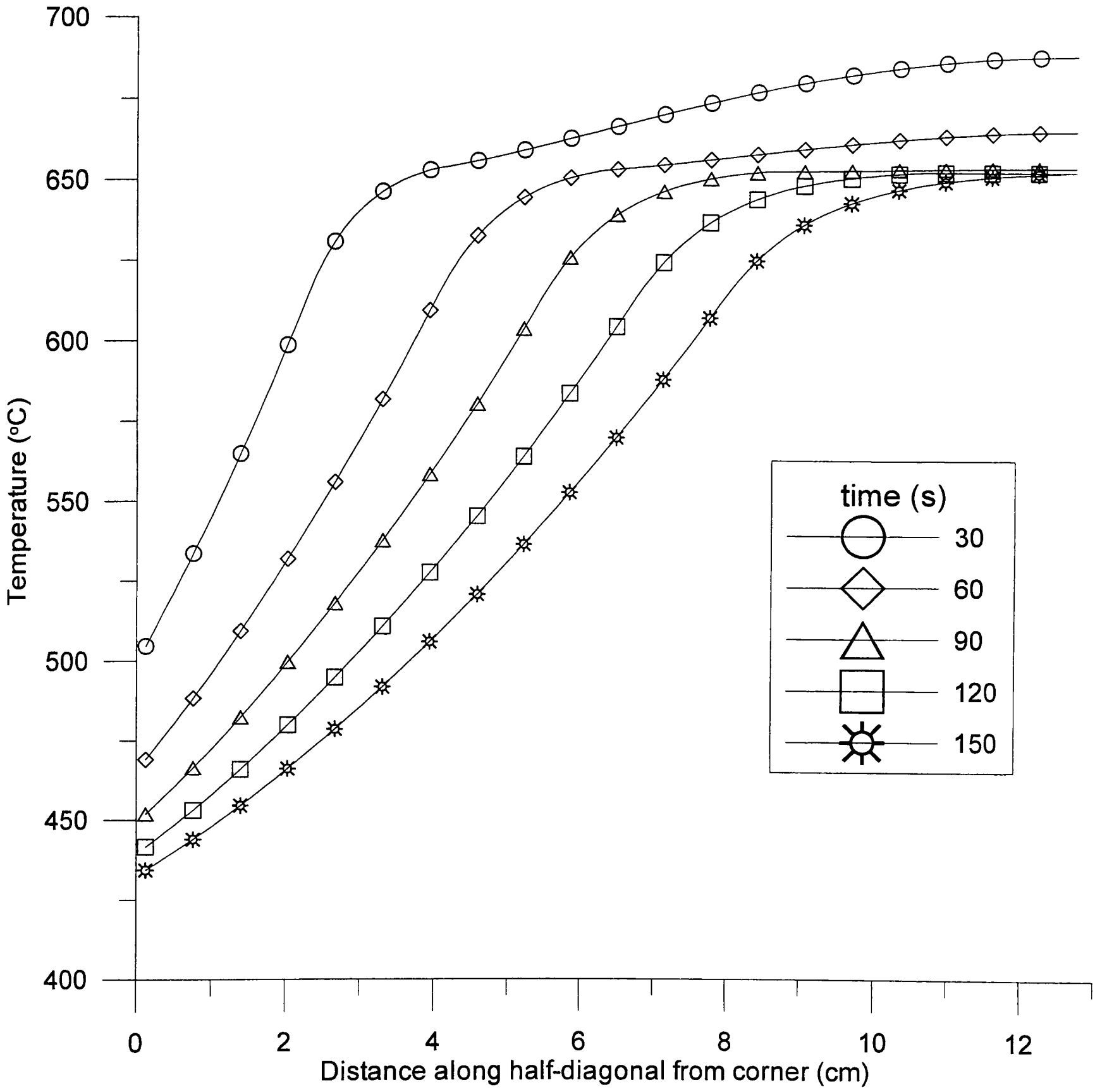

Figure 4.22 Thermal profile along half-diagonal from mould corner to centre of casting; Al-2%Cu; h=0.3 W/cm^{2}K

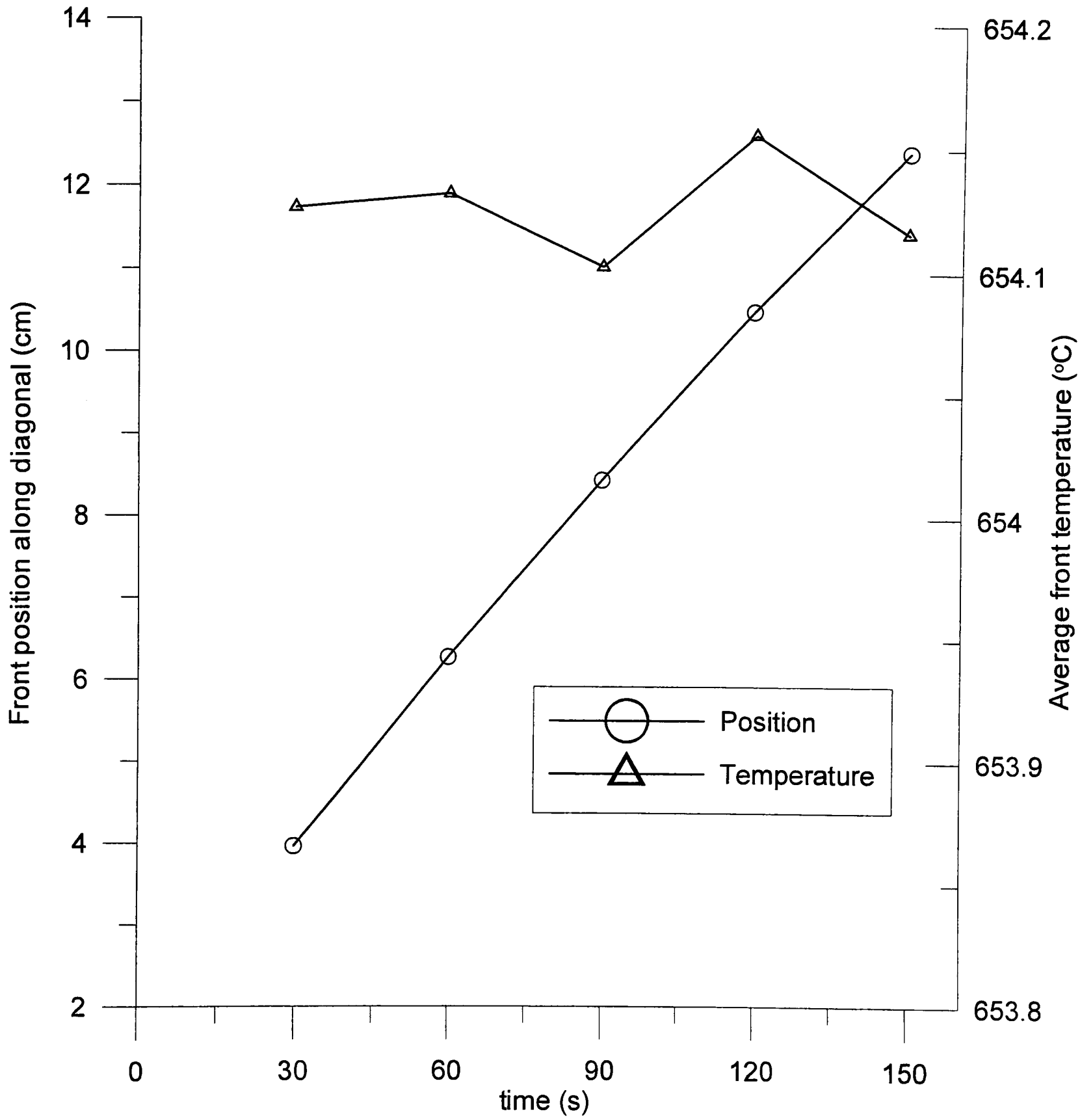

Figure 4.23 Variation of front temperature, and position along half-diagonal, with time; Al-2%Cu; h=0.3 W/cm²K

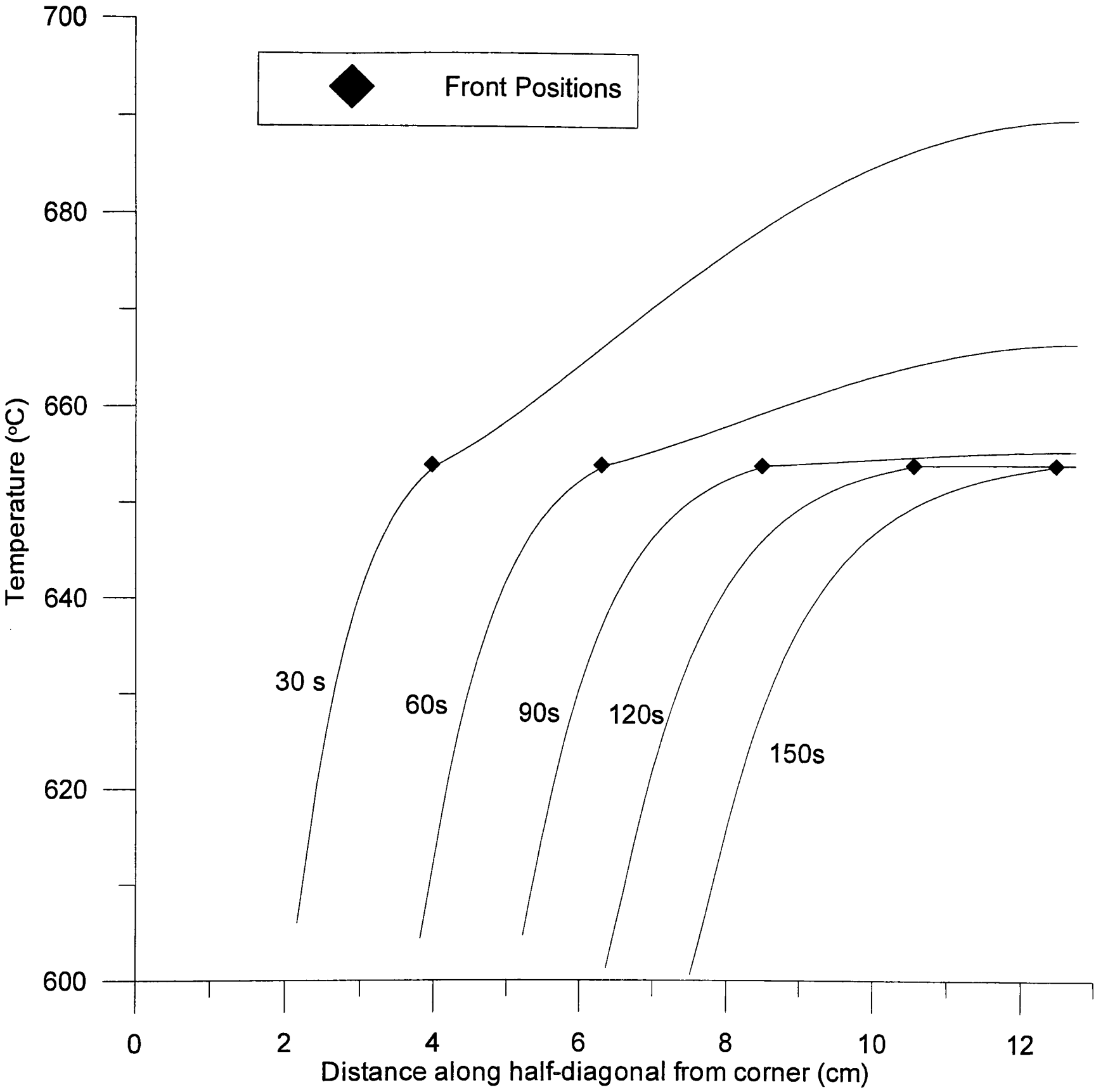

Figure 4.24 Front position and thermal profile along half-diagonal from mould corner to centre of casting, at various times

compared with those of the front-tracking one, in Figures 4.25 and 4.26. In Fig. 4.25 it can be seen that the thermal data along the mould half-diagonal is very similar for both models, throughout solidification. Fig. 4.26 shows the advance of the front (front-tracking model) plus the advance of the 655°C (liquidus) and 654.1°C isotherms along the diagonal. From Fig. 4.23 it can be seen that the temperature of the tracked front is about 654.1°C, and Fig. 4.26 shows that the plots of the advance of the front position and the enthalpy prediction of the 654.1°C isotherm match very closely. As expected, the liquidus isotherm reaches the centre of the casting ahead of the cooler isotherm, and the spatial divergence between the two increases towards the end of solidification where, as illustrated in Fig. 4.25, the thermal gradient gets much smaller.

Professor Jerzy Banaszek, Institute of Heat Engineering, Warsaw University of Technology, kindly provided the enthalpy method predictions. Although Figs. 4.25 and 4.26 provide verification of the front-tracking model via comparison with a well-established numerical technique, the closeness of the results should not hide the superiority of the new interface-tracking approach. For example, the enthalpy method cannot provide predictions of undercooled liquid, nor of equiaxed nucleation and growth (see next Section), and so is not capable of predicting a CET.

Grid refinement analysis was also carried out to establish that, on continuous refinement of the computational grid, the new model's predictions converge. Using the same data as was used for verification of the model, the first check was on the position of the columnar front, at 120s. As it has been shown that at this time the thermal gradients in the system are quite low, this is a severe test of the model. The results of this analysis are presented in Fig. 4.27(a). This shows that the variation of the grid density from 30 x 30 to 50 x 50 and then to 100 x 100 does have a small effect on the predicted front position. However, further increasing the density to 150 x150 has little effect upon the front. This graph is printed at very high spatial resolution, so the distances between the different front predictions are very small. As the model output converges at the 100 x 100 resolution, this is the optimum

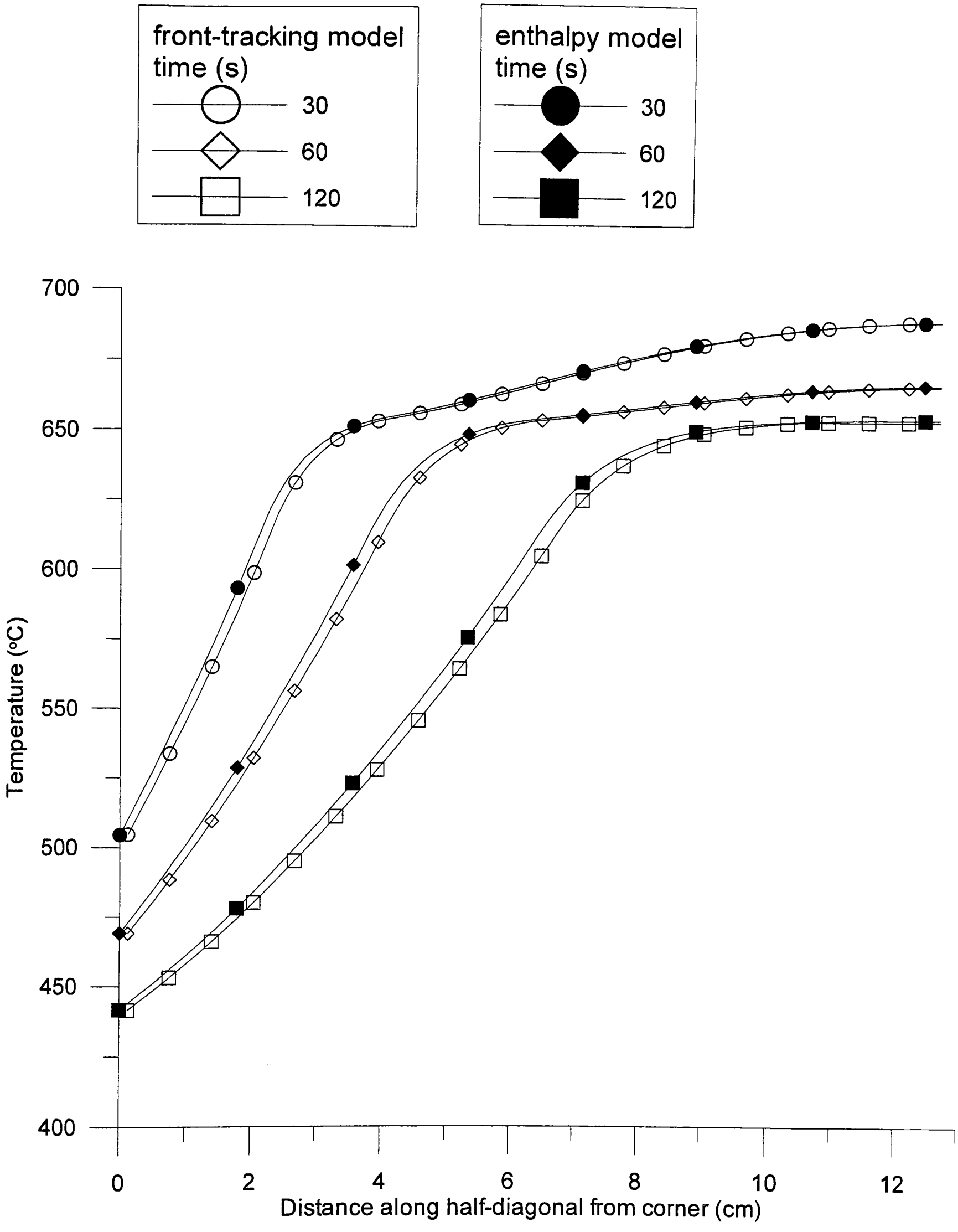

Figure 4.25 Comparison of predicted thermal profiles : front-tracking and enthalpy method

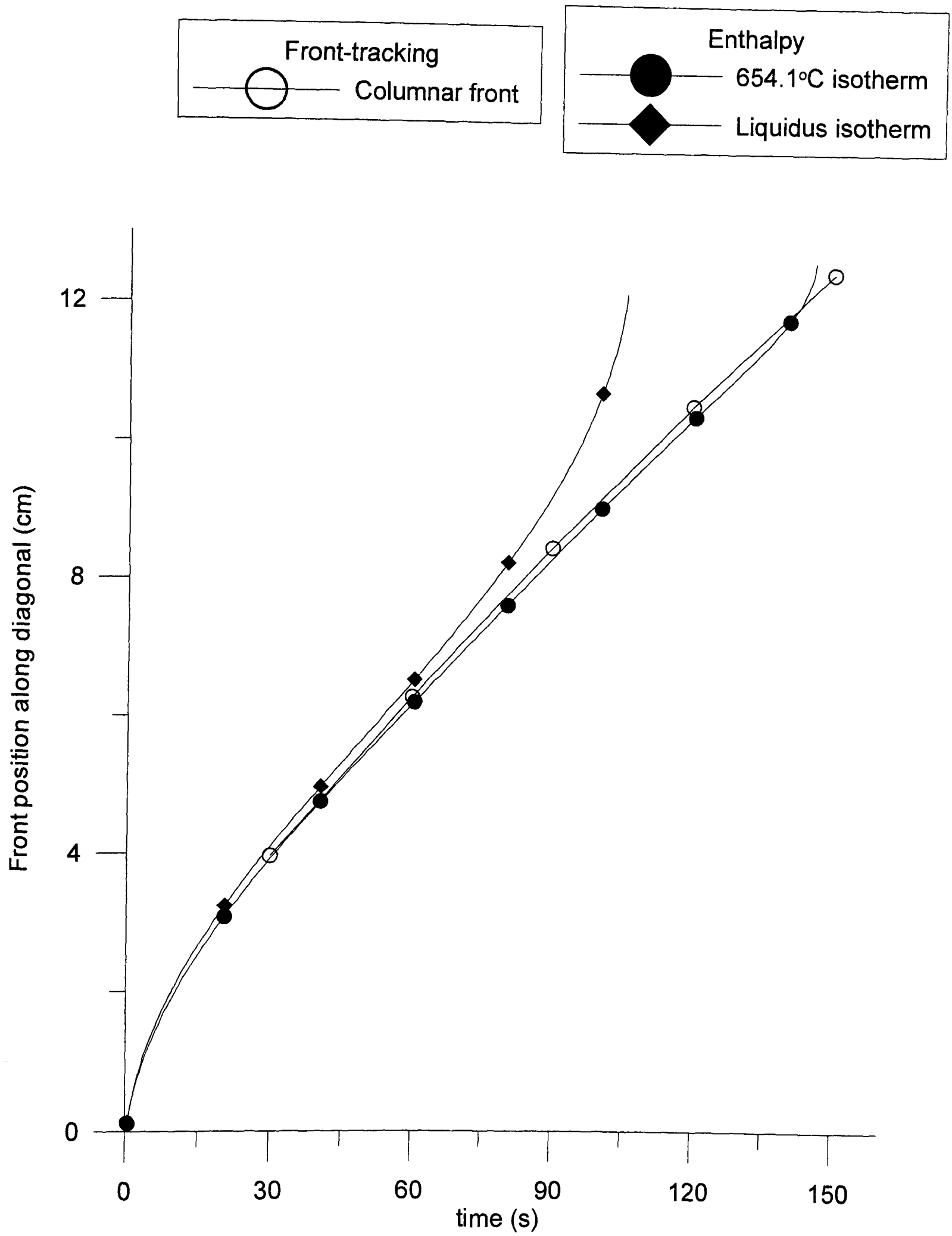

Figure 4.26 Advance of enthalpy model isotherms and tracked columnar front across the mould half-diagonal; Al-2%Cu

computational resolution to use. A denser grid consumes computational resources, with no attendant improvement in accuracy. In addition, the temperature along the casting half-diagonal was also plotted using three different grid densities (Fig. 4.27(b)). Very little difference in these predicted thermal profiles can be distinguished.

4.4 Equiaxed Solidification

4.4.1 Single grain

In order to test the equiaxed model, a single site for potential nucleation was placed in the domain. Again, this is a 18 x 18 cm mould, represented by its lower left quadrant. The alloy was Al-2%Cu in an isothermal (400°C) mould. The equiaxed nucleation undercooling (ΔT_{nuc}^{ex}) was chosen to be 0.4°C. This is somewhat arbitrary, but one can expect a low value if these sites are embryonic crystals e.g. from "big bang" or dendrite detachment sources. Also, in Section 4.3 it was shown that the columnar front undercooling is of the order of 1°C (Fig. 4.21), so at this value of ΔT_{nuc}^{ex}, activation ahead of the columnar front could occur. The value of ΔT_{nuc}^{ex} is kept constant during this study. With a 100 x 100 computational grid there are 10,000 sites from which to chose, each 0.9 mm apart in either the horizontal or vertical direction. In order to have initial growth in a relatively low thermal gradient, a low pour temperature (T_a=675°C) and heat transfer coefficient (h=0.05 W/cm^{2}K) were used, and the site was chosen quite close to the centre of the casting, in control volume (90,80), which represents x = 8.1cm, y = 7.2 cm. Columnar growth was disabled by setting the undercooling for columnar nucleation artificially high (ΔT_n=400°C). The computational time step was again 0.00575s.

Site nucleation occurred after 55.982 s. The initial growth is to the north, south, east and west of the nucleus, as described in Section 3.7.1. The growth of the grain during the first 9 time steps is illustrated in Fig. 4.28. The grain diagonal is still just 16 μm, having being growing

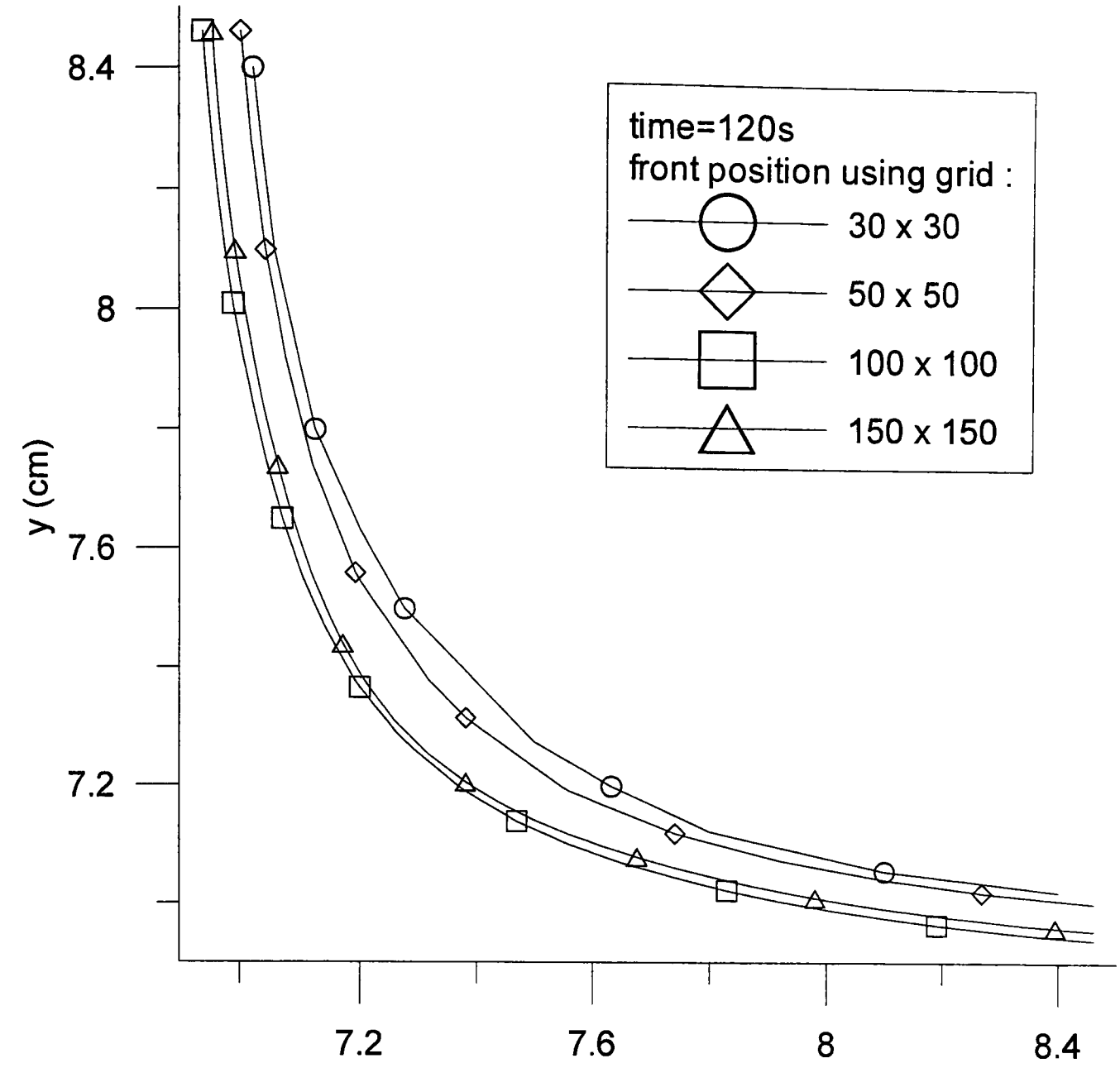

Figure 4.27(a) Grid refinement study - front position; Al-2%Cu, h=0.3 W/cm^{2}K

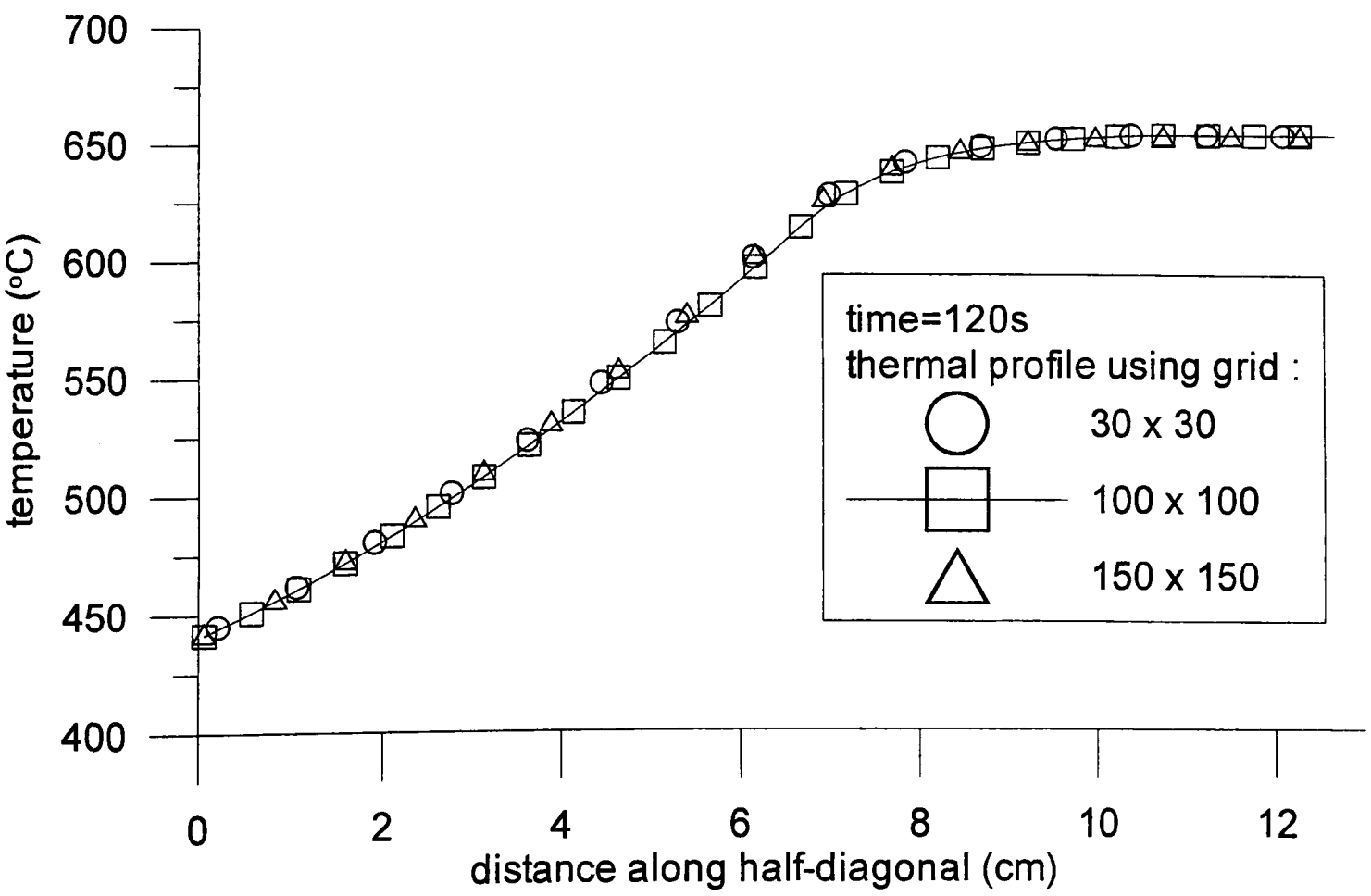

Figure 4.27(b) Grid refinement study - thermal gradient along diagonal; Al-2%Cu, h=0.3 W/cm^{2}K

for only 0.05175 s. It is still within the four control volumes surrounding its origin, and so there are only 4 identifying markers. These are practically all at the same temperature, and so the grain is essentially an isotropic diamond. Fig. 4.29 shows the grain boundary every 0.5 s after nucleation, superimposed on the computational grid. The points represent the intersections with the fixed grid. The increasing grain anisotropy due to the thermal gradient is obvious. After 1.5 s of growth, the grain has crossed the control volume faces to the west and south of the nucleus. This should be compared to the schematic of Fig. 3.18 - growth behaviour is qualitatively as expected.

The grain continues to grow, its boundary being mapped every second after nucleation in Fig. 4.30. The increasing anisotropy is due to the thermal gradient. The grain is advancing most rapidly to the south i.e. into the coolest liquid. Its growth towards the relatively hot centre of the casting is very slow. The grain boundary is represented by 86 markers (not shown) 6 s after nucleation. These markers *are* shown in Fig. 4.31, which is a bubble chart - the diameter of the circle at each marker indicating its relative undercooling. The maximum boundary undercooling (3.78°C) is obviously at the bottom of the grain. The minimum marker undercooling (0.97°C) is at the upper right of the grain. The mean boundary marker undercooling is 1.72 °C. These figures compare with values of between 1 and 4°C predicted by a simpler, one-dimensional, model of equiaxed growth in solidifying aluminium alloys [125]. A thermal map of this area at the same time (61.97925s) is shown in Fig. 4.32. The effect of the local release of latent heat of fusion can be seen, especially in the area where the grain is growing fastest. The effect on distortion of local isotherms can be seen in Fig. 4.33; here the entire domain is illustrated. A cooling curve at the position of grain nucleation (Fig. 4.34) clearly shows the local recalescence. This should be compared to a typical cooling curve (Fig. 4.10) in columnar solidification. The acceleration of certain parts of the grain is due to its growth into increasingly undercooled liquid. This is illustrated in Fig 4.35, which is a 3D plot of undercooling in the domain. The depression near the centre of the casting represents the footprint of the hotter grain. Of course such a situation is highly unlikely to occur in reality.

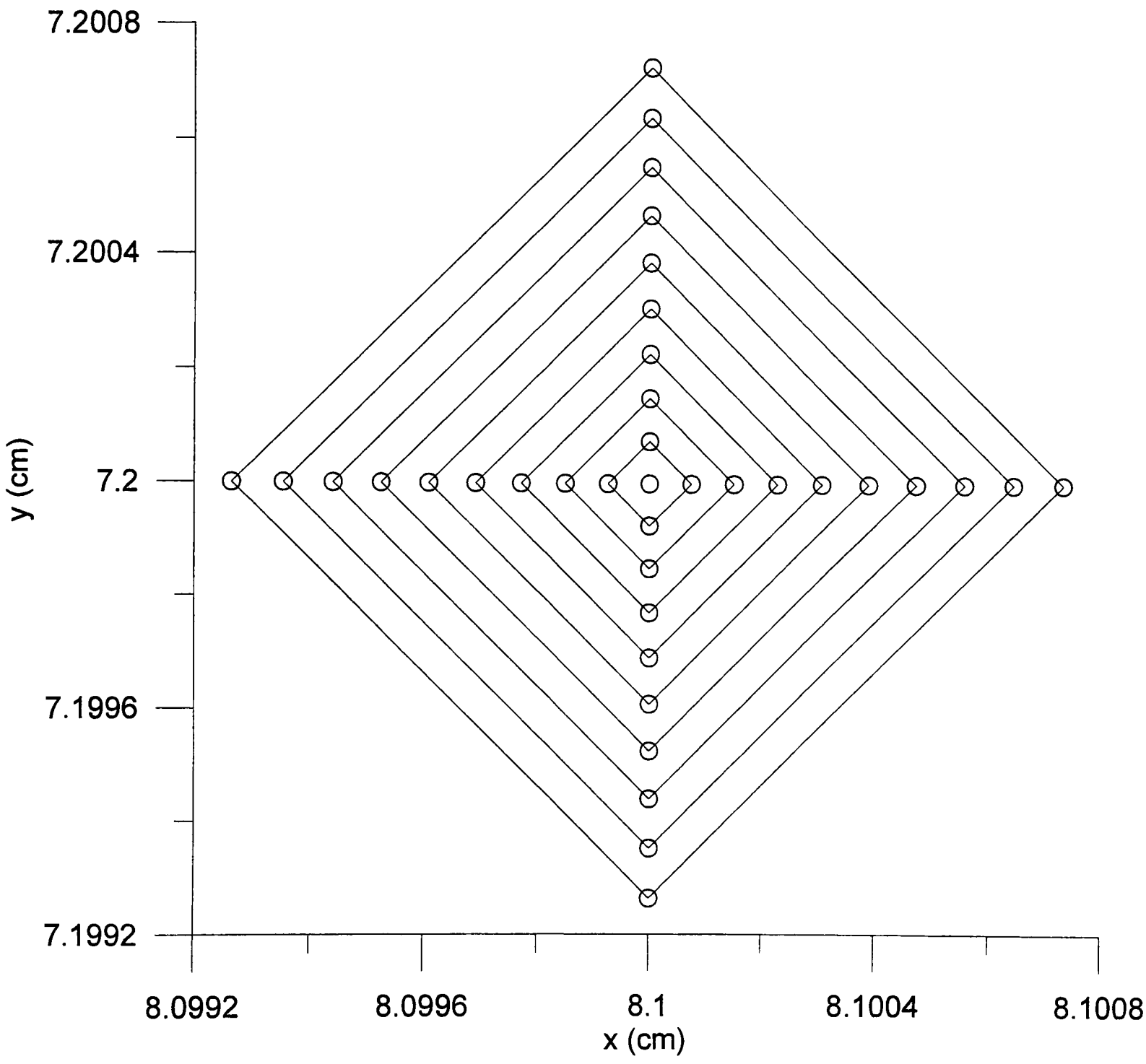

Figure 4.28 Initial growth of single equiaxed grain, showing central nucleus and grain boundary position for the first 9 time steps after nucleation; Al-2%Cu; h=0.05 W/cm^{2}K, T_a=675^{o}C

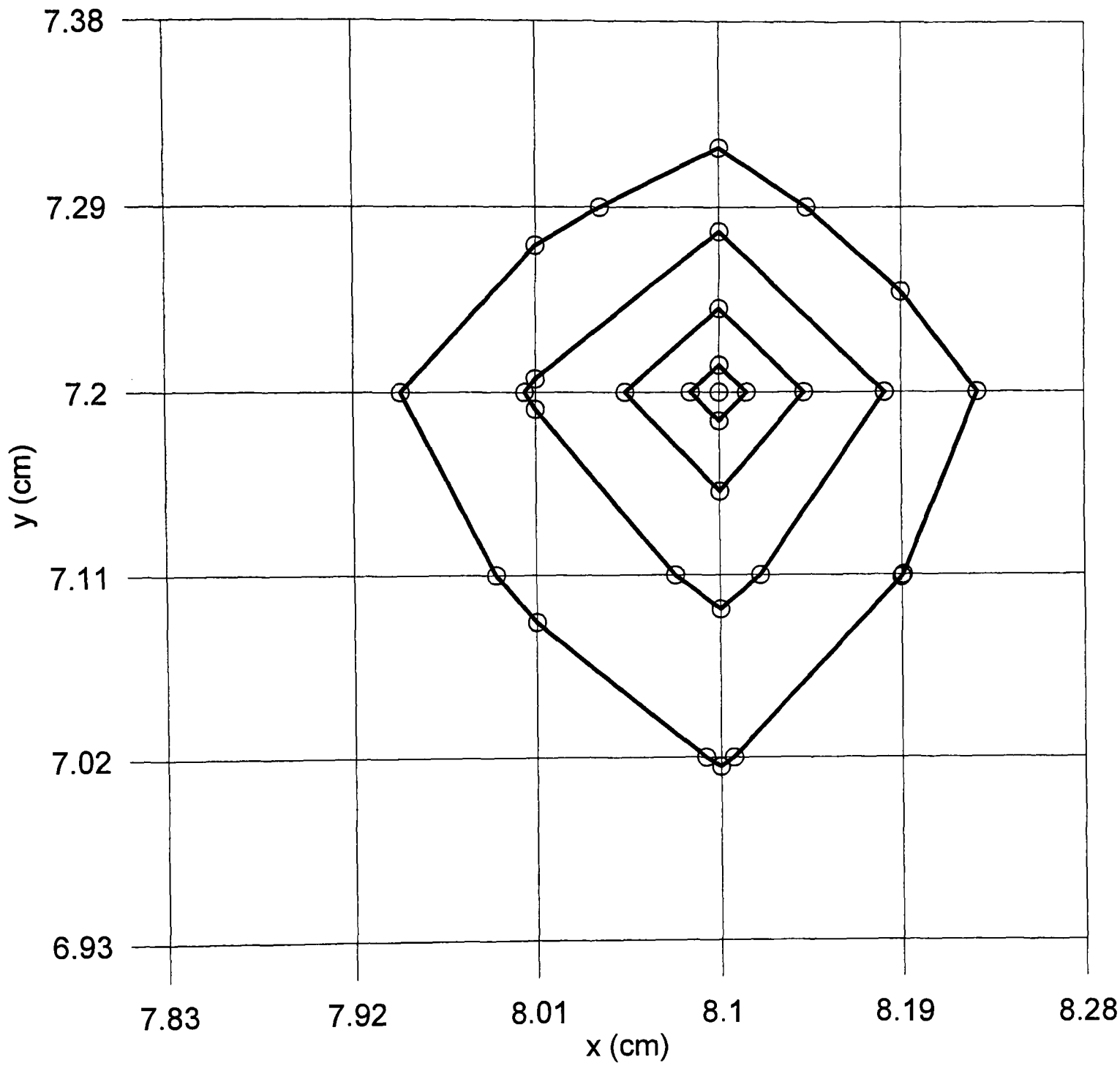

Figure 4.29 Grain boundary position every 0.5 s after nucleation; Al-2%Cu; h=0.05 W/cm^{2}K; T_a=675^{o}C

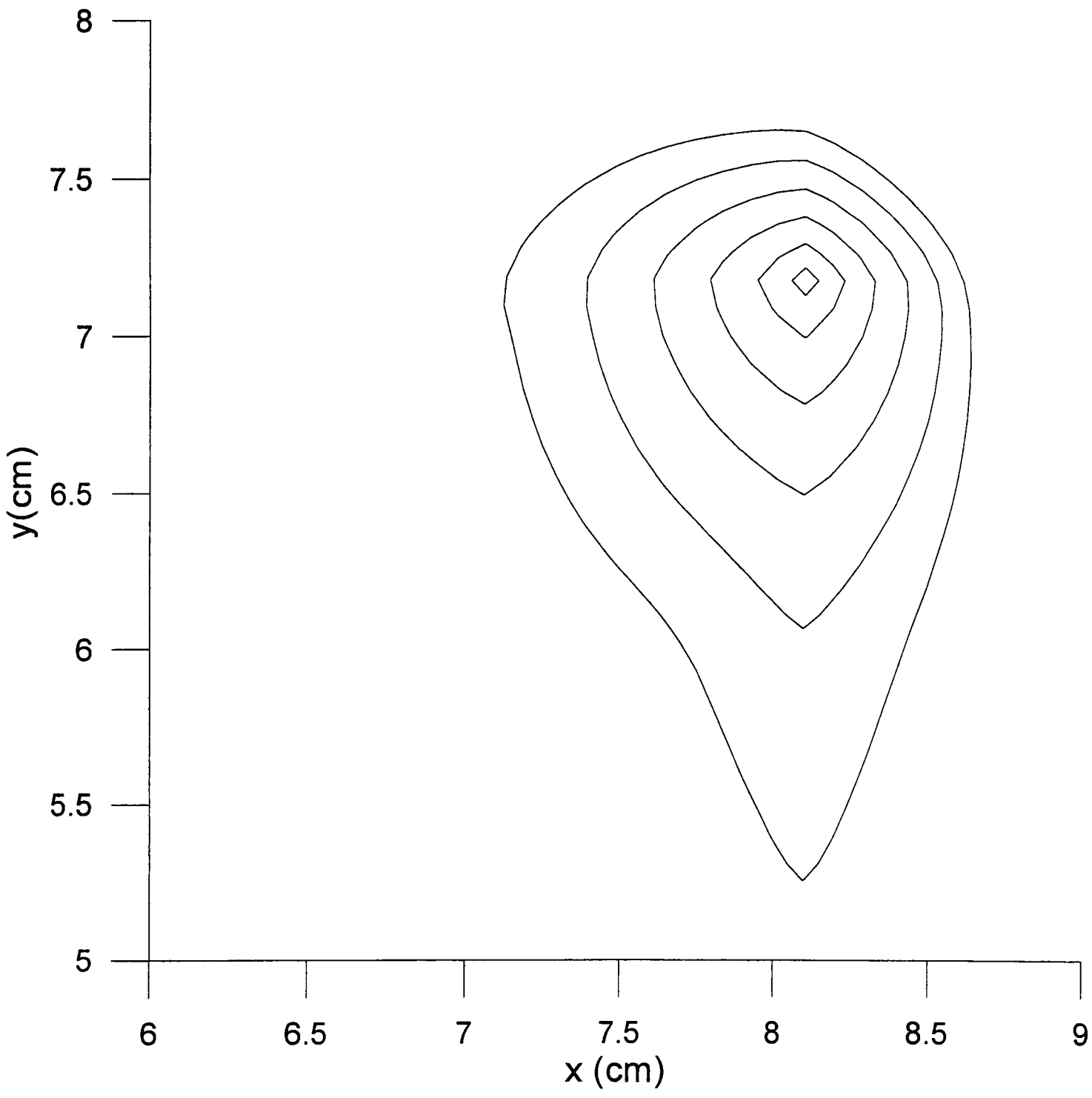

Figure 4.30 Grain boundary position every 1 s after nucleation; Al-2%Cu; h=0.05 W/cm^{2}K; T_a=675°C

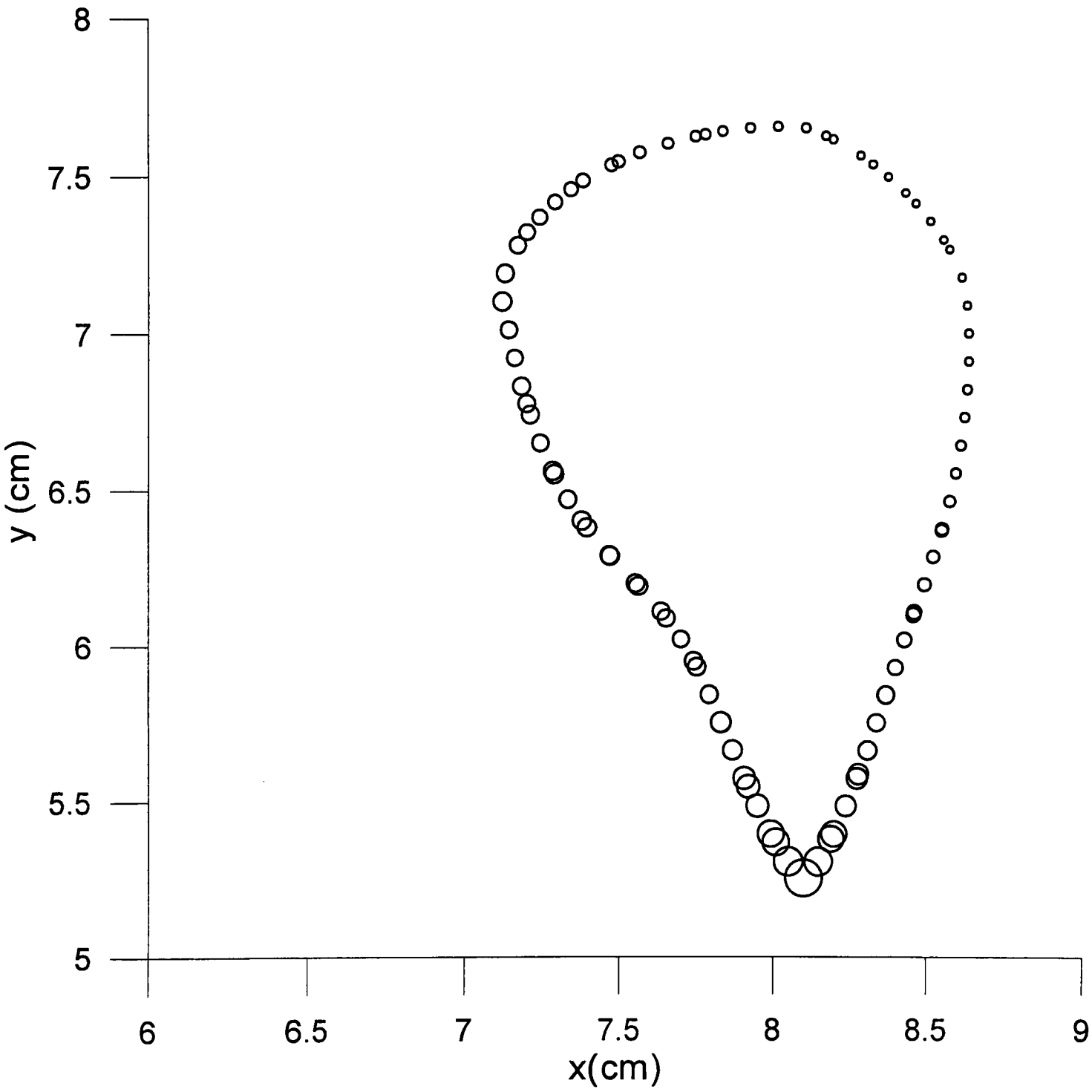

Figure 4.31 Bubble chart showing grain boundary marker positions 6 s after nucleation (t=61.97925 s); bubble diameter indicates marker undercooling : maximum 3.78°C, minimum 0.97°C; Al-2%Cu; h=0.05 W/cm^{2}K; T_a=675°C

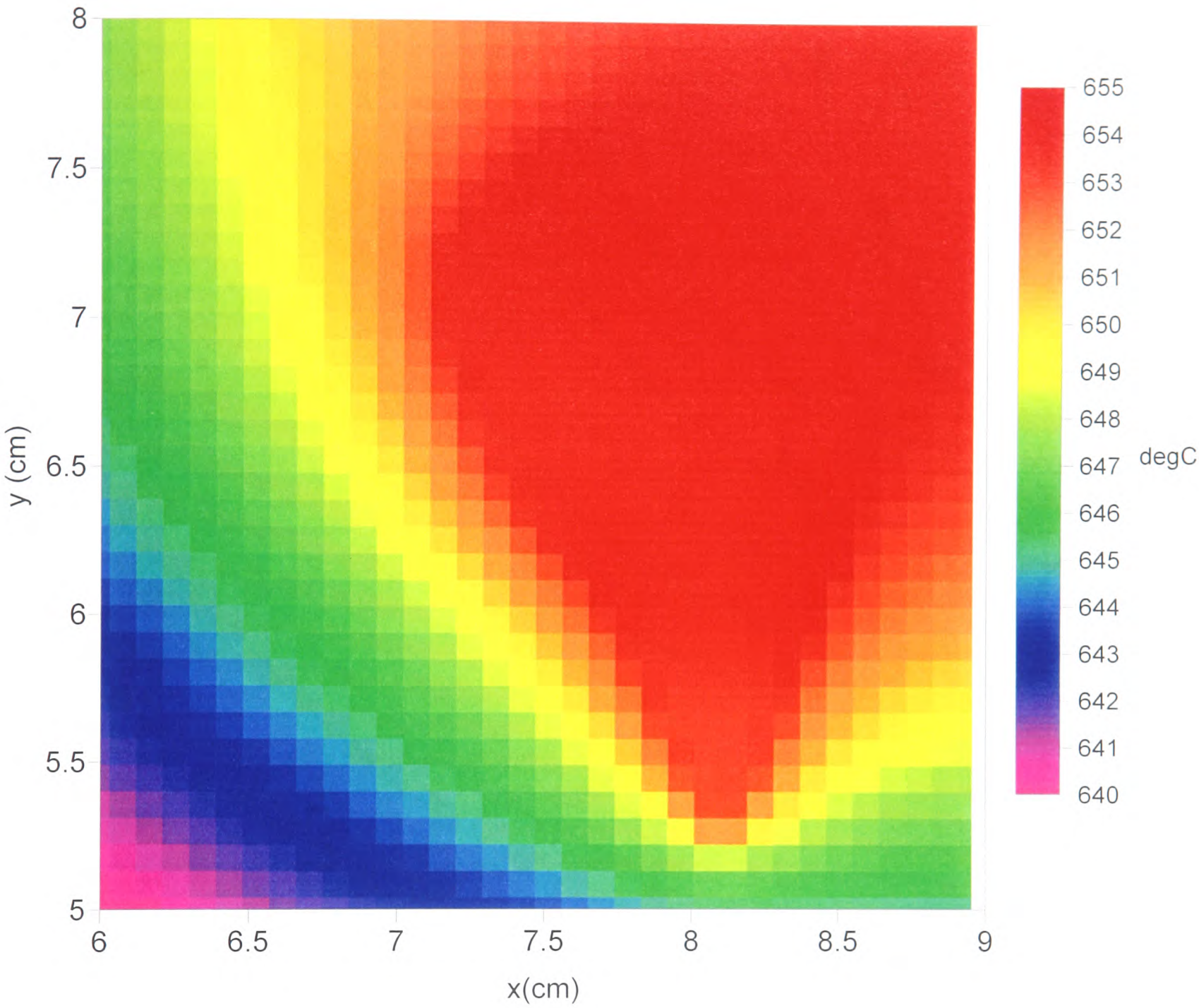

Figure 4.32 Thermal field, t=61.97925 s, showing recalescence due to equiaxed grain growth

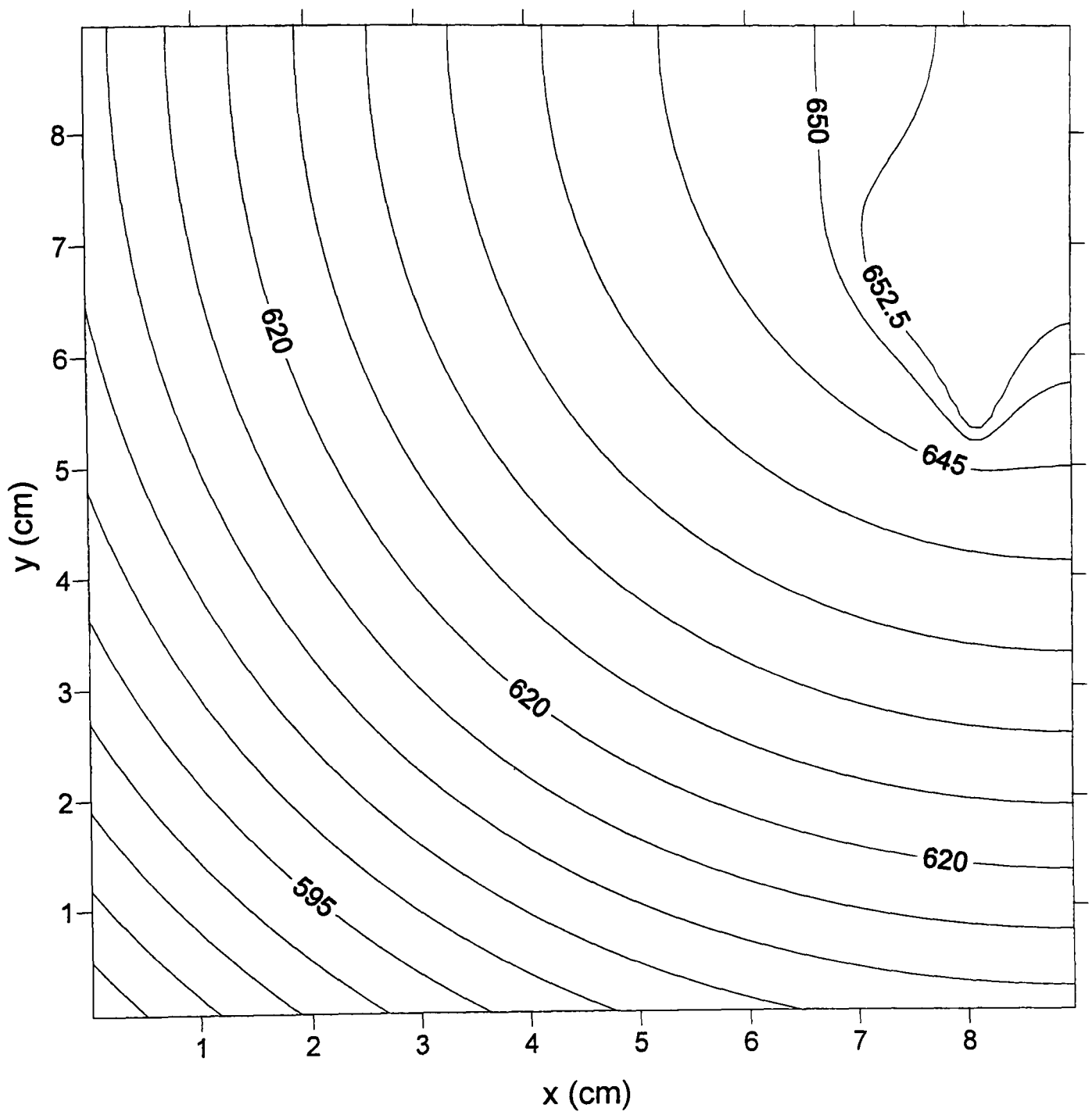

Figure 4.33 Thermal contour plot; Al-2%Cu; t=61.97925 s; equiaxed nucleus at (8.1,7.2) cm

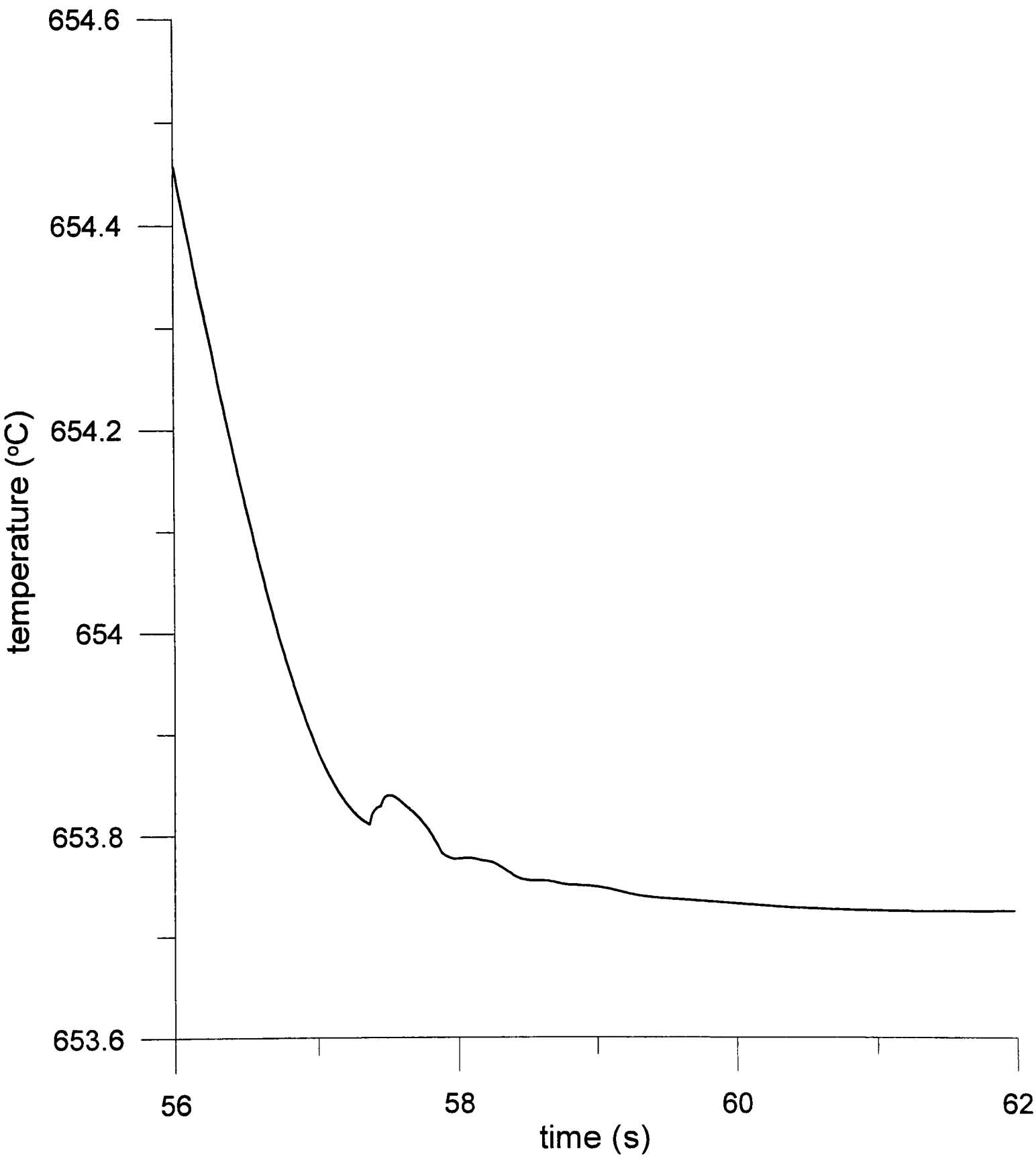

Figure 4.34 Cooling curve - T(90,80) i.e. grain nucleation point; Al-2%Cu

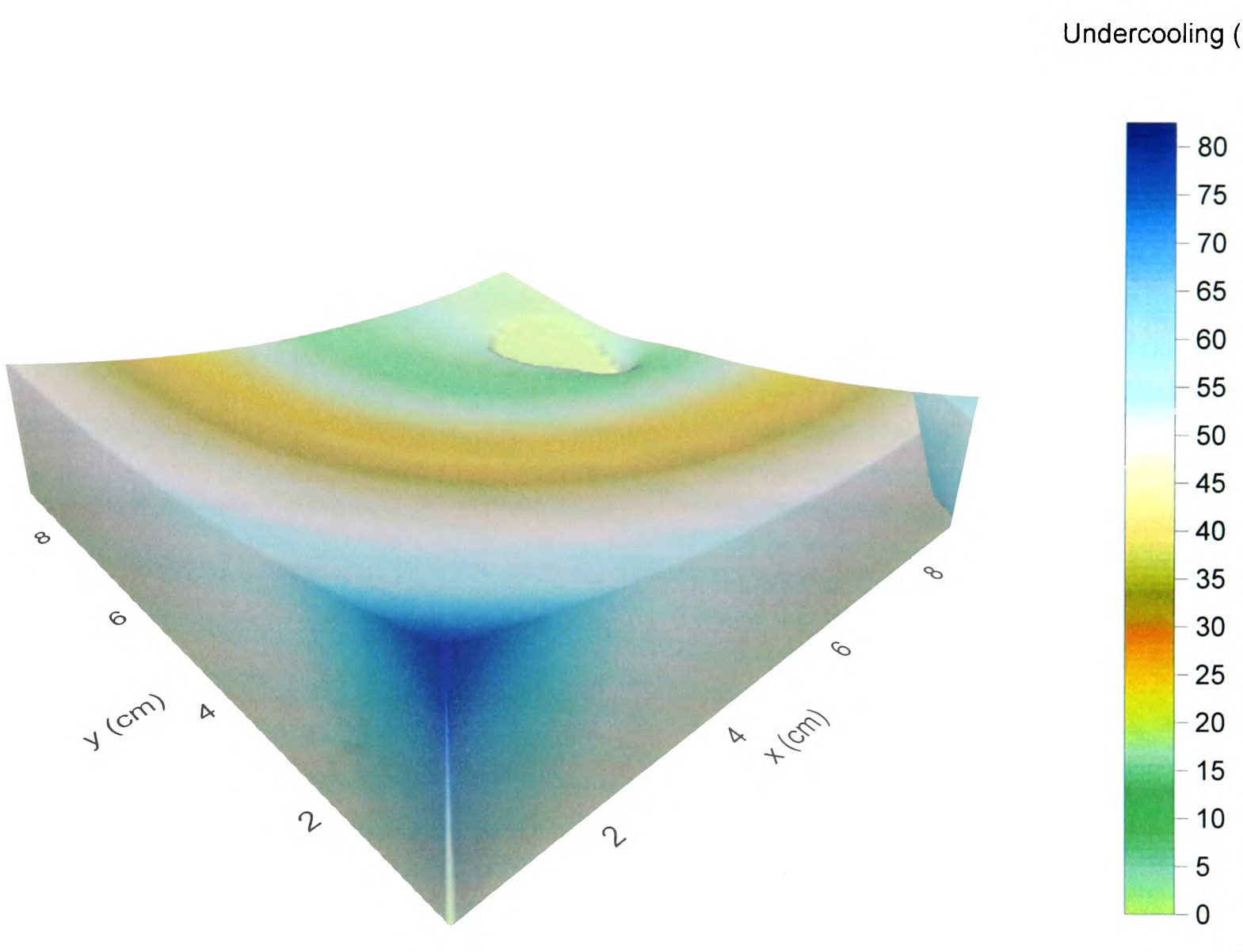

Figure 4.35 Liquid undercooling; Al-2%Cu; t=61.9725 s

The model can be used to study the effects of variables such as heat extraction rate, initial superheat, and nucleation location on the shape of the growing grain.

First of all, the heat transfer coefficient was increased, to a value of 0.15 W/cm^2K. As expected, nucleation occurred earlier - after 36.271 s. The grain boundary 1, 2 and 3 s after this nucleation is illustrated in Fig. 4.36(a). This should be compared with the equivalent results for the lower h.t.c. in Fig. 4.30. With the greater rate of heat loss to the mould, the grain grows more rapidly into the area of highly undercooled liquid; it becomes elongated much more quickly. In fact, as it is growing into increasingly undercooled liquid, the growth becomes unstable, and 3.5995 s after nucleation, the program crashes. At this time the grain boundary is as shown in Fig. 4.36(b). Comparison with Fig. 4.36(a) -it is drawn at the same scale- illustrates the rapid acceleration in growth southwards. The instabilities are reminiscent of the onset of (thermal) dendritic growth, although this model is not intended to capture this effect - the boundary is not a solid-liquid interface. And, unlike microscopic models of dendritic growth, there is no surface-energy damping of instabilities in this model. The grain boundaries shown so far are drawn from the revised position of the front markers, calculated by the intersection routine (indicated by square points in Fig. 3.7). This routine has broken down due to these instabilities, giving the output shown in Fig. 4.36(b). The position of the advanced markers (like those indicated by stars in Fig. 3.7) used to *generate* the intersection points at the same time, are shown in Fig. 4.36(c), at greater resolution (truncating the grain). The prediction is one of the initiation of side-branching. In practical situations, even if a lone grain could grow so deeply into undercooled liquid, such highly anisotropic growth may not occur, as the grain may rotate during solidification due to liquid convection.

With the h.t.c. reset to 0.05 W/cm^2K, the initial temperature was set to 656°C, representing a superheat of just 1°C. In this case nucleation occurred even earlier than the case above with enhanced heat extraction - after 20.24575 s. The growth of the grain every second after this is shown in Fig 4.37. In comparison to the previous conditions (Fig. 4.30 and Fig. 4.36), growth

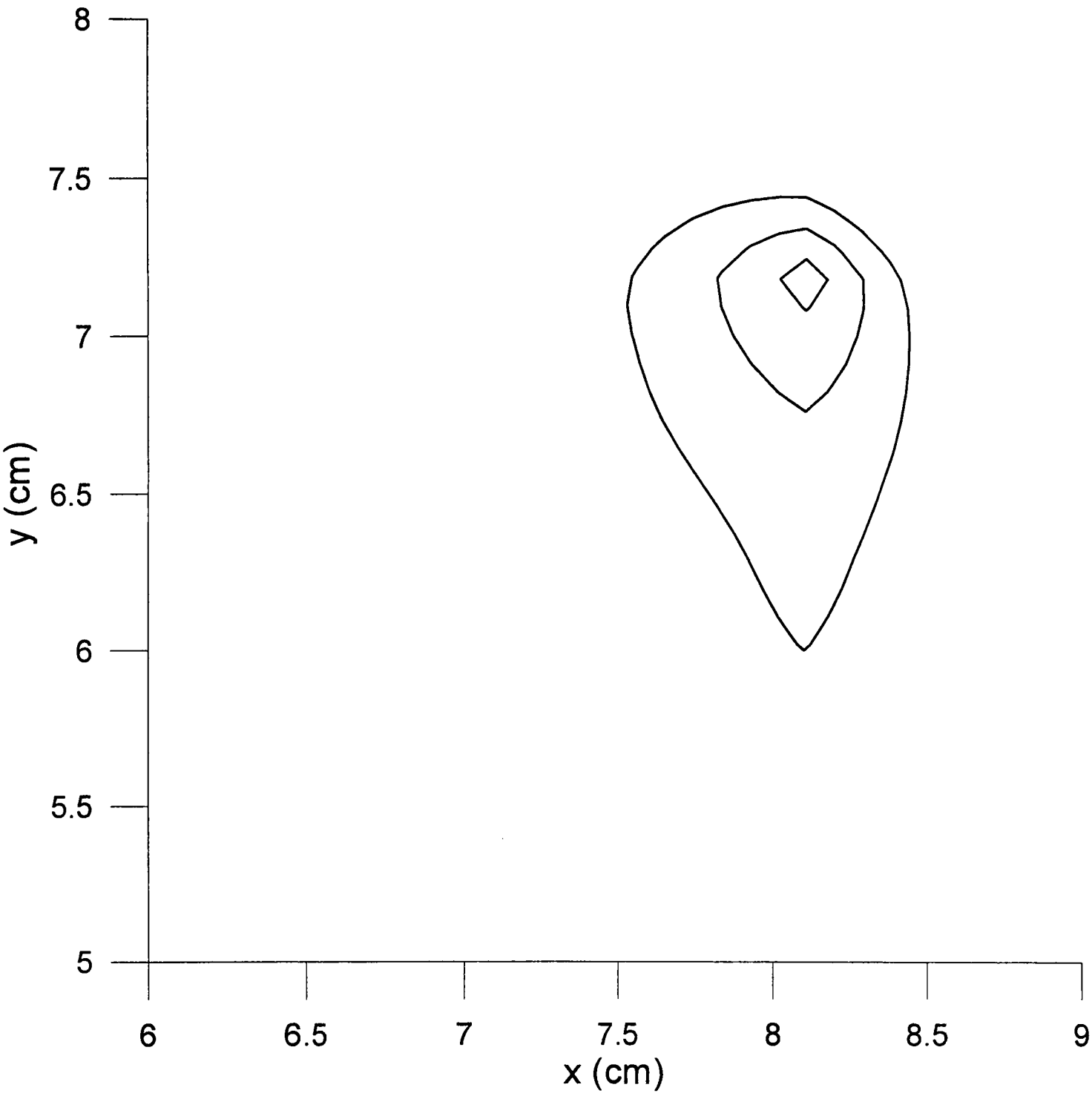

Figure 4.36(a) Grain boundary position every 1 s after nucleation; Al-2%Cu; h=0.15 W/cm^{2}K; T_a=675°C

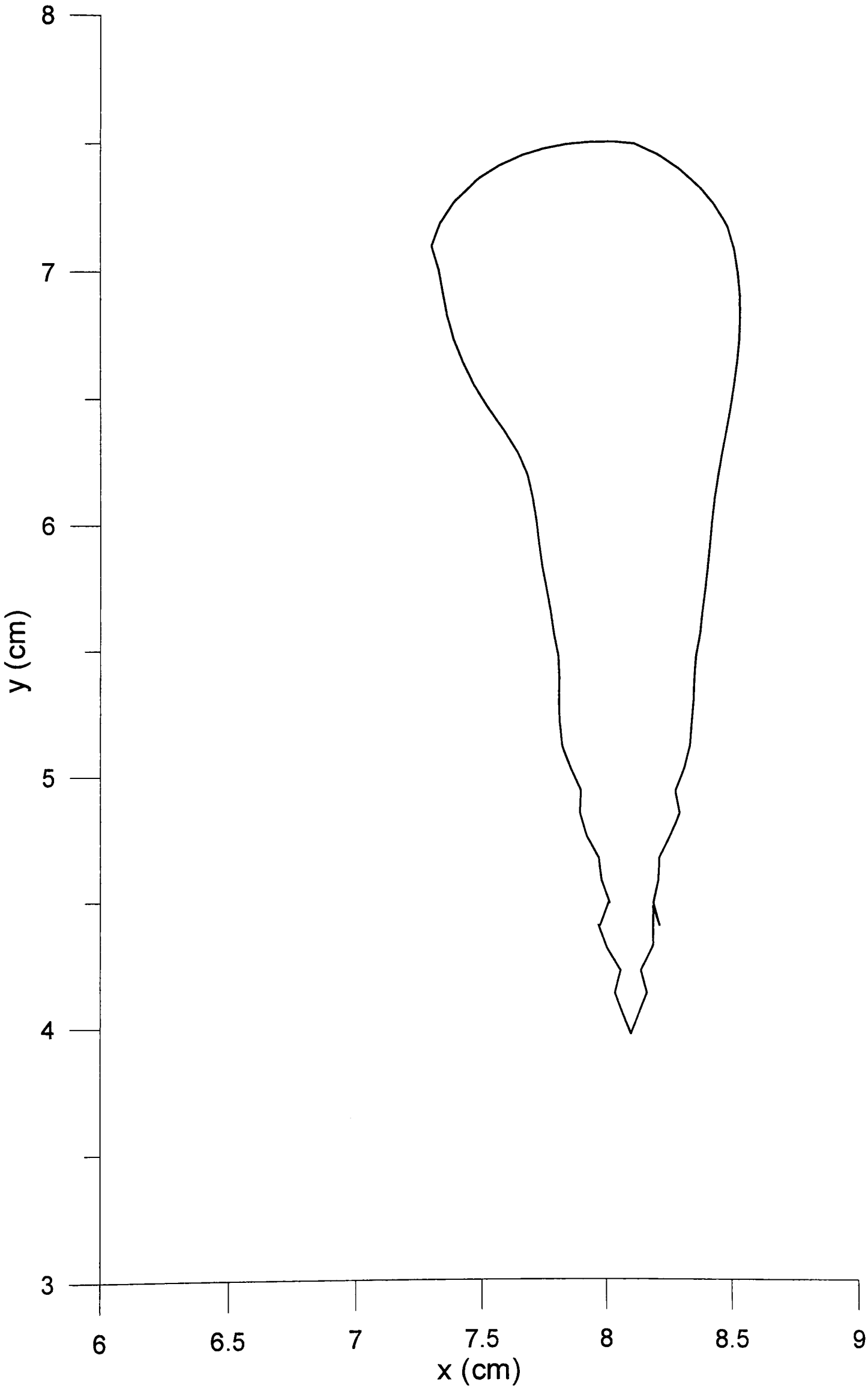

Figure 4.36(b) Grain boundary 3.5995 s after nucleation (t=39.8705s); Al-2%Cu; h=0.15 W/cm^{2}K, T_a=675^{o}C

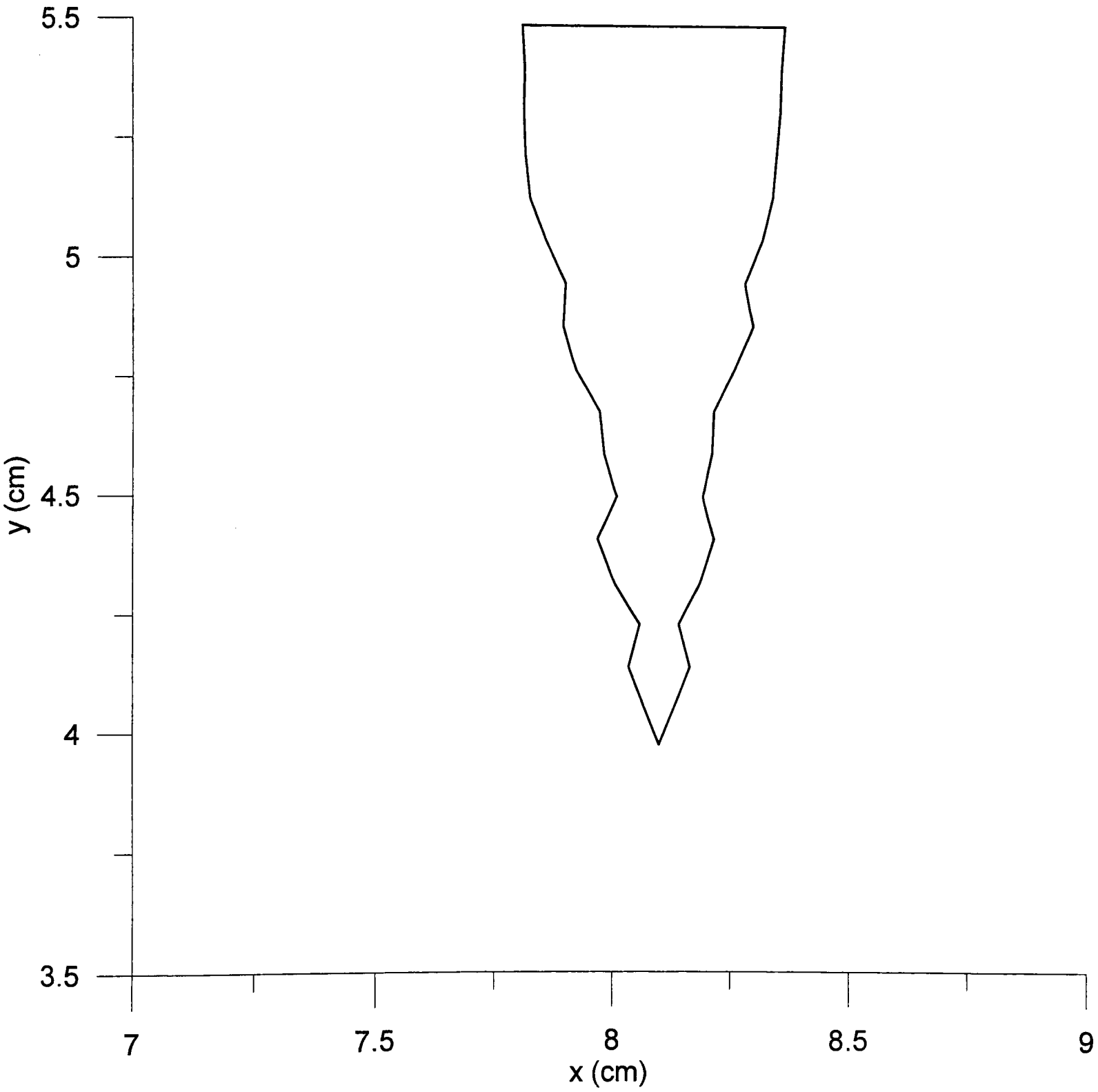

Figure 4.36 (c) Line joining advanced marker positions; t=39.8705s; Al-2%Cu; h=0.15 W/cm^{2}K; T_a=675^{o}C

is initially quite isotropic, and relatively slow. This is due to the smaller thermal gradient at nucleation in the current system. The grain does start extending to the south, but not until after a significant period of relatively isotropic growth. After 12 s of growth (the final grain envelope shown) the grain boundary is represented by 130 markers.

Using the original data, the location of the grain nucleus was then changed to control volume (45,40), which corresponds to a position x=4.05 cm, y=3.6 cm i.e. the distance to the mould walls was halved. The resultant growth of this grain, which nucleated after 26.4425 s, is shown in Fig. 4.38. The grain boundary is shown every second after nucleation, except for the outer boundary which is at 3.95025 s after nucleation (at which time the program crashed). The rapid acceleration in growth velocity is obvious, and here *two* unstable protuberances emerge from the grain : one to the south, as before, and another to the west. This is because of the proximity of this grain to the mould walls - the plot includes the origin so the axes represent the mould.

It should be noted that one would not expect grains to grow far into undercooled bulk liquid (as reported here) prior to the development of columnar growth or other equiaxed grains closer to the mould wall i.e. this is a stern test of the model. However, these predictions *are* related to the observation of large aspect ratios in "equiaxed" grains (such that they can look columnar) - a better term for these is unconstrained grains - their origin determines the term rather than the shape. Indeed it is often difficult to distinguish, via metallographic study [146], between columnar and equiaxed grains in castings.

In order to develop a more realistic picture of equiaxed solidification, the nucleation, growth and impingement of multiple grains has to be treated.

4.4.2 Multiple grains

Initially two grains were treated. One originated (100 x 100 grid) at position (90,80) as in Section 4.4.1. The origin of the other grain was chosen to be at a mirror image (in the

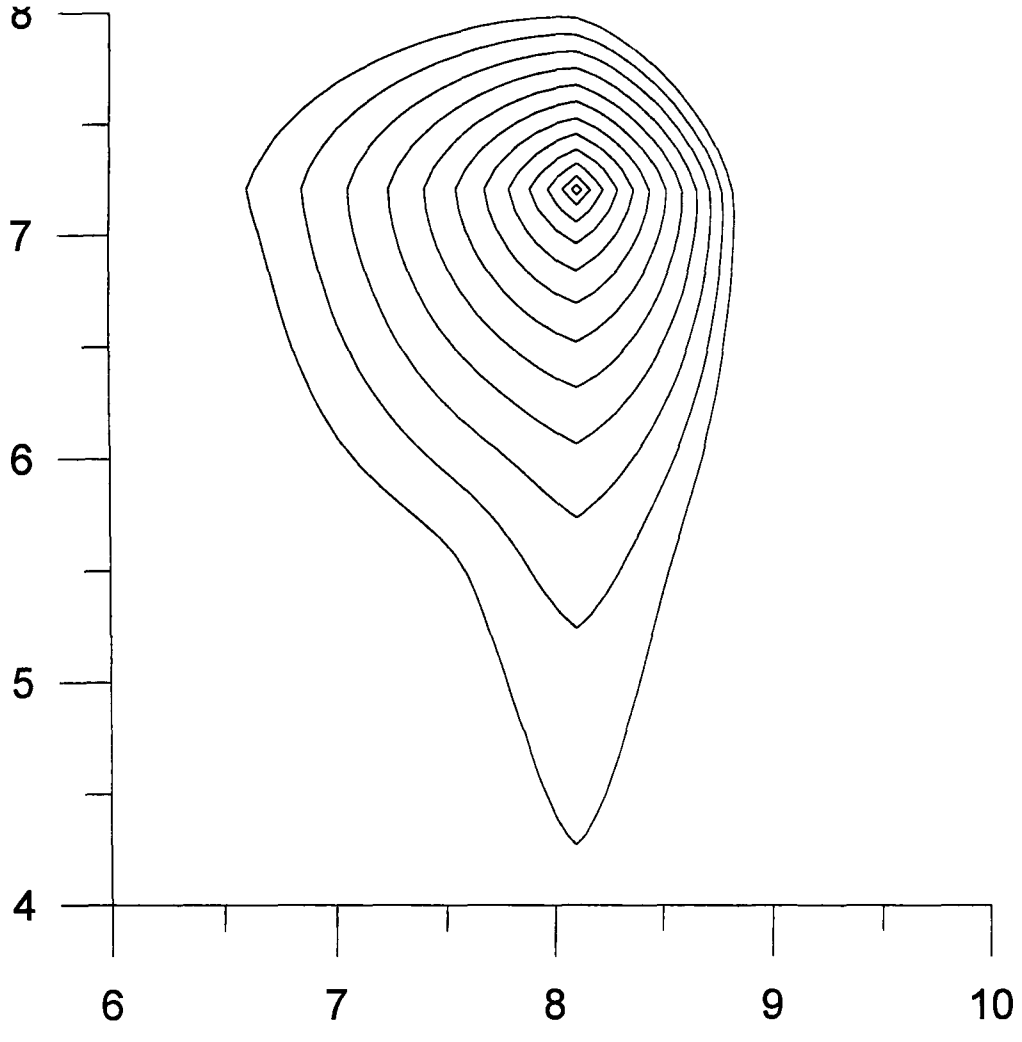

Figure 4.37 Grain boundary position every 1 s after nucleation; Al-2%Cu; h=0.05 W/cm^{2}K; T_a=656°C; nucleus at (8.1,7.2) cm

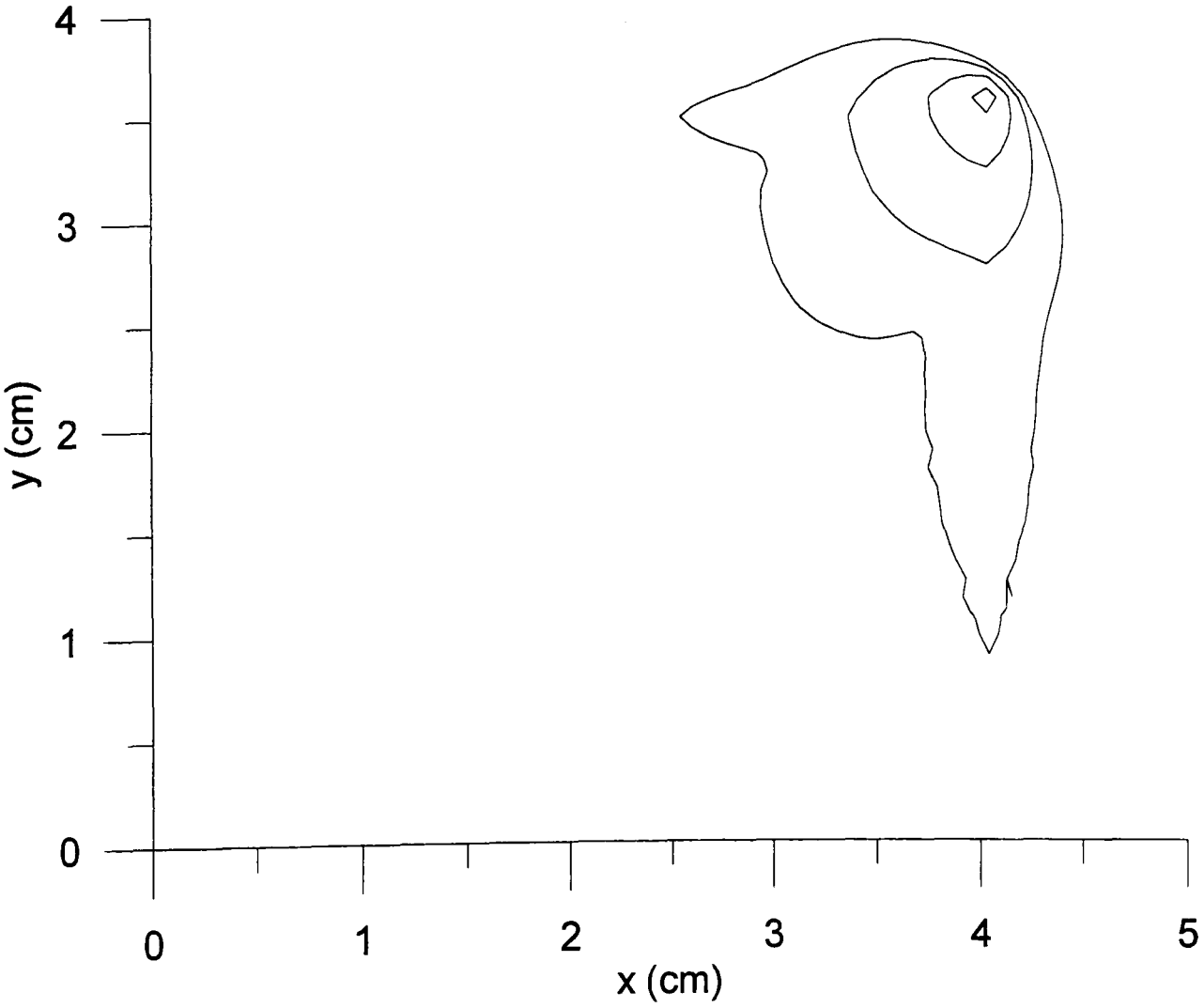

Figure 4.38 Grain boundary position every 1 s after nucleation, except last grain boundary is 3.95025s after nucleation; Al-2%Cu; h=0.05 W/cm^{2}K; T_a=675°C; nucleus at (4.05,3.6) cm

diagonal) position (80,90) or at x=7.2 cm, y=8.1 cm. There were a few reasons for this approach. Firstly, the grains should nucleate together, and the shape of one grain boundary at any time should be a reflection of the other in the diagonal. The realisation of this feature is a test of the model. Secondly, the control volume at which the first impingement of these grains occurs should be along the diagonal. And finally, this approach guarantees that one nucleation point is not overgrown by the other grain before it is activated. The alloy is Al-2%Cu, h=0.05 W/cm^{2}K, T_a=675°C, with other data as before.

The growth of (the original) grain number 1 is shown in Fig 4.39. If the grain boundary after 6 s is compared to that (Fig. 4.30) of the single grain, it can be seen that the growth in the northwest corner is restricted in this case. This is due to the interaction with the thermal field of grain number two (Fig 4.40). Symmetry in the diagonal is obvious. The bubble chart in Fig. 4.41 illustrates the lower undercooling (compare with Fig 4.31) at the northwest boundary of the grain. Here the maximum, minimum and mean undercoolings are 3.822, 0.821 and 1.614°C, respectively.

The two grains start to impinge upon one another, which in this case means that the grain boundaries of both enter the same control volume in one or more places. This happens first in c.v. (82,82) - Fig 4.42 shows the grain boundaries at t = 62.7785 s. As expected, impingement is along the casting diagonal. So FLAG(82,82)=7, and there are two separate contributions to latent heat evolution in this c.v.. At this point the program crashes, not due to this impingement, but due to instability at the other end of the grains, like that illustrated in Fig.4.36(b). In order to avoid this, equiaxed nuclei must be placed closer to the mould walls.

In addition to the two nuclei above, seven other nuclei, all closer to the mould wall, were placed in the domain. The c.v. coordinates of these were (38,62), (47,46), (47,34), (65,32), (66,22), (43,47), (50,32). The one closest to the mould wall (66,22) ; x=5.94 cm, y=1.98cm; nucleated first. At t=24.081 s (well before the nucleation time for the inner two nuclei above) it reached the mould wall (Fig 4.43). At this time, none of the other nuclei had been

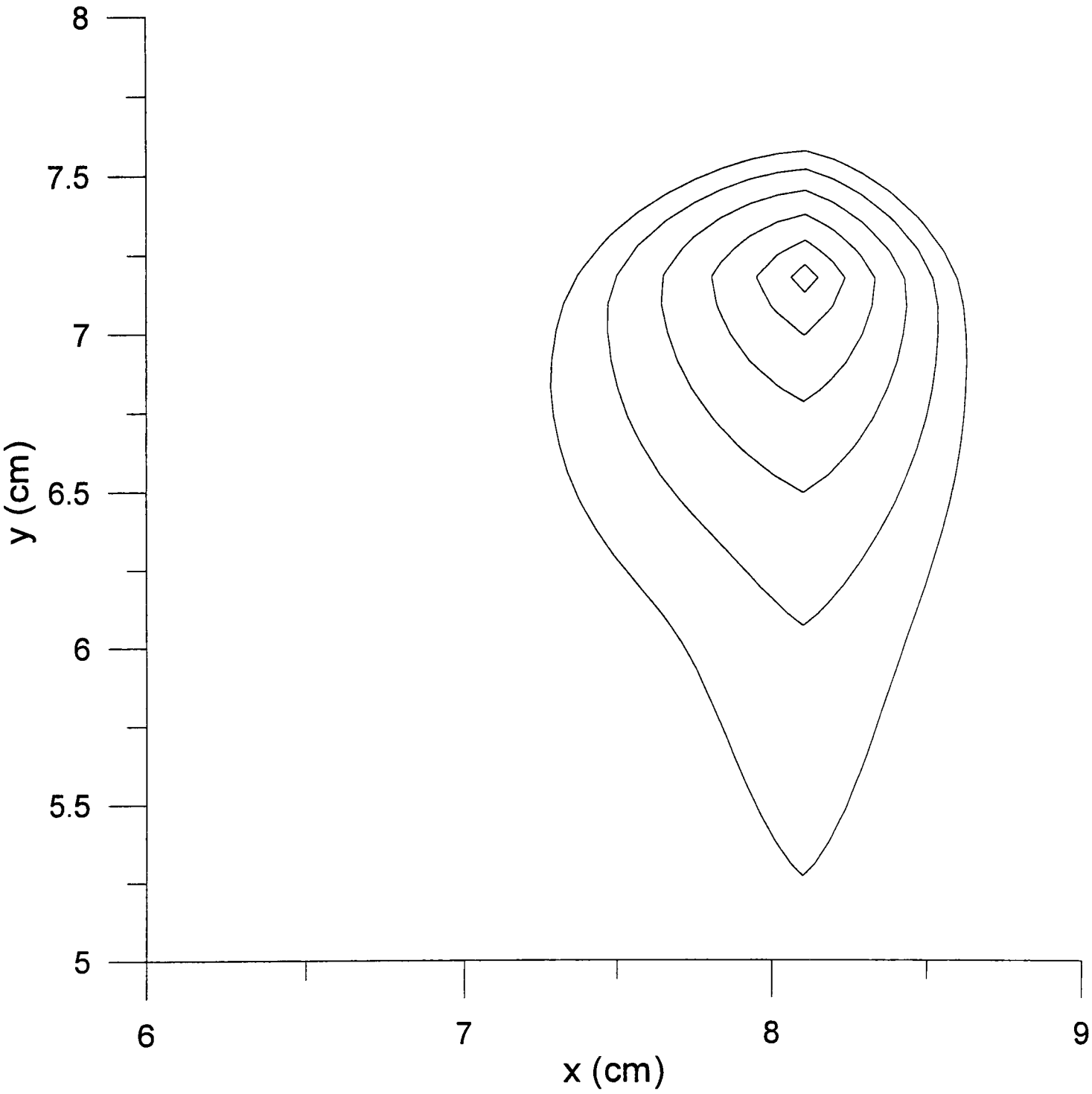

Figure 4.39 Grain boundary position every 1 s after nucleation; one grain of "twins"; Al-2%Cu; h=0.05 W/cm^{2}K; T_a=675°C

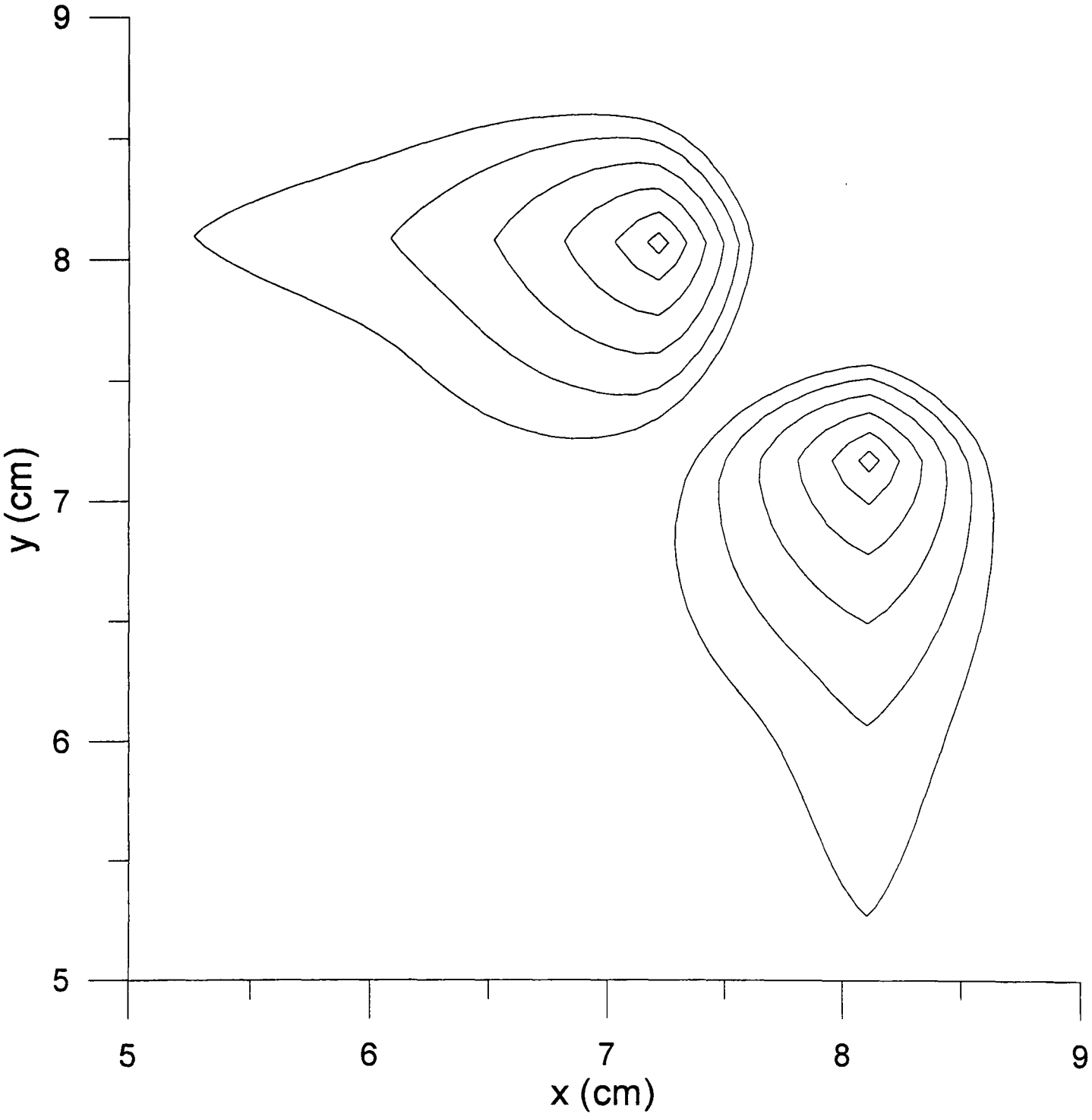

Figure 4.40 Grain boundary position every 1 s after nucleation;
"twin" grains;
Al-2%Cu; h=0.05 W/cm^{2}K; T_a=675^{o}C

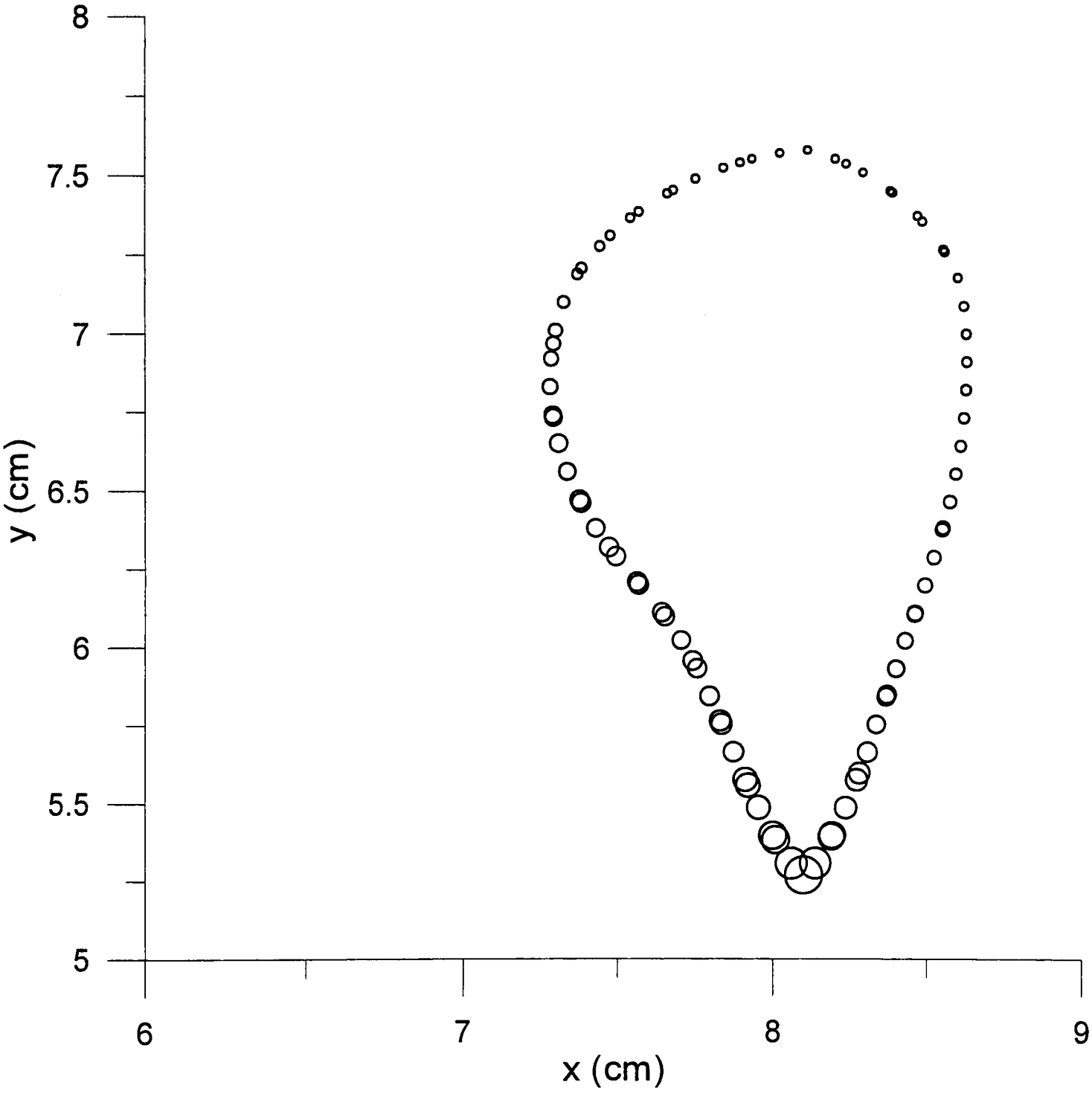

Figure 4.41 Bubble chart showing grain boundary marker positions 6 s after nucleation (t=61.97925 s);
one grain of "twins";
bubble diameter indicates marker undercooling :
maximum 3.822°C, minimum 0.821°C;
Al-2%Cu; h=0.05 W/cm²K; T_a=675°C

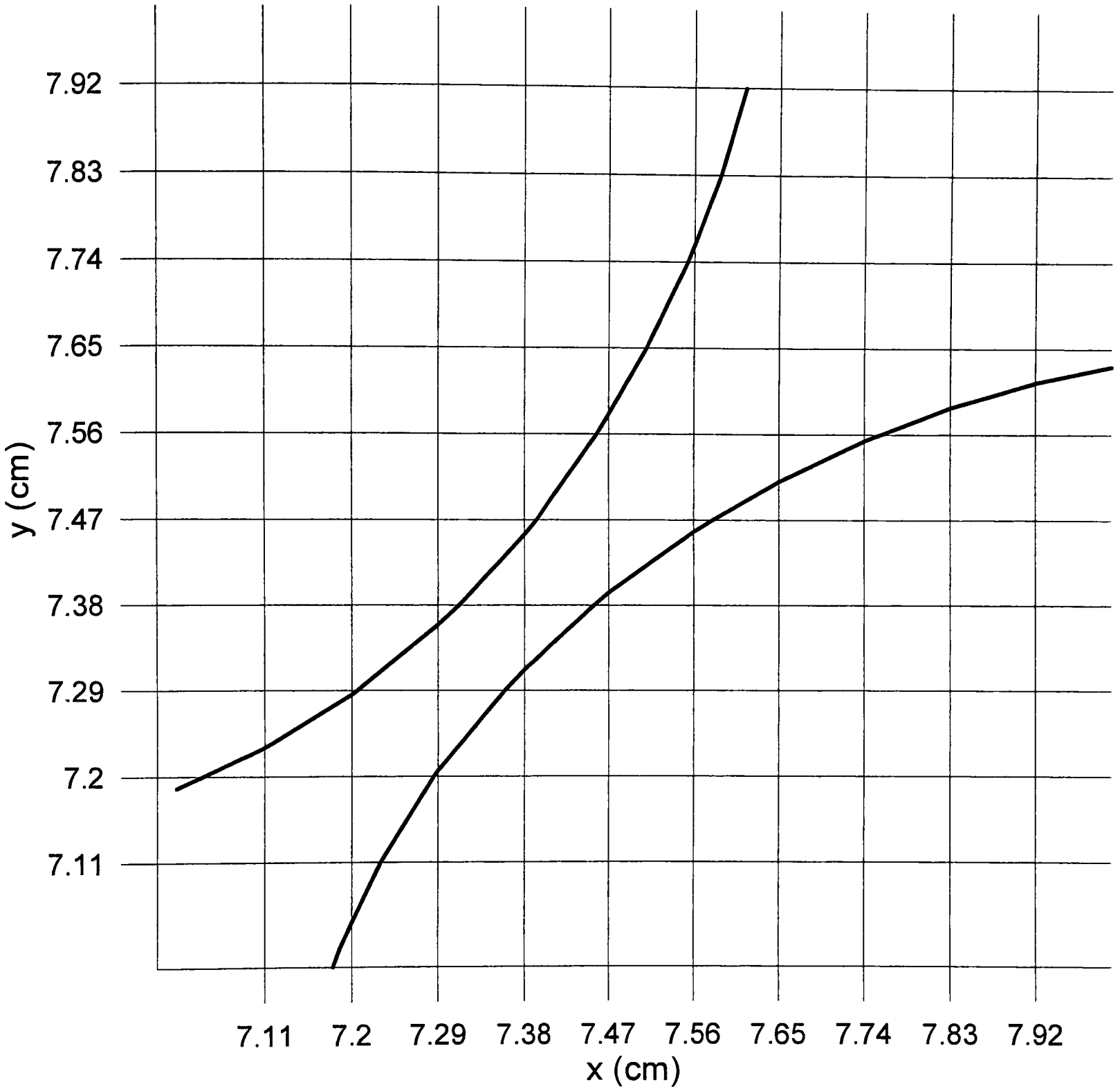

Figure 4.42 Twin grain boundary positions at t=62.7785 s;
first impingement is in c.v. (82,82);
Al-2%Cu; h=0.05 W/cm^{2}K; T_a=675°C

activated. With a small number of nuclei, spread over a large area in a relatively large temperature gradient, those in cooler locations are at a huge advantage. At this point the program stops, as a routine to deal with impingement with the mould wall has yet to be designed and implemented. It should be noted that, although this is an "equiaxed" grain, it could appear in microstructural examination as if it were part of a columnar zone.

It has been shown (Fig. 4.15) that there is only a small band of undercooled liquid in which equiaxed solidification can occur at any time. If potential nuclei are spread over the entire domain, only those in a confined subset of that domain can nucleate. The best way to model this and to predict the CET is a full implementation of simultaneous columnar and equiaxed growth models. In the meantime, the equiaxed model can be tested under more realistic constraints by limiting the region in which nuclei are placed. The simplest way to do this is by use of a buffer zone a certain distance from the mould walls and another a certain distance from the centrelines of the domain. This is shown in Fig. 4.44. Comparison should be made with Figs. 4.15 and 4.19. In addition to being a mock-up of a limited region of undercooled liquid, these buffer zones also serve to avoid the situations of early impingement with the mould walls or reaching the centre-lines of the casting, as noted in Section 3.7.2. Within this region, sites for nucleation are placed probabilistically, as opposed to the deterministic placement used to date.

A buffer zone of 4 cm from the mould wall and 3 cm from the centreline was chosen in which to randomly place 10 sites for nucleation. The result of the first simulation is shown in Fig. 4.45. Here three grains have nucleated and grown. It can be seen that two grains have impinged upon one another. The program stops when a c.v. into which both have grown has a total volume overgrown (by both grains) greater than the volume of the c.v. itself i.e. A=B in Fig. 3.19. The routine to deal with impingement and definition of as-cast grain boundaries, outlined in Section 3.7.2, has yet to be implemented.

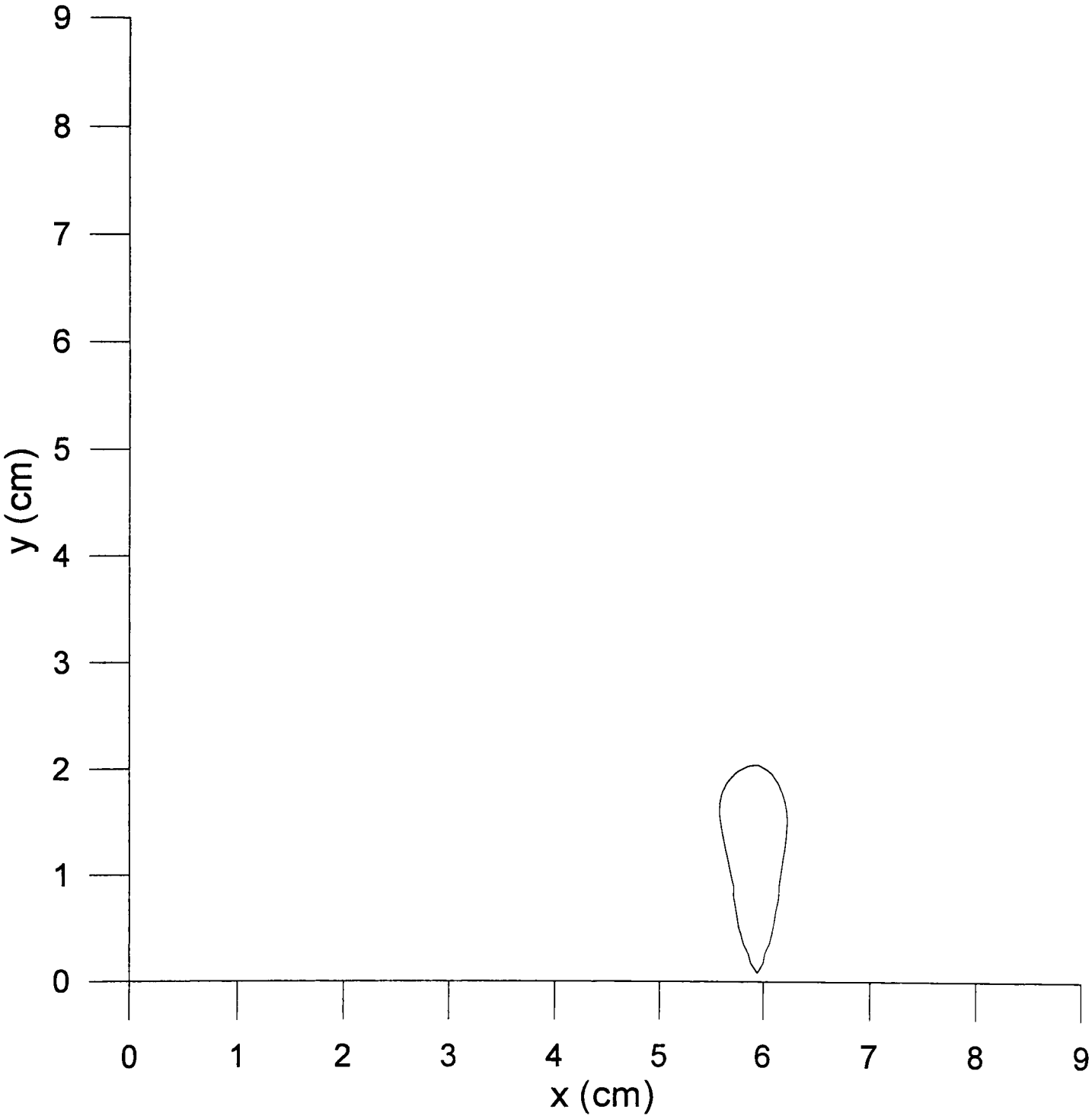

Figure 4.43 One of nine grains nucleated and grown; nucleus at (5.94, 1.98) cm; t=24.081 s
Al-2%Cu, h=0.05 W/cm^{2}K, T_a=675^{o}C

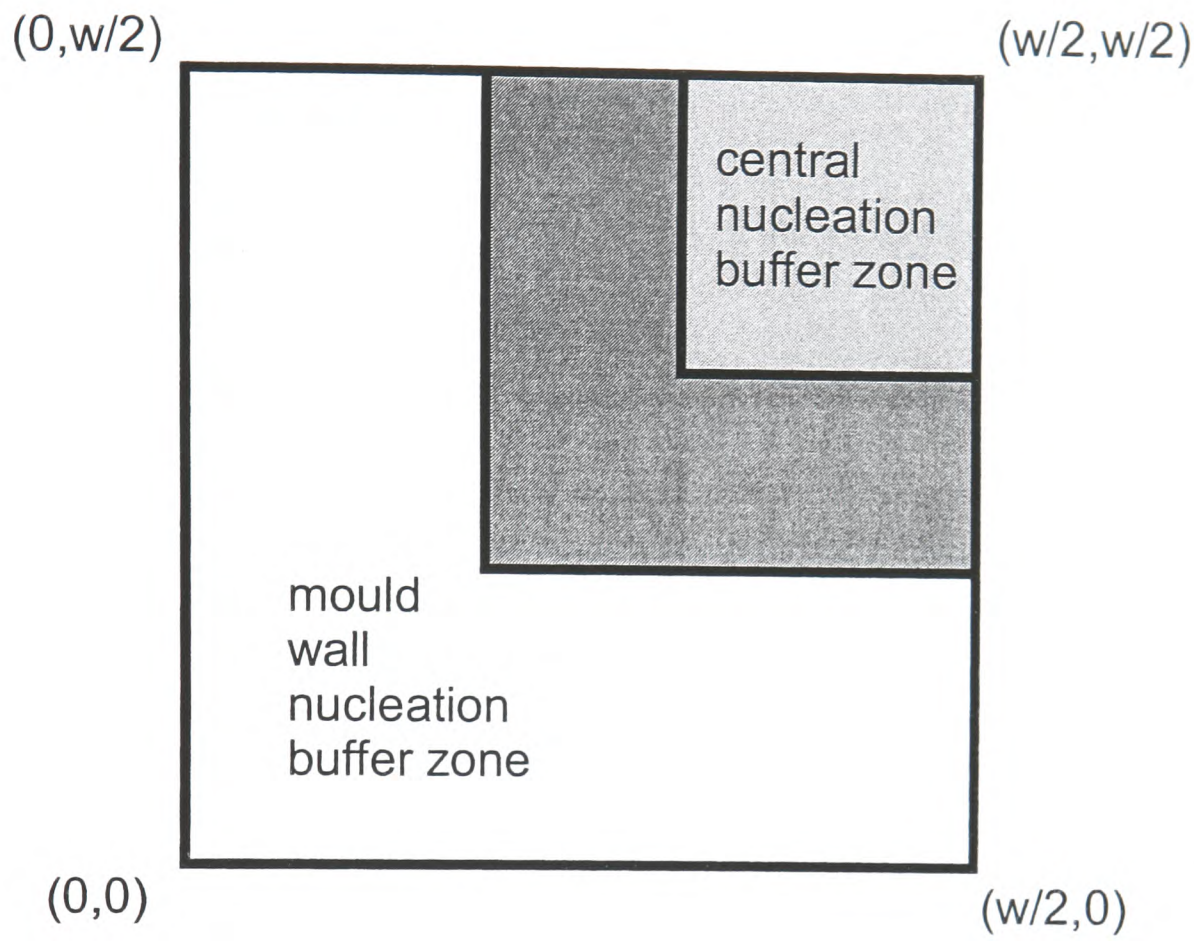

Figure 4.44 nucleation buffer zones

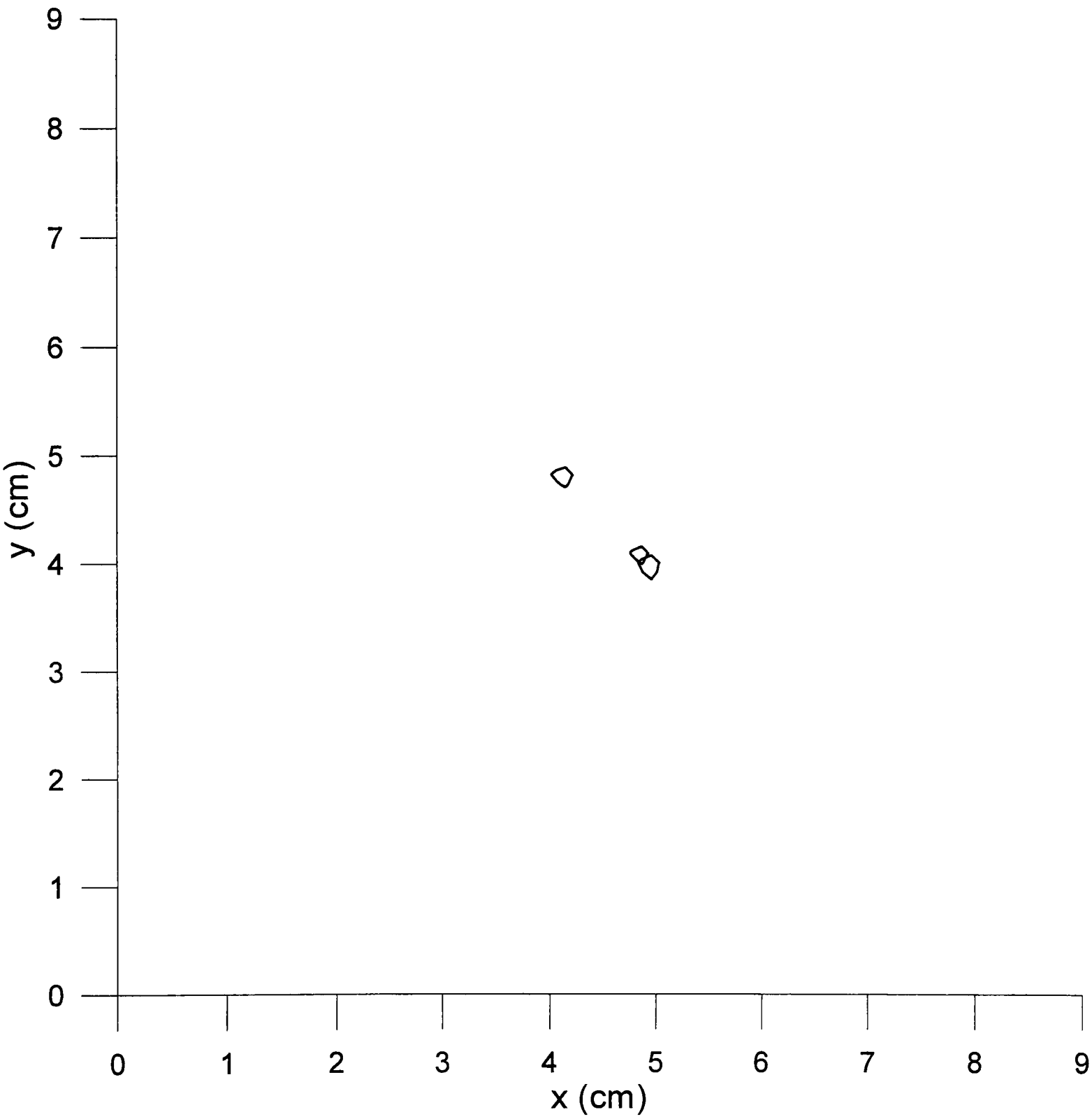

Figure 4.45 Grains grown from 10 randomly placed nuclei;
buffer zones 45 c.v.s from mould wall,
33 c.v.s from centre;
Al-2%Cu; h=0.05 W/cm^{2}K; T_a=675°C
t=33.856 s

As the sites are chosen randomly, 6 further simulations were carried out using identical input data. The output is shown in Fig. 4.46. Each axis is 9 cm long i.e. the full domain is shown. In two of the cases presented ((b) and (e)), only one grain grew, and became unstable as their protuberances reached towards the mould wall. In the last case (f), five grains are growing; although two of these are very small and difficult to see at this resolution.

The program was then tested with a lower superheat - of 1°C - i.e. initial liquid temperature of 656°C. Again, there are 10 sites for nucleation, placed in the same restricted area of the domain. It has already been shown that use of this lower superheat results in grain growth in a lower thermal gradient (see Fig. 4.37). The earlier nucleation is important in this respect. The results of 6 simultaneous simulations are shown in Fig. 4.47. In this case it can be seen that more of the grains actually nucleate. Also, none of these grains are at a very large relative advantage with respect to others in terms of growth. This was not true when the superheat was relatively high. In Fig. 4.47(a), 9 of the 10 sites have been activated. Those closest to the mould walls have grown larger than the others, but the growth instabilities obvious in a higher thermal gradient (Fig. 4.46(b) and (e)), do not occur, at least not before grain impingement has halted the program. In Fig. 4.47(c), all 10 grains have nucleated. This would indicate that low superheat favours smaller grain size. This is true even without consideration of the remelting of "big bang" or dendrite detachment embryos.

It remains to complete the algorithm for impingement to enable grain growth beyond that reported in this work. The same approach should be used for both impingement of equiaxed grains with one another, and with the columnar front. Impingement with the mould wall should also be treated, as this can occur of the solidification structure is completely equiaxed. This should be *relatively* simple as it is a stationary flat surface.

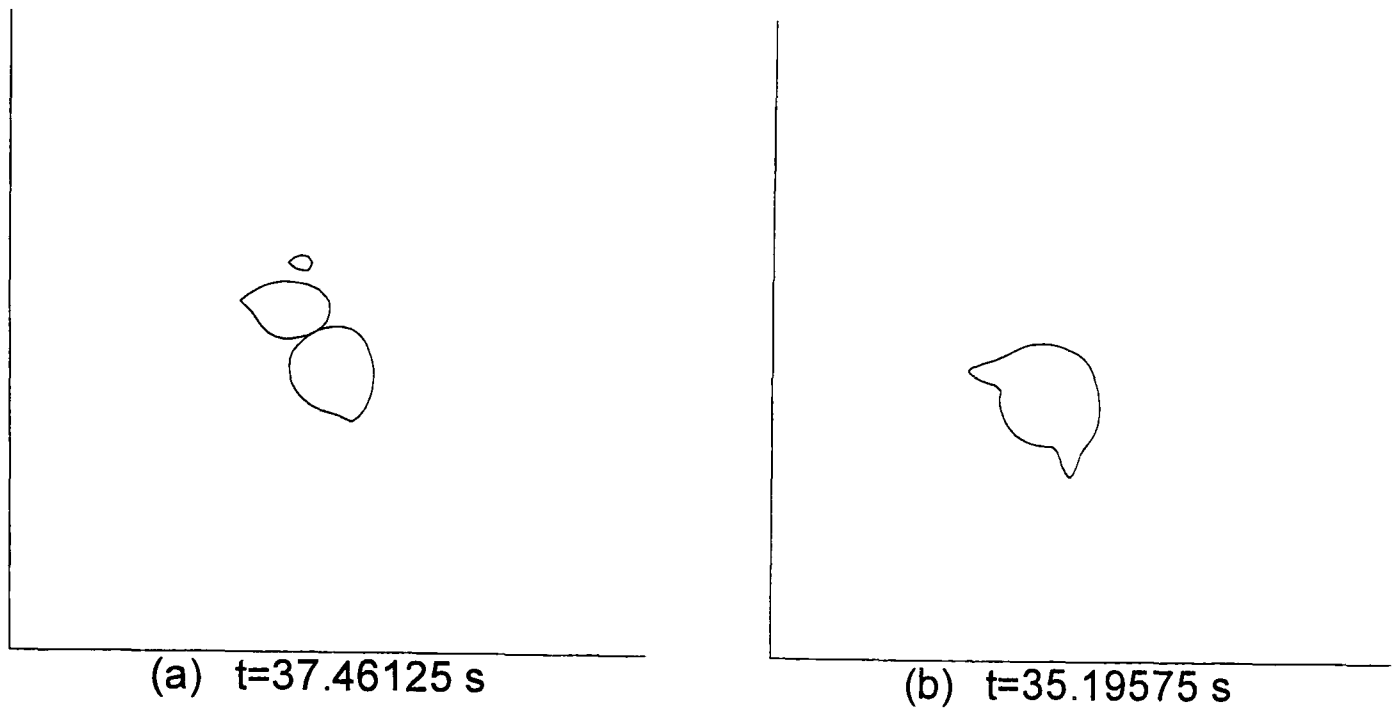

Figure 4.46 Grains grown from 10 randomly placed nuclei; buffer zones as for Fig. 4.45; times as shown; Al-2%Cu; h=0.05 W/cm^{2}K; T_a=675°C

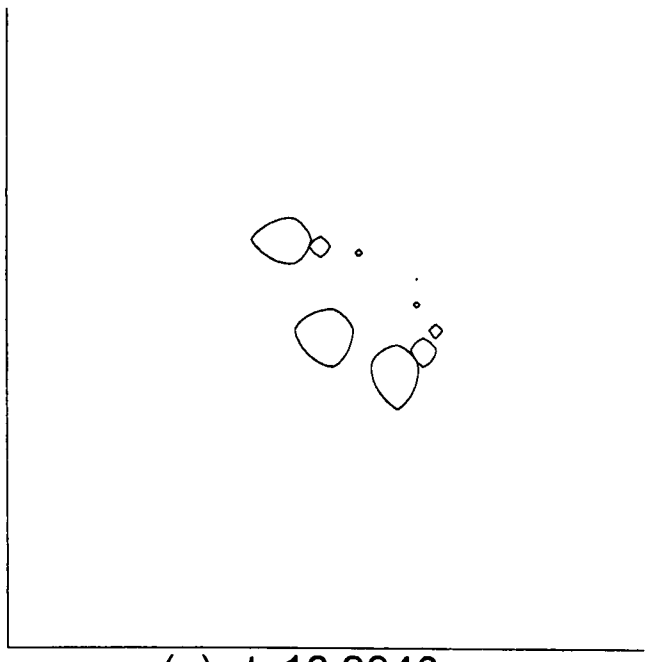

(a) t=13.2940 s

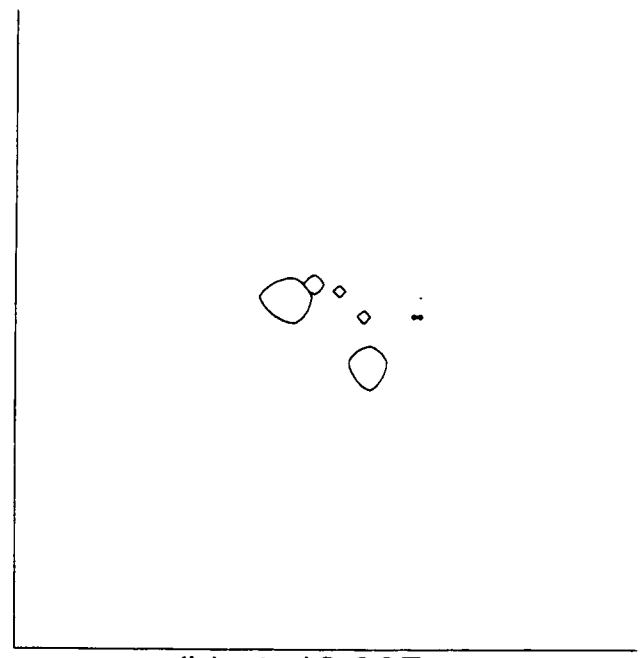

(b) t=12.397 s

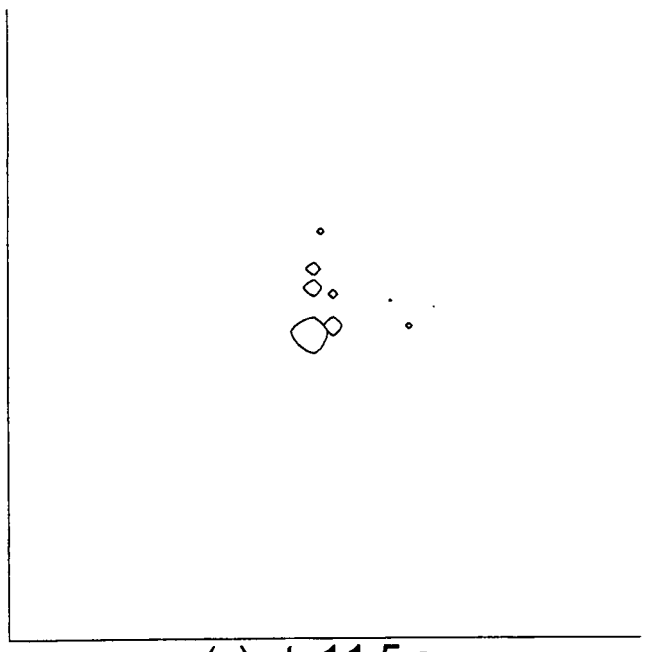

(c) t=11.5 s

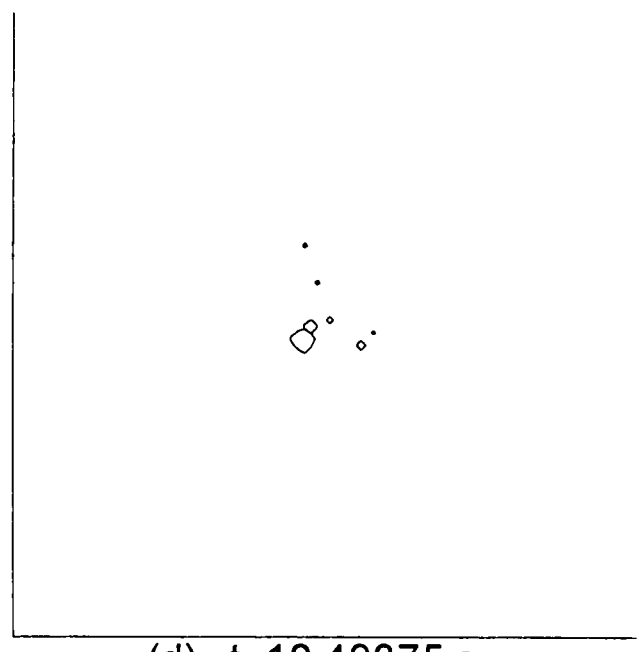

(d) t=10.49375 s

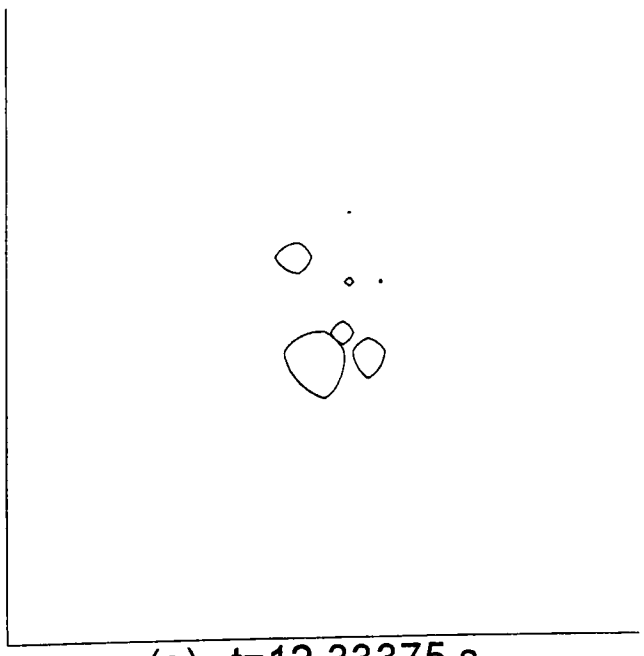

(e) t=12.33375 s

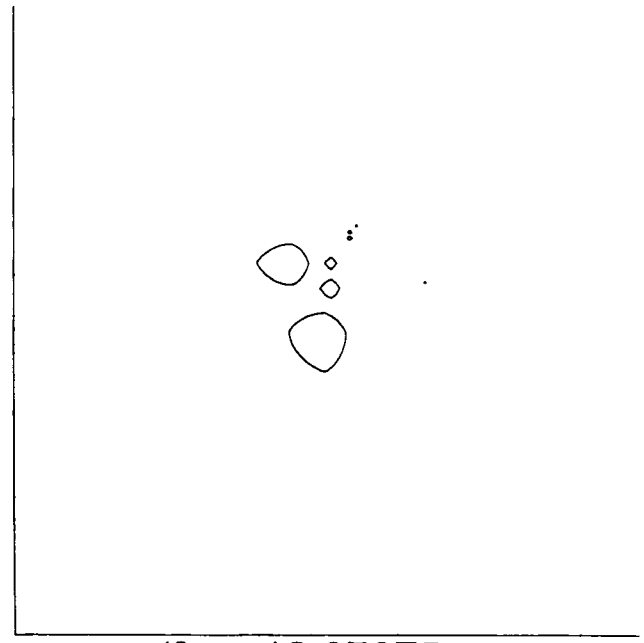

(f) t=12.67875 s

Figure 4.47 Grains grown from 10 randomly placed nuclei; buffer zones as for Fig. 4.45; times as shown; Al-2%Cu; h=0.05 W/cm^{2}K; T_a=656°C

4.5 Experimental

As stated in Section 4.3.3, it is not possible to validate this model with experimental results, because the gravitational effects which contribute to the formation of grain structure in castings are not treated. However, in order to illustrate this, a few simple solidification experiments were carried out. These involved solidification of Al-Cu alloys in a rectangular metallic mould. The mould was of internal dimensions 7 x 7 x 23 cm, of machined grey cast iron, and preheated to 200°C. The mould wall thickness was 4 cm. During solidification, the mould temperature was between 330 and 420°C. The casting was sectioned at mid-length, exposing the square cross-section, ground, polished and etched in 1 part HNO_3, 1 part HF and 8 parts H_2O. It was estimated that, at mid-length, heat transfer could be assumed to be 2D i.e. in the plane of the section. The macrostructure of 3 castings are presented. These are Al-5%Cu (100°C superheat), Al-10%Cu (100°C superheat), and Al-10%Cu (150°C superheat) - Figures 4.48, 4.49 and 4.50 respectively. In Fig. 4.48, it can be seen that there is a sizeable columnar zone at the top of the casting, but not at the bottom. It is presumed that this is due to the settling of equiaxed crystals in the melt as they grow. With a higher Cu content, Fig. 4.49 shows that no columnar zone at all is present. This agrees with the conclusion drawn via use of the peak $I_{ex}(t)$ as a metric for equiaxed solidification (Table 4.3). However, the growth of equiaxed eutectic grains is a complication with this alloy (See Fig. 4.1), not treated by the model. If the superheat is increased (Fig. 4.50), a columnar zone appears again, and there is a much coarser equiaxed grain structure. This dependence of grain size upon superheat has been predicted qualitatively by the model (Fig. 4.46 v. 4.47). Care must be taken, however, in identification of the columnar zone in such metallographic studies, because - as shown in Fig 4.43 - unconstrained nucleation events can give rise to elongated grains which may mistakenly be identified as having emerged from the outer chill zone by competitive constrained growth. Indeed choice of the direction of section could influence our judgement on what is a columnar and what is an equiaxed grain.

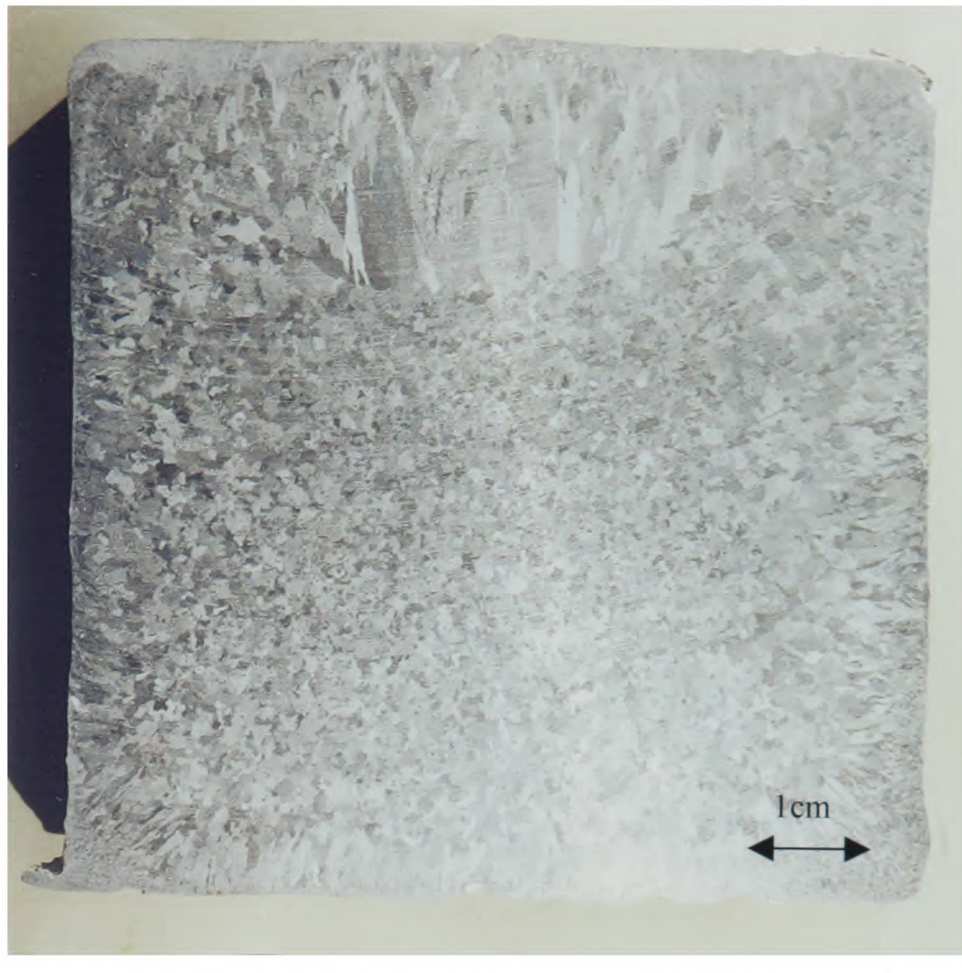

Figure 4.48 Macrostructure of Al-5wt.%Cu casting, 100°C superheat

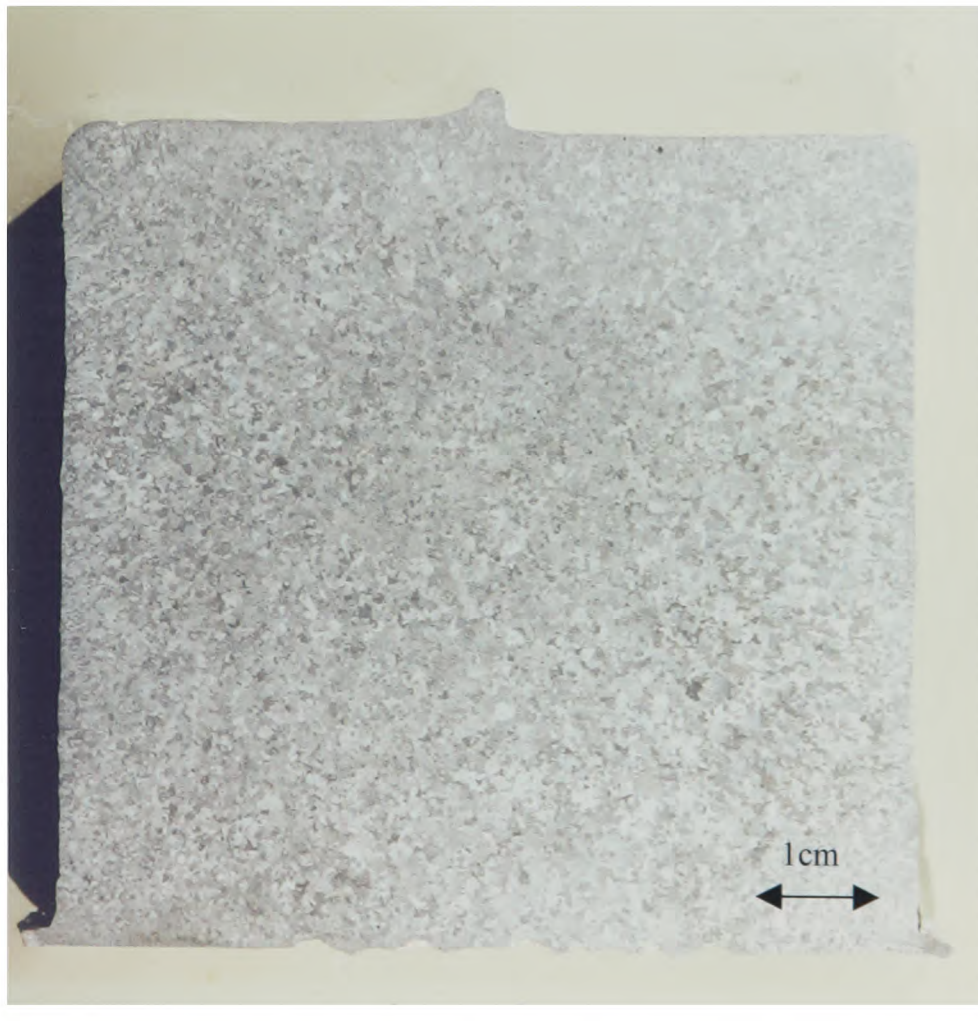

Figure 4.49 Macrostructure of Al-10wt.%Cu casting, 100°C superheat

Figure 4.50 Macrostructure of Al-10wt.%Cu casting, 150°C superheat

As discussed in the final Chapter of this thesis, future work will include the extension of this model to treat convection.

Chapter Five

Conclusions and Future Work

Chapter 5

Conclusions and Future Work

In this Chapter, conclusions are drawn regarding the new model of microstructural evolution and its predictions, and recommendations are made for extending the model in the future.

5.1 Conclusions

The objective of this work at the outset was to develop a methodology whereby the evolving grain structure in a shape casting could be simulated, in at least 2D. In particular, it was a target to distinguish between columnar and equiaxed solidification, with a view to prediction of the presence and position of the columnar-equiaxed transition (CET), under certain casting configurations and conditions. Given the casting geometry, important variables to study included alloy composition, initial superheat, and heat extraction rate (process heat transfer coefficient). After a review of the techniques used by others in attempts at creating such models (Chapter 2), it was decided to develop a novel model using a different approach - that of sharp interface or front tracking. A control volume finite difference model of heat transfer, with latent heat source terms, was employed. Following nucleation, solid growth was modelled via consideration of non-equilibrium dendrite tip kinetics. The algorithm used was based on expressions developed from considerations of isolated dendrite tip growth, and, unlike in previous work, the erroneous additional treatment of diffusion of solute through a layer in front of the growing dendrites was not employed. The solidification fronts were represented as boundaries joining discrete computational markers which moved, according to their temperature, in a direction normal to the front. The front could be considered as a line separating liquid from a zone of partially solid alloy. This front was not the liquidus

isotherm, but rather was undercooled according to the local thermal and solidification conditions. Latent heat terms were calculated via consideration of the growth of solid.

The test problem chosen was that of solidification of binary Al-Cu alloys in a square isothermal mould, represented by one quadrant because only diffusive phenomena were modelled. The model used the explicit formulation. Columnar and equiaxed solidification were treated separately.

The model predicted that columnar solidification started via nucleation along the mould walls. Growth then continued towards the centre of the casting. Both nucleation and growth of the columnar front were symmetrical in a diagonal line from the corner to the centre of the casting. As such symmetry was not imposed, its realisation is a measure of the robustness of the model. The advancing columnar front was not isothermal, although the temperature did not vary greatly along it. The difference between the position of the tracked front and that of the isotherm indicating its *average* temperature at any time was very small. As a result, a thermal contour plot could be used a map delineating solid, semi-solid, undercooled and superheated liquid; these zones being separated from each other by the solidus, front isotherm, and liquidus lines, respectively. The model predicted the appearance, advance and widening, and final disappearance of an undercooled liquid zone during columnar solidification. The thermal gradient ahead of the growing front was, in all cases, predicted to be much lower than that in the (partially) solid material behind. These gradients became progressively smaller throughout solidification.

The extent (magnitude plus area covered) of the undercooled liquid zone was presented as 3D wireframe and surface plots : the undercooled "ridge". It is postulated that the volume under this ridge, which varies with time (t), is an indication of the potential for equiaxed solidification, and was therefore denoted as the equiaxed index $I_{ex}(t)$. This index grows, peaks and then drops throughout columnar solidification. Study of the peak value suggests that equiaxed solidification is more likely in alloys with a high solute content and where the rate

of heat extraction to the mould is low. This is in agreement with experimental observation from the literature. The level of solute in the alloy was found to have a significant effect on the front undercooling, with more pure alloys growing at higher temperature. Increasing the heat transfer coefficient was shown to lower the front temperature, but only very slightly. Simply using the columnar front undercooling as an indicator of the tendency for equiaxed solidification indicates that pure alloys solidifying with low rates of heat extraction would be less likely to form an equiaxed zone, but this metric is not as sensitive to alterations in the h.t.c. as is $I_{ex}(t)$. Another metric used involved the numerical integration of $I_{ex}(t)$ with respect to time, but this was not found to be a satisfactory indicator of the tendency to form an equiaxed zone.

Comparison of results with an enthalpy method model was used to verify the new interface-tracking model. Grid refinement studies on the new model showed that, for simulation of columnar solidification, employment of a 100 x 100 c.v. mesh was optimal, this being the resolution at which the predictions of the model converged.

The treatment of equiaxed solidification was demonstrated via placement of a single potential site for the nucleation of an unconstrained grain in the cooling melt (columnar growth being artificially disabled). This site became activated on being undercooled by the chosen value of ΔT_{nuc}^{ex}, which was lower than the undercooling predicted at and ahead of columnar dendrites. The grain grew with a large aspect ratio, due to the thermal gradient in the domain. The dendrites grew most rapidly into the coolest liquid. Recalescence was predicted at the grain origin. The growing grain showed up as a "footprint" in a 3D plot of liquid undercooling in the domain. Growth into an increasingly undercooled liquid near the mould wall caused the grain envelope to destabilise via side-branching, exhibiting the onset of a convoluted dendrite-type shape, although the model was not created to capture such effects (the envelope being an interface between liquid and mushy solid). Such instability did not occur in columnar solidification due to the lower curvature of this front and because it grows into a

positive temperature gradient. Here a protuberance is not favoured, at least from a thermal perspective.

Increasing the h.t.c. caused the grain elongation and destabilisation to occur more rapidly. Use of a very low initial superheat resulted in growth in a lower thermal gradient and a slower and more isotropic expansion of the grain. Placing a single grain closer to the mould corner resulted in the prediction of *two* unstable protuberances into ever-cooler liquid : one towards each side of the mould.

The multiple grain model was initially tested using two grains placed in equivalent locations via symmetry in the domain diagonal. The grains nucleated simultaneously, and converged until final impingement along this diagonal, as expected. As the thermal fields of both grains overlapped, growth slowed.

Site location for equiaxed nucleation was then allocated probabilistically within a defined subset of the computational domain, to mirror the limited region of undercooled liquid available for nucleation and growth in a real casting situation. A study of the nucleation and growth of these crystals indicated that lowering the melt superheat would result in an advantage to nucleation over growth, and a resultant decrease in as-cast grain size. This finding is consistent with other reports in the literature, and with the results of a limited programme of experiments carried out by the author. In practice, high superheat can also affect grain size by facilitating the remelting of embryonic crystals, and this would tend to reinforce the predictions above. The macrographs from these experiments on Al-Cu alloys also confirmed the link between alloy composition and the formation of an equiaxed zone as indicated by the metrics described from consideration of the prediction of the model of columnar solidification alone.

The model showed that under some conditions, the aspect ratio of a so-called equiaxed grain can be quite large, making it appear columnar. Distinguishing between columnar and

equiaxed zones in a casting on the basis of observed grain shape can therefore be hazardous. Perhaps a better distinction relates to the origin of grains. Those that grow via a competitive process from the outer chill zone or mould should be defined as constrained grains; those which originate via isolated nucleation in the bulk liquid should be termed unconstrained grains. But even with this approach, it may be impossible, from the study of the 2D as-cast macrostructure, to determine the origin of any grain. In order to do this, use of 3D metallographic techniques such as reconstruction from serial sectioning [183] or X-ray tomography [184] must be used. If the full physics of the process can be captured, models such as those presented here (if developed further - see Section 5.2) can also be of use in tackling this problem.

The explicit formulation places a restriction on the time step which can be used. Despite this, execution time for the model was less than five minutes in all cases, on a 1999 Pentium machine. The explicit model is easier to implement and test than a implicit formulation, as shown. Also, although a much larger time step would decrease CPU time, too large a time step may result in the loss of some physical resolution. The front-tracking method developed here would seem to be a most efficient way of modelling microstructural evolution.

5.2 Future Work

The capability of the new front-tracking model has been proven. The results are sufficiently encouraging to suggest the work be extended. Suggestions for further development of the model are the subject of this Section.

The top priority for future work is the completion of the implementation of the algorithm for the impingement of equiaxed grains with each other (Section 3.7.2), with the columnar front, and with the mould wall. This will enable the modelling of the evolution of grain structure

right through to complete solidification, including CET prediction. This is quite achievable in the medium term.

The variation of thermophysical properties with temperature and phase should be incorporated into the model. A model of microsegregation should be used to define latent heat evolution during solidification. The non-linear lever or Scheil rules could be used, or the variation of enthalpy with temperature and cooling rate could be based upon numerical models of microsegregation during dendritic growth (e.g. as described in [87]). Dendritic growth was modelled according to the analysis of Burden and Hunt (equation (2.10)). However, as described in Chapter 2, since this work a more complete analysis has been carried out by Lu and Hunt, based on a numerical model of array growth. This led to an equivalent equation - (2.13) - which can also be used to calculate the dependence of V upon ΔT. Use of this more complete analysis is recommended for future versions of the current front-tracking model. Yet these models are really only valid where the spacing is sufficiently large to ensure that there is very little overlap between neighbouring solute fields. Longer term research is needed to develop expressions for solid growth which are valid for ever-decreasing spacings which lead, in the limit, to planar or spherical morphologies. The eutectic arrest should also be included in the model, thus extending the range of alloys that can be modelled.

As symmetry in the diagonal was not pre-set, even for columnar solidification, the model could be used to study the effects of varying (randomly or otherwise) the activation undercooling along the mould wall. The use of chills and insulators set into the mould could be studied; non-square casting geometries and directional solidification processes could be simulated. The model could be used to support a study of hot tearing, especially if it were to be used as a basis for a prediction of the evolution of stress and strength during alloy solidification.

In some cases (see Fig. 4.36), sharp instabilities emerge from equiaxed grains, causing the program to crash. If the radius of curvature of the dendrite tip were limited, e.g. according to the marginal stability criterion, this instability could be moderated, enabling study of the formation of super dendrites.

The treatment of nucleation leading to growth of solid is not very sophisticated in this work, and is deserving of further attention. However, it has been shown before [160] that the nucleation process postpones the start of columnar solidification, but once underway, roughly the same growth velocity and temperature distribution is attained irrespective of the nucleation undercooling required to initiate columnar growth. More complex equiaxed nucleation models could also be tested. For example, it is expected that "big bang" crystals would require no undercooling for growth. On the other hand, the efficacy of grain refiners would be inversely proportional to their activation undercooling. A numerical study could be carried out to correlate the distribution of nucleating agents and their potency with the predicted grain structure, and comparisons made with experimental studies. As well as a random allocation of nucleating sites, the nucleation undercooling could also be assigned according to some statistical distribution.

However, if experimental data (such as that presented in Section 4.5) is to match the predictions of such a model, more physics will have to be treated. In particular the effects of convection (Sections 1.8 and 2.1.4) should be included in the model. This would necessitate study of the entire casting cavity, or at the very least the left or right hand half of it. Work on this has already started [182]. And unlike in the enthalpy approach, the presented front tracking method allows more precise modelling of momentum transport within the domain between the solidus and liquidus temperatures. Here a model of Darcy flow can be used only in the region of *columnar* morphology, with the definition of solid fraction given by a relationship like equation (3.14) leading to an expression for permeability. Such a region can be specified directly from the front tracking technique. In the remaining area - liquid parts of interface control volumes and in control volumes that contain only the undercooled liquid -

the Darcy source term of the momentum equation is equal to zero and the classical momentum equation for a pure liquid can be applied, with modified viscosity in the case when *equiaxed* structure is formed there. The European Space Agency are funding this work [185]. In the meantime, the diffusion-only model reported in this thesis can only be validated in microgravity conditions e.g. via experiments on board the International Space Station.

An extension of the model to 3D would require significant work. For example, the piecewise linear approximation to the solidification front would have to be replaced by a set of co-joined tiles, each tile moving in a different 3D direction. Higher order front interpolations would be even more complicated. More sophisticated visualisation would be needed.

Finally, the front-tracking approach presented here has potential use in the modelling of other multi-phase problems [186] e.g. transformations and growth in biological systems.

References

References

(1) Christian, J.W., *The Theory of Transformations in Metals and Alloys. Part 1. Equilibrium and General Kinetic Theory*, 2nd edition, Pergamon Press, Oxford, 1975.

(2) Kurz, W. and Fisher, D.J., *Fundamentals of Solidification, 3rd edition*, Trans Tech Publications, Aedermannsdorf, Switzerland, 1989.

(3) Campbell, J., *Castings*, Butterworth Heinemann, Oxford, 1991.

(4) Flemings, M.C., *Solidification Processing*, McGraw Hill, New York, 1974.

(5) Davies, G.J., *Solidification and Casting*, Applied Science Publishers Ltd., London, 1973.

(6) Flemings, M.C. and Nereo, G.E., Macrosegregation : Part I, *Trans. Met. Soc. AIME*, **239**, 1449-1461, 1967.

(7) Kirkwood, D.H., Microsegregation, *Mater. Sci. Eng.*, **65**, 101-109, 1984.

(8) Burden, M.H. and Hunt, J.D., Cellular and Dendritic Growth. II, *J. Cryst. Growth*, **22**, 109-116, 1974.

(9) Lipton, J., Glicksman, M.E. and Kurz, W., Dendritic growth into undercooled alloy melts, *Mater. Sci. Eng.*, **65**, 57-63, 1984.

(10) Lipton, J., Glicksman M.E. and Kurz, W., Equiaxed dendritic growth in alloys at small undercooling, *Metall. Trans. A*, **18A**, 341-345, 1987.

(11) Ivantsov, G.P., Doklady Akademi Nauk SSR, **58**, 567-569, 1947.

(12) Spiegel, M.R., *Schaum's Mathematical Handbook of Formulas and Tables*, McGraw-Hill, Inc., New York, 1968.

(13) Langer, J.S. and Muller-Krumbhaar, Stability effects in dendritic crystal growth, *J. Cryst. Growth*, **42**, 11-14, 1977.

(14) Langer, J.S. and Müller-Krumbhaar, Theory of dendritic growth - I. Elements of a stability analysis, *Acta Metall.*, **26**, 1681-1687, 1978.

(15) Langer, J.S. and Müller-Krumbhaar, Theory of dendritic growth - II. Instabilities in the limit of vanishing surface tension, *Acta Metall.*, **26**, 1689-1695, 1978.

(16) Muller-Krumbhaar, H. and Langer, J.S., Theory of dendritic growth - III. Effects of surface tension, *Acta Metall.*, **26**, 1697-1708, 1978.

(17) Kessler, D.A., Koplik, J. and Levine, H., Steady-state dendritic crystal growth, *Phys. Rev. A*, **33**(5), 3352-3357, 1986.

(18) Langer, J.S., Existence of needle crystals in local models of solidification, *Phys. Rev. A*, **33**(1), 435-441, 1986.

(19) Burden, M.H. and Hunt, J.D., Cellular and dendritic growth. I, *J. Cryst. Growth*, **22**, 99-108, 1974.

(20) Hunt, J.D., Experimental and numerical methods for determining the solidification path in commercial alloys, *Private Report* (for NPL), 2000.

(21) Porter, D.A. and Easterling, K.E., *Phase Transformations in Metals and Alloys, 2nd edition*, Chapman and Hall, London, 1992.

(22) Mallet, R., *On the Physical Conditions Involved in the Construction of Artillery*, Longman, Brown, Green, Longmans and Roberts, London, 1856.

(23) Cox, R.C. (Ed.), *Robert Mallet (1810-1881); Centenary Seminar Papers*, Institution of Engineers of Ireland and The Royal Irish Academy, Dublin, 1982.

(24) Jackson, K.A. and Hunt, J.D., Transparent compounds that freeze like metals, *Acta Met.*,**13**, 1212-1215, 1965.

(25) Glicksman, M.E., Schaefer, R.J. and Ayers, J.D., Dendritic growth - a test of theory, *Metall. Trans.*, **7A**, 1747-1759, 1976.

(26) Somboonsuk, K., Mason, J.T. and Trivedi. R., Interdendritic spacing : Part I - experimental studies, *Metall. Trans.*, **15A**, 967-975, 1984.

(27) Eshelman, M.A., Seetharaman, V. and Trivedi, R., Cellular spacings -I. Steady-state growth, *Acta Metall.*, **36**, 1165-1174, 1988.

(28) Ding, G.L., Huang, W.D., Huang, X., Lin, X. and Zhou, Y.H., On primary dendritic spacing during unidirectional solidification, *Acta Mater.*, **44**, 3705-3709, 1996.

(29) Kauerauf, B., Zimmermann, G., Rex, S., Mathes, M. and Grote, F., Directional cellular growth of succinonitrile-0.075wt% acetone bulk samples : Part I - Results of space experiments, *J. Cryst. Growth*, **223**, 265-276, 2001.

(30) Chilton, R.A. and Hunt, J.D., Experimental study and modelling of the cell-dendrite transition, *Proceedings Euromat 2001*, Rimini, Italy, Article 584, 2001.

(31) Borisov, A.G., Federov O.P., Maslov, V.V., Growth of succinonitrile dendrites in different cystallographic directions, *J. Cryst. Growth*, **112**, 463-466, 1991.

(32) Jackson, K.A., Hunt, J.D., Uhlmann, D.R. and Seward III, T.P., On the origin of the equiaxed zone in castings, *Trans. Met. Soc. AIME*, **236**, 149-158, 1966.

(33) Chalmers, B., The structure of ingots, *J. Australian Inst. Metals*, **8**(3), 255-263, 1963.

(34) Flood, S.C. and Hunt, J.D., Columnar to equiaxed transition, *Metals Handbook, 9th edition*, ASM International, **15**, "Casting", 130-136, 1988.

(35) Pekguleryuz, M.O. and Pedneau, N., In-situ method for the investigation of equiaxed grain growth in hypoeutectic and hypereutectic Al-Si alloys, *Scripta Materialia*, **38**(10), 1533-1539, 1998.

(36) Crossley, F.A., Fisher, R.D. and Metcalfe, A.G., Viscous shear as an agent for grain refinement in cast metal, *Trans. Met. Soc. AIME*, **221**, 419-420, 1961.

(37) Langenberg, F.C., Pestel, G. and Honeycutt, C.R., Grain refinement of steel ingots by solidification in a moving electromagnetic field, *Trans. Met. Soc. AIME*, **221**, 993-1001, 1961.

(38) Metz, S.A. and Flemings, M.C., A fundamental study of hot tearing, *Transactions of the AFS*, **78**, 453-460, 1970.

(39) Guven, Y.F. and Hunt, J.D., Hot-tearing in aluminium-copper alloys, *Cast Metals*, **1**, 104, 1988.

(40) Liu, Q., Smith, R.W.and Sahoo, M., Control of hot tearing in cast-to-shape products, *Solidification Processing* (Eds.J. Beech and H. Jones), University of Sheffield, UK, 213-216, 1997.

(41) McDonald, R.J. and Hunt, J.D., Fluid motion through the partially solid regions of a casting and its importance in understanding A type segregation, *Trans. Met. Soc. AIME*, **245**, 1993-1997, 1969.

(42) McDonald, R.J. and Hunt, J.D., Convective fluid motion within the interdendritic liquid of a casting, *Metall. Trans.*, **1**, 1787-1788, 1970.

(43) Hebditch, D.J. and Hunt, J.D., Fluid motion within the partially solid region of a casting, *Metall. Trans.*, **4**, 2008-2010, 1973.

(44) Streat, N. and Weinberg F., Macrosegregation during solidification resulting from density differences in the liquid, *Metall. Trans.*, **5**, 2539-2548, 1974.

(45) Hebditch, D.J. and Hunt, J.D., Observations of ingot macrosegregation on model systems, *Metall. Trans.*, **5**, 1557-1664, 1974.

(46) Tewari, S.N. and Shah, R., Macrosegregation during steady-state arrayed growth of dendrites in directionally solidified Pb-Sn alloys, *Metall. Trans.*, **23A**, 3383-3392, 1992.

(47) Mehrabian R., Keane, M. and Flemimgs, M.C., Interdendritic fluid flow and macrosegregation; influence of gravity, *Metall. Trans.*,**1**, 1209-1220, 1970.

(48) Fisher, K.M. and Hunt, J.D., Observations on the nature and extent of gravitational interdendritic fluid flow, *Solidification and Casting of Metals*, The Metals Society, London, 325-330,1979.

(49) Fisher, K.M. and Hunt, J.D., Investigation of time required for gravitational interdendritic fluid flow mechanism to produce appreciable macrosegregation, *Solidification Technology in the Foundry and Cast House*, The Metals Society, London, 176-181, 1983.

(50) Chen, C.F.,Experimental study of convection in a mushy layer during directional solidification, *J. Fluid Mech.*, **293**, 81-98, 1995.

(51) Hellawell A., Sarazin, J.R. and Steube, R.S., Channel convection in partly solidified systems, *Phil. Trans. R. Soc. Lond. A*, **345**, 507-544, 1993.

(52) Combeau, H., Appolaire, B. and Lesoult, G., Recent progress in understanding and preciction of macro and microsegregations, *Modeling of Casting, Welding and Advanced Solidification Processes VIII* (Eds. B.G. Thomas and C. Beckermann), TMS, Warrendale, PA, USA, 245-256, 1998.

(53) Tait, S., Jarrling, K. and Jaupart, C., The planform of compositional convection and chinmey formation in a mushy layer, *Nature*, **359**, 406-408, 1992.

(54) Griffiths, W.D., Xiao, L. and McCartney, D.G., The influence of bulk natural convection on the formation of the equiaxed regions in Al-Cu and Al-Si alloys, *Mater. Sci. Eng.*, **A205**, 31-36, 1996.

(55) Billia, B. and Fecht, H.-J., Microstructure and control in advanced casting processes, *A World Without Gravity*, ESA, Noordwijk, The Netherlands, 186-210, 2001.

(56) Camel, D. and Dupouy, M.D., Comparative study of the columnar-equiaxed transition in microgravity and on ground during directional solidification of a refined Al-3.5 wt% Ni alloy, *J. Phys. IV*, **11**(6), 119-126, 2001.

(57) Jaluria, Y. and Torrance, K.E., *Computational Heat Transfer*, Hemisphere Publising Corporation, Washington, USA, 1986.

(58) Mampaey, F., A stable alternating direction method for simulating multi-dimensional soldification problems, *International Journal for Numerical Methods in Engineering*, **30**, 711-728, 1990.

(59) Smith, G.D., *Numerical Solution of Partial Differential Equations. Finite Difference Methods*, 3rd edition, Clarendon Press, Oxford, 1985.

(60) Patankar, S.V., *Numerical Heat Transfer and Fluid Flow*, Hemisphere Publishing Corporation, Washington, USA, 1980.

(61) Lewis, R.W., Morgan, K., Thomas, H.R. and Seetharamu, K.N., *The Finite Element Method in Heat Transfer Analysis*, John Wiley and Sons, Chichester, UK, 1996.

(62) Martin, C.H. and Carey, G.F., *Introduction to Finite Element Analysis*, McGraw Hill, New York, 1973.

(63) Press W.H., Flannery, B.P., Teukolsky, S.A. and Vetterling W.T., *Numerical Recipes: the Art of Scientific Computing*, Cambridge University Press, Cambridge, 1986.

(64) Pozridikis, C., *Introduction to Theoretical and Computational Fluid Dynamics*, Oxford University Press, Oxford, 1997.

(65) Abbott, M.B. and Basco D.R., *Computational Fluid Dynamics : an Introduction for Engineers*, Longman Scientific and Technical, Harlow, Essex, UK, 1989.

(66) *Using MATLAB Version 5*, The Mathworks, Inc., Natick, MA, USA, 1998.

(67) George, A., Nested dissection of a regular finite element mesh, *SIAM J. Numer. Anal.*, **10**(2), 345-363, 1973.

(68) George, J.A. and Liu, J.W., *Computer Solution of Large Sparse Positive Definite Systems*, Prentice-Hall, Englewood Cliffs, NJ, USA, 1981.

(69) George, A. and Ng, E., SPARSPAK : *Waterloo Sparse Matrix Package User's Guide for SPARSPAK-B.*, **CS-84-37.**, Department of Computer Science, University of Waterloo, Ontario, Canada.

(70) Duff, I.S., Erisman, A.M. and Reid, J.K., *Direct Methods for Sparse Matrices*, Clarendon Press, Oxford, 1986.

(71) Saad, Y., *Iterative Methods for Sparse Linear Systems*, PWS Publishing Company, Boston, USA, 1996.

(72) Voller, V.R., An overview of numerical methods for solving phase change problems, *Advances in Numerical Heat Transfer. Volume 1.* (eds. W.J. Minkowycz and E.M. Sparrow), Taylor & Francis, Washington, 341-380, 1997.

(73) Drezet, J.-M. and Rappaz, M., Modeling of ingot distortions during direct chill casting of aluminum alloys, *Metall. Mater. Trans.*, **27A**, 3214-3225, 1996.

(74) M'Hamdi M., Combeau H. and Lesoult, G., Modelling of heat transfer coupled with columnar dendritic growth in continuous casting of steel, *International Journal of Numerical Methods for Heat and Fluid Flow*, **9**(3), 296-317, 1999.

(75) Bradbury, P., *A Mathematical Model for the Twin Roll Casting Process*, D.Phil. Thesis, University of Oxford, 1994.

(76) Browne, D.J., *The Measurement of Heat Transfer Coefficients in Roll Casting*, M.Sc. Thesis, University of Oxford, 1989.

(77) Brody, H.D. and Flemings, M.C., Solute redstribution in dendritic solidification, *Trans. Met. Soc. AIME*, **236**, 615-624, 1966.

(78) Bower, T.F., Brody, H.D. and Flemings, M.C., Measurement of solute distribution in dendritic solidification, *Trans. Met. Soc. AIME*, **236**, 624-634, 1966.

(79) Kirkwood, D.H. and Evans, D.J., Calculations on microsegregation in binary alloys, *The Solidification of Metals*, The Iron and Steel Institute, Publication 110, London, 108-111, 1968.

(80) Ogilvy, A.J.W. and Kirkwood, D.H., A model for numerical computation of microsegregation in alloys, *Applied Scientific Research*, **44**, 43-49, 1987.

(81) Howe, A.A., Development of a computer model of dendritic microsegregation for use with multicomponent steels, *Applied Scientific Research*, **44**, 51-59, 1987.

(82) Howe, A.A. and Kirkwood, D.H., Computer prediction of microsegregation in peritectic alloy systems, *Materials Science and Technology*, **16**, 961-967, 2000.

(83) Voller, V.R., A semi-analytical model of microsegregation and coarsening in a binary alloy, *J. Cryst. Growth*, **197**, 333-340, 1999.

(84) Sarreal, J.A. and Abbaschian, G.J., The effect of solidification rate on microsegregation, *Metall. Trans.*, **17A**(11), 2063-2073, 1986.

(85) Hunt, J.D. and Thomas, R.W., Microscopical modelling of binary/multicomonent alloys, *Solidification Processing* (Eds.J. Beech and H. Jones), University of Sheffield, UK, 350-353, 1997.

(86) Hunt, J.D. and Lu, S.-Z., Numerical modelling of cellular/dendritic array growth : spacing and structure predictions, *Metall. Mater. Trans.*, **27A**, 611-623, 1996.

(87) Shin, M.R.M. and Hunt, J.D., Numerical modelling of microsegregation in multi-component eutectic and peritectic alloys, manuscript in preparation for submission for publication, 2002.

(88) Davies, R.H., Dinsdale, A.T., Chart, T.G., Barry, T.I and Rand, M.H., Application of MTDATA to the modeling of multicomponent equilibria, *High Temp. Sci.*, **26**, 251-262, 1989.

(89) Launder B.E. and Massey, T.H., The numerical prediction of viscous flow and heat transfer in tube banks, *ASME J. Heat Transfer*, **100**, 565-571,1978.

(90) Sangani, A.S. and Acrivos, A., Slow flow past periodic arrays of cylinders with application to heat transfer, *Int. J. Multiphase Flow*, **8**(3), 193-206, 1982.

(91) Drummond, J.E. and Tahir, M.I., Laminar viscous flow through regular arrays of parallel solid cylinders, *Int. J. Multiphase Flow*, **10**(5), 515-540, 1984.

(92) Ferréol, B. and Rothman, D., Lattice-Boltzmann simulations of flow through Fontainebleau stone, *Transport in Porous Media*, **20**, 3-20, 1995.

(93) King, M.J., King, P.R., McGill, C.A. and Williams, J.K., Effective properties for flow calculations, *Transport in Porous Media*, **20**, 169-196, 1995.

(94) Emms, P.W. and Fowler, A.C., Compositional convection in the solidification of binary alloys, *J. Fluid Mech.*, **262**, 111-139, 1994.

(95) Schneider, M.C., Beckermann, C., A numerical study of the combined effects of microsegregation, mushy zone permeability and flow, caused by volume contraction and thermosolutal convection, on macrosegregation and eutectic formation in binary alloy solidification, *Int. J. Heat Mass Transfer*, **38**(18), 3455-3473, 1995.

(96) Poirier, D.R., Permeability for flow of interdendritic liquid in columnar-dendritic alloys, *Metall. Trans.*, **18B**, 245-255, 1987.

(97) Dupouy, M.D. and Camel, D., Effects of gravity on columnar dendritic growth of metallic alloys : flow pattern and mass transfer, *J. Cryst. Growth*, **183**, 469-489, 1998.

(98) Krane, M.J.M., Incropera, F.P. and Gaskell, D.R., Solidification of a ternary metal alloy : a comparison of experimental measurements and model predictions in a Pb-Sb-Sn system, *Metall. Mater. Trans.*, **29A**, 843-853, 1998.

(99) Vreeman, C.J., Krane, M.J.M. and Incropera, F.P., The effect of free floating dendrites and convection on macrosegregation in direct chill cast aluminum alloys. Part I : model development, *Int. J. Heat Mass Transfer*, **43**, 677-686, 2000.

(100) Vreeman, C.J. and Incropera, F.P., The effect of free floating dendrites and convection on macrosegregation in direct chill cast aluminum alloys. Part II : predictions for Al-Cu and Al-Mg alloys, *Int. J. Heat Mass Transfer*, **43**, 687-704, 2000.

(101) Ahmed, N., Combeau, H., Desbiolles, J.L., Jalanti, T., Lesoult, G., Rappaz, J., Rappaz, M. and Stomp, C., Numerical simulation of macrosegregation : a comparison of FVM and FEM predictions with experiments, *Solidification Processing* (Eds.J. Beech and H. Jones), University of Sheffield, UK, 341-345, 1997.

(102) Felicelli, S.D., Heinrich, J.C. and Poirier, D.R., Three-dimensional simulations of freckles in binary alloys, *J. Cryst. Growth*, **191**, 879-888, 1998.

(103) Sarazin, J.R. and Hellawell, A., Channel formation in Pb-Sn, Pb-Sb, and Pb-Sn-Pb alloy ingots and comparison with the system NH_4Cl-H_2O, *Metall. Trans.*, **19A**, 1861-1871, 1988.

(104) Frueh, C., Poirier, D.R. and Felicelli, S.D., Predicting freckle-defects in directionally solidified Pb-Sn alloys, *Mater. Sci. Eng.*, **A328**, 245-255, 2002.

(105) Trivedi R., Growth of dendritic needles from a supercooled melt, *Acta Met.*, **18**, 287-296, 1970.

(106) Burden, M.H., *Factors Affecting Grain Size in Castings*, D. Phil. Thesis, University of Oxford, 1973.

(107) Flemings, M.C., New solidification processes and products, *Solidification and Casting of Metals*, The Metals Society, London, 479-485, 1979.

(108) Hunt, J.D., Cellular and primary dendrite spacings, *Solidification and Casting of Metals*, The Metals Society, London, 3-9, 1979.

(109) Tiller, W.A., Foreword. Quantitative solidification science, *Mater. Sci. Eng.*, **65**, 3-5, 1984.

(110) Hunt, J.D., Steady state columnar and equiaxed growth of dendrites and eutectic, *Mater. Sci. Eng.*, **65**, 75-83, 1984.

(111) Hunt, J.D. and McCartney, D.G., Numerical finite difference model for steady state cellular array growth, *Acta Metall.*, **35**(1), 89-99, 1987.

(112) Hunt, J.D., A numerical analysis of time dependent isolated dendritic growth for conditions near the steady state, *Acta Metall. Mater.*, **38**(3), 411-418, 1990.

(113) Lu, S.-Z. and Hunt, J.D., A numerical analysis of dendritic and cellular array growth : the spacing adjustment mechanisms, *J. Cryst. Growth*, **123**, 17-34, 1992.

(114) Tassa, M. and Hunt, J.D., The measurement of Al-Cu dendrite tip and eutectic interface temperatures and their use for predicting the extent of the eutectic range, *J. Cryst. Growth*, **34**, 38-48, 1976.

(115) Hunt, J.D. and Thomas, R.W., *"Alloy" software manual, Version 2*, University of Oxford, 1997.

(116) Jones, H., On array model theoretical calculations versus measurements for the growth undercooling of aluminide dendrites in Bridgman solidified aluminium alloys, *Scripta Mater.*, **45**, 95-101, 2001.

(117) Rappaz, M. and Thevoz, Ph., Solute diffusion model for equiaxed dendritic growth, *Acta Metall.*, **35**(7), 1487-1497, 1987.

(118) Rappaz, M. and Thevoz, Ph., Solute diffusion model for equiaxed dendritic growth : analytical solution, *Acta Metall.*, **35**(12), 2929-2933, 1987.

(119) Esaka, H. and Kurz, W., Columnar dendrite growth : a comparison of theory, *J. Cryst. Growth*, **69**, 362-366, 1984.

(120) Avrami, M., Kinetics of phase change II. Transformation-time relations for random ditsribution of nuclei, *J. Chem. Phys.*, **8**, 212-224, 1940.

(121) Flood, S.C. and Hunt, J.D., Columnar and equiaxed growth. II. Equiaxed growth ahead of a columnar front, J. Cryst. Growth, **82**, 552-560, 1987.

(122) Thevoz, Ph., Desbiolles J.L. and Rappaz, M., Modeling of equiaxed microstructure formation in casting, *Metall. Trans.*, **20A**, 311-322, 1989.

(123) Nielsen, O., Appolaire, B., Mo., A. and Combeau, H., Determination of the grain morphology in equiaxed Al-Cu alloys, *Modeling of Casting, Welding and Advanced Solidification Processes IX* (Eds. P.R. Sahm, P.N. Hansen and J.G. Conley), Shaker Verlag, Aachen, 513-520, 2000.

(124) Appolaire, B., Combeau, H. and Lesoult, G., Modelling of equiaxed growth with convection, *Solidification Processing* (Eds.J. Beech and H. Jones), University of Sheffield, UK, 295-298, 1997.

(125) Steinbach, I. and Prieler, R., A deterministic nucleation model for equiaxed solidification, *Transport Phenomena in Solidification (HTD-Vol. 284/AMD-Vol. 182)*, ASME, 69-74, 1994.

(126) Malvern. L.E., *Introduction to the Mechanics of a Continuous Medium*, Prentice Hall, 1969.

(127) Lubliner, J., On the thermodynamic foundations of non-linear solid mechanics, *Int. J. Non-Linear Mechanics*, **7**, 237-254, 1972.

(128) Lubliner, J., *Plasticity Theory*, Macmillan, New York,1990.

(129) Celentano, D., Oller, S. and Oñate, E., A coupled thermomechanical model for the solidification of cast metals, *Int. J. Solids Structures*, **33**(5), 647-673, 1996.

(130) Grong, Ø.,Dahle, A.K., Onsøien, M.I. and Arnberg, L., Analytical modelling of equiaxed solidification, *Acta Mater.*, **46**(14), 5045-5052, 1998.

(131) Gardner, M., The fantastic combinations of John Conway's new solitaire game "Life", *Scientific American*, **223**(10), 120-123, 1970.

(132) Wolfram, S., Preface - Proceedings of an interdisciplinary workshop on Cellular Automata, Los Alamos, NM, USA, March 1983, *Physica D*, **10**, vii-xii, 1984.

(133) Toffoli, T., Cellular automata as an alternative to (rather than an approximation of) differential equations in modelling physics, *Physica D*, **10**, 117-127, 1984.

(134) Vichniac, G.Y., Simulating physics with cellular automata, *Physica D*, **10**, 96-116, 1984.

(135) Montheillet, F. and Gilormini, P., Predicting the mechanical behaviour of two-phase materials with cellular automata, *International Journal of Plasticity*, **12**(4), 561-654, 1996.

(136) Packard, N.H., Lattice models for solidification and aggregation, *Theory and Applications of Cellular Automata* (Ed. S. Wolfram), World Scientific, 305-310, 1987.

(137) Rappaz, M. and Gandin, Ch.-A., Probabilistic modelling of microstructure formation in solidification processes, *Acta Metall. Mater.*, **41**(2), 345-360, 1993.

(138) Kurz, W., Giovanola, B. and Trivedi R., Theory of microstructural development during rapid solidification, *Acta Metall.*, **34**(5), 823-830, 1986.

(139) Gandin, Ch.-A. and Rappaz, M., A coupled finite element-cellular automaton model for the prediction of dendritic grain structures in solidification processes, *Acta Metall. Mater.*, **42**(7), 2233-2246, 1994.

(140) Rappaz, M., Gandin, Ch.-A., Desbiolles, J.-L., and Thevoz, Ph., Prediction of grain structures in various solidification processes, *Metall. Mater. Trans.*, **27A**, 695-705, 1996.

(141) Carter, P., Cox, D.C., Gandin, Ch.-A. and Reed, R.C., Process modelling of grain selection during the solidification of single crystal superalloy castings, *Mater. Sci. Eng.*, **A280**, 233-246, 2000.

(142) O'Mahoney, D. and Browne, D.J., Use of experiment and an inverse method to study interface heat transfer during solidification in the investment casting process, *Experimental Thermal and Fluid Science*, **22**, 111-222, 2000.

(143) Browne, D.J. and O'Mahoney, D., Interface heat transfer in investment casting of aluminum alloys, *Metall. Mater. Trans.*, **32A**, 3055-3063, 2001.

(144) Beck, B.V. and Blackwell, B., *Inverse Heat Conduction : Ill Posed Problems*, Wiley Interscience, New York, 1985.

(145) Warnken N., Rezende J., Schadt, R., Wagner, I. and Sahm, P.R., Simulating grain structure formation with a rotated-grid cellular automaton model, *Modeling of Casting, Welding and Advanced Solidification Processes IX* (Eds. P.R. Sahm, P.N. Hansen and J.G. Conley), Shaker Verlag, Aachen, 566-573, 2000.

(146) Vandyoussefi, M. and Greer, A.L., Application of cellular automata-finite element model to the grain refinement of directionally solidified Al-4.15 wt.%Mg alloys, *Acta Mat.*, **50**, 1693-1705, 2002.

(147) Nastac, L. and Stefanescu, D.M., Stochastic modelling of microstructure formation in solidification processes, *Modelling Simul. Mater. Sci. Eng.*, **5**, 391-420, 1997.

(148) Pang, H. and Stefanescu, D.M., Stochastic modelling of dendrite and eutectic grain structure evolution during solidification, *Solidification Science and Processing* (Eds. I. Ohnaka and D.M Stefanescu), TMS, Warrendale, PA, USA, 149-156, 1996.

(149) Crank, J., *Free and Moving Boundary Problems*, Oxford University Press, Oxford, 1984.

(150) Shamsundar, N. and Sparrow, E.M., Analysis of multidimensional conduction phase change via the enthalpy model, *J. Heat Transfer*, **97**, 333-340,1975.

(151) Ayyub, B.M. and McCuen, R.H., *Numerical Methods for Engineers*, Prentice Hall, Upper Saddle River, NJ, USA, 1996.

(152) Jaluria, Y., *Computer Methods for Engineering*, Taylor and Francis, Washington, DC, USA, 1996.

(153) Daly, B.J., A technique for including surface tension effects in hydrodynamic calculations, *J. Comp. Phys.*, **4**, 97-117, 1969.

(154) Charbon, Ch. and LeSar, R., A fully coupled 2D model of equiaxed eutectic solidification, *Solidification Science and Processing* (Eds. I. Ohnaka and D.M Stefanescu), TMS, Warrendale, PA, USA, 141-148, 1996.

(155) Shyy, W., *Computational Modelling for Fluid Flow and Interfacial Transport*, Elsevier, Amsterdam, 1994.

(156) Slıyy, W., Udaykumar, H.S., Rao, M.M. and Smith, R.W., *Computational Fluid Dynamics with Moving Boundaries*, Taylor and Francis, Washington DC, USA, 1996.

(157) Juric, D. and Tryggvason, G., A front-tracking method for dendritic solidification, *J. Comp. Phys.*, **123**, 127-148, 1996.

(158) Lakehal, D., Meier, M. and Fulgosi, M., Interface tracking towards the direct simulation of heat and mass transfer in multiphase flows, *Int. J. Heat and Fluid Flow*, **23**, 242-257, 2002.

(159) Yadigaroglu, G., Application of cascades of CFD methods to two-phase flow problems, *Proc. 3rd Int. Conf. Transport Phenomena in Multiphase Systems* (Eds. M.E. Poniewski, T. Wójcik and R. Pastuszko), Baranów Sandomierski, Poland, 179-186, 2002.

(160) Flood, S.C. and Hunt, J.D., Columnar and equiaxed growth. I. A model of a columnar front with a temperature dependent velocity, *J. Cryst. Growth*, **82**, 543-551, 1987.

(161) McCartney, D.G., *Studies on Cellular and Dendritic Solidification*, D. Phil. Thesis, University of Oxford, 1981.

(162) Hunt, J.D., A numerical analysis of dendritic and cellular growth of a pure material investigating the transition from "array" to "isolated" growth, *Acta Metall. Mater.*, **39**(9), 2117-2133, 1991.

(163) Derby, J.J., Atherton, L.J. and Gresho, P.M., An integrated process model for the growth of oxide crystals by the Czochralski method., *J. Cryst. Growth*, **97**, 792-826, 1989.

(164) Lan, C.W. and Liang, M.C., A three-dimensional finite volume/Newton method for thermal-capillary problems, *International Journal for Numerical Methods in Engineering*, **40**, 621-636, 1997.

(165) Wheeler, A., Modelling microstructure with phase field methods, Seminar, Department of Materials, University of Oxford, 18th June, 1999.

(166) Langer, J.S., Models of pattern formation in first-order phase transitions, *Directions in Condensed Matter Physics* (Eds. G. Grinstein and G. Mazenko), World Scientific, Singapore, 164-186, 1986.

(167) Caginalp, G., Surface tension and supercooling in solidification theory, *Applications of Field Theory to Statistical Mechanics* (Ed. L. Garrido), Springer, Berlin, 216-226, 1985.

(168) Warren, J.A. and Boettinger, W.J., Prediction of dendritic microsegregation patterns using a diffuse interface phase field model, *Modelling of Casting, Welding and Advanced Solidification Processes VII* (Eds. M. Cross and J. Campbell), TMS, Warrendale, PA, USA, 601-607, 1995.

(169) Nestler, B. and Wheeler, A.A., Multi-phase modelling of peritectic, eutectic and monotectic solidification, *Modeling of Casting, Welding and Advanced Solidification Processes IX* (Eds. P.R. Sahm, P.N. Hansen and J.G. Conley),Shaker Verlag, Aachen, 505-512, 2000.

(170) Tong, X., Beckermann, C. and Karma, A., Phase field simulation of dendritic growth with convection, *Modeling of Casting, Welding and Advanced Solidification Processes VIII* (Eds. B.G. Thomas and C. Beckermann), TMS, Warrendale, PA, USA, 613-620, 1998.

(171) Dantzig, J.A., Provatas, N., Goldenfeld, N., LaCombe, J.C., Lupulescu, A., Koss, M.B. and Glicksmann, M.E., A comparison of phase-field computations with experimental microgravity measurements for dendritic growth in pure materials, *Modeling of Casting, Welding and Advanced Solidification Processes IX* (Eds. P.R. Sahm, P.N. Hansen and J.G. Conley), Shaker Verlag, Aachen, 453-460, 2000.

(172) Diepers, H.J., Beckermann, C. and Steinbach, I., A phase-field method for alloy solidification with convection, *Solidification Processing* (Eds. J. Beech and H. Jones), University of Sheffield, UK, 426-430, 1997.

(173) Steinbach, I., Beckermann, C., Kauerauf, B., Li. Q. and Guo, J., Three-dimensional modeling of equiaxed dendritic growth on a mesoscopic scale, *Acta Mater.*, **47**(3), 971-982, 1999.

(174) Jacot, A. and Rappaz, M., A pseudo-front tracking technique for the modelling of solidification microstructures in multi-component alloys, *Acta Mater.*, **50**, 1909-1926, 2002.

(175) Quested, P.N., Mills, K.C., Brooks, R.F., Monaghan, B., Dinsdale, A.T., Day, A., Richardson, M.J., Andon, R.J.L., Taylor, R. and Szelagowski, H., Physical property measurements for the mathematical modelling of heat and fluid flow in solidification processes, *Modelling of Casting, Welding and Advanced Solidification Processes VII* (Eds. M. Cross and J. Cambpell), TMS, Warrendale, PA, USA, 407-415, 1995.

(176) Abramowitz.M. and Stegun, I., *Handbook of Mathematical Functions*, Dover, London, 1965.

(177) Davis, P.J., *Interpolation and Approximation*, Dover, London, 1975.

(178) Turnbull, D. and Fisher, J.C., Rate of nucleation in condensed systems, *J. Chem. Phys.*, **17**(1), 71-73, 1949.

(179) Szelagowski, H., Taylor, R., Hunt, J.D. and Quested, P.N., A numerical analysis of the laser flash technique applied to a semi-solid material, *Solidification Processing* (Eds.J. Beech and H. Jones), University of Sheffield, UK, 151-154, 1997.

(180) *ASM Handbook, Volume 3, Alloy Phase Diagrams*, ASM International, Materials Park, OH, USA, 1992.

(181) Banaszek, J., Browne, D.J. and Furmanski, P., Some aspects of modelling of binary system solidification on a fixed grid, *Proc. 3rd Int. Conf. Transport Phenomena in Multiphase Systems* (Eds. M.E. Poniewski, T. Wójcik and R. Pastuszko), Baranów Sandomierski, Poland, 201-209, 2002.

(182) Browne, D.J., Banaszek, J. and Hunt. J.D., Front tracking on a fixed grid versus enthalpy approach in modelling of binary alloy solidification, *Proceedings of the International Mechanical Engineering Congress and Exhibition*, New Orleans, USA, paper IMECE2002-32871, 2002.

(183) Wojnar, L. and Kurzydlowski, K.J., *Practical Guide to Image Analysis; Chapter 7 : Analysis and Interpretation*, ASM International, Materials Park, OH, USA, 145-202, 2000.

(184) Barushel, J., Buffière, J.-V., Maire, E., Merle, P. and Peix, G., *X-Ray Tomography in Materials Science*, Hermes Science Publications, Paris, 2000.

(185) Billia, B. (Ed.), *Columnar-Equiaxed Transition in Solidification Processing*, ESA MAP Project No. 14313, Mid-Term Report, January, 2002.

(186) Browne, D.J. and Hunt, J.D., Modelling of moving boundaries in multi-phase systems : a front-tracking approach, *Proc. 3rd Int. Conf. Transport Phenomena in Multiphase Systems* (Eds. M.E. Poniewski, T. Wójcik and R. Pastuszko), Baranów Sandomierski, Poland, 227-232, 2002.

Appendix

Appendix A

Implicit Model Development - Details

Figure 3.6 was used to illustrate the explicit model, where each marker *m* was advanced a distance z_m as calculated from its temperature at the *start* of the time step (equations (3.8) and (3.9)). With an implicit approach, the velocity at the *end* of the time step must be consistent with the temperature field at that time. This marker velocity is consistent with a tip temperature, via equation (3.8). The temperature of any marker T_m^* must be same as the temperature at that location T_m^{cv} found from interpolation from the surrounding control volume nodes. The goal then is to reduce the error term

$$e_m = T_m^* - T_m^{cv} \qquad \text{(A.1)}$$

for each marker *m*. The problem must be solved for all markers simultaneously. With the implicit method, the use of Cartesian identifiers (i,j) for each node or c.v. must be replaced with a system whereby each cell has a single unique identifier *q*. The problem is a non-linear one. It can be linearised by use of the Newton method [59,63], after which it is expressed in matrix form as

$$[A]\{x\} = \{b\} \qquad \text{(A.2)}$$

where [A] is a matrix, {x} and {b} are column vectors. The problem is solved when {x} is known. The right hand side {b} contains essentially error terms which must be eliminated i.e. the solution {x} is that for which (b}={0}. The error terms are: inaccuracy in heat balance in each control volume f_q, and the thermal errors e_m. From equation (3.15 b),

$$f_q = f_{tot} - f_n - f_s - f_e - f_w - f_l \tag{A.3}$$

So if there are Q control volumes and M markers, then {x} and {b} are of length $Q+M$. The solution {x} consists of iterative updates δT_q and δz_m to the temperature of the control volumes and the position of the markers : these updates should progressively reduce f_q and e_m in {b}, respectively.

The elements of the Jacobian matrix [A] must be assembled. They are all gradient terms. Some of the entries are of the general form $\partial f_q/\partial T_r$, as would be used for the conventional conduction heat equation, and can be calculated analytically. Others take account of the fact that the position of the markers will be affected by variations in the temperature field, and vice-versa. These terms are of the form $\partial e_m/\partial z_n$, $\partial f_q/\partial z_n$, and $\partial e_m/\partial T_r$. These three terms express the effects of changing the position of marker n on the temperature error term for marker m, of changing the position of marker n on the flux error term for c.v. q, and of changing the temperature of control volume r on the temperature error term for marker m, respectively. These terms can only be found by numerical perturbation, or numerical differentiation e.g.

$$\frac{\partial e_m}{\partial T_r} \approx \frac{e_m(T_r + \Delta T_r) - e_m(T_r)}{\Delta T_r} \tag{A.4}$$

It can already be seen that, for an algorithm for which the general feasibility is as yet unknown, the implicit method becomes highly complicated. It becomes increasingly difficult to distinguish between flaws in the underlying algorithm and problems with, for example, assembling [A]. Also, the method outlined to solve the problem implicitly is based only on columnar growth (Fig 3.6). The level of complication is expected to increase significantly when multiple equiaxed grains are also to be treated.

The problem expressed in equation (A.2) is linear and can be solved by direct methods. This will give an approximate solution to the problem, and iteration must be used in order to achieve convergence to the true solution.